A STUDY OF DAMAGE CLUSTERS PRODUCED BY HEAVY-ION IRRADIATION OF NICKEL AND ITS ALLOYS

T.M. ROBINSON

Oriel College, Oxford

A dissertation submitted for the degree of Doctor of Philosophy in the University of Oxford, June 1978.

To my Mother

ABSTRACT

A Study of Damage Clusters Produced by Heavy-Ion Irradiation of Nickel and its Alloys

T.M. Robinson

Oriel College, Oxford

A dissertation submitted for the degree of Doctor of Philosophy, Trinity term 1978.

The damage clusters produced by low dose, 80 keV Ni^+ and W^+ heavy-ion bombardment of pure nickel; of two nichrome alloys (with 8% and 17%Cr); and of a ternary alloy and 321 stainless steel which have the same base composition (Fe/Ni10%/Cr17%) have been studied by means of transmission electron microscopy. In all cases where the defects could be identified with confidence they were found to be vacancy in nature. Most of the defects were identified as Frank loops, some of which had partially dissociated. The number of loops that were identified as dissociated and the average degree of dissociation were dependent on the stacking fault energy γ, being greater in the low-γ ternary alloy and the stainless steel than in the high-γ nickel and nichrome alloys. In the high-γ materials a small proportion (< 5%) of perfect loops was also observed. Defect yield values were between a factor of 2 and 5 higher for W^+ ion bombardment than for the corresponding Ni^+ ion irradiations, but the effect on the mean defect size and cascade efficiency was much less pronounced. In the case of the Ni^+ ion bombardment, the defect yields in the two nichrome alloys were lower than in pure Ni. No such effect was observed for the W^+ ion irradiations, when defect yield and cascade efficiency values very similar to those of pure nickel were obtained. The defect yield in the W^+ ion irradiated ternary alloy was considerbly smaller than in the nichrome alloys and there was a further major decrease in the stainless steel. These reductions in defect yields were not accompanied by a change in the mean defect size nor in the distribution of the defect sizes which were very similar in all the materials for irradiation by a given ion species. The defect yield in W^+ ion irradiated Ni remained constant with increasing irradiation temperature up to $\sim$450°C and then decreased sharply at higher irradiation temperatures. The defect yield in W^+ ion irradiated Ni/Cr17% remained constant up to at least 500°C. Possible physical explanations for these results are discussed.

PREFACE

This dissertation is an account of the research carried out by the author in the Department of Metallurgy and Science of Materials in the University of Oxford, between October 1973 and June 1978. The work was carried out initially under the supervision of Dr. M.J. Whelan, F.R.S., and since December 1975 under the supervision of Dr. M.L. Jenkins. The research described in this thesis is original, although the work of others has been drawn on freely, with due acknowledgement being made in the text. A complete list of references appears at the end of the thesis.

The author would like, in particular, to express his sincere gratitude to Dr. M.L. Jenkins for his constant interest, encouragement and advice throughout the major part of this work. He would like to thank Dr. D.J. Mazey for his patience and understanding and Dr. C.A. English for many useful and stimulating discussions. He is grateful for the help of, and for useful discussions with, many members of the Oxford Department of Metallurgy and Science of Materials.

The author would like to thank Mr. G. Dixon-Brown and Mr. D. Tansley for their maintenance of the electron microscope. He would also like to thank: Mr. A.E. Symonds of the Metallurgy Division, AERE Harwell, for the fabrication of the alloys; Mr. D.J. Chivers of the Chemistry Division, AERE Harwell, for carrying out the heavy-ion irradiations; and Mr. A.G. Morton and Mr. D.R. Williams of the Environmental and Medical Sciences Division, AERE Harwell, for the spectrographic and activation analyses of the specimens.

The author would like to record his gratitude to Professor Sir Peter Hirsch, F.R.S., and Dr. R.S. Nelson for the provision of laboratory facilities. He is grateful for the financial support which was provided during this work by the Science Research Council and the United Kingdom Atomic Energy Authority.

Turning now to the preparation of this thesis; it gives the author

much pleasure to thank Miss E.J. Swain for her careful typing of the manuscript. He would also like to express his appreciation to AERE Harwell for assistance with the diagrams and with the photographic work.

Finally, the author would like especially to thank his wife, Francine, for her understanding and encouragement while this thesis was being written.

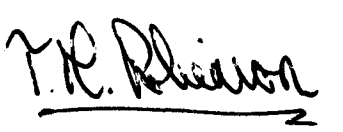

T.M. Robinson
June, 1978.

Oriel College,
Oxford.

CONTENTS

CHAPTER 1

Introduction to Radiation Damage Studies

1.1 The Interaction Between Fast Neutrons and the Atomic Lattice

1.1.1 The Void Problem in Nuclear Reactors

The achievement of a chain reaction in a nuclear reactor requires that, on average, one of the neutrons produced in the fission reaction will itself cause the fission of a further nucleus. Naturally occurring uranium consists mainly of U_{238} (99.28%), which can only be fissioned by neutrons having energies greater than about 1 MeV, and U_{235} (0.71%), which can be fissioned by neutrons of any energy. The fission of a U_{235} nucleus releases approximately 200 MeV of energy, about 85% of which is dissipated as kinetic energy of the fission fragments. The remaining 15% is divided among the β particles, γ rays, neutrinos and neutrons that are produced in the fission reaction. Approximately 2.5 neutrons are produced per fission with an energy spectrum that peaks at about 1 $\rightarrow$ 2 MeV. The macroscopic cross section (Σ), which takes into account the relative abundance of an isotope, for 1 $\rightarrow$ 2 MeV neutrons to be inelastically scattered by U_{238} ($\Sigma \sim 10^{-1}$ cm^{-1}) is greater than the macroscopic fission cross section for these neutrons in either U_{235} ($\Sigma \sim 10^{-3}$ cm^{-1}) or U_{238} ($\Sigma \sim 10^{-2}$ cm^{-1}). Thus it is more probable for a fission neutron to lose a large amount of energy in an inelastic collision rather than for it to produce further fission. Inelastic collisions are possible for neutron energies down to about 100 keV, below which the neutron looses energy more slowly in elastic collisions with the more massive uranium nuclei. The neutron will eventually be absorbed by a uranium atom and, in the energy range 100 eV $\rightarrow$ 100 keV, the probability of it being captured by a U_{238} atom is about forty times the probability of it producing fission in U_{235}. Thus in natural uranium, the majority ($\sim$ 90%) of the fission neutrons are eventually captured by U_{238} and a spontaneous chain reaction does not occur (see for example Jakeman, 1966).

For neutron energies below about 1 eV, the macroscopic cross section to produce fission in U_{235} is greater than the macroscopic cross section

for capture by U_{238}. Thus one way to achieve a chain reaction is to rapidly slow the neutrons down so that their energies are reduced to below 1 eV before they are absorbed. Thus in thermal reactors, the reactor core contains only a small percentage of uranium which is contained in a moderator of low atomic mass and the resulting neutron spectrum consists mainly of low energy (0.025 eV) thermal neutrons.

An alternative way to sustain the chain reaction is to increase the proportion of fissile material so that the macroscopic cross section for fission at energies above 100 keV is comparable with the inelastic collision cross section. This can be achieved by either enriching naturally occurring uranium so that it contains more U_{235}, or by using Pu_{239}. Thus in fast reactors, the core consists almost entirely of fissile material, with little or no moderation, and most of the fission is produced by neutrons having energies above 100 keV. The neutron spectrum from a fast reactor is therefore similar to the fission neutron spectrum. A typical fast reactor neutron spectrum is shown in figure 1.1 (Dean 1974). The energy transferred from these neutrons to the atoms in the lattices of the reactor structural components, that is the primary knock-on atom spectrum, is shown in Figure 1.2 for the case of structural components made of iron (Marwick 1975). These primary knock-on atoms can themselves displace further atoms and because of the energies involved (up to 500 keV), a high concentration of vacancy-interstitial pairs is generated. At the operating temperatures of fast reactors (400°C to 600°C) these vacancy and interstitial point defects are both mobile and their interactions give rise to such phenomena as embrittlement, irradiation induced creep and void swelling.

The problem of void swelling induced dimensional and mechanical instability is important with respect to the fast reactor core components (fuel element cladding, fuel element supports and spacers, control rod guide tubes), but the most severe design and performance problems have arisen

from the void swelling induced in the sub-assembly wrappers (Bishop 1974). Due allowance must be made in the design of fast reactor cores for the elongation and increase in diameter of sub-assemblies, and a critical problem is the bowing of these sub-assemblies due to the non-uniform neutron flux that they experience. One method of overcoming this sub-assembly bowing is to use wrapper materials with low void swelling properties, but the factors that influence void swelling in a given material are still not completely understood and the development of a low swelling alloy is still of major importance.

The advantage of fast reactors over thermal reactors arises because there is only a finite supply of naturally occurring fissile material, that is U_{235}. Pu_{239} is also a fissile material, but it does not occur naturally. It is however formed by the β decay of neutron bombarded U_{238}. Thus if non-fissile U_{238} is placed as a blanket around a reactor core, fissile Pu_{239} will be formed, and in the fast reactor it is possible to generate more fissile material than the amount being consumed. This so called 'breeder' process also takes place in thermal reactors, but the conversion of the uranium takes place more efficiently in the fast reactor environment because of the higher neutron energies. The long term (> 50 years) supply of fissile material therefore depends on the development of the fast reactors, and this development requires a more complete understanding of the factors influencing void swelling.

1.1.2 Displacement Cascades

A fission neutron loses energy in collisions with the lattice atoms of the reactor structural components, and the range of transferred energies (E_T) can be conveniently divided into three sections:-

(1) $E_T < E_D$, where E_D is the threshold displacement energy which depends on the crystallographic direction of the displacement, and typically has values in the range 15 to 50 eV. In general, no permanent lattice damage results in this case.

(2) $E_C > E_T > E_D$, where E_C is some energy of about 1 keV below which essentially isolated Frenkel (vacancy-interstitial) pairs are created.

(3) $E_T > E_C$, which results in the formation of so called 'displacement cascades'.

When the energy transferred to a lattice atom is high enough ($E_T > E_C$), the lattice atom is projected through the lattice as a "primary knock-on" losing energy both elastically in collisions with other atoms creating further displacements, and inelastically by electronic excitation. The relative contributions of elastic and inelastic collisions to the total rate of energy loss of a primary knock-on are shown in Figure 1.3. Most primary knock-ons have energies (< 100 keV) such that the elastic collisions predominate. Thus the mean free path of a primary knock-on is very small and it generates a high local concentration of Frenkel pairs in what Brinkman (1954) called a displacement spike. The spatial distribution of vacancies and interstitials in a displacement cascade is illustrated schematically in figure 1.4.

The importance of these displacement cascades in relation to the lattice damage generated in fast reactor core assemblies arises from the fact that for the unmoderated neutrons in the fast reactor cores, the average energy of a primary knock-on iron atom is approximately 50 keV, and 99% of the atomic displacements are produced by primary knock-on atoms that have $E_T > 5$ keV (Marwick 1975).

A typical displacement cascade generated by a 50 keV primary knock-on iron atom in an austenitic stainless steel contains approximately 350 Frenkel pairs in a region 120 Å long and 80 Å in diameter (Matthews 1974, 1976). Some recombination of the vacancy and interstitial point defects occurs within the cascade region, but there is strong evidence that mechanisms operate which separate the interstitials from the vacancies. One possible mechanism was proposed by Silsbee (1957). He suggested that knock-on atoms

could be focussed along low index directions in crystals by replacement collision sequences. This would result in an interstitial point defect being produced at a large distance from the vacancy at the beginning of the sequence. A recent review of the experimental evidence for the existence of replacement collision sequences has been given by Blewitt et al (1975). Experimental measurements of the length of replacement collision sequences have given values of up to 250 Å (Diehl et al 1968). Replacement collision sequences could, however, only operate for low energy ($< \sim 100$ eV) knock-ons as at higher energies the knock-ons would not be focussed in a collision sequence. Possible separation mechanisms that operate at higher energies are the channelling or quasi-channelling of the knock-on atoms.

The cascade region then consists of a vacancy-rich core surrounded by a shell of interstitials. The vacancy concentration in the core of the cascade ($C_v \sim 10^{21}$ vacancies/cc) is extremely high compared with the equilibrium vacancy concentration in the surrounding crystal ($C_o \sim 10^7$ vacancies/cc at room temperature). The chemical potential ($\mu = kT \ln C_v/C_o$) that arises from this vacancy supersaturation results in a strong driving force for collapse of the vacancy rich region. The hydrostatic pressure arising from the increased density of atoms in the interstitial shell may also be a contributory factor in causing collapse. In all materials so far studied where vacancy loops are produced at cascade sites, it has been found that the initial collapse is onto the close-packed planes. Whether a cascade collapses or not is therefore thought to depend on the energy balance between the chemical and elastic strain energies of the uncollapsed cascade and the nucleation energy of the relevant faulted loop (English et al 1977). The probability of a cascade collapsing to form a loop can be quite high (~ 1) at room temperature (see section 1.5.2.2). In F.C.C. materials cascade collapse appears to take place independently of temperature, but there is evidence to suggest that in some materials the probability of cascade collapse decreases as

the temperature increases (see section 1.5.4.2).

As opposed to vacancy point defects, interstitial point defects are mobile at room temperature. Thus the interstitials that escape from the cascade region can migrate and they may therefore be lost to various sinks or they may aggregate to form interstitial loop nuclei. Bourret and Dautreppe (1968) concluded that this nucleation could take place homogeneously in pure materials, while Eyre et al (1971) and Maher et al (1971) have shown that the presence of impurities in molybdenum results in a finer distribution of the interstitial loops, suggesting that the interstitials react strongly with impurity atoms resulting in heterogeneous nucleation of the loops. At room temperature, these interstitial loop nuclei will grow with increasing dose, due to the migration of interstitials from other cascades.

Interstitial loops are inherently stable, even at reactor operating temperatures, when vacancies as well as interstitials are mobile. The interaction energy between a dislocation and a point defect has a first-order dependence on the size of the distortion field associated with the point defect (Cottrell 1953). Since there is a larger distortion field associated with an interstitial point defect than with a vacancy point defect, edge dislocations have a bias for interstitials. Thus interstitial loops will tend to preferentially attract interstitials, and they will therefore increase in size as the dose increases.

The vacancy clusters, on the other hand, are unstable. At room temperature, the dominant mechanism for vacancy cluster shrinkage is due to the bounding dislocation preferentially attracting interstitials. This process is only weakly dependent on temperature but it depends on the cluster geometry since this determines the strength of the interaction between the vacancy cluster and the freely migrating interstitial point defects. More specifically, if there is a tendency for the dislocation bounding a Frank loop to dissociate, then this will reduce the strength

of the interaction with the interstitials and thus prolong the vacancy cluster lifetime. As the temperature increases, the rate of thermal emission of vacancies from the cluster increases and for F.C.C. materials at fast reactor operating temperatures, this becomes the dominant mechanism for vacancy cluster shrinkage. The rate of thermal emission of vacancies depends on the size of the cluster, due to the line tension driving force, and on the stacking fault energy of the material if the cluster is faulted. It also depends on the geometry of the defect as the energy of formation of a jog increases when a faulted loop dissociates. In the case of undissociated loops, it is believed that the rate of thermal emission of vacancies is governed by the rate of diffusion of vacancies away from the loop rather than the concentration of jogs and the jog velocities (English et al 1976b), and thus the vacancy loop shrinkage will depend on the vacancy diffusion coefficients rather than the jog formation energies.

1.2 The Formation of Voids

For vacancy clusters containing more than a few vacancies, the void morphology is not energetically favourable compared with other possible cluster configurations such as the dislocation loop, the uncollapsed vacancy sponge or the stacking fault tetrahedron. In αFe, a material of high stacking fault energy, this number of vacancies has been calculated as about twenty (Bullough and Perrin 1969). Some heterogeneity must therefore be present for voids to nucleate and grow. It is thought that helium, which is highly insoluble and is produced in (n,α) reactions in the core component materials, may stabilise void nuclei or voids may nucleate heterogeneously on precipitates. The grown-in dislocations and the irradiation produced dislocation network, consisting of the populations of stable interstitial loops and transient vacancy loops, preferentially remove interstitials and so the net defect flux into a neutral sink will be vacancy in character. Thus void nuclei will grow when biased sinks

such as dislocations are present. However, a very high dislocation density may lead to saturation in the void swelling since the close proximity of dislocations to voids results in a spatially varying stress field that causes interstitials to preferentially drift into the voids. This is therefore a possible saturation mechanism for void growth at high irradiation doses (see for example Bullough and Nelson, 1973).

Although the phenomenon of void formation was predicted in 1959 (Greenwood, Foreman and Rimmer 1959), it was not until 1966 that the first experimental observation of void swelling was reported in an austenitic stainless steel (Cawthorne and Fulton 1966). In realisation of the importance of the phenomenon in terms of the dimensional and mechanical stability of core component materials, a considerable amount of theoretical and experimental work has been carried out to try and predict the percentage volume increase of a given material in the fast reactor environment.

In austenitic stainless steels, significant void swelling ($^{\Delta V}/V > 0.1\%$) occurs after doses of approximately ten displacements per atom (dpa), while the same amount of swelling is produced in pure materials such as Ni after much lower doses ($\sim$ 1 dpa) (Nelson et al 1974). For all materials, the temperature range for void formation is approximately $^{T_m}/3$ to $^{T_m}/2$, where T_m is the material melting temperature measured in degrees Kelvin. The fast reactor operating temperatures unfortunately lie within this range for materials of technological interest such as the stainless steels. For temperatures lower than $^{T_m}/3$, long range vacancy migration is not possible and the vacancies preferentially recombine with migrating interstitials. Also, some of the vacancies are contained in the vacancy clusters that are produced by the collapse of displacement cascades. At these low temperatures ($T < {}^{T_m}/3$) the clusters are stable against thermal emission of vacancies, and the net vacancy concentration is therefore reduced. For temperatures greater than $^{T_m}/2$, the thermal equilibrium vacancy concentration is comparable with the radiation induced vacancy concentration, and

voids do not form when their rate of thermal emission of vacancies, as a result of surface tension forces, exceeds the rate at which the radiation induced vacancies arrive. The exact temperature at which this occurs depends on the radiation induced vacancy concentration and therefore depends on such parameters as the defect sink density and the damage rate. More specifically, a higher damage rate will increase the temperature at which void swelling still occurs.

Because of the considerable time required to produce significant swelling using the neutron flux from a fast reactor, void swelling has been investigated in materials irradiated with electrons or heavy ions. Using suitable heavy-ion accelerators such as the Variable Energy Cyclotron (VEC), or by irradiating in situ in the High Voltage Microscope (HVM); damage rates of 10^{-3} dpa/sec. can be obtained as compared with 10^{-6} dpa/sec. in the fast reactor environment. Theoretical considerations are then used to try and correlate the experimental results obtained under the different irradiation regimes. Many of the factors controlling the growth of voids in irradiated materials have been explored using a rate theory in which a homogeneous generation of interstitials and vacancies is assumed (Brailsford and Bullough 1972). While this approach has been used with some success to investigate the sensitivity of swelling to dose rate, it does not take into account the different damage mechanisms that prevail under the different irradiation conditions. More specifically, the homogeneous production model can deal with electron damage in the HVM, but it ignores the significance of cascade collapse and the corresponding heterogeneous point defect distribution that is generated during heavy-ion or fast neutron irradiation. A modified form of the rate theory that includes cascade collapse (Bullough, Eyre and Krishan 1975) has enabled a more accurate correlation to be made between the observed swelling in an austenitic stainless steel (type 316) irradiated under the different conditions. In addition, rate equations that include a steady-state

density of transient vacancy loops have been solved analytically by Heald and Speight (1977). They found that the physical effect of cascades collapsing was to provide additional sites for vacancy-interstitial recombination, and this reduced the effective damage rates and consequently the void swelling rates.

Experimental observations on the void swelling in 316 stainless steel have served to underline the important role that collapse of displacement cascades plays in determining void swelling characteristics. If point defects were generated homogeneously in a material, then the threshold temperature for visible void formation (T_{min}) would be related to long range vacancy migration. This occurs at temperatures much lower than those at which thermal emission of vacancies from clusters becomes appreciable and so the formation of vacancy clusters, due to the collapse of displacement cascades, is expected to increase T_{min} relative to the case of homogeneous defect production. Experimental confirmation of this is given by the fact that T_{min} increases from between 0.2 and 0.25 T_m (Makin, M.J., unpublished) to 0.42 T_m (Williams 1971) on going from HVM to VEC irradiation conditions. The maximum swelling is also affected by cascade collapse as the presence of vacancy clusters results in a reduction of the free vacancy concentration and an increase in vacancy-interstitial recombination at the bounding dislocation, thereby reducing void growth. Experimentally it has been observed that the peak swelling for a given dose is reduced by a factor of 2 or 3 in the VEC situation as compared with the HVM situation (Williams 1971, Makin and Walters 1974).

The steady-state vacancy cluster concentration depends on the vacancy cluster production rate and also the vacancy cluster lifetimes. The vacancy cluster lifetime is therefore thought to be an important parameter in determining void swelling characteristics. It has been observed experimentally that at high temperatures ($\sim 600^{o}C$) the void swelling in austenitic stainless steels varies with the recoil energy spectrum, while the swelling

in nickel at similar temperatures depends only on the total dose and not on the type of irradiation employed (Nelson et al 1974). Observations on the combined heavy-ion accelerator and microscope link at Harwell (Mazey, D.J., unpublished) have shown that the vacancy clusters in the austenitic steels have significantly longer lifetimes than those observed in the pure nickel. The vacancy damage structure generated by heavy-ion or neutron irradiation of the austenitic steels is therefore considered to involve two stages, the first being the collapse of the displacement cascades to form vacancy clusters, while the second is the thermal emission of vacancies from the clusters and their migration to voids. In nickel, however, the cluster lifetimes are so short at high temperatures that cascade effects can be neglected and the point-defect generation may be considered uniform throughout the material, as in the case of electron irradiation.

The reason for the shorter cluster lifetimes in the nickel was attributed to its higher stacking fault energy as compared with the stainless steels. However, vacancy cluster lifetimes depend not only on the stacking fault energy of the irradiated material, but also on the defect geometries, defect sizes and diffusion coefficients. In the experiments carried out at Harwell, the dynamic structure observed in the heavy-ion accelerator-microscope link was recorded on cine film and a qualitative comparison of the vacancy cluster lifetimes in the different materials was therefore relatively easy. However, information regarding cluster geometry could only be obtained from single frames of the cine film and the variation in contrast of the small vacancy defects was only half a percent above or below background when imaged on a single frame. This meant that no quantitative measurements could be made to investigate a possible difference in defect geometries between the pure nickel and the stainless steels.

1.3 Void Swelling in Nickel Alloys

The void swelling characteristics of pure nickel have been widely investigated as it is one of the major constituents of austenitic stainless

steels and is therefore of technological interest. The effect on the void swelling in nickel of alloying it with other metals has also received some attention and a brief review of the results obtained will serve to illustrate the influence that compositional variables have on void growth. The different explanations that have been proposed to account for the observed changes will demonstrate the uncertainty that still surrounds the factors affecting void swelling in complex materials.

In a series of experiments carried out on the Harwell VEC using high energy (46.5 MeV) nickel ions, the dose dependence of the void swelling in three nickel-aluminium alloys was compared with that obtained in pure nickel (Hudson et al 1973). The three alloys studied contained 6, 8.5 and 13.5 atomic percent aluminium. The nickel-aluminium system is an age-hardening system with the α/γ' phase boundary occurring at about 10 atomic percent aluminium at 500°C. The first two alloys were therefore simple α solid solutions and the third a precipitation-hardened alloy aged to produce γ' precipitates. Thin foils of the alloys were implanted with 10 appm helium prior to irradiation to simulate the production of inert gases in reactor cladding materials by (n,α) reactions, and the irradiations were carried out at a temperature of 525°C. It was found that the swelling for a given dose decreased with the amount of aluminium in solid solution and this was due to a decrease in the void concentration rather than the void size. There was no significant change of void concentration with dose and the individual voids grew at approximately the same rate in all four materials. To account for the observed reduction in swelling the authors considered the possibility that the aluminium solute atoms could suppress swelling by trapping the radiation induced interstitial or vacancy point defects, thereby increasing recombination. However, they concluded in this case that the reduction in swelling more likely indicated the possibility of an interaction between the aluminium solute atoms and the helium gas, which thus prevented the voids from nucleating at the usual

concentration.

Because the dislocation structures developed during irradiation play an important role in determining void growth kinetics, the dislocation structures were investigated concurrently with swelling behaviour. In pure nickel at 525°C the large (> 200 Å diameter) interstitial loops observed after small doses soon gave way to a network of dislocation lines, the dislocation density increasing from 1 x 10^{10} lines/cm^2 at 1 dpa to 5 x 10^{10} lines/cm^2 at 50 dpa. The addition of aluminium in the two solid-solution alloys stabilised the loop structure so that the dislocation density of 5 x 10^{10} lines/cm^2 after 50 dpa was still composed mainly of loops. Most of the loops had unfaulted to $\frac{a}{2}$ <110> perfect loops, but some faulted (Frank) loops were also present and these were identified as interstitial in nature. Thus it can be seen that the addition of aluminium to nickel changes the radiation induced interstitial dislocation structure. In the alloy containing γ' precipitates the dislocation structure was similar to that in nickel, developing from individual faulted and unfaulted loops to a dense network of lines, the dislocation density rising to 10^{11} lines/cm^2 after 40 dpa. However, the swelling behaviour of the two alloys containing the most aluminium was very similar, suggesting that the swelling was independent of the observed difference in the dislocation structures. No conclusions could be made as to the effect of dislocation density on the void swelling as the dislocation densities were somewhat similar in all cases. In addition, no mention was made of the possible effect that the aluminium in solution might have on the collapse of the displacement cascades to form small (< 100 Å diameter) vacancy clusters. The addition of aluminium to nickel changes the stability of the interstitial loops produced during irradiation, and it is possible that it may also change the lifetimes of the transient population of vacancy clusters, thus altering the void swelling characteristics of the alloys as compared with the pure nickel.

In a further series of experiments, the dose dependence of the void swelling was extended to include the binary nickel-copper (10%), nickel-iron (5%) and nickel-chromium (9% and 27.5%) alloys (Hudson and Ashby 1974). The irradiations were carried out under the same conditions as for the nickel-aluminium alloys and again a reduction in swelling was observed for all the alloys, as compared with pure nickel. The effect was greatest for the Ni/Cr 27.5% alloy and the reductions in void swelling were again accompanied by a reduction in void concentrations. However, in the case of the Ni/Cr 9% alloy the void concentration was observed to increase with dose, while in the other alloys it was observed to be independent of dose. The dose dependence of the void swelling in the Ni/Cr 27.5% alloy was also investigated at temperatures in the range 525°C to 700°C. It was found that the low swelling characteristics found at 525°C were repeated at 540°C but above this temperature the swelling rapidly increased for all doses. In conclusion, the authors suggested that the low void swelling and low void concentrations observed at the lower temperatures were due to a reduction in the vacancy supersaturation due to point-defect trapping, although they did not exclude the possibility that the reduction in void concentration could be due to an interaction between the substitutional impurity and the implanted helium atoms. Again, no account was taken of the possible effect of alloying producing a change in the lifetimes of the vacancy clusters generated by collapse of the displacement cascades.

Turning to a more complex alloy system, a comparison of the swelling produced in a number of commercial iron-chromium-nickel alloys has been carried out (Johnston et al 1974). The irradiations were carried out on a Tandem Van de Graaff accelerator and the alloys were bombarded with 5 MeV Ni^{++} ions to a damage level of 140 dpa at 625°C, the peak swelling temperature of the austenitic stainless steels. Some of the lower swelling alloys that were identified were also bombarded at other temperatures to ensure that the observed low swelling behaviour was not due to the peak swelling

temperature being appreciably different from 625°C. The swelling of each alloy was marked on a ternary Fe-Cr-Ni diagram as a function of the nickel and chromium contents of the alloys, and this was compared with the Fe-Cr-Ni phase diagram at 650°C. When plotted simply as a function of their nickel and chromium contents, all the alloys appeared to be γ phase and the results showed that the austenitic stainless steels were in a particularly poor compositional range from the point of view of void swelling. In addition, there were apparent trends in swelling behaviour with respect to alloy composition. More specifically, increasing the nickel content tended to result in lower swelling, while increasing the chromium content led to higher swelling. In order to evaluate the importance of major composition, four special alloys were prepared of composition Fe-15Cr-XNi with X = 15, 20, 30 and 35 wt.%. These alloys were also irradiated to a damage level of 140 dpa at 625°C and the percentage void swelling produced in each alloy was observed to decrease approximately linearly with increasing nickel content of the alloy. Thus the authors concluded that the major composition of a commercial alloy plays a dominant role in determining swelling behaviour.

As a possible explanation for the relatively high swelling observed in the stainless steels, it has been pointed out that the small amounts of impurity elements present in stainless steels result in equivalent nickel and chromium contents which must be used in locating the position of the steel on a phase diagram. This position may be different from that which is obtained using just the amounts of nickel and chromium present. This, coupled with the uncertainty in the exact position of the γ:γ+σ phase boundary, results in the possibility of the austenitic stainless steels lying within the two phase (γ+σ) field at 625°C (Harries 1974). The resulting σ phase would be enriched in chromium and chromium equivalent elements and so the austenite would be depleted in those elements. If the void swelling of the austenite is controlled by elements in solid solution

acting as trapping sites for the irradiation induced point defects or the inert gas atoms, and if the σ stabilising elements are most effective as trapping sites, then enhanced void swelling would be expected in the austenite of the two phase (γ+σ) alloy as compared with a higher nickel content single (γ) phase alloy. In addition, if cascade collapse to form vacancy clusters is less favaourable in the σ phase, then there could be an enhanced release of vacancies to the austenite-σ phase interface, thereby accelerating the growth of voids nucleated near to an interface.

An alternative explanation for the dependence of void swelling on the nickel and chromium content of alloys has been proposed in terms of an irradiation induced solute segregation (Okamoto and Wiedersich 1974). Auger electron spectroscopy was used to compare the surface chemical composition of an 18/8/Si stainless steel both before and after high energy (3.25 MeV) nickel ion irradiation, and it was observed that the bombarded surface became enriched in nickel and silicon, that is undersized solute atoms, while it became depleted in chromium, which is an oversized solute atom. This segregation was explained in terms of a "drag" mechanism which depended on the size of the solute atom. If undersized solute atoms are more readily accommodated in interstitial sites than oversized solute atoms, the interstitial flux in the dumb-bell configuration will be disproportionately compromised of undersized solute atoms, resulting in a build up of these solute atoms at voids and external surfaces. Also, if oversized solute atoms have a preference for substitutional sites, they will be preferentially depleted by vacancy migration resulting in a loss of these solute atoms from around voids and at external surfaces. Thus the authors suggested the possibility of void growth being limited by the build up of undersized nickel atoms at the void surface. The void swelling would therefore be expected to decrease with increasing nickel content of an alloy.

The foregoing discussion has outlined some possible explanations that have been proposed to account for the variation in void swelling characteristics

with changing material composition. The situation in the commercial alloys is more complicated than in the binary nickel alloys, but even in these simple alloys there is still some uncertainty as to the exact reasons for the observed reductions in swelling. One factor which is common to all the alloys, and which so far has received little attention, is the fundamental damage process of displacement cascades collapsing to form the transient population of vacancy clusters. At present, no quantitative information exists as to a possible variation of vacancy defect numbers, defect sizes and defect geometries, with the change in composition of technologically important materials.

1.4 The Simulation of Fast Neutron Damage by Heavy Ion Bombardment

The primary knock-on atom spectrum produced by neutrons from a fast reactor incident on iron has been given in Figure 1.2 (Marwick 1975). Since the atomic weights of chromium and nickel are similar to iron, the primary knock-on atom spectra for these materials should not be appreciably different from that applicable to iron. Figure 1.2 shows that the primary knock-on atom energies range from the threshold displacement energy, that is approximately 40 eV, up to 500 keV. Because of the uncertainty in this energy of the primary knock-on that generates a particular displacement cascade, the parameters that affect displacement cascade collapse are difficult to define using fast neutron irradiations.

Since the primary knock-on is a lattice atom having an energy typically in the range 1 → 100 keV, it should be possible to simulate some aspects of fast neutron damage by irradiating a metal with heavy ions (preferably self-ions) having energies of this order. The use of mono-energetic heavy ions offers the advantage over fast neutron irradiation that the energy deposited in a displacement cascade is essentially constant, and the use of low doses ($\sim 10^{11}$ ions cm^{-2}) means that, in general, cascades do not overlap with each other and it is therefore not necessary to take into account interference between different cascades. The use of low doses and low dose

rates also suppresses the clustering of interstitials originating from different cascades. Thus the conditions under which the displacement cascade damage is generated can be more precisely defined.

However, the range of an incident heavy ion is generally less than the sample thickness and for mono-energetic ions the damage zone is located within a narrow layer. Thus one disadvantage of heavy-ion irradiations is the possibility of impurity effects, arising from the deposition of the irradiating ions in the crystal lattice. The mean projected range of an 80 keV Ni^+ ion into nickel has been calculated as 193 Å and the mean depth of deposited energy as 114 Å (Matthews 1974, 1976 (see section 4.6)). Thus another disadvantage arises from the proximity of the specimen surface which acts as a sink for migrating point defects. The experimental evidence from low dose heavy-ion irradiation experiments (see section 1.5 for a review of this subject) indicates that some of the interstitials are lost to the surface while the others, in general, form submicroscopic clusters. This results in most cases in only vacancy type defects being observed. In addition, the geometry of these defects may be influenced by the surface and there is the possibility that loops may glide out to the surface under the influence of surface image forces. This point is considered in more detail in section 4.4.1. A further disadvantage may arise because of the difference in the inelastic collision cross-sections of a heavy ion and an uncharged primary knock-on. However, since the primary knock-ons lose electrons in moving through the crystal lattice so that they also become charged, the energy loss due to inelastic collisions should be similar in the two cases.

Despite these limitations, irradiations using heavy ions have been used extensively to investigate the damage structures generated in pure materials. Two important quantities in these experiments are the 'defect yield', defined as the fraction of cascades collapsing to form visible vacancy clusters, and the 'cascade efficiency', defined as the fraction of

vacancies surviving in each cascade to form a visible cluster (Merkle 1969). Using mono-energetic ions has enabled studies to be made of the relationship between the numbers and sizes of the damage clusters, as obtained from examination of the irradiated materials in a transmission electron microscope, with the numbers and energies of the displacement cascades, as obtained from the parameters of the irradiating ion-beam. It has also been possible to study the defect geometries, and to see how the above relationship varies with other parameters such as the irradiation temperature, the crystal orientation or the presence of impurities in the crystal lattice.

To give the reader a background to the present state of knowledge concerning the mechanisms involved in the generation and collapse of displacement cascades, and the factors that are thought to influence these mechanisms, the following section presents some of the more relevant experimental results that have been obtained in this field.

1.5 Displacement Cascade Damage Structures in Heavy Ion Irradiated Metals

1.5.1 Introduction

In general, the irradiation of metals with heavy ions having energies in the range 5 → 200 keV results in vacancy clusters that form as a result of the collapse of displacement cascades. The interstitials which escape from the cascade region are thought to either form clusters which, in general, are too small to produce visible contrast in the electron microscope, or alternatively they may be lost to the surface.

Such heavy-ion irradiations have been used extensively to investigate the displacement cascade damage structures generated in pure metals. Recent reviews of the subject have been given by Eyre (1973) and Wilkens (1975). Some of the recent investigations include those in gold (Ruault et al 1975, Schindler et al 1976), copper (Jenkins 1974, English et al 1976b, Schindler et al 1976, Stathopoulos 1977), silver (Jenkins 1974) and nickel (Schindler et al 1976) of the F.C.C. materials; molybdenum

(Häussermann 1972c, English et al 1977), tungsten (Häussermann 1972c, Jäger and Wilkens 1975), chromium (English, C.A., unpublished) and iron (Jenkins et al 1977) of the B.C.C. materials; and cobalt (Föll and Wilkens 1977) of the H.C.P. materials.

1.5.2 Damage in F.C.C. Metals at Room Temperature

1.5.2.1 Defect Geometry

Wilson and Hirsch (1972) carried out a detailed study of the damage produced in copper by self-ion irradiation. They concluded that the defect clusters had a structure based on the vacancy-type Frank sessile loop with Burgers vectors $\underline{b} = \frac{a}{3}\langle 111\rangle$, but there was evidence that parts of the circumference of many of the loops had dissociated into stair-rod dislocations and Shockley partials according to a mechanism proposed by Silcox and Hirsch (1959). This dissociation gives rise to areas of stacking fault on {111} planes other than that of the loop plane. This interpretation, which was open to some doubt since it was concerned with details of the fine structure of black-white dynamical images (see Chapter 2), was later confirmed in weak-beam studies by Jenkins (1974). Jenkins also showed that the elastic interaction of the Shockley partials with the adjacent specimen surface influenced the detailed cluster geometry.

The geometry of the defect clusters in other F.C.C. materials may be different from those observed in copper, due to differences in stacking fault energies. Because of the enclosed area of stacking fault, it is energetically more favourable for the Shockley partial dislocations to bow out in their slip planes in materials with low stacking fault energies such as copper, silver and gold, than in materials with high stacking fault energies such as aluminium and nickel. Schindler et al (1976) found that for 35 keV Cu^+ irradiations, all the defects in nickel were Frank type dislocation loops while in gold about half the defects were complete stacking fault tetrahedra. It may also be possible that the unfaulted perfect loop configuration with $\underline{b} = \frac{a}{2}\langle 110\rangle$ is the more stable form in

materials with high stacking fault energies. Thus if stresses are present which serve to nucleate the necessary partial dislocations, the Frank loops may unfault to perfect loops. The relative stabilities of Frank and perfect loops in nickel are considered in section 4.3.

1.5.2.2 Defect Yield and Cascade Efficiency

The F.C.C. metals which have been most extensively investigated are gold and copper. Merkle (1966) carried out the first quantitative studies on displacement cascades using these materials and he found that a large fraction of the vacancies at the centre of displacement cascades survived to form visible clusters. Typical values for the cascade efficiency in F.C.C. materials are between 0.3 and 0.5 (Wilkens 1975). Merkle found that the average cluster size in gold and the defect yields increased with increasing primary knock-on energy (E_T). The defect yield in gold was greater than one for $E_T \geq 60$ keV. In copper, the average cluster size and the defect yields were smaller than in gold for similar E_T.

Häussermann (1972a) has shown that for 35 keV heavy-ion bombardment of copper, changing the ion from copper to gold increases the defect yield from 0.2 to 0.6. Similar increases in defect yield, and also cascade efficiency, with increasing ion mass have been found in F.C.C. materials by English et al (1975) and Stathopoulos (1977). The net effect of increasing the ion mass while keeping the ion energy constant is to produce approximately the same number of vacancy-interstitial pairs, but within a reduced volume. Thus the cascade is more compact and the density of energy deposited within the cascade increases. Wilkens (1975) has shown qualitatively that a higher vacancy supersaturation, due to a reduction in the size of a cascade region and a more efficient separation of interstitials from vacancies in a more compact cascade, increases the probability of a cascade collapsing to form a visible loop.

The results of Häussermann (1972a) are consistent with a model for cascade collapse proposed by Merkle (1966). In this model, each cascade

region consists of discrete subcascades. The collapse of an individual subcascade does not produce a visible cluster and the formation of a visible cluster therefore requires the overlapping of two or more subcascades. Thus decreasing the cascade volume, thereby decreasing the average separation of the subcascades, would increase the probability of the cascade collapsing to form a visible cluster.

1.5.3 Damage in B.C.C. Metals at Room Temperature

1.5.3.1 Defect Geometry

Häussermann et al (1972) analysed the geometries of the defect clusters generated by 60 keV gold ion irradiation of tungsten. They found that most of the loops were glissile with $\underline{b} = \frac{a}{2}$ <111> and $\underline{n}$ = {110}, although a few ($\sim$ 1%) faulted loops with $\underline{b} = \frac{a}{2}$ <110> were also identified. They also found that the glissile loops were not uniformly distributed over the available {110} planes.

A nucleation model for interstitial loops that accounts for the formation of $\underline{b} = \frac{a}{2}$ <111> and $\underline{b} = \frac{a}{2}$ <110> type loops in B.C.C. metals has been proposed by Eyre and Bullough (1965). They suggested that the interstitials initially aggregated on {110} planes to form faulted loops having $\underline{b} = \frac{a}{2}$ <110>. Such loops could then shear in <100> or <110> directions to form $\underline{b} = \frac{a}{2}$ <111> or $\underline{b}$ = a <100> type loops respectively.

To explain the observed distribution of loop geometries, Häussermann (1972b) applied this nucleation model to the vacancy loops in B.C.C. materials. He suggested that in the core of the displacement cascades, vacancy loops are nucleated on {110} planes as pure edge loops with $\underline{b} = \frac{a}{2}$ <110> and that this nucleation occurred with equal probability on all six {110} planes. When such a loop reached a certain critical size, the stacking fault over the loop area could be removed by shear in a <100> direction, resulting in perfect loops with $\underline{b} = \frac{a}{2}$ <111>. Each pure edge loop could unfault to one of two possible perfect loop configurations, and because of the proximity of the surface the total energies of these

loops might be different. It was therefore assumed that the critical loop size, at which shear could take place, was first reached for that shear direction which would result in the lower total energy. The resulting perfect loop would then be attracted to the surface by surface image forces and the strength of this attraction would depend on the loop's Burgers vector. Thus only suitably orientated loops would slip out of the foil, and there would therefore be an uneven distribution amongst the {110} planes for the loops remaining in the foil.

The original work by Häussermann was only carried out on specimens of a single orientation and his suggested model had only a qualitative basis. Since that time, the frequencies of the different loop types that occur in specimens of different orientations have been investigated (Jäger and Wilkens 1975) and quantitative calculations have been performed for the elastic interaction of a loop of general orientation with an adjacent surface (Jäger et al 1975). Jäger and Wilkens irradiated tungsten foils of two different orientations with 60 keV gold ions and they compared their results with those obtained by Häussermann. Using the calculations of Jäger et al, they concluded that the experimentally observed frequencies of the individual loop types could be satisfactorily explained in terms of the model of Häussermann.

The nucleation model of Eyre and Bullough could result in the formation of a <100> perfect loops as well as the $\frac{a}{2}$ <111> and $\frac{a}{2}$ <110> loop types identified by Häussermann et al. The formation of an a <100> loop by shear over an $\frac{a}{2}$ <110> loop is thought to be energetically unfavourable, compared with that loop shearing to an $\frac{a}{2}$ <111> loop. This is consistent with the fact that the a <100> loop type was not observed in the experiments of Häussermann (1972b). However, recent results in αFe (Jenkins et al 1977) irradiated with xenon or tungsten ions have shown the presence of both types of perfect loops with $\underline{b}$ = a <100> as well as $\underline{b} = \frac{a}{2}$ <111>. Perfect loops with $\underline{b}$ = a <100> have also been identified in molybdenum irradiated

with molecular ions, and it was found that the relative frequency of these loops increased as the mass of the irradiating ions increased (English 1977a). A detailed analysis of the geometry of these loops showed that they had {110} habit planes, indicating that they had formed by shear over $\underline{b} = \frac{a}{2}$ <110> loops.

The reason why apparently energetically unfavourable $\underline{b}$ = a <100> loops should form is not yet understood. By considering the influence of the surface interaction energy on the direction of unfaulting of $\frac{a}{2}$ <110> loops, Jenkins et al concluded that the observed $\underline{b}$ = a <100> loop types, some of which were 'edge-on', were not consistent with the surface interaction energy influencing significantly the unfaulting process. They considered that one of the factors influencing the production of a <100> loops might be the energy density within a cascade. The results in molecular ion irradiated molybdenum suggested that the high energy density in a compact cascade may have provided the source of energy required in the shear process to form metastable a <100> loops.

1.5.3.2 Defect Yield and Cascade Efficiency

Maher (1970) first demonstrated that self-ion irradiation of molybdenum results in the formation of visible vacancy loops, indicating that it behaves similarly to F.C.C. metals. However, Häussermann (1972c) in studying 60 keV gold ion irradiated molybdenum and tungsten found important differences in behaviour with that observed in the F.C.C. metals. Firstly, the measured defect yield values were about an order of magnitude lower than in F.C.C. metals and they were more sensitive to crystal orientation. Secondly, the cascade efficiency values were also lower and they were sensitive to material purity. (The effect that impurities are thought to have on the generation and collapse of displacement cascades is discussed in section 1.5.5.)

Häussermann considered that one of the reasons for the lower fraction of vacancies surviving in the form of visible clusters was due to a

reduction in the number of Frenkel pairs generated, as a result of the incident ions being channelled through the crystal. A channelled ion loses proportionately more energy inelastically by electronic interactions; thus when it is de-channelled, the energy available for elastic interactions with the lattice atoms may be considerably reduced. Thus channelling can account for the difference in average cluster size between B.C.C. and F.C.C. metals if it is assumed that either the critical angle for channelling is greater for B.C.C. metals, or alternatively, the average energy loss of channelled ions is less for F.C.C. metals.

The lower measured defect yields in the B.C.C. metals was thought to be the result of an increase in the number of loops that were removed by surface image forces. When displacement cascades collapse, the vacancies are thought to aggregate initially on the close-packed planes, that is {111} in F.C.C. materials and {110} in B.C.C. materials. Both these loop types are sessile and therefore they will not be removed by surface image forces. However, because of the higher stacking fault energies of B.C.C. metals, it is thought that the critical loop sizes at which shear takes place are lower than in F.C.C. materials. Thus the probability of a sessile loop unfaulting to a perfect loop which might then glide out of the foil is thought to be higher for B.C.C. metals, and this would result in the measured defect yields being lower than in F.C.C. materials. Recent work in αFe (Jenkins et al 1977) indicates that when loop loss at the surface is taken into account, the true defect yield generated by 80 keV W^+ ions is close to unity and comparable to the yields obtained in ion-bombarded F.C.C. metals.

1.5.4 Temperature Dependence of Cascade Collapse

1.5.4.1 Low Temperature Irradiations

Howe et al (1966) irradiated aluminium, copper and gold with 100 keV oxygen ions at a temperature of approximately 20 K. They observed small defect clusters with diameters in the range 10 Å → 50 Å and they concluded

that these clusters were vacancy in character. Their results therefore indicate that cascade collapse occurs in F.C.C. metals at temperatures where neither interstitials nor vacancies can freely migrate.

1.5.4.2 High Temperature Irradiations

The temperature dependence of the defect yield in F.C.C. materials is discussed in detail in Chapter 6 in relation to the experimental results presented in that Chapter. In brief, the temperature dependence of the defect yield in self-ion irradiated copper has been satisfactorily explained in terms of a temperature independent cascade collapse process, a reduction in defect yield at temperatures above 300°C being due to thermal emission of vacancies from the resulting loops (English et al 1976). A similar explanation is believed to hold for the case of self-ion irradiated nickel (English, unpublished).

The situation in B.C.C. metals appears to be less clear. It has been found that the defect yield produced by heavy-ion bombardment of molybdenum is dependent on both the irradiation temperature and on the mass of the incident ions (English et al 1977, English 1977b). For 60 keV self-ions the defect yield decreased at irradiation temperatures greater than 200°C, while using 60 keV xenon or tungsten ions the defect yield remained unchanged at temperatures up to 425°C. The decrease observed in the self-ion case could not be explained in terms of an athermal cascade collapse process followed by thermal emission of vacancies, nor by an increase in the number of loops lost to the surface. Also, since the mean cluster size was greater for higher irradiation temperatures, it was not thought that increased vacancy-interstitial recombination could account for the observed decrease. It therefore appeared that the cascade collapse process itself was temperature dependent. It is perhaps possible that the driving force for cascade collapse is reduced at temperatures where vacancy migration can occur due to vacancies migrating from the cascade core into the surrounding lattice. If the nucleation energy of a faulted loop is high (corresponding to a high

stacking fault energy term, as in B.C.C. metals), the probability of the cascade collapsing may then be less than at room temperature, where long-range vacancy migration is not possible. The higher vacancy supersaturation generated by the heavier ions illustrated the balance that existed between the cascades collapsing to vacancy loops or their retaining an uncollapsed configuration and perhaps dispersing in the lattice.

1.5.5 Effect of Impurities

Häussermann (1972c) found that the cascade efficiency in both molybdenum and tungsten was sensitive to material purity, the mean cluster size being smaller in the less pure materials. In a more detailed study of the effect that impurities have on the collapse of displacement cascades, English et al (1977) found that interstitial impurity atoms were more effective than substitutional impurity atoms in reducing both the defect yield and cascade efficiency values in self-ion irradiated molybdenum.

One possible effect that impurities might have is to defocus replacement collision sequences, resulting in less efficient separation of the interstitials and vacancies and therefore increased recombination. However, English et al found that as little as 17 atomic ppm nitrogen, which is an interstitial impurity, reduced the number of vacancies retained in visible clusters by an order of magnitude. Because of the low concentration of nitrogen involved, it was not thought that defocussing of replacement collision sequences could completely account for the size of the reduction, although it may have been a contributory factor. It was suggested that the nitrogen impurities might trap vacancies in the cascade centres, thus inhibiting their migration and collapse to vacancy loops. Alternatively, the nitrogen might directly influence the collapse process resulting in the vacancies aggregating to form sub-microscopic voids rather than loops. However, the available information was not sufficient for the authors to differentiate between the proposed, or any possible alternative, mechanisms. Thus the exact role that impurities play in determining the vacancy damage

structure is still uncertain.

1.5.6 Interstitial Clustering

In general, interstitial clusters are not observed in low dose heavy-ion irradiation experiments. This is thought to be due partly to the proximity of the surface, which acts as a sink for the mobile interstitial point defects, and partly to the low doses employed (typically $10^{11} \rightarrow 10^{12}$ ions cm^{-2}). The use of low doses reduces the possibility of visible cluster formation arising from the aggregation of interstitials originating from different displacement cascades.

The probability of interstitials forming clusters has been considered in some detail by Wilson (1970) for the case of 30 keV self-ion irradiation of copper. He concluded that a substantial fraction of the interstitials were retained in the form of submicroscopic clusters rather than being lost to interstitial sinks or to the surface. These submicroscopic clusters would be expected to increase in size with increasing dose and this is consistent with the fact that Norris (1969) observed interstitial clusters in aluminium after irradiating with heavy ions to the high doses of 10^{15} ions cm^{-2}. Also, the results of English et al (1976b) indicate that for low dose 30 keV self-ion irradiation of copper, a fraction of the interstitials aggregate to form visible loops during irradiation at elevated temperatures. This is thought to be the result of the interstitials clustering on a coarser scale at higher temperatures.

In contrast to other metals, interstitial clusters have been observed in gold following low dose heavy-ion irradiations at room temperature. Ruault et al (1975) found that for incident ion masses less than that of krypton, the majority (> 80%) of the defect clusters in gold were interstitial in nature. In addition, a recent investigation by Schindler (1978) in 30 keV Cu^{+} ion irradiated metals has shown that while only vacancy type defects were visible in Cu, Ni, Ag and Pt, approximately 20% of the visible defects in Au were interstitial in nature. The proportion of interstitial

clusters was found to be independent of dose in the range $1.10^{10} \rightarrow 2.10^{11}$ ions cm^{-2}, and Schindler concluded that the interstitial loops were formed by individual cascades. However, the reason why visible interstitial clusters should form in Au and not in other metals is not yet fully understood.

1.5.7 Direct Observation of Cascade Regions

The ordered nature of the lattice in an ordered alloy makes it possible to observe directly the disordered regions of a lattice by forming an electron microscope image in dark-field using a superlattice reflection. Jenkins and Wilkens (1976) have used this method to observe directly the cascade regions in Cu_3Au irradiated with Cu^+ ions of energy $5 \rightarrow 100$ keV. They found that each incident ion of energy ≥ 10 keV created, at the core of the resulting displacement cascade, a zone of reduced long-range order which could be imaged in the electron microscope. At ion energies $\gtrsim 30$ keV, many of the disordered zones developed extrusions and some discrete subcascades were observed. These were thought to have been formed by quasi-channelled knock-ons. From a comparison of the disordered regions in a particular area of the foil with the vacancy clusters observed in the same area of the foil, it was confirmed that the vacancy clusters nucleated heterogeneously at the disordered regions, that is at the sites of the displacement cascades.

1.5.8 Conclusions

There appears to be consistent agreement among different workers that low dose heavy-ion irradiation of metals generates vacancy clusters which are formed by the collapse of displacement cascades. In F.C.C. and B.C.C. metals, the collapse always seems to occur onto a close-packed plane. The resulting faulted loops may or may not subsequently unfault to form perfect loops. This also appears to be true for H.C.P. metals, where the close-packed plane depends on the axial ratio $^c/_a$ (Föll and Wilkens 1977). Interstitial clusters are not normally observed in this

type of experiment.

The separation of interstitials from vacancies by replacement collision sequences appears to have a sound theoretical and experimental basis. However, it should be borne in mind that the existence of replacement collision sequences has not yet been unambiguously proved and the interpretation of some aspects of these heavy-ion irradiation experiments is therefore still open to question.

1.6 Heavy Ion Irradiation of Alloys

1.6.1 Previous Work by Other Authors

Compared with the numerous heavy-ion irradiation experiments that have been carried out in pure metals, very little work has been done on the effect that impurities have on the generation and collapse of displacement cascades.

English et al (1975) have studied the vacancy damage structure in an austenitic stainless steel irradiated with chromium ions. They found that the defect yield and cascade efficiency were much lower than in a pure F.C.C. material such as copper. The results also indicated that reducing the amount of carbon in solution increased the defect yield, although a further experiment to confirm this proved inconclusive (Williams, T.M., unpublished). The authors attributed these results to the role played by the alloying elements and impurities in defocussing replacement collision sequences, resulting in increased vacancy-interstitial recombination within the cascades.

English et al (1977) have also studied the effect of material purity on self-ion damage in molybdenum (see also section 1.5.5). They compared the vacancy damage structure generated in molybdenum of three different purities, although apart from one specimen doped with nitrogen, an interstitial impurity, it was not known what the other impurities actually were, although they were thought to be substitutional impurities. However, in agreement with the earlier work of Häussermann (1972c), they found

that both the defect yield and cascade efficiency decreased with decreasing material purity.

The only systematic investigation of the effect of alloying on the collapse of displacement cascades has been carried out by Stathopoulos (1977) in copper and substitutional copper alloys irradiated with copper or tungsten ions. This work was carried out concurrently with the research work that is presented in this thesis and the results obtained will be discussed in relation to the present work in Chapter 5.

1.6.2 The Present Work

Because no information existed as to the effect that alloying had on cascade collapse in materials of technological importance and, as discussed in sections 1.2 and 1.3, because of the possible relevance of this information to the interpretation of the void swelling characteristics of technologically important alloys, an investigation has been carried out into the damage structures generated by low dose, heavy-ion bombardment of the following materials:-

Ni

Ni/Cr 8%

Ni/Cr 17%

Fe/Ni 10%/Cr 17%

321 stainless steel (Fe 70%/Ni 10%/Cr 17%).

This investigation has been primarily concerned with the variations of defect yields, defect sizes and defect geometries, that is parameters which are thought to influence the steady-state vacancy cluster concentrations at fast reactor operating temperatures, with the changes in alloying compositions. In addition, the temperature dependence of the defect yields in the Ni and the Ni/Cr 17% alloy and the orientation dependence of the defect yields in the nickel and the nichrome alloys have been investigated. Because of the known variation of defect yield with orientation in B.C.C. materials, an investigation was carried out to see

if there was a similar dependence in F.C.C. materials with relatively high stacking fault energies. This was necessary to ensure that any variation in defect numbers and defect sizes between the alloys was a real effect rather than an orientation effect.

The materials that have been examined were chosen such that several of the factors that were thought to influence cascade collapse could be investigated. The Fe/Ni/Cr alloy was made up with the same basic composition as the 321 stainless steel, and thus a comparison between the Ni/Cr17% alloy and the Fe/Ni/Cr alloy, and between the Fe/Ni/Cr alloy and the 321 stainless steel should indicate whether a major compositional change or the addition of minor impurities has the greater effect on the defect structures generated. 321 stainless steel, which is an austenitic steel, was chosen for the present experiments as it has been considered as one of the possible materials for fast reactor structural components and while its void swelling properties have been extensively investigated (Nelson et al 1974, Hudson 1975), no quantitative information existed about the vacancy clusters generated by the collapse of displacement cascades.

A comparison between the nickel and the two nichrome alloys, as well as being of interest purely from the point of view of the effect of alloying on cascade generation and cascade collapse, is of direct relevance to the interpretation of the work of Hudson and Ashby (1974) on the void swelling characteristics of nickel and nichrome alloys (see section 1.3). Since their work was carried out at temperatures greater than 500°C, the present work includes a comparison of the defect yields in the Ni and Ni/Cr 17% alloy over a range of temperatures up to the void formation temperature range.

This work should also be relevant to the investigation of the temperature dependence of the cascade collapse process (see section 1.5.4.2). In F.C.C. materials this process is believed to be athermal, but the only

previous work has been carried out on copper, a material of low stacking fault energy. In B.C.C. materials the collapse process is thought to be dependent on temperature and this may be due to the much higher stacking fault energies in B.C.C. materials as compared with copper. Thus the present work on the Ni and the Ni/Cr 17% alloy should indicate whether the collapse process is still athermal in F.C.C. materials with relatively high stacking fault energies.

Figure 1.1 A typical neutron spectrum from a fast reactor (Dean 1974).

Figure 1.2 Primary knock-on atom spectrum for fast reactor neutrons in iron (Marwick 1975).

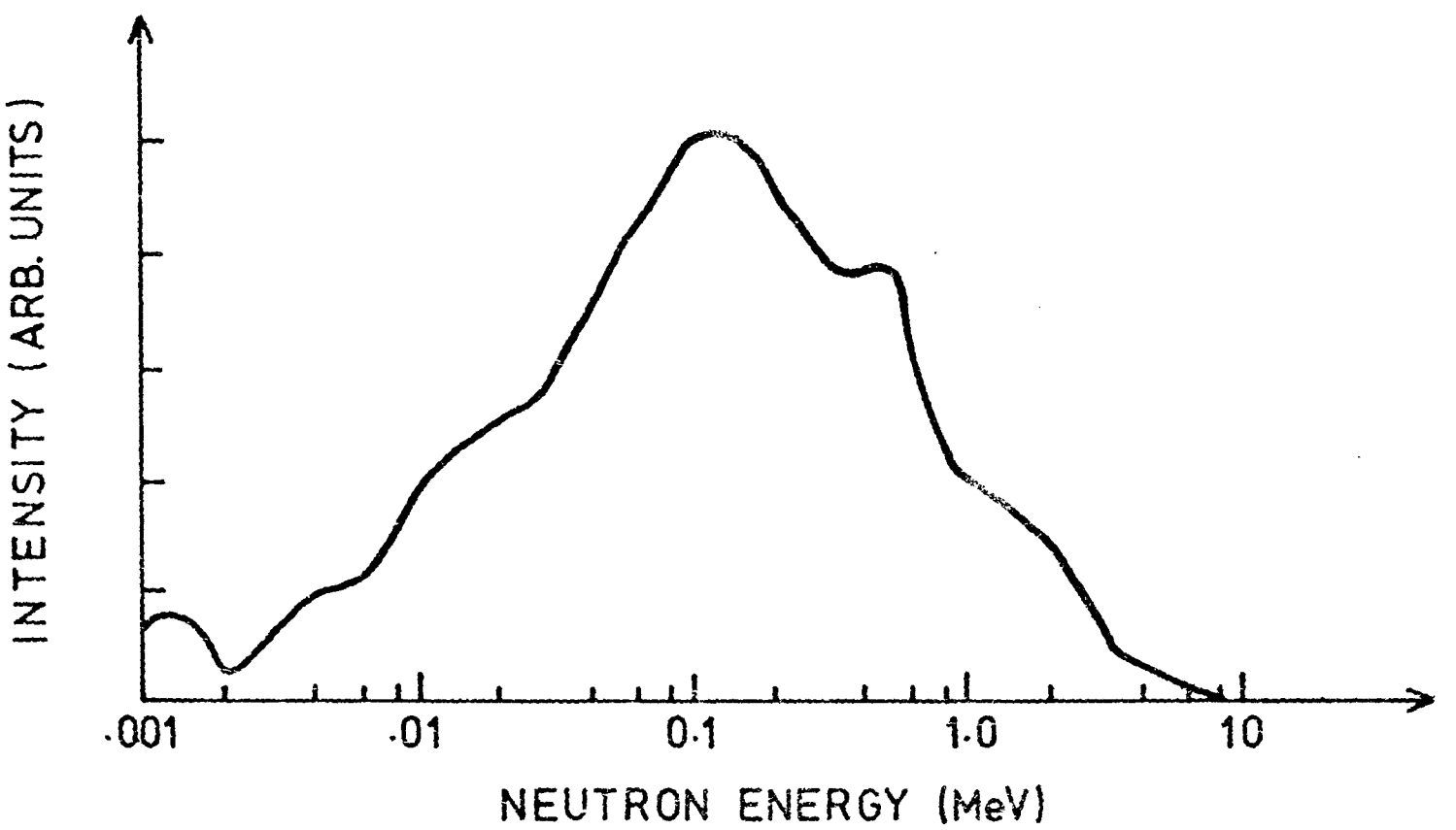
INTENSITY (ARB. UNITS)
·001
·01
0·1
1·0
10
NEUTRON ENERGY (MeV)

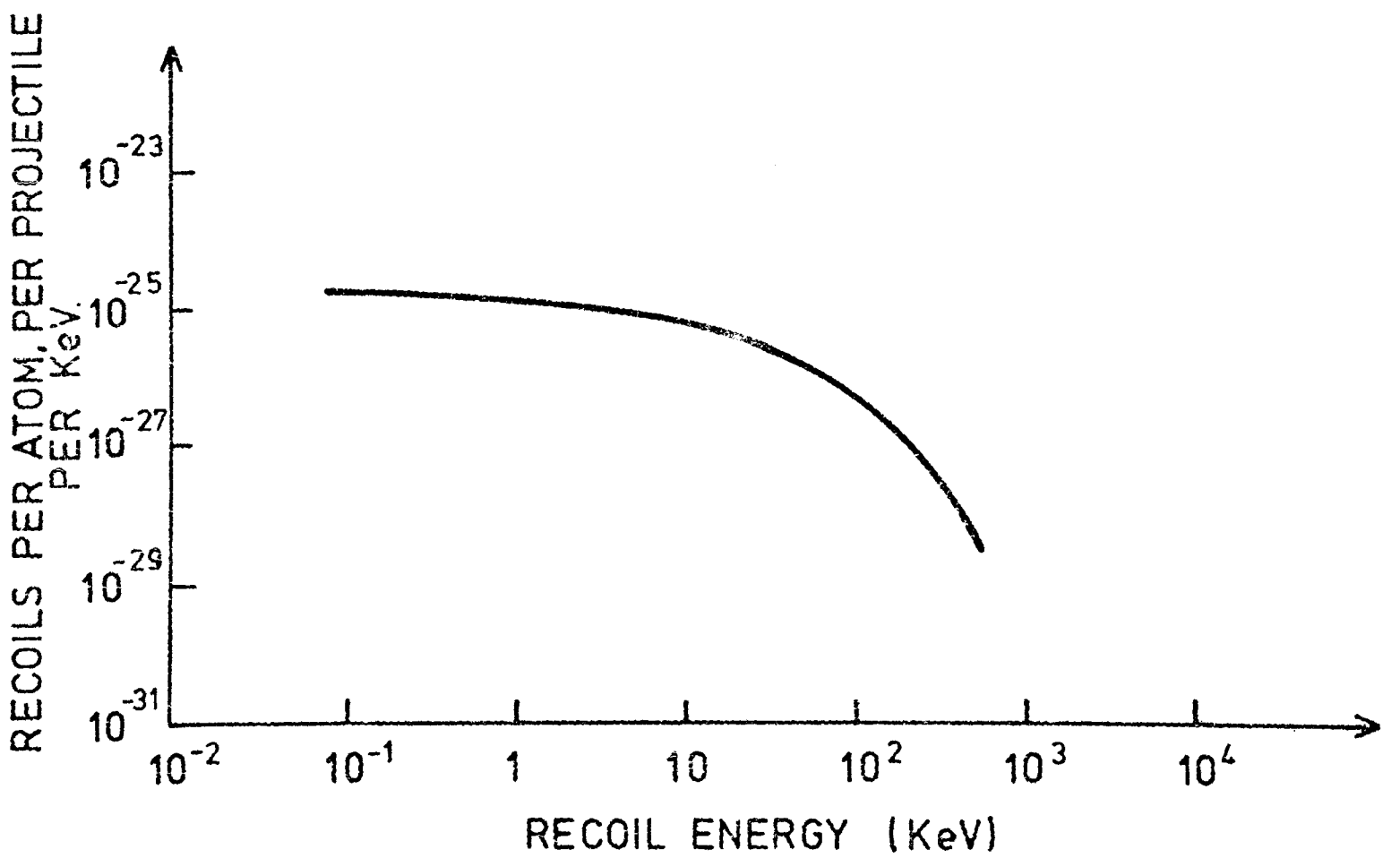
RECOILS PER ATOM, PER PROJECTILE PER KeV.
10^-23
10^-25
10^-27
10^-29
10^-31
10^-2
10^-1
1
10
10^2
10^3
10^4
RECOIL ENERGY (KeV)

Figure 1.3 Relative contributions of elastic and inelastic collisions to the total rate of energy loss of a primary knock-on (from Chadderton, 1965).

Figure 1.4 Schematic representation of the spatial distribution of vacancies and interstitials in a displacement cascade (Brinkman 1954).

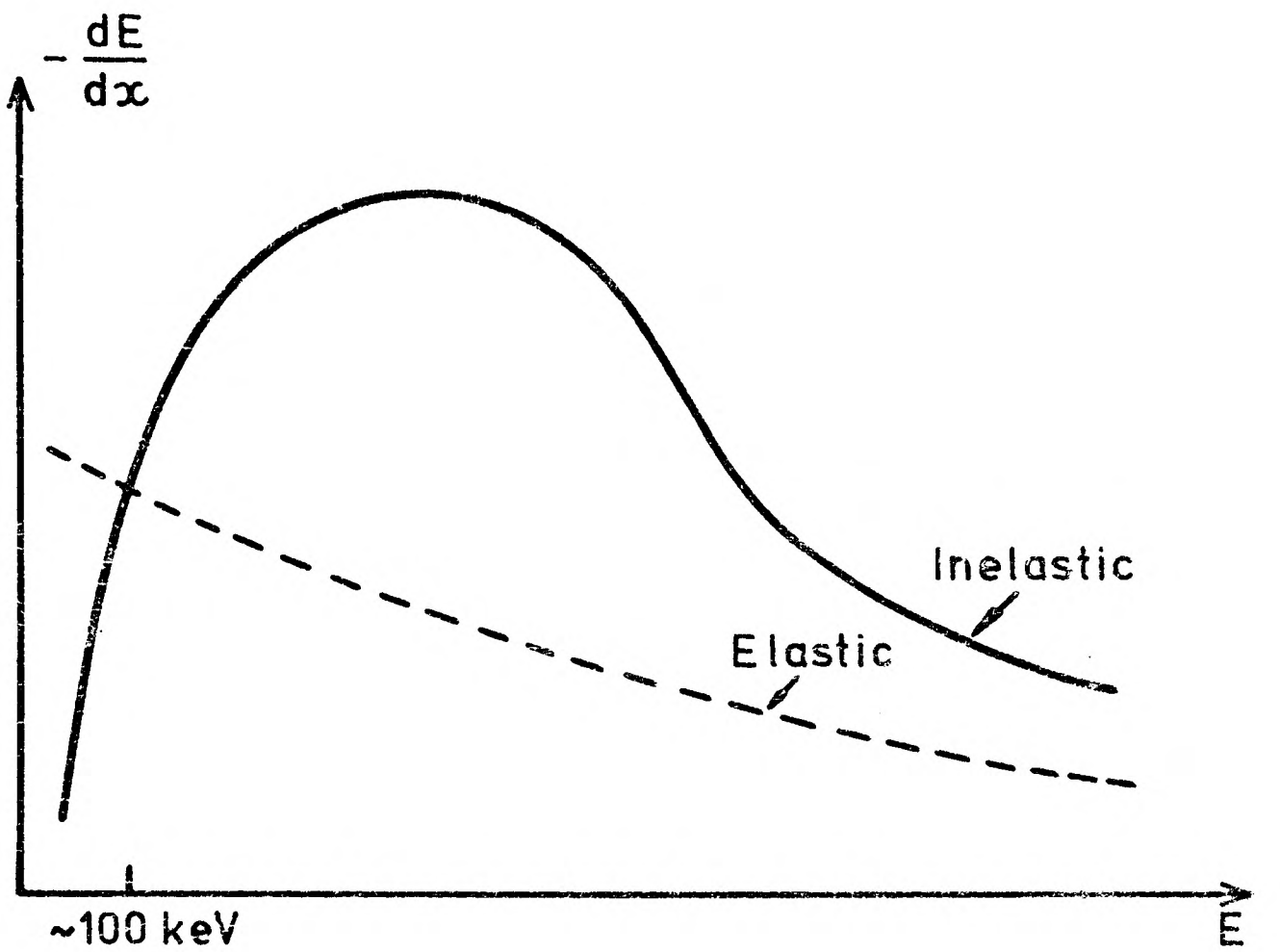
$-\frac{dE}{dx}$
Inelastic
Elastic
~100 keV
E

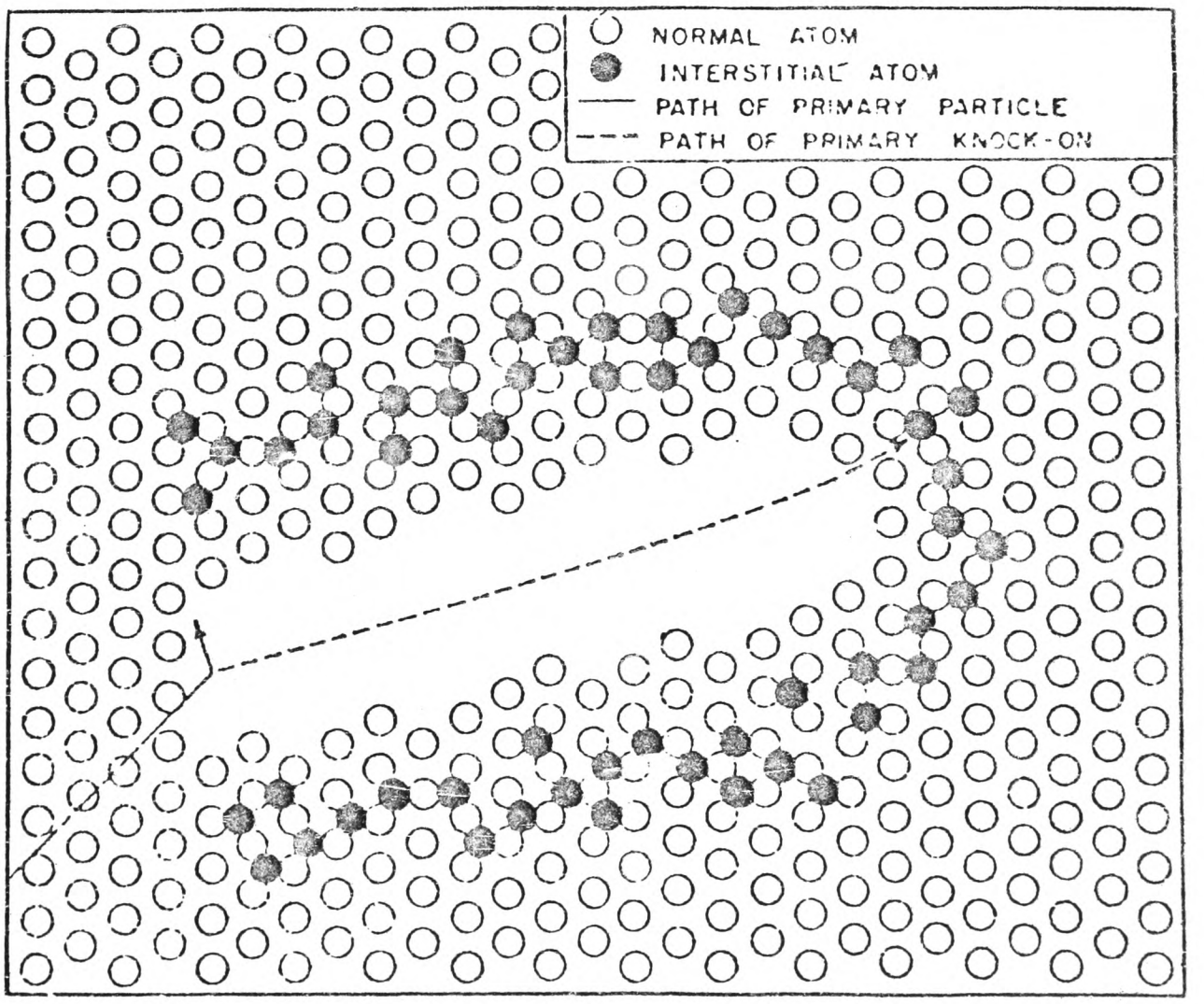
NORMAL ATOM
INTERSTITIAL ATOM
PATH OF PRIMARY PARTICLE
PATH OF PRIMARY KNOCK-ON

CHAPTER 2

Contrast from Small Point Defect Clusters by Electron Microscopy

2.1 Introduction

In an electron microscope, the high energy electrons incident on a crystalline specimen are scattered by the atoms of the crystal lattice. The effect of this scattering can be explained by considering a plane wave of wavelength $\lambda = {}^{h}/_{p}$ (p = electron momentum, h = Planck's constant) that is reflected by successive planes of the crystal lattice (Bragg 1913). Thus if the incident electron beam is inclined at an angle θ to the (hkl) planes such that the Bragg condition for those planes ($2d_{hkl} \sin\theta = n\lambda$) is satisfied, then an intense diffracted beam of electrons will propagate at an angle 2θ to the incident electron direction.

The complete pattern of diffracted beams that may arise simultaneously from a given specimen can be understood by making use of the reciprocal lattice and the Ewald sphere constructions. The relationship between the incident electron beam, a given set of real lattice planes, the corresponding reciprocal lattice point, the Ewald sphere and the direction of the diffracted beam is shown in figure 2.1. In this figure, the Bragg condition is satisfied for the reflection $\underline{g}_{hkl}$ and a strong diffracted beam occurs with the Ewald sphere intersecting the G_{hkl} reciprocal lattice point. The curvature of the Ewald sphere for 100 keV electrons ($^{1}/\lambda$ = 27.02 Å^{-1}) compared with the separation of the reciprocal lattice points (typically 0.5 Å^{-1}) results in it being possible for the Ewald sphere to intersect effectively just one reciprocal lattice point in addition to the origin. This corresponds to the electron beam being strongly diffracted by a single set of lattice planes and there is therefore only one intense first order ($n = 1$) diffracted beam. In this position, the Ewald sphere also passes close to the reciprocal lattice points located at $n\,\underline{g}_{hkl}$, but because of its curvature, its distances from these points are large enough that the corresponding higher order ($n > 1$) systematic diffracted beams are only weakly excited. Thus by suitably orientating the atomic lattice with respect to the incident electrons, it is possible

to approximate to "two-beam" conditions using 100 keV electrons.

If the lattice planes of a perfect crystal are bent locally by any kind of lattice distortion, the local intensity in both the direct beam and the diffracted beams may be altered as the diffraction conditions near the lattice defect will be changed. Thus if an objective aperture is used so that an image is formed using only one of the beams, the lattice defect may be visible as a result of the local change that it may produce in the diffracted intensity of that beam. If the direct beam is used a so called 'bright-field' image is produced; if one of the diffracted beams is used a 'dark-field' image results. When there is only one intense diffracted beam, the conditions under which this diffraction contrast arises are well defined. Thus small defect clusters can show characteristic and well-defined diffraction contrast when imaged under "two-beam" conditions, the exact variation in intensity of an image depending, among other variables, on the particular diffraction vector (g) being used.

The remaining sections of this Chapter are concerned with the theoretical image contrast of small defect clusters when imaged under these "two-beam" diffraction conditions. The dynamical theory of electron diffraction is outlined in section 2.2 and the general features of the image contrast of small defect clusters are described. A discussion follows of the methods by which defect natures and defect geometries may be analysed, and theoretical images of small defect clusters obtained under different diffraction conditions are presented. The variation in the size and visibility of such images with the diffraction conditions and the position of the cluster in the foil is discussed, as this illustrates the difficulties involved in trying to describe accurately the damage structures produced in heavy-ion irradiation experiments.

2.2 The Dynamical Theory of Electron Diffraction

2.2.1 Bloch Wave Formulation

In order to predict the theoretical image intensities produced by

a perfect or a distorted crystal, it is necessary to be able to describe the propagation of the electrons in the crystal since an image corresponds to the distribution of electrons at the exit surface of the crystal. The approach used here is based on that given by Bethe (1928) and later developed by Howie and Whelan (1961). The notation used is that of Hirsch, Howie, Nicholson, Pashley and Whelan (1965) who give a detailed account of the theory.

The wave function $\psi(\underline{r})$ describing the motion of an electron of energy Ee moving in a periodic crystal potential $V(\underline{r})$ is found by solving Schrödinger's equation

$$\nabla^2\psi(\underline{r}) + (8\pi^2 me/h^2)\,[E + V(\underline{r})]\,\psi(\underline{r}) = 0.$$

The most general form for the potential of a perfect crystal is

$$V(\underline{r}) = \frac{h^2}{2me}\sum_g U_g \exp(2\pi i\, \underline{g}.\underline{r}) = \sum_g V_g \exp(2\pi i\, \underline{g}.\underline{r})$$

where the summation extends over all the reciprocal lattice vectors $\underline{g}$ of the crystal and the U_g are constants. $\psi(\underline{r})$ can be expanded as a Bloch wave function of wave vector $\underline{k}$

$$\psi(\underline{r}) = b(\underline{k},\underline{r}) = \sum_g C_g(\underline{k}) \exp(2\pi i(\underline{k} + \underline{g})\,.\,\underline{r}). \qquad (2.1)$$

Substituting these expressions for $V(\underline{r})$ and $\psi(\underline{r})$ into Schrödinger's equation gives a set of equations satisfied by the wave amplitudes $C_g(\underline{k})$:-

$$\{K^2 - (\underline{k} + \underline{g})^2\}\, C_g(\underline{k}) + \sum_{h\neq 0} U_h\, C_{g-h}(\underline{k}) = 0 \qquad (2.2)$$

where

$$K = [2me(E + V_o)/h^2]^{\frac{1}{2}}$$

is the magnitude of the incident electron wave vector after correction for the wavelength change due to the mean crystal potential V_o (refractive index effect).

The Bloch wave function given for $\psi(\underline{r})$ is of general validity since it can consist of a combination of all the possible diffracted waves. When there is only one intense first order diffracted beam ($\underline{g}$), it is

possible to use a many-beam theory which ignores the non-systematic reflections while including the effect of the systematic reflections (n$\underline{g}$). However, for simplicity the following discussion will be limited to the "two-beam" theory which ignores the effect of both the non-systematic and the systematic reflections. In this case, the motion of the electrons can be described by two Bloch waves each containing contributions from just the forward scattered and the intense first order diffracted beams.

2.2.2 The "Two-Beam" Theory

Under the "two-beam" approximation, equations (2.2) for the Bloch wave amplitudes reduce to

$$(K^2 - k^2)\ C_o(\underline{k}) + U_{-g}\ C_g(\underline{k}) = 0$$

$$(K^2 - (\underline{k} + \underline{g})^2)\ C_g(\underline{k}) + U_g\ C_o(\underline{k}) = 0$$

These coupled equations can only be solved if the determinant formed by the coefficients vanishes and this gives

$$(k - K)(|\underline{k} + \underline{g}| - K) = |U_g|^2/4K^2.$$

This equation defines the possible wave vectors ($\underline{k}$) in the crystal for electrons of energy eE and the loci of the wave vectors lie on a surface in the reciprocal lattice known as the dispersion surface. The surface for high energy electrons is shown in figure 2.2 (Howie and Whelan 1961). Each point on either branch of the surface is associated with allowed wave vectors $\underline{k}$ and $\underline{k} + \underline{g}$ drawn to the points O and G in the reciprocal lattice. The Brillouin zone boundary is defined by points having $k = |\underline{k} + \underline{g}|$ and it therefore represents the exact Bragg condition. The distance (y) of a point on the surface from the zone boundary is given by $2y \tan \theta_B = S$ where θ_B is the Bragg angle and S describes the deviation from the exact Bragg condition and is equal to the distance in the incident electron direction (z-direction) from the reciprocal lattice point G to

the Ewald sphere.

The two branches of the dispersion surface correspond to two Bloch wave functions of slightly differing wave vectors $\underline{k}^{(1)}$ and $\underline{k}^{(2)}$. These wave vectors have the same tangential components as the incident electron wave vector $\underline{\chi}$ with their z components related by

$$\begin{aligned} k_z^{(1)} - \chi_z &= (2\xi_o)^{-1} + (S - \sqrt{S^2 + {}^1/\xi_g{}^2})/2 \\ k_z^{(2)} - \chi_z &= (2\xi_o)^{-1} + (S + \sqrt{S^2 + {}^1/\xi_g{}^2})/2 \end{aligned} \qquad (2.3)$$

The equal increases in the z components of the wave vectors by $(2\xi_o)^{-1} = U_o/2K\cos\theta_B$ results from the forward scattering of the electrons by the mean crystal potential V_o, while a difference between the second terms arises because of the crystal potential V_g. This potential couples the incident and diffracted plane waves together through the Bragg reflections and this results in a perturbation in the energy that splits the dispersion surface near the Brillouin zone boundary. A physical explanation for this difference in the wave vectors is given later. At the exact Bragg condition (S = 0), the difference is given by

$$\Delta k_{s=0} = k_z^{(2)} - k_z^{(1)} = \xi_g^{-1} = U_g/K\cos\theta_B$$

where ξ_g is known as the two-beam extinction distance for the reflection $\underline{g}$.

The electron wave function in the crystal has two independent solutions corresponding to the two Bloch wave functions. In a given situation the total wave function will consist of a definite linear combination of these two Bloch wave functions and by normalising the $C_g(\underline{k})$ of equation (2.1) so that $|C_o^{(1)}|^2+|C_g^{(1)}|^2 = |C_o^{(2)}|^2+|C_g^{(2)}|^2 = 1$, the electron wave function may be shown to have the form (Hirsch et al 1965 p.201)

$$\psi(\underline{r}) = \sum_{i=1,2} \psi^{(i)} b^{(i)} (\underline{k}^{(i)}, \underline{r}) = \psi^{(1)}\{\mathrm{Cos}(\tfrac{\beta}{2})\exp(2\pi i\underline{k}^{(1)}.\underline{r}) - \sin(\tfrac{\beta}{2})\exp(2\pi i(\underline{k}^{(1)}+\underline{g}).\underline{r})\}$$

$$+\psi^{(2)}\{\mathrm{Sin}(\tfrac{\beta}{2})\exp(2\pi i\underline{k}^{(2)}.\underline{r}) + \cos(\tfrac{\beta}{2})\exp(2\pi i(\underline{k}^{(2)}+\underline{g}).\underline{r})\} \qquad (2.4)$$

where the deviation parameter $\beta = \cot^{-1} S\xi_g$. The amounts $\psi^{(1)}$ and $\psi^{(2)}$ of the two Bloch waves excited depend on the orientation of the crystal and by satisfying the boundary conditions that $\psi(\underline{r})$ and $d\psi(\underline{r})/dZ$ should be continuous at the surface of the foil it may be shown (Hirsch et al 1965 p.214) that

$$\psi^{(1)} = \cos(\frac{\beta}{2}), \quad \psi^{(2)} = \sin(\frac{\beta}{2}).$$

Thus at the exact Bragg condition equal amounts of both Bloch waves are excited.

It is instructive to consider the intensities $|b^{(1)}(\underline{k}^{(1)}, \underline{r})|^2$ and $|b^{(2)}(\underline{k}^{(2)}, \underline{r})|^2$ of the two Bloch waves at the Bragg condition. Setting $\beta = \frac{\pi}{2}$ (i.e. S=0) in equation (2.4) gives

$$b^{(1)}(\underline{k}^{(1)}, \underline{r}) = {}^1/_{\sqrt{2}} \{\exp(2\pi i\, \underline{k}^{(1)} . \underline{r}) - \exp(2\pi i\, (\underline{k}^{(1)} + \underline{g}) . \underline{r})\}$$

$$= i\sqrt{2} \sin(\pi \underline{g} . \underline{r}) \exp(2\pi i\, (\underline{k}^{(1)} + \tfrac{1}{2}\underline{g}) . \underline{r})$$

$$b^{(2)}(\underline{k}^{(2)}, \underline{r}) = {}^1/_{\sqrt{2}} \{\exp(2\pi i\, \underline{k}^{(2)} . \underline{r}) + \exp(2\pi i\, (\underline{k}^{(2)} + \underline{g}) . \underline{r})\}$$

$$= \sqrt{2} \cos(\pi \underline{g} . \underline{r}) \exp(2\pi i\, (\underline{k}^{(2)} + \tfrac{1}{2}\underline{g}) . \underline{r})$$

Therefore

$$|b^{(1)}(\underline{k}^{(1)}, \underline{r})|^2 = 2\sin^2(\pi \underline{g} . \underline{r})$$

$$|b^{(2)}(\underline{k}^{(2)}, \underline{r})|^2 = 2\cos^2(\pi \underline{g} . \underline{r}).$$

Thus while the current in each of the two wave fields flows, on average, parallel to the Bragg planes, the modulation across the planes is such that the maxima of wave (1) are peaked between the atomic planes while the maxima of wave (2) are peaked about the atomic planes. This difference between the two waves is most marked at the Bragg condition but it also holds to a lesser extent for other orientations. It is this difference which accounts for the difference between $k_z^{(1)}$ and $k_z^{(2)}$ as given by equations (2.3). While both Bloch waves correspond to the same total energy, electrons in wave (2) spend more time in a region of low potential energy near the atoms in the crystal and therefore they must have a greater

average kinetic energy, i.e. a larger wave vector, than electrons in wave (1).

The difference in the modulation of the Bloch waves also results in a difference in the way these waves are inelastically scattered, resulting in the so called anomalous absorption effect. Because wave (2) is concentrated near the atoms, where scattering processes occur with greater probability than in other regions of the crystal, it will be scattered more than wave (1). When large angle scattering occurs, for example as a result of phonon scattering, the Bloch waves are scattered outside the aperture of the objective lens and are therefore effectively absorbed. Thus wave (2) will be more strongly absorbed than the less strongly scattered wave (1). Hashimoto et al (1960, 1962) have shown that the effect of this scattering can be accounted for by adding a small imaginary term to the crystal potential so that the Fourier coefficients change to $U_g + iU'_g$. The effect of the mean absorption is then given by $\xi'_o = K\cos\theta_B/U'_o$, while the anomalous absorption coefficient $\xi'_g = K\cos\theta_B/U'_g$.

2.2.3 Bloch Waves in a Distorted Crystal

The presence of imperfections in a crystal causes a redistribution of amplitude between the Bloch waves. This redistribution can be calculated using the "column approximation" (Hirsch et al 1960). In this approximation, a crystal is divided into thin columns parallel to the electron beam and it is assumed that because of the small scattering angle ($2\theta_B \sim 1^o$) of the electrons, there is no interaction between waves from neighbouring columns. The electron wavefunction at the emergent surface of each column is then the same as that for an infinite slab of crystal with the same lattice displacements as those in the column. By using this approximation and for simplicity neglecting absorption effects, Howie (1963) has shown that the coupled differential equations linking $\psi^{(1)}$ and $\psi^{(2)}$, the relative amounts of the two Bloch waves excited, have the form

$$\left.\begin{aligned} d\psi^{(1)}/dZ &= 2\pi i\beta'_g \{\sin^2\tfrac{\beta}{2}\,\psi^{(1)} - \cos\tfrac{\beta}{2}\sin\tfrac{\beta}{2}\,\psi^{(2)}\exp(2\pi i(k_z^{(2)}-k_z^{(1)})Z)\} \\ d\psi^{(2)}/dZ &= 2\pi i\beta'_g \{\cos^2\tfrac{\beta}{2}\,\psi^{(2)} - \sin\tfrac{\beta}{2}\cos\tfrac{\beta}{2}\,\psi^{(1)}\exp(-2\pi i(k_z^{(2)}-k_z^{(1)})Z)\} \end{aligned}\right\} \quad (2.5)$$

where $\beta'_g = d(\underline{g}.\underline{R}(z))/dZ$ is the strain field due to $\underline{R}(z)$, the lattice displacement at depth Z due to the imperfection.

The first terms on the right-hand side of equation (2.5) describe scattering within a Bloch wave, the intraband scattering, while the second terms describe scattering between Bloch waves, the interband scattering. Howie (1963) has shown that the phase changes of $\psi^{(1)}$ and $\psi^{(2)}$ due to the intraband scattering are equal at the exact Bragg condition, and thus the diffraction contrast arises mainly from the interband scattering. From equations (2.3), the difference in the wave vectors of the two Bloch waves is $k_z^{(2)} - k_z^{(1)} = (S^2 + {}^1/\xi_g{}^2)^{\frac{1}{2}}$, and thus the only strain fields that are effective in causing interband scattering will be those where the arguments of the Fourier components correspond to wavelengths of less than ξ_g (Hirsch et al 1965 p.259). Dislocation images therefore have a width which is dependent on the extinction distance since the distance from a dislocation where the strain field varies rapidly enough to cause interband scattering will increase for larger values of ξ_g.

The Bloch wave differential equations adapted to take account of absorption can be numerically integrated to give the bright-field and dark-field intensities in a distorted crystal. The integration is generally complex and analytical solutions are not normally obtained. However, the equations may be simplified by neglecting the intraband scattering and by only considering diffraction occurring at the exact Bragg condition. In addition, it is possible to make certain simplifying assumptions for localised displacement fields. In this way Hirsch (1966), Wilkens and

Rühle (1972) and Katerbau (1976) have derived analytic expressions describing the image characteristics of small dislocation loops imaged under dynamical two-beam conditions. A discussion of their results is given in Section 2.2.5.

2.2.4 Plane Waves in a Distorted Crystal

In the two-beam approximation, the Bloch wave equations are equivalent to a transmitted plane wave

$$\phi_o(z)\ \exp(2\pi i \underline{\chi}.\underline{r}) \;=\; \sum_{i=1,2} \psi^{(i)} C_o^{(i)}\ \exp(2\pi i \underline{k}^{(i)}.\underline{r}) \tag{2.6}$$

and a diffracted plane wave

$$\phi_g(z)\ \exp(2\pi i(\underline{\chi}+\underline{g}).\underline{r}) \;=\; \sum_{i=1,2} \psi^{(i)} C_g^{(i)}\ \exp(2\pi i(\underline{k}^{(i)}+\underline{g}).\underline{r}).$$

The differential equations describing the redistribution of amplitude between the Bloch waves due to lattice distortions can therefore be rewritten in terms of a redistribution of amplitude between these plane waves. When absorption effects are included, the equations become (Howie and Whelan 1961),

$$\left.\begin{aligned} \frac{d\phi'_o}{dZ} &= -\frac{\pi\phi'_o}{\xi'_o} + \pi\left(\frac{i}{\xi_g} - \frac{1}{\xi'_g}\right)\phi'_g \\ \frac{d\phi'_g}{dZ} &= \pi\left(\frac{i}{\xi_g} - \frac{1}{\xi'_g}\right)\phi'_o + \left\{-\frac{\pi}{\xi'_o} + 2\pi i(S+\beta'_g)\right\}\phi'_g \end{aligned}\right\} \tag{2.7}$$

where ϕ'_o and ϕ'_g are simply related to the bright-field ϕ_o and dark-field ϕ_g plane wave amplitudes. Equations (2.7) are particularly suited to solution by numerical methods. If the strain field β'_g of a defect is known, then by applying the boundary conditions that $\phi'_o = 1$ and $\phi'_g = 0$ at $z = 0$ (the top surface of the foil), the bright-field and dark-field amplitudes at the bottom surface of the foil, $\phi_o(t)$ and $\phi_g(t)$, may be evaluated. This method has been used by several authors (e.g. Bullough et al 1971, Saldin and Whelan 1975, Eyre et al 1976, Holmes et al 1976, Ohr 1976) to calculate the image intensities of dislocation loops in

isotropic cubic crystals. These theoretical image intensities are discussed later in this chapter.

2.2.5 General Contrast Features of Small Defect Clusters

If the diameter of a dislocation loop is less than about ξ_g, the geometrical shape of the loop is not directly resolvable under two-beam diffraction conditions. If the deviation away from the Bragg condition is such that the dimensionless deviation parameter $w = S\xi_g \geq 0.8$ (so called kinematic conditions), then such small loops show only 'black dot' contrast which provides no information about the loop nature or the loop geometry. The following discussion is therefore concerned with the general contrast features of these small loops when imaged at the Bragg condition. Hirsch (1966) has derived analytic expressions for the bright-field and dark-field wave amplitudes for localised displacement fields in thick foils by considering the interband scattering between Bloch waves (see section 2.2.3). The results given here, which are discussed in more detail by Wilson (1970), follow from these analytic expressions.

The strain field β'_g down a column on either side of a small vacancy dislocation loop is shown schematically in figure 2.3(a) (Wilson 1970). It can be seen that β'_g has opposite signs on either side of the line, drawn normal to $\underline{g}$, that passes through the middle of the strain field. Since the wave amplitudes have a linear dependence on the Fourier transforms of β'_g (Hirsch 1966), the image will look dark on one side of this line and bright on the other. This so called black-white contrast is characteristic of small defect clusters lying within about 1.5 ξ_g of the foil surface when imaged at the Bragg condition, and the line joining the centre of the black lobe to the centre of the white lobe is defined by the unit vector $\underline{l}$. The variation in the strain field on either side of a small interstitial dislocation loop is shown by figure 2.3(b), and it can be seen that the direction of $\underline{l}$ in relation to $\underline{g}$ will be reversed compared with the vacancy loop. The sign of $\underline{g}.\underline{l}$ therefore varies with

the loop nature.

The expression derived by Hirsch for the bright-field wave amplitude of a small centre of strain is antisymmetric in relation to the top and bottom surfaces of the foil, while the expression for the dark-field wave amplitude is symmetric. Thus a small dislocation loop of a given nature at distance t_1 from the top surface of a foil will give opposite contrast to a similar loop at distance t_1 from the bottom surface of the foil when imaged in bright-field, and the same contrast when imaged in dark-field. In addition, the expressions show that for defect clusters located next to the top surface of the foil, the dark-field contrast is the same as the bright-field contrast for the same operating reflection $\underline{g}$.

The expressions derived by Hirsch also show that the direction of $\underline{l}$ for a given dislocation loop will oscillate with distance from the foil surface. This oscillation of the black-white contrast with depth originates from the interband scattering between the Bloch waves. The small difference between the wave vectors $\Delta k_z = (S^{2+1}/\xi_g^{\,2})^{\frac{1}{2}}$ results in interference beats occurring in the z-direction and the bright-field and dark-field intensities oscillate with a wavelength given by $(\Delta k_z)^{-1}$. Thus at the exact Bragg condition this wavelength is equal to ξ_g, while away from the Bragg condition this wavelength is reduced by a factor $(S^2\xi_g^{\,2}+1)^{-\frac{1}{2}}$. This dependence of $\underline{l}$ on the distance of a loop from the surface of a foil is discussed further in section 2.3.

Because of the strong absorption of Bloch wave (2), defect clusters only show strong black-white contrast if they lie within about 1.5 ξ_g of either foil surface. The reason for this can be understood qualitatively from the following argument given by Wilson (1970). For a defect near the top of a foil, wave (2) still has a large intensity and electrons may be scattered and enhance wave (1). Near the bottom of a foil, a defect will scatter electrons from wave (1) into wave (2), which will not be absorbed much in reaching the foil exit surface. However, for defects

lying near the centre of thick foils neither of these single scattering processes give much contrast because of the strong absorption of wave (2). Katerbau (1976) has shown analytically that the contrast of defects lying near the centre of a thick foil arises mainly from double scattering between the Bloch waves and this results in 'black dot' image contrast.

Katerbau (1976) has also shown analytically that the inner structure of black-white contrast figures depends on the value of $|\underline{g}.\underline{b}|$. For $0 < |\underline{g}.\underline{b}| \leq 1$, a simple black-white contrast is found while for $1 < |\underline{g}.\underline{b}| \leq 2$, a more complicated contrast figure occurs showing a black spot in the white lobe and a white spot in the black lobe. This dependence of the symmetry of an image on $|\underline{g}.\underline{b}|$ is discussed further in section 2.4.2.

2.3 Determination of Defect Nature

The discussion of section 2.2.5 has shown that while the direction of $\underline{l}$ relative to $\underline{g}$ for defect clusters imaged under "two-beam" diffraction conditions depends on the nature (vacancy or interstitial) of the defect cluster, it also depends on the distance, measured in terms of $\xi_g^w = \xi_g / (S^2\xi_g{}^2+1)^{\frac{1}{2}}$, of the defect cluster from the neighbouring surface of the foil.

In the absence of surface relaxation of the loop displacement field, the depths at which contrast reversals occur have been calculated as $0.25\ \xi_g^w$, $0.75\ \xi_g^w$, $1.25\ \xi_g^w$ ... (McIntyre 1967). The thickness of the first layer depends on the derivative of the displacement field and the effect of surface relaxation is to produce additional displacements, which decrease with distance from the foil surface. Rühle et al (1965) included surface relaxation in their calculations and they found that contrast reversal occurred at depths of $0.3\ \xi_g^w$, $0.75\ \xi_g^w$, $1.25\ \xi_g^w$ ... , although the thickness of these layers was found to depend slightly on the size of the dislocation loop. Both the above calculations were carried out for pure edge loops and the results are therefore only applicable to Frank loops. However, as discussed in section 2.4.3, the

habit planes of perfect loops that are formed by shear over Frank loops tend to rotate towards the edge configuration, and Rühle (1969) states that provided the derivative of the displacement field of a perfect loop $d(\underline{g}.\underline{R}^{(P)})/dZ = d(\underline{g}.\underline{R}^{(F)})/dZ + d(\underline{g}.\underline{R}^{(S)})/dZ$ is mainly determined by the derivative of the Frank component (F), that is the edge component, rather than by the derivative of the shear component (S), then the width of the first layer for the perfect loop should not be appreciably different from that calculated for Frank loops.

Because of this depth oscillation, the position of a defect cluster relative to the crystal surface must be known before its nature can be determined. This depth measurement may be carried out using the stereo-microscopy technique (e.g. Wilkens and Rühle 1966, Diepers and Diehl 1966). However, it may be that the range of the incident ions and the value of ξ_g^w are such that the damage is all located within the first layer and then it is not necessary to determine the precise depth of the defect cluster. The depth of the first layer depends on the value of ξ_g^w, which in turn depends on the deviation from the Bragg condition 'S', the operating reflection '$\underline{g}$' and the electron velocity. Thus it is possible to increase the depth of the first layer, either by increasing the accelerating potential or by using a higher-order reflection, so that more, or perhaps all, of the defect clusters lie within it.

If the defect cluster is imaged in bright-field, then it is also necessary to know which surface the defect cluster is located next to (see section 2.2.5). This can be easily achieved by a comparison of the bright-field and dark-field images, since for the same operating reflection $\underline{g}$, the direction of $\underline{l}$ will be the same in both bright-field and dark-field if the defect cluster is located next to the top surface of the foil.

Both Rühle et al (1965) and McIntyre and Brown (1966) have shown that small vacancy clusters lying in the first depth layer produce dark-field images for which $\underline{g}.\underline{l} > 0$. The relationship between $\underline{l}$ and $\underline{g}$ for a small

vacancy cluster as a function of the distance of the centre of the cluster from the surface of a foil is therefore as shown by figure 2.4. Thus the defect nature can be determined when its distance from a foil surface is known. However, small defect clusters lying at depths greater than about the fourth layer ($Z > 1.5\ \xi_g$) do not in general show black-white contrast, and therefore their natures can not be determined.

2.4 Determination of Defect Geometry

2.4.1 "$\underline{l}$-Vector" Analysis

A comparison between early theoretical image calculations for dislocation loops of pure edge character and the experimentally observed images indicated that the direction of the line from the centre of the black lobe of the image to the centre of the white lobe, the $\underline{l}$ vector, was independent of the operating reflection $\underline{g}$ and was parallel or anti-parallel to $\underline{b}p$ (Rühle et al 1965, Rühle 1967a) or nearly so (McIntyre and Brown 1966, McIntyre 1967), where $\underline{b}p$ is the projection of the dislocation Burgers vector onto the image plane. This result was also believed to hold in the case of perfect loops (Rühle et al 1965) and was the basis of the "$\underline{l}$-vector" analysis method for determining the Burgers vectors of small dislocation loops.

However, more recent results using better image simulation techniques have shown that for loops with shear components, $\underline{l}$ is not in general parallel or anti-parallel to $\underline{b}p$ (Rühle and Wilkens 1970, Wilkens and Rühle 1972, Holmes et al 1976). Also, Eyre et al (1974) have shown that for edge dislocation loops the angle between $\underline{l}$ and $\underline{b}p$ increases as the angle between $\underline{b}p$ and $\underline{g}$ increases. This deviation of $\underline{l}$ away from $\underline{b}p$ for both edge and non-edge loops has been put on a quantitative basis by Ohr (1976). He found that for loops in an elastically isotropic medium, the deviation of $\underline{l}$ away from $\underline{g}$ is directly proportional to the sum of the deviations of $\underline{b}$ and $\underline{n}$ projected onto the image plane. The way this relationship would be modified by the inclusion of elastic anisotropy is unknown, although

Yoffe (1970) has found that for edge loops, $\underline{l}$ lies more closely parallel to $\underline{b}p$ when anisotropy is included. These results therefore show that a knowledge of the $\underline{l}$ direction is not, in general, sufficient to determine the loop geometry.

2.4.2 The Symmetry of Images

The accepted method of analysing the geometry of small defect clusters is now to either compare the experimental images with simulated micrographs (e.g. Häussermann et al 1972, Eyre et al 1976b) or to consider the general symmetry of the images (Wilson and Hirsch 1972, Wilkens and Rühle 1972, Katerbau 1976, Eyre et al 1976). In particular, the computer simulated micrographs of Eyre et al (1976) have shown that the symmetry of an image depends on the value of $|\underline{g}.\underline{b}|$. This result has also been formed analytically by Katerbau (1976) (see section 2.2.5).

Eyre et al (1976) have classified the image symmetries into four main types. For $|\underline{g}.\underline{b}| = 0$, the type of image depends on the angle between the loop plane normal ($\underline{n}$) and the image plane normal ($\underline{z}$). When this angle is less than about 45^{o}, the images show simple black-white contrast which is, in general, too weak to be detected experimentally. However, when this angle is greater than about 80^{o}, the images show characteristic 'butterfly' contrast with three black lobes alternating with three white lobes (see figure 2.5a). For $0 < |\underline{g}.\underline{b}| \leq 1$, the images show simple black-white contrast while for $|\underline{g}.\underline{b}| > 1$, the interface between the black and white lobes becomes more complex with a white region appearing within the black lobes (see figures 2.5d and 2.5k).

If the experimental images of a dislocation loop are sufficiently well defined, then it is easy to distinguish experimentally between those images which do not show simple black-white contrast and those that do. Thus if a small dislocation loop is imaged under suitably chosen diffraction conditions, the absence or presence of 'butterfly' or $|\underline{g}.\underline{b}| > 1$ images allow firm conclusions to be drawn with regard to both loop Burgers vector

and loop habit plane.

2.4.3 Computer Simulated Micrographs of Small Defect Clusters in F.C.C. Materials

Cascade collapse in F.C.C. materials is believed to occur onto the close-packed {111} planes. This results in the formation of so called Frank loops which are faulted loops with Burgers vectors $\underline{b} = \frac{a}{3}\langle 111\rangle$ and loop plane normals $\underline{n} = \langle 111\rangle$. The stacking fault enclosed by a Frank loop may be removed by a Shockley partial dislocation causing shear in a $\langle 211\rangle$ direction. This Shockley partial dislocation reacts with the bounding Frank dislocation in a reaction of the type

$$\frac{a}{6}[11\bar{2}] + \frac{a}{3}[111] \rightarrow \frac{a}{2}[110]$$

and the shear therefore results in the formation of perfect loops with $\underline{b} = \frac{a}{2}\langle 110\rangle$. The lowest energy state of a perfect loop of a given size occurs when the loop Burgers vector is normal to the loop habit plane, and there will therefore be a tendency for the loop plane normal to rotate from the $\langle 111\rangle$ direction to the appropriate $\langle 110\rangle$ direction. However, this rotation increases the length of loop dislocation line, thereby increasing the loop energy, and thus the lowest energy state of the perfect loop will have the loop plane normal lying somewhere between the relevant $\langle 111\rangle$ and $\langle 110\rangle$ directions.

Alternatively, the $\underline{b} = \frac{a}{3}\langle 111\rangle$ partial dislocation bounding a Frank loop may dissociate according to a reaction of the type first proposed by Silcox and Hirsch (1959), that is

$$\frac{a}{3}[111] \rightarrow \frac{a}{6}[101] + \frac{a}{6}[121].$$

The $\underline{b} = \frac{a}{6}\langle 211\rangle$ Shockley partial dislocations can then bow out in their slip planes to give areas of stacking fault on other {111} planes in addition to the Frank loop habit plane. This results in the formation of either partially dissociated Frank loops, which have unequal areas of stacking fault on the four {111} planes, or fully dissociated Frank loops,

that is stacking fault tetrahedra, which have equal areas of stacking fault on the four {111} planes that meet along the six <110> directions at $\underline{b} = \frac{a}{6}$ <110> stair-rod dislocations.

Both Saldin and Whelan (1975) and Eyre et al (1976b) have produced computer simulated micrographs for some of the defect geometries that occur in F.C.C. materials. The method used by both groups was the same, differing only in the expression used for the displacement fields. The electron intensities at the exit surface of the deformed crystal were calculated from the Howie-Whelan equations (equations (2.7)) and the results of these calculations were displayed in the form of two-dimensional computer simulated micrographs using a simulation method similar to that of Maher et al (1971).

In the calculations of Eyre et al, the displacement function used was that of a circular interstitial dislocation loop in an elastically isotropic medium (Bullough et al 1971). The defect geometries considered were Frank loops and perfect loops and the results of the calculations for edge-on edge loops imaged using several different $\underline{g}$s in a foil with an [011] normal are shown in figure 2.5. While these calculations were carried out for loops in an elastically isotropic medium, it was not thought that the inclusion of elastic anisotropy would significantly alter the image symmetries (see section 2.4.2).

The defect geometries considered by Saldin and Whelan were the Frank loop and the stacking fault tetrahedron. The displacement field for a dislocation loop in an elastically isotropic medium was found by considering an nexagonal loop constructed from angular dislocations and that for the tetrahedron was found by constructing the tetrahedron from four triangular edge loops situated on the four faces of the tetrahedron. The results of these calculations for the defect clusters imaged using several different $\underline{g}$s in a foil with an [011] normal are shown in figures 2.6 and 2.7. The images of an edge-on Frank loop on the 'γ' plane show good

agreement, in terms of both symmetry and $\underline{1}$ direction, with those of Eyre et al, indicating that the exact shape of the defect cluster does not greatly influence the theoretical image contrast. In the case of the stacking fault tetrahedron, it can be seen that the images are characterised by well defined black-white interfaces that correspond to the projection of the two 'edge-on' {111} planes of the tetrahedron onto the image plane.

So far, no calculations have been reported for the theoretical image contrast of partially dissociated Frank loops.

2.5 Relationship Between Image Size and Cluster Size

2.5.1 Introduction

The size of the electron microscope image of a small defect cluster of a given size depends on a number of variables. These include the operating diffraction vector $\underline{g}$ and its deviation S from the exact Bragg condition, the depth 'Z_o' of the defect in the foil, the thickness 't' of the foil, the loop habit plane $\underline{n}$ and the loop Burgers vector $\underline{b}$. The optimum conditions to use for a determination of defect sizes are those where the shapes and widths of the images are fairly insensitive to the parameters that are difficult to determine during the experiment, that is 'Z_o' and 't'. The different experimental conditions that have been used to determine defect cluster sizes are discussed below with particular reference to the way the factor $R = \frac{W}{d}$, which relates the cluster diameter 'd' to its image width 'W', varies with these parameters.

2.5.2 Kinematical Conditions

Images obtained under kinematical conditions ($w = S\xi_g \geq 0.8$) have been widely used in the past for defect size measurements (e.g. Rühle 1967b). When imaged under such conditions, small defect clusters show 'black-dot' contrast and a possible measure of the image size is given by the largest diameter of the black dot. What is actually measured depends on how sensitive the human eye is in differentiating between the image

intensity of the black dot and the background intensity and this depends on the contrast gradient as well as the actual difference in intensity. In theoretical calculations (Rühle 1976b, Katerbau et al 1974) it has been assumed that the edge of the image contrast in quantitative visual measurements lies where the intensity differs from background intensity by 20%.

Katerbau et al (1974) have determined the dependence of the contrast curves of the kinematical images of an inclined Frank loop on Z_o and t by numerically integrating differential equations of the Bloch wave type. They found a quasiperiodical dependence of the contrast figure on Z_o, the contrast being weak for $Z_o \approx (n + \frac{1}{4})\ \xi_g^w$ (n = integer) and strong and more sharply defined for $Z_o \approx (n + \frac{1}{2})\ \xi_g^w$. The contrast was also strong but distinctly broader for $(n + 0.7)\ \xi_g^w < Z_o < (n + 1)\ \xi_g^w$. They also found that for a given value of Z_o, the contrast was much stronger for $t = (n + \frac{1}{2})\ \xi_g^w$ than for $t = n\ \xi_g^w$. They concluded that the width of the contrast curve of the image was sensitive to both Z_o and t, and that the factor R could have values lying between R = 1.1 and R = 1.6 depending on the value of Z_o.

This strong dependence of the measured image width on the depth of the cluster in the foil is one of the major disadvantages of using kinematical images to determine defect cluster sizes. Another disadvantage is that defect clusters with diameters between 15 → 25 Å may not show detectable image contrast under kinematical conditions, although they might when imaged at the exact Bragg condition (see section 2.6).

2.5.3 Weak-Beam Conditions

The weak-beam technique of electron microscopy (Cockayne et al 1969) in which images are formed by a weakly excited ($w = |\xi_g S_g| > 5$) beam allows the geometrical shape of small dislocation loops with diameters as low as approximately 50 Å to be directly resolved. Several authors (e.g. Jenkins et al 1973, Stathopoulos 1977) have used this technique to

directly measure the size of small defect clusters from their weak-beam images.

Theoretical calculations by Cockayne (1972) and Häussermann et al (1973) have shown that the shape of the contrast figure of small defect clusters imaged under weak-beam conditions is not very sensitive to the foil thickness, but Häussermann et al found a strong oscillatory dependence on the depth position Z_o of the defect centre. In practice, Jenkins et al (1973) found no strong depth dependence and this was attributed to the large beam divergence employed smearing out the contrast oscillations. Jenkins et al showed that the geometric shape of edge dislocation loops of diameter ≥ 80 Å could be resolved under weak-beam conditions, and their theoretical calculations suggested that the size of planar loops with diameters ≥ 50 Å viewed normal to their plane could be directly determined from their weak-beam images.

In the present series of experiments, only a small percentage (< 10%) of the defect clusters had diameters ≥ 50 Å, and thus images obtained under weak-beam conditions would not enable the sizes of the majority of the defect clusters to be measured directly.

2.5.4 Dynamical Conditions

The dynamical image of a small defect cluster, that is the image formed at or close to the Bragg condition, displays black-white contrast. Wilson (1970) has used such images for determining defect sizes and he took the size of an image showing simple black-white contrast to be the width of the interface between the black and white parts of the contrast. In recent theoretical calculations, Katerbau (1977) has found that the effect of varying 'Z_o' is to alter the size of such an image as measured in the sense of $\underline{1}$, that is from the black lobe to the white lobe. He found that the width of the black-white interface is relatively insensitive to 'Z_o' and 't' and is approximately equal to the diameter of the defect cluster (i.e. $R = \frac{W}{d} = 1$). Thus the width of the black-white interface

of a dynamical image appears to be less sensitive to variations in 'Z_o' and 't' than does the width of an image obtained under kinematic conditions.

Even when image widths are measured from dynamical images, additional precautions need to be taken to obtain consistent determinations of defect sizes because while the calculations of Katerbau indicate that the factor R is approximately equal to one, its exact value also depends on the cluster geometry, that is $\underline{b}$ and $\underline{n}$, and on the operating reflection $\underline{g}$. This dependence has not yet been given a rigorous theoretical basis, so the variation in the width of the black-white interface of the image of a Frank loop with these parameters will be discussed qualitatively, along with the measures that can be taken to minimise these variations.

The diffraction contrast from dislocations arises from interband scattering between the Bloch waves and so dislocation images have a width which is dependent on the extinction distance. The value of ξ_g depends on the operating reflection $\underline{g}$, being larger the higher the order of the reflection. Thus image widths obtained using a low order reflection such as $\underline{g}$ = <111> would be expected to be smaller than those obtained using a higher order reflection such as $\underline{g}$ = <022>. This can be seen from figure 2.5 which shows how the image width of a Frank loop of a given size is smaller when imaged using $\underline{g} = [1\bar{1}1]$ or $[11\bar{1}]$ than when imaged using $\underline{g} = [0\bar{2}2]$. Thus to obtain consistency when comparing image widths it is better to use images that have been obtained using the same operating reflection $\underline{g}$.

Equation (2.5) shows that the redistribution of amplitude between the Bloch waves depends on $\beta'_g = d(\underline{g}.\underline{R}(z))/dZ$. Thus the intensity of the image contrast and therefore the measured width of an image will depend on the value of $\underline{g}.\underline{b}$. Images with $|\underline{g}.\underline{b}| = 0$ or $\frac{1}{3}$ are, in general, relatively weak while images with $|\underline{g}.\underline{b}| \geq \frac{2}{3}$ are, in general, relatively strong. Physically this can be understood from the fact that the contrast

is weak when the major component of the displacement field is parallel to the reflecting planes. The Burgers vectors of Frank loops in F.C.C. materials have four possible directions given by $\underline{b} = \frac{a}{3}\langle 111\rangle$, and in general a given reflection $\underline{g}$ will result in both weak images ($|\underline{g}.\underline{b}| < \frac{2}{3}$) and strong images ($|\underline{g}.\underline{b}| \geq \frac{2}{3}$) among these four different Frank loops. This is shown by table 2.1 which gives the $\underline{g}.\underline{b}$ values of the different Frank and perfect loops when imaged using the low order reflections at a <110> pole. From this table it can be seen that if the damage structure is imaged using a $\underline{g} = \langle 002\rangle$ reflection, then $|\underline{g}.\underline{b}| = \frac{2}{3}$ for all the four different Frank loops, which in the present case corresponded to more than ninety five percent of the total loop population. Thus by imaging the defects using a $\underline{g} = \langle 002\rangle$ reflection, any difference that might arise in measuring image widths as a result of a difference in the image intensities will be minimised.

Even when the above precautions are taken, that is only comparing images which have the same $|\underline{g}.\underline{b}|$ values and which have been imaged using the same operating reflection $\underline{g}$, the image widths still vary with the loop habit plane $\underline{n}$. This can be seen from figure 2.7 (Saldin 1977) which shows the theoretical image contrast for the four Frank loops ($\underline{n} = \langle 111\rangle$) when imaged at the [011] pole. At the [011] pole, two of the Frank loops are 'edge-on' to the electron beam and two are 'inclined' to the electron beam, and it can be seen from figure 2.7 that the image width of one of the 'inclined' loops is substantially smaller than for the other three loops when imaged using $\underline{g} = [200]$.

While the dependence of the factor R on $\underline{n}$, $\underline{b}$ and $\underline{g}$ has only been illustrated for Frank loops, a similar dependence exists for perfect loops. However, the quantitative dependence is not exactly the same and figure 2.5 shows the difference between the theoretical image widths of an edge perfect loop with $\underline{b} = \frac{a}{2}[0\bar{1}1]$ and a Frank loop with $\underline{b} = \frac{a}{3}[\bar{1}\bar{1}1]$ of the same size, when imaged using the same $\underline{g}$s at the [011] pole. Thus

when trying to relate accurately image widths to defect sizes an analysis of each cluster configuration is necessary. But even then, the theoretical knowledge of the quantitative variation of R on $\underline{n}$, $\underline{b}$ and $\underline{g}$ is rather poor so that the precise relationship between 'W' and 'd' for a given cluster would still not be exactly known.

Thus in the present series of experiments, the following procedure was adopted in order to obtain a consistent and as accurate as possible determination of the defect cluster sizes. Defect size measurements were taken from images obtained under 'two-beam' conditions at the exact Bragg angle using a $\underline{g}$ = <002> operating reflection. The width of an image was measured as the length of the interface between the black and white lobes of the image, and in relating this image width to the actual defect size an average value of R = 1 was applied to all the clusters, independent of their geometry or their position in the foil.

2.6 Defect Visibility

For a defect cluster to be detectable in a thin crystal it must produce an image which is distinguishable from background. The results of Stathopoulos (1977) indicate that defect clusters with diameters as small as 8 Å may produce visible diffraction contrast. However, in the present experiments, the lower size limit for defect cluster visibility was found to be approximately 15 Å.

Defect clusters with diameters greater than 25 Å do, in general, produce detectable image contrast when imaged at or close to the Bragg condition (provided $\underline{g}$ is chosen such that $|\underline{g}.\underline{b}| \geq \frac{2}{3}$). The visibility of the images of defect clusters with diameters less than this depends on the size of the defect cluster, its inclination to the electron beam, the value of the deviation parameter $w = S\,\xi_g$, the position of the loop in the foil and the thickness of the foil, and on the quality of the foil surface. The dependence of the strength of the image contrast on the inclination of the loop to the surface was discussed in section 2.5.4.

In deviating away from the Bragg condition, the diffraction contrast from a cluster of a given size is reduced. The dependence of the image contrast of small defect clusters on the value of 'w' has been discussed by Rühle (1967b). This dependence is illustrated by figure 2.8 (Saldin 1977) which shows how the theoretical image contrast of an edge-on or an inclined Frank loop is considerably reduced for values of $w \geq 0.8$. Thus small defect clusters which are visible when imaged at the exact Bragg condition ($w = 0$) may no longer show detectable image contrast when imaged under kinematic conditions ($w \geq 0.8$).

Theoretical calculations by Katerbau (1976) have shown that for defects imaged under dynamical conditions, the contrast of defects lying more than about 1.5 ξ_g from the surface of a thick foil is a black spot. This image contrast arises from double scattering between the Bloch waves which only occurs near the centre of a defect cluster where the strain field β'_g is sufficiently large. The width of the contrast figure of these defects is considerably smaller than if the defects were lying close to the foil surface, where they would show black-white contrast, and thus small defect clusters near the centre of thick foils may be invisible while similar defects of the same size near the foil surfaces may show clear image contrast. Small defect clusters are also less visible if they are located close to the top surface of a thick foil than if they are located the same distance from the bottom surface of the foil (Noggle et al 1970, English, C.A, unpublished). This is thought to be a consequence of either beam divergence or chromatic abberation spreading out the image contrast in traversing the thick foil, so that the contrast from the smaller defects may no longer be distinguishable from background.

The visibility of small defect clusters is important when trying to determine accurate 'defect yield' values. The best conditions for observing defect clusters are therefore when the clusters are located next to the bottom (electron exit) surface of the foil and to image these clusters

at the exact Bragg condition. However, theoretical calculations (Katerbau 1976) have shown that even under these conditions, the image contrast from defects centred on $Z_o = (2n - 1)\ \xi_g/4$ is weaker than for similar defects centred on $Z_o = (n - 1)\ \xi_g/2$.. This depth dependence is illustrated by figure 2.9 (Saldin 1977) which shows how the theoretical image contrast of an 'edge-on' and an 'inclined' Frank loop at the [011] pole varies as a function of the distance, measured in terms of ξ_g, of the loop from the foil surface. It can be seen that the image contrast of the loops at the boundary between the first two depth layers ($Z_o = 0.25\ \xi_g$) is considerably reduced and thus small defect clusters that lie close to the boundary between two depth layers may not produce visible diffraction contrast.

The visibility of these defects may be improved by changing the position of the depth layer boundaries by altering ξ_g. This can be achieved by using a different operating reflection. However, as discussed in section 2.5.4, a given reflection will, in general, result in both weak ($|\underline{g}.\underline{b}| < \frac{2}{3}$) and strong ($|\underline{g}.\underline{b}| \geq \frac{2}{3}$) images among the four different Frank loop geometries. Thus if a reflection other than $\underline{g} = \langle 002 \rangle$ is used, some of the Frank loops will form weak images which may not be visible. It is possible to alter ξ_g while still imaging with a $\underline{g} = \langle 002 \rangle$ reflection by deviating away from the Bragg condition so that the effective extinction distance given by $\xi_g^w = \xi_g/(w^2 + 1)^{\frac{1}{2}}$ is reduced. However, for values of the deviation parameter $w \geq 0.8$, the small defect clusters may not produce visible diffraction contrast and this limits the maximum change in the extinction distance to $\xi_g - \xi_g^w = 0.16\ \xi_g$. Thus the position of the boundary between the first two depth layers will only change from $0.25\ \xi_g$ (neglecting surface relaxation effects) to $0.21\ \xi_g$, and reference to figure 2.9 shows that this small change will not greatly increase the image contrast of defect clusters lying close to this depth layer boundary.

An alternative method of increasing the visibility of small defect

clusters located close to the boundary between two depth layers is to tilt the foil, keeping ξ_g constant, so that the effective distance of a cluster from the foil surface is altered (Stathopoulos 1977). This method has the advantage that the defect clusters can always be imaged at the exact Bragg condition using $\underline{g}$ = <002>, which results in strong image contrast ($|\underline{g}.\underline{b}| = \frac{2}{3}$, w = 0) for all the four different Frank loop geometries. However, in the present case of nickel, which is magnetic, it was not possible to correct the objective astigmation caused by the magnetic material when the foil was tilted through an angle $\gtrsim 10^{o}$. Thus none of the smaller defect clusters produced detectable image contrast when the foil was tilted through a large angle, and so it was not possible to use this method.

Table 2.1 The $|\underline{g}.\underline{b}|$ values of the different Frank and perfect loops at a <110> orientation when imaged using the low order reflections at this orientation.

$\underline{b}$	Loop Type	$\underline{g} = [002]$	$\underline{g} = [1\bar{1}1]$	$\underline{g} = [\bar{1}\bar{1}1]$	$\underline{g} = [\bar{2}\bar{2}0]$
$a/3\,[1\bar{1}1]$	Edge-On Frank Loop	2/3	1	1/3	4/3
$a/3\,[\bar{1}\bar{1}1]$	Edge-On Frank Loop	2/3	1/3	1	4/3
$a/3\,[111]$ $a/3\,[\bar{1}\bar{1}1]$	Inclined Frank Loop Inclined Frank Loop	2/3	1/3	1/3	0
$a/2\,[1\bar{1}0]$	Edge-On Perfect Loop	0	1	1	2
$a/2\,[011]$ $a/2\,[10\bar{1}]$	Inclined Perfect Loop Inclined Perfect Loop	1	0	1	1
$a/2\,[01\bar{1}]$ $a/2\,[101]$	Inclined Perfect Loop Inclined Perfect Loop	1	1	0	1
$a/2\,[110]$	Flat-On Perfect Loop	0	0	0	0

TABLE 2.1.

Figure 2.1 Diagram showing the relationship between the incident electron beam, a given set of real lattice planes, the corresponding reciprocal lattice point, the Ewald sphere and the direction of the diffracted beam. The Ewald sphere is constructed so that it passes through O, the origin of the reciprocal lattice, with radius $1/\lambda$. (The diagram is not to scale since for high energy electrons, $1/\lambda >> 1/d$).

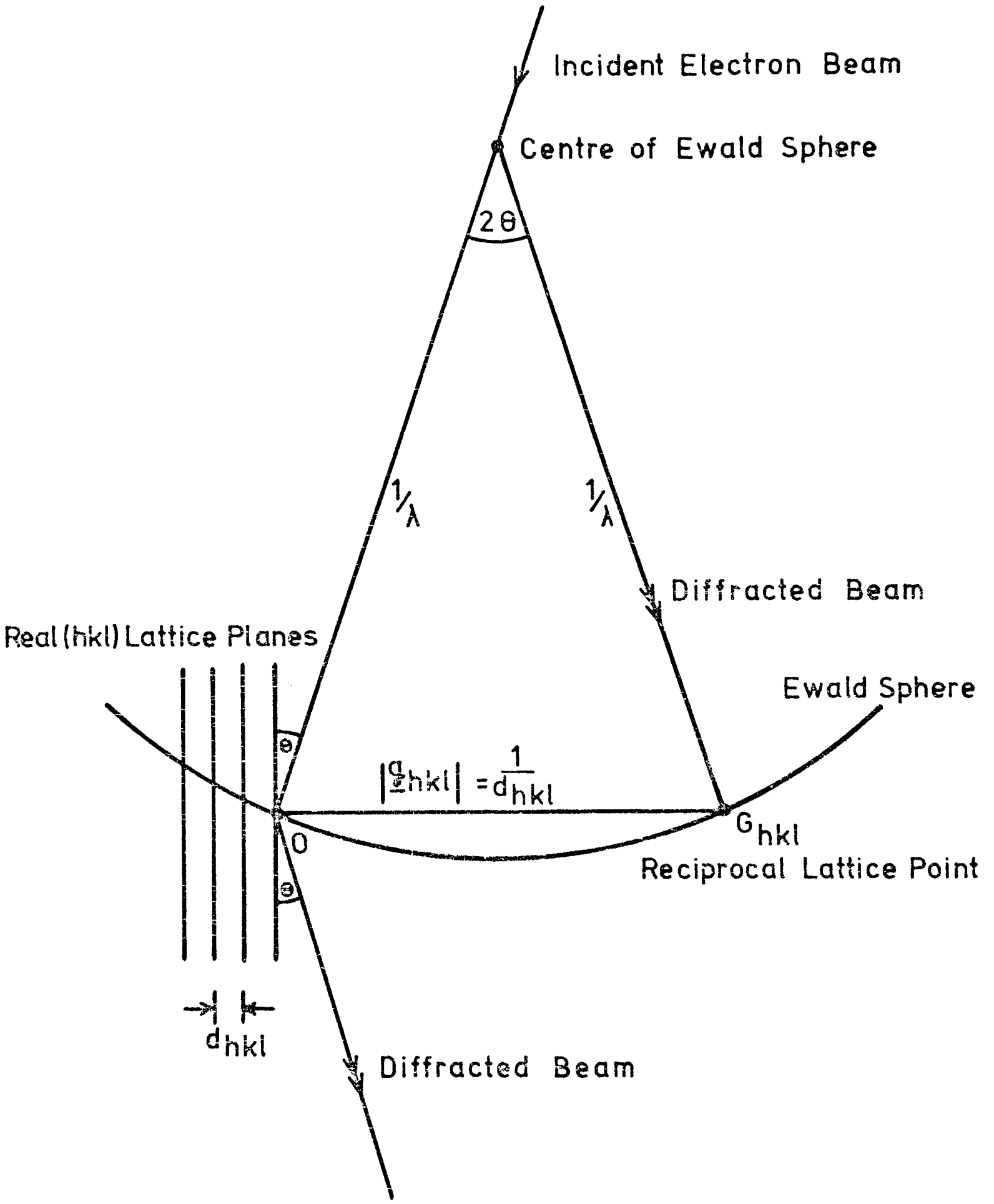
Incident Electron Beam
Centre of Ewald Sphere
2θ
1/λ
1/λ
Diffracted Beam
Real (hkl) Lattice Planes
Ewald Sphere
θ
$|\underline{g}_{hkl}| = \frac{1}{d_{hkl}}$
O
G_{hkl}
Reciprocal Lattice Point
θ
d_{hkl}
Diffracted Beam

Figure 2.2 The dispersion surface for high energy electrons in the "two-beam" approximation. χ is the incident electron wave vector, while the wavevector after refraction by the mean crystal potential V_o lies on the sphere, radius K, centred on O. The waves excited in the crystal correspond to the points $D^{(1)}$ and $D^{(2)}$, which lie on the dispersion surface, and have wave vectors $\underline{k}^{(i)}$ and $\underline{k}^{(i)} + \underline{g}$ $(i = 1,2)$. (For clarity, only the wave vectors corresponding to point $D^{(2)}$ are shown). At the Brillouin zone boundary, the separation of the two branches of the dispersion surface is given by $\xi_g^{-1} = U_g/K \cos \theta_B$. Away from the Brillouin zone boundary, where the affect of the perturbing crystal potential U_g is reduced, the two branches of the dispersion surface asymptotically approach the spherical surfaces of radius K centred on O and G (from Howie and Whelan, 1961).

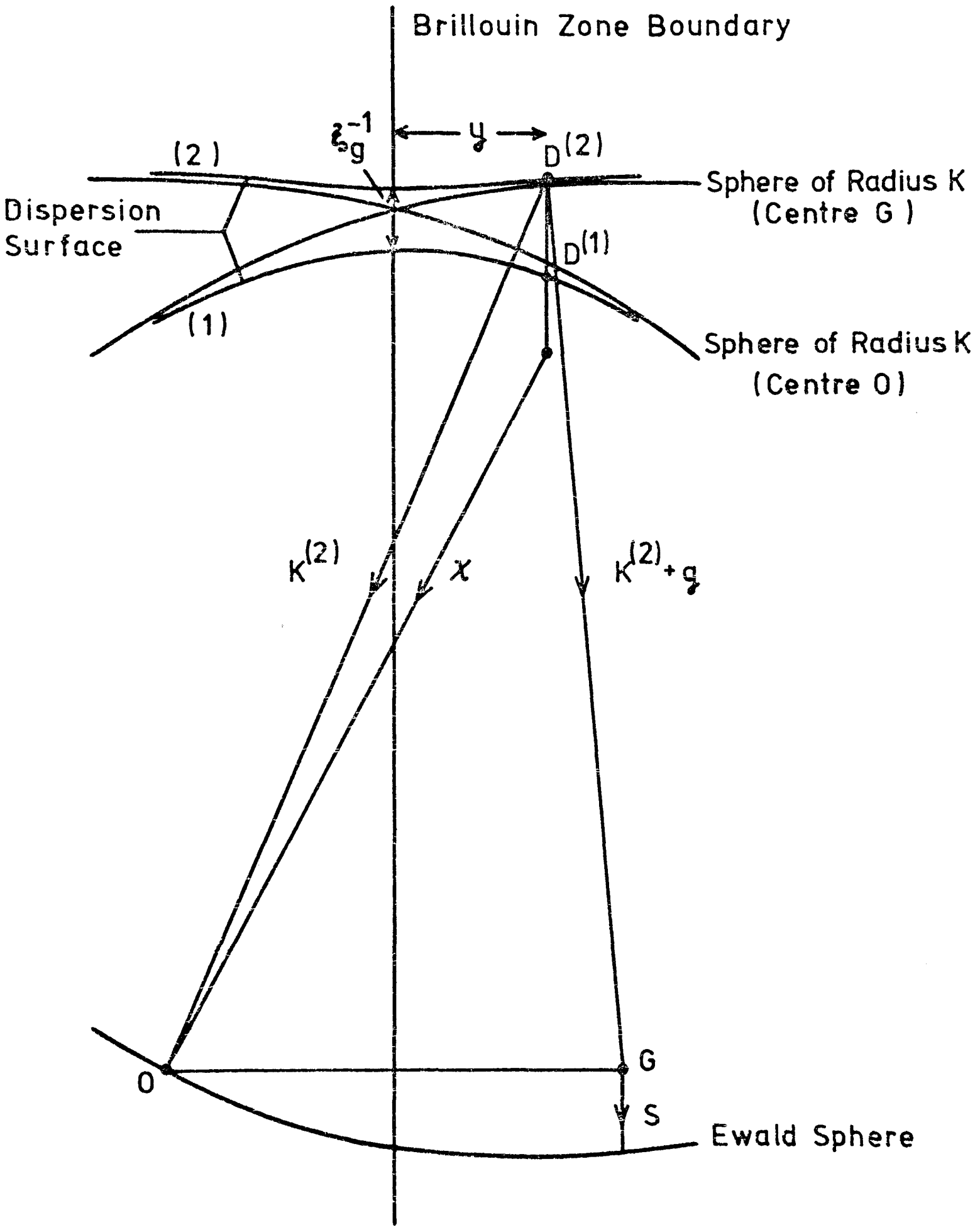
Brillouin Zone Boundary
ξ_g^{-1}
y
(2)
D(2)
Sphere of Radius K
(Centre G)
Dispersion
Surface
D(1)
(1)
Sphere of Radius K
(Centre O)
$K^{(2)}$
x
$K^{(2)}+g$
O
G
S
Ewald Sphere

Figure 2.3 Schematic diagrams of the lattice displacements around (a) a small vacancy dislocation loop and (b) a small interstitial dislocation loop, together with diagrams showing the variation of the strain field $\beta' g = d(\underline{g}.\underline{R}(z))/dZ$ down columns (marked AB) on either side of the loops (after Wilson, 1970).

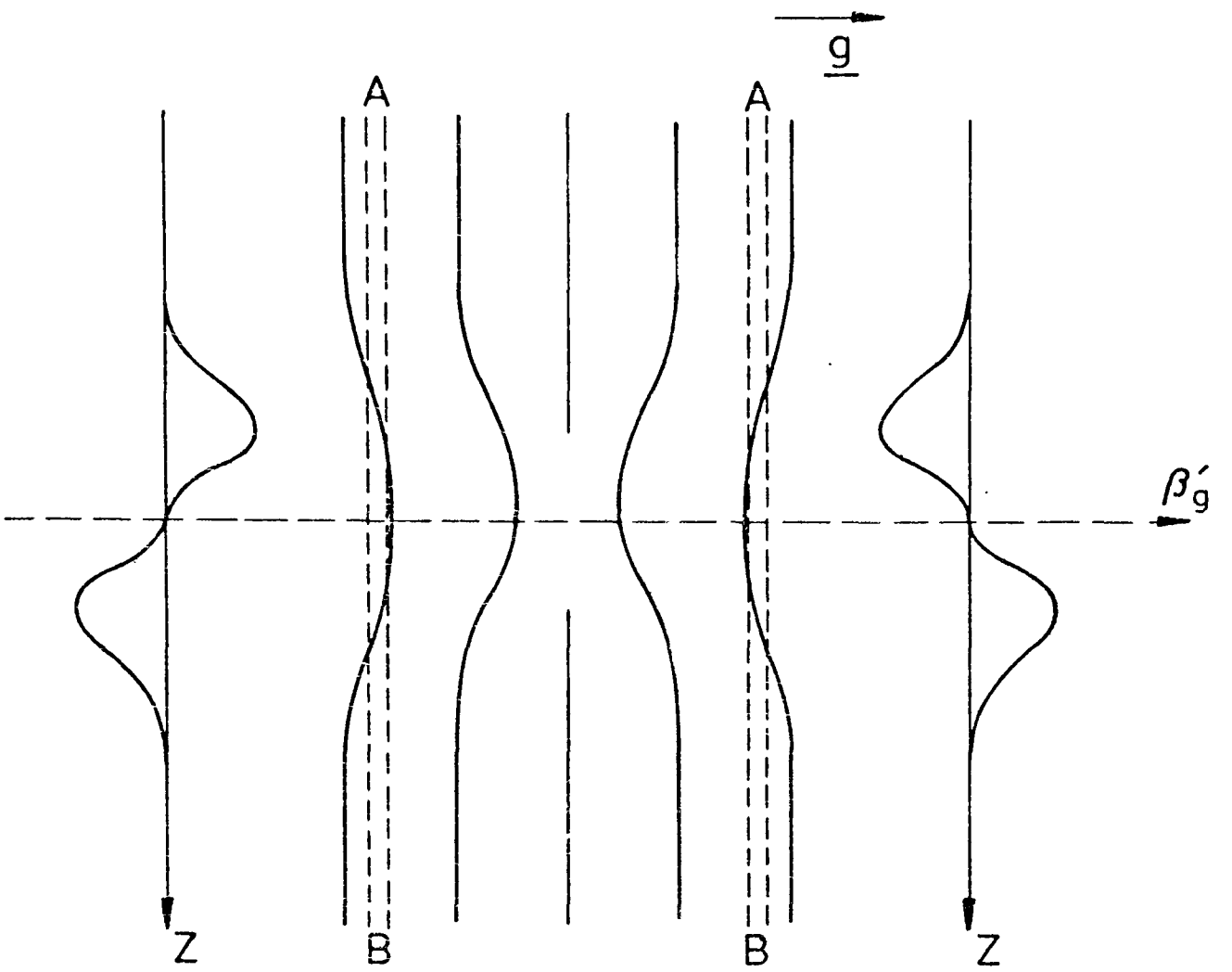

(a)

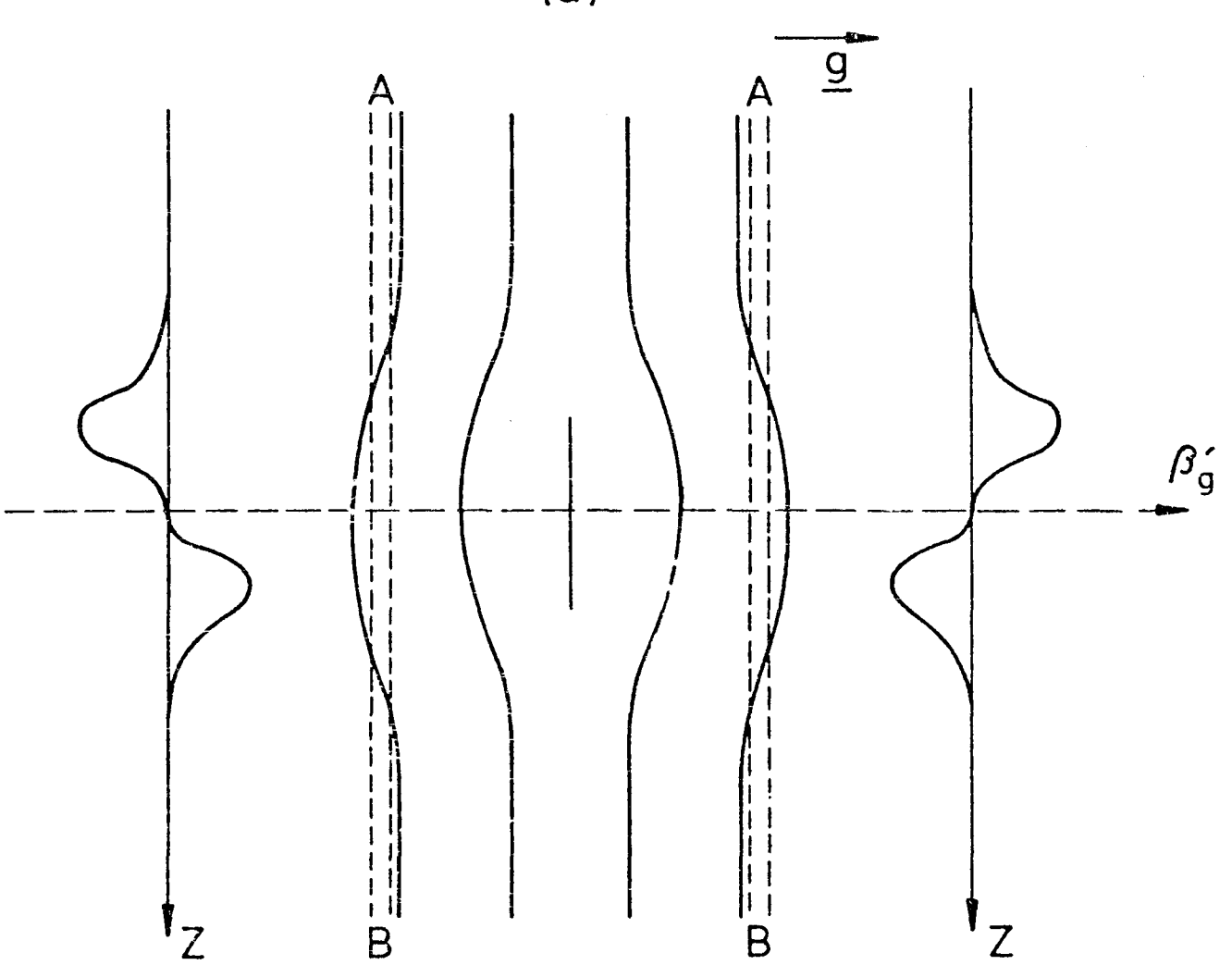

(b)

Figure 2.4 Schematic diagram showing the relationship between $\underline{l}$ and $\underline{g}$ for a small vacancy cluster as a function of the distance of the centre of the cluster from the surface of a foil. The schematic representations of the directions of black-white streaking, drawn with $\underline{l}$ parallel or anti-parallel to $\underline{g}$, are for the special case of an edge vacancy cluster with $\underline{b}p$ parallel to $\underline{g}$.

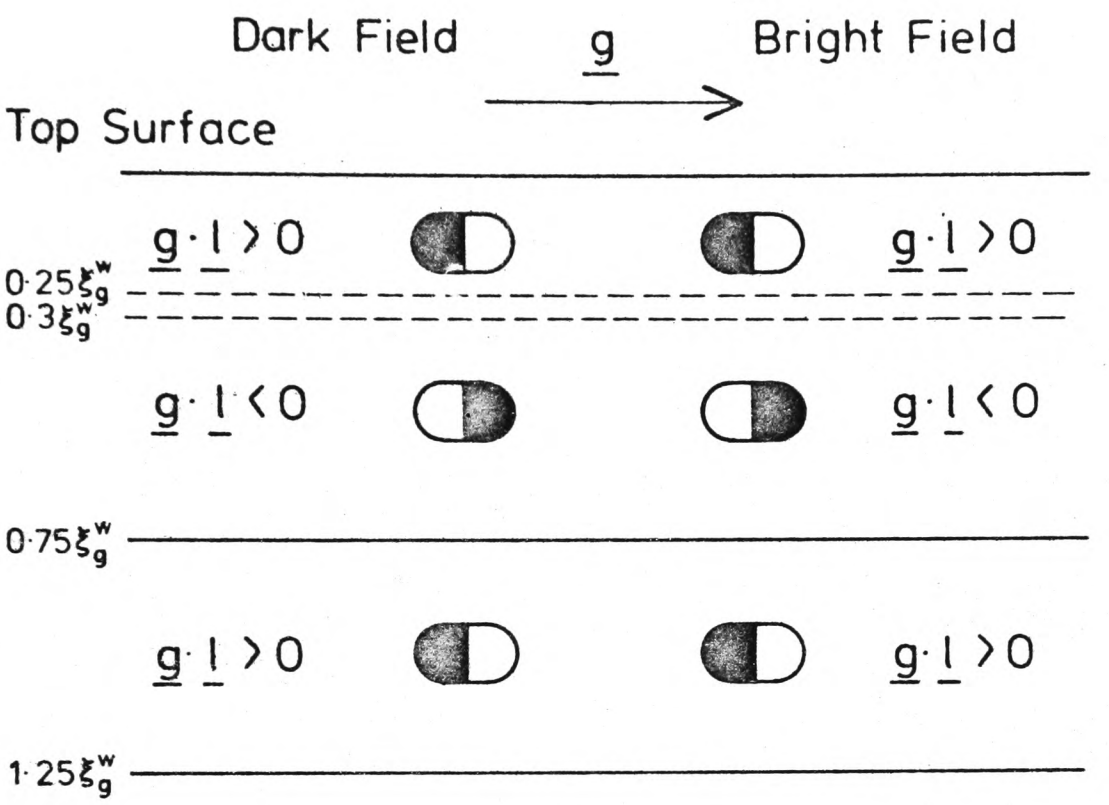
Dark Field
g
Bright Field
Top Surface
g·l > 0
g·l > 0
0·25ξ_g^w
0·3ξ_g^w
g·l < 0
g·l < 0
0·75ξ_g^w
g·l > 0
g·l > 0
1·25ξ_g^w
1·25ξ_g^w
g·l > 0
g·l < 0
0·75ξ_g^w
g·l < 0
g·l > 0
0·3ξ_g^w
0·25ξ_g^w
g·l > 0
g·l < 0
Bottom Surface

Figure 2.5 Computer simulated micrographs for an edge-on, edge perfect loop and an edge-on Frank loop at the [011] orientation when imaged using the low order reflections at this orientation (Eyre et al 1976b).

Figure 2.6 Computer simulated micrographs for a stacking fault tetrahedron at the [011] orientation when imaged using the low order reflections at this orientation (Saldin and Whelan 1975).

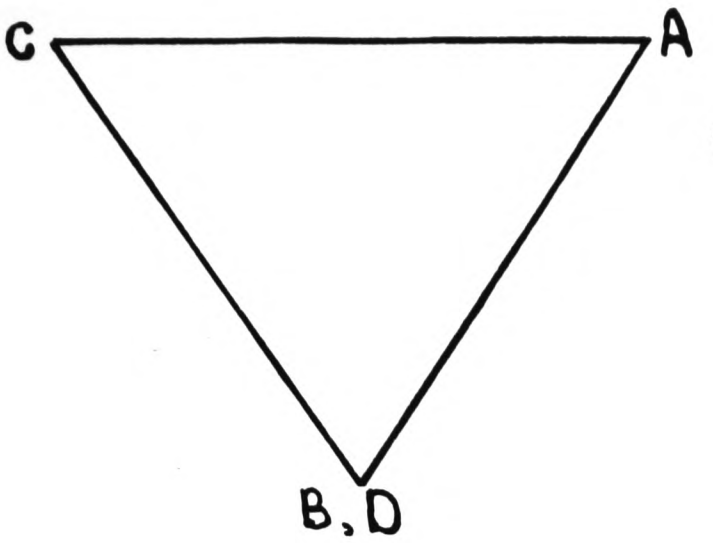

THOMPSON'S TETRAHEDRON

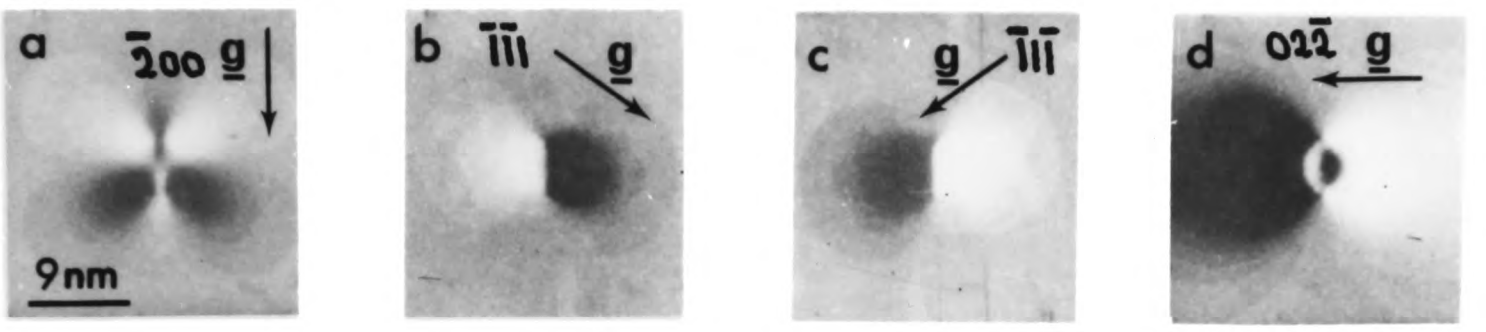

EDGE-ON PERFECT LOOP

$\underline{b} = a/2[0\bar{1}1]$ →

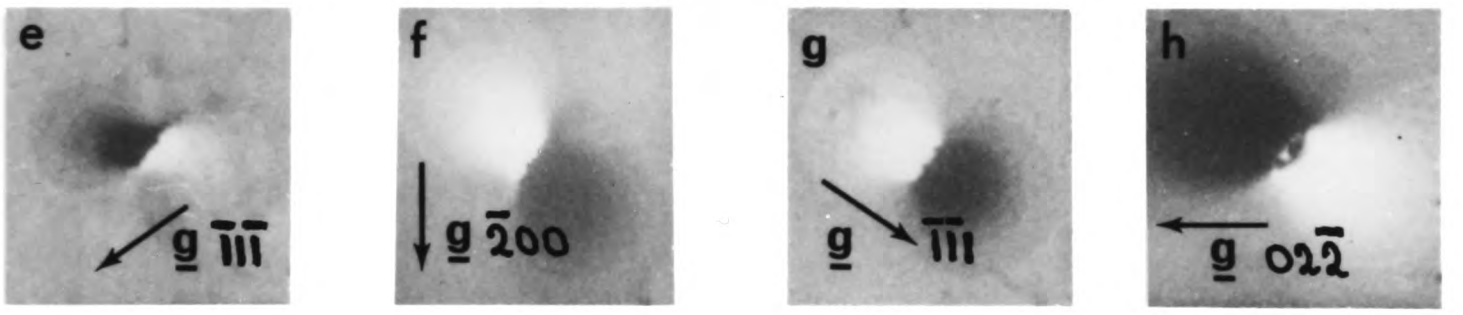

EDGE-ON FRANK LOOP

$\underline{b} = a/3[\bar{1}\bar{1}1]$ ↘

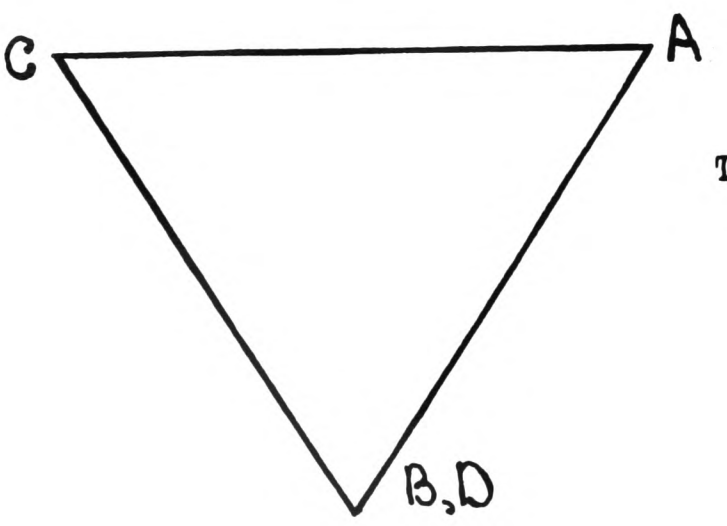

THOMPSON'S TETRAHEDRON

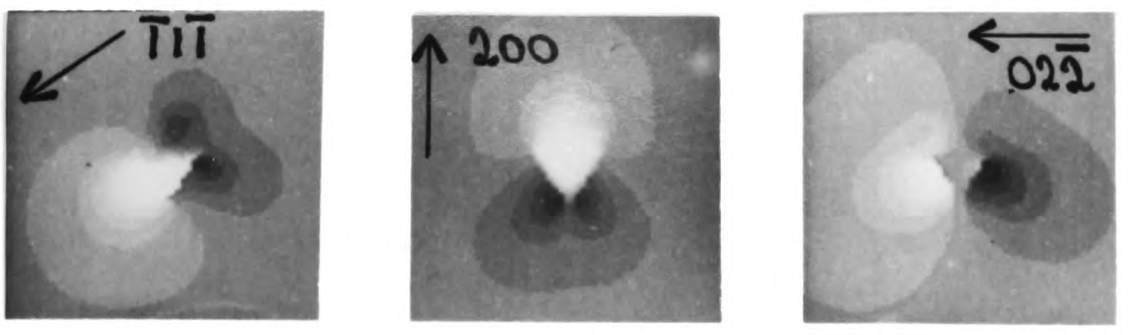

STACKING FAULT TETRAHEDRON

Figure 2.7 Computer simulated micrographs for the two edge-on and the two inclined Frank loops at the [011] orientation when imaged using the low order reflections at this orientation (Saldin and Whelan 1975).

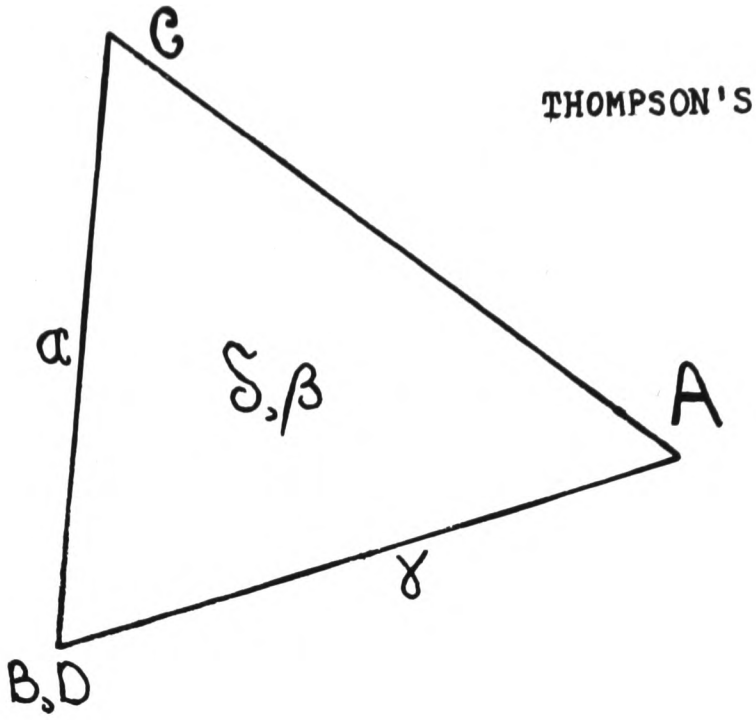

THOMPSON'S TETRAHEDRON

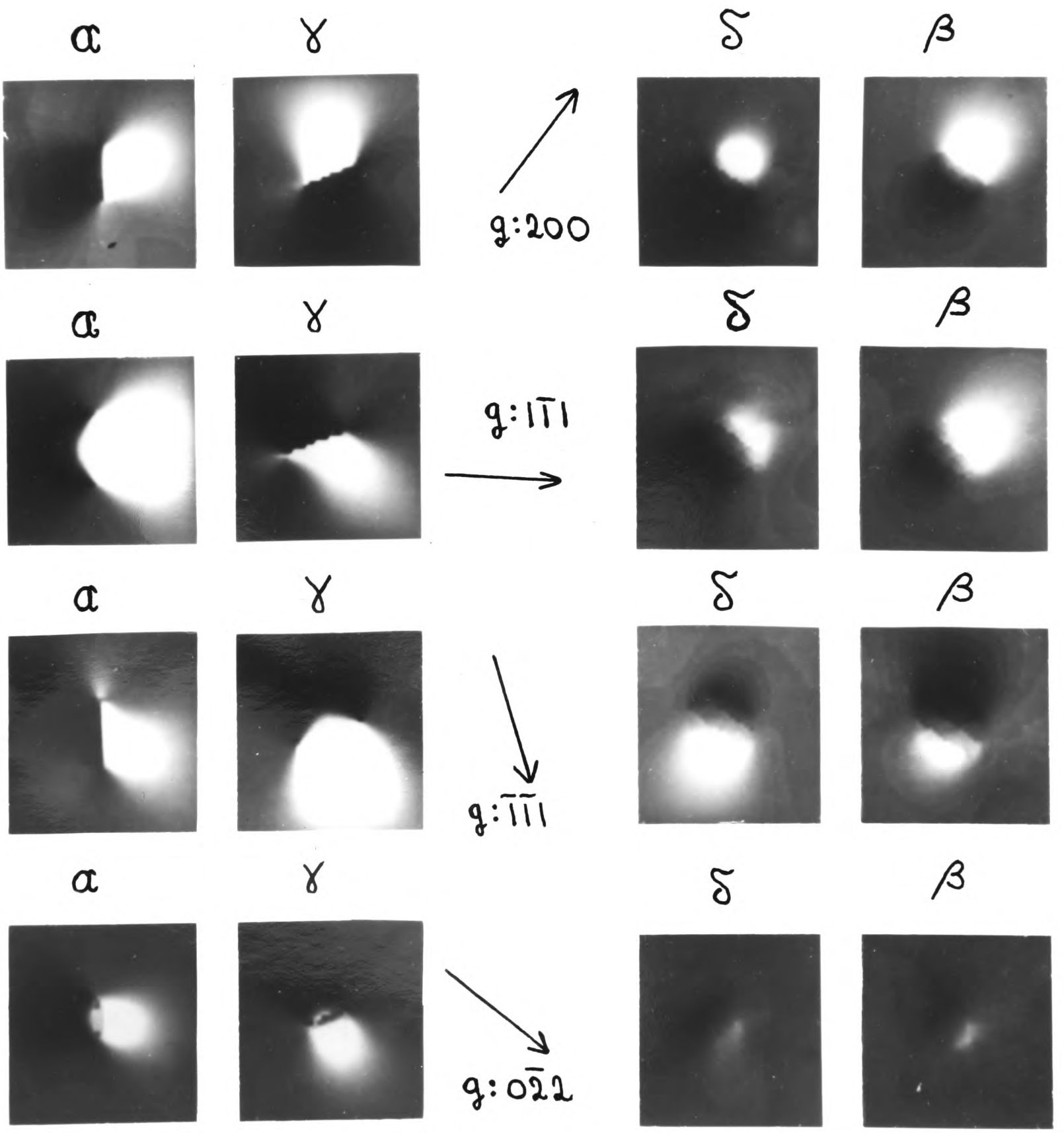

Edge on loops

Inclined loops

Figure 2.8 Computer simulated micrographs showing the variation in the $\underline{g}$ = [200] image contrast of an edge-on and an inclined Frank loop at the [011] orientation in deviating away from the Bragg condition (Saldin 1977).

CONTRAST VARIATION WITH 'w'

(Frank loops) $\bar{z}=\bar{N}=[011]$

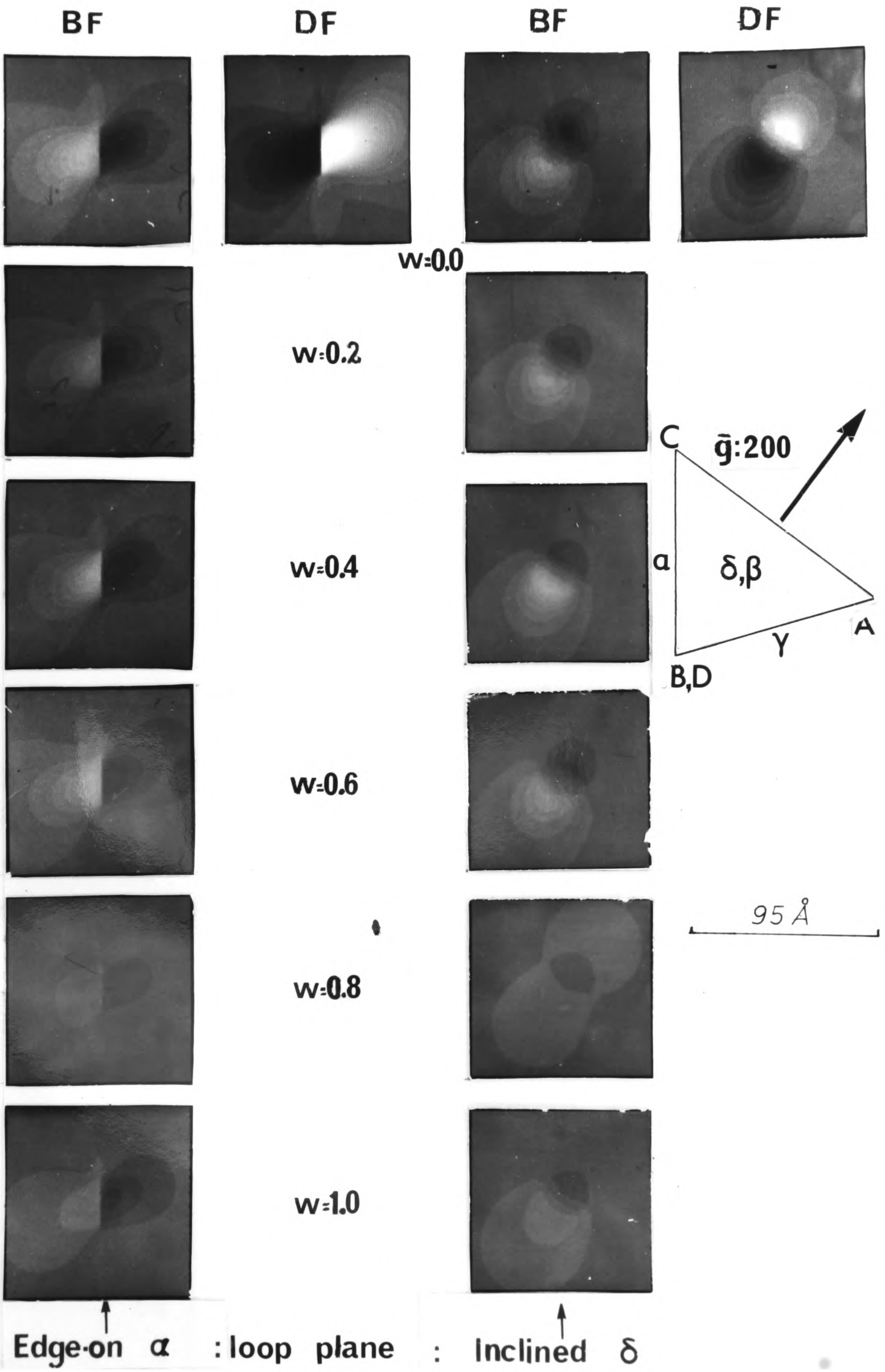

Figure 2.9 Computer simulated micrographs showing how the $\underline{g}$ = [200] image contrast of an edge-on (α) and an inclined (δ) Frank loop at the [011] orientation varies as a function of the distance, measured in terms of ξ_g, of the centre of the loop from the foil surface (Saldin 1977).

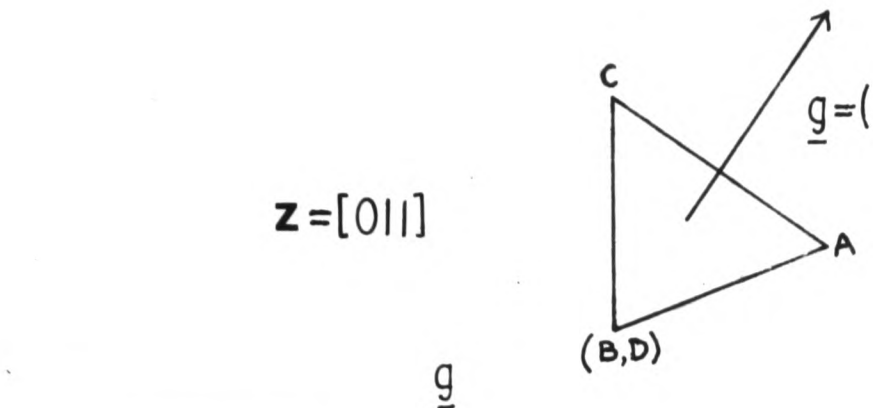

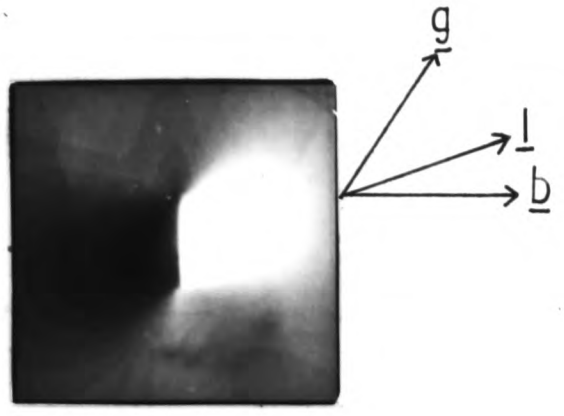

0·125 ξ_g

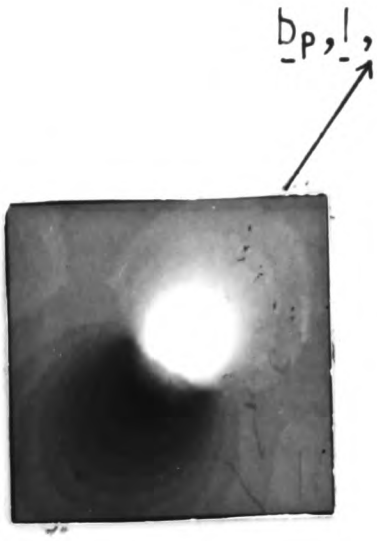

L1

82Å

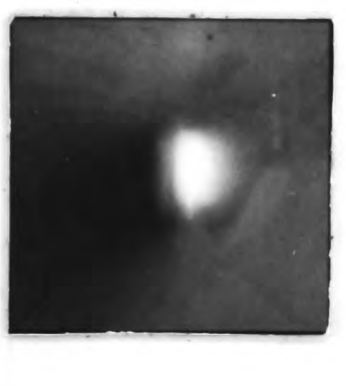

0·188 ξ_g

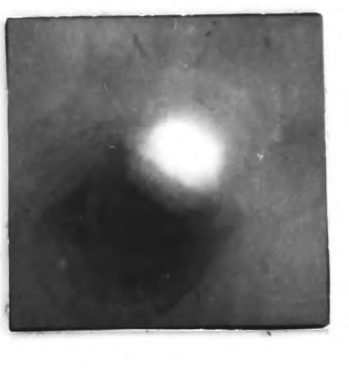

L1

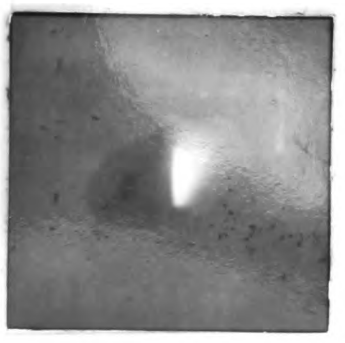

0·25 ξ_g

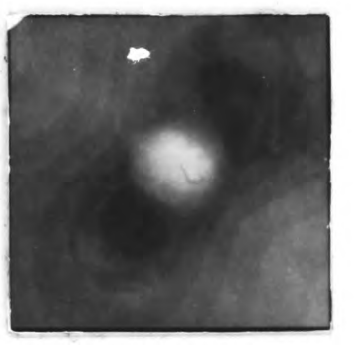

L1-L2 boundary

0·313 ξ_g

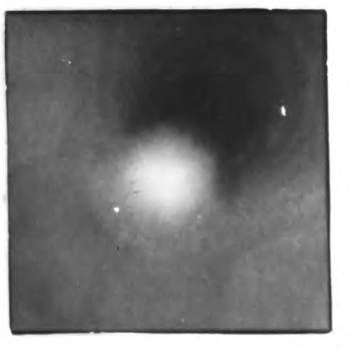

L2

α : loop plane : δ

CHAPTER 3

Experimental Procedures

3.1 Specimen Preparation

3.1.1 Introduction

The irradiation of nickel or 321 stainless steel with 80 keV nickel or tungsten ions produces displacement cascade damage structures that are located within about 300 Å of the irradiated specimen surface (Matthews 1976, see figure 4.6). In the present experiments it was therefore necessary to irradiate specimens which had already been thinned so that they were suitable for examination in a transmission electron microscope, as any thinning of the specimens after irradiation would have removed part or all of the damage structure. To prevent dislocations from being introduced into the thin areas of a specimen while it was being handled, the specimens used in the irradiations were in the form of 2.3 mm or 3 mm diameter discs with a firm outer rim protecting a thinned central region. The way these specimens were prepared is described below.

3.1.2 Preparation of the Specimen Discs

The polycrystalline nickel specimens used in these experiments were obtained from a 99.998% pure nickel rod (Lab. No. WI2352) supplied by Johnson Matthey Chemicals Limited. This rod was cold rolled to a final thickness of 0.003" ($\approx 75\mu$) and 3 mm diameter discs were then punched out on a press. The discs were flattened between glass slides to remove any bending caused by the press, cleaned ultrasonically in an acetone bath to remove surface impurities, and then annealed for 2 hrs at 1050°C under a vacuum of 5×10^{-6} torr. The purpose of the anneal was two-fold; firstly to remove the dislocation structure produced by deformation in the preparation, and secondly to produce large grains ($\sim 5\mu$ in diameter) which considerably facilitated the electron microscopy. The annealed discs were electro-chemically thinned as described in section 3.1.3.

The starting materials for the nichrome alloys and the ternary (Fe/Ni/Cr) alloy were supplied by Johnson Matthey Chemicals Limited in the form of 99.998% pure nickel rods (Lab. No. WI2352), 99.998% pure iron

rods (Lab. No. W12094) and 99.999% pure chromium pellets (Lab. No. S53595). These alloys were made up by the Metallurgy Division at A.E.R.E. Harwell. For each alloy, the relevant weight percentages of the constituent metals were placed on a water cooled copper hearth in an atmosphere of static argon and heated past their melting points by means of an arced discharge from a tungsten electrode. The resulting alloys were then hot rolled down to a final thickness of 0.003" ($\approx 75\mu$). Discs suitable for electrochemical thinning were then punched out and prepared in the same way as described for the polycrystalline nickel specimens.

On analysis after being rolled down (see section 3.2) it was found that the alloys all contained a significant amount (between 190 → 1070 ppm (w/w)) of oxygen, the amount of this interstitial impurity increasing with increasing chromium content of an alloy (see table 3.5). It is thought that this impurity arose because of the very low dissociation pressure of Cr_2O_3 (10^{-20} atmsphs at 1200°C). If an oxide has a low dissociation pressure, small traces of oxygen bearing gases may promote the formation of the oxide, and in the case of chromium, as little as 10 ppm water vapour in a reducing hydrogen atmosphere can cause chromium to oxidise (Smithells 1976). Thus the manufacture of oxygen free chromium alloys requires a very clean atmosphere. In the present experiments, in which the effect of alloying chromium to nickel was to be investigated, the presence of a minor impurity that increased with increasing chromium content meant that any effect observed could have either been due to the change in the major composition of the alloy, or alternatively could have been caused by the change in the minor impurity level. It was therefore decided to take one of the chromium alloys and to try and reduce its oxygen impurity level. A comparison between the same alloy with different oxygen levels might then yield information as to the effect of the oxygen on the generation of the displacement cascade damage structures. The alloy chosen was Ni/Cr 17% and this alloy was annealed for 2 hrs. at 950°C in a flowing

argon/hydrogen 5% reducing atmosphere. Reference to table 3.5 shows that this anneal did not reduce the oxygen impurity level. It was therefore decided to make up a new Ni/Cr 17% alloy using the same nickel (Lab. No. W12352) as in the original alloy but a different batch of chromium pellets (Lab. No. S80184). To avoid confusion, the new alloy will be referred to as Cr/Ni 83%. This alloy was made up in the same way as for the first alloy, but on analysis after being rolled down it was found that the oxygen impurity level was approximately half that of the first alloy (see table 3.5). This reduction may have been due to a lower oxygen impurity level in the chromium pellets as supplied, or alternatively, less oxidation may have occurred during the fabrication of the alloy. The results obtained in the Ni/Cr 17% and Cr/Ni 83% alloys and the conclusions drawn as to the effect of oxygen on the generation of displacement cascade damage structures are discussed in Chapter 5.

Finally, amongst the polycrystalline specimens, the stainless steel specimens used were obtained from an En58B austenitic stainless steel (cast 57590) supplied by Samuel Fox and Co. The composition of this steel is given in Table 3.1 and this composition lies within the AISI 321 specification. Specimens of this steel were cold rolled to a final thickness of 0.003" ($\approx 75\mu$) and discs suitable for electro-chemical thinning were then punched out and prepared in the same way as described for the polycrystalline nickel specimens, except that to prevent the carbon in the steel from precipitating out of solution, the anneal at $1050^{o}C$ was carried out for one hour only.

As well as using polycrystalline specimens, some of the earlier experiments designed to investigate the orientation dependence of the damage structure were carried out using a single crystal of nickel. The single crystal was supplied by Metals Research Ltd. as an unorientated offcut. It was orientated on a double tilt goniometer stage to within $\leq 2^{o}$ of either a {110} or a {100} orientation using the Laue back

reflection method (Friedrich, Knipping and Laue 1913). The orientated goniometer stage was then transferred to a 'spark cutting' machine and {110} or {100} orientated slices of the crystal, approximately 0.5 mm (500μ) thick, were then cut off by spark erosion (Cole et al 1961). To reduce the mass of nickel in the microscope, and thus reduce the objective astigmatism caused by the presence of magnetic material, the spark eroded crystal slices were further thinned mechanically using a very fine (0.25μ) diamond paste until they were less than 200μ thick. It was found that by using a low spark energy and a very fine diamond paste that no observable plastic deformation was introduced into the central region of the slice which was later to be examined in the electron microscope. Discs suitable for electro-chemical thinning were then cut from the thinned slices by spark erosion. 2.3mm diameter discs were chosen in preference to 3mm diameter discs as this reduced still further the mass of magnetic material of the specimen.

The electro-chemical thinning of both the single crystal specimen discs and the polycrystalline specimen discs is discussed in detail in the following section.

3.1.3 Electropolishing of the Specimen Discs

The success of the experimental work that is described in this thesis depended on the preparation of specimens that were suitable for high-resolution examination in an electron microscope. This required that the electropolished foils contained thin areas less than about 1,000 Å thick which were almost completely flat. In addition, for the present study, it was necessary that these thin areas were initially dislocation free and also that the electropolishing did not produce any surface structure which might be confused with the black-white contrast shown by small defect clusters when imaged under dynamical "two-beam" conditions.

The basic method of thinning the specimen discs was to jet polish them from each side in turn until perforation occurred. The discs,

whether 2.3 mm or 3 mm in diameter, were held in tweezers and the rims of the discs were coated with a non conducting lacquer. It was necessary to ensure that the tweezer tips were well protected by the lacquer as otherwise it was very difficult to wash away all the electropolishing solution when polishing had finished. The jet polishing apparatus that was used is shown schematically in figure 3.1. The light source which was focussed on the specimen enabled the moment when perforation occurred to be detected. The chemical composition of the electropolishing solution (Lenoir's solution) that was used to polish all the materials except the Fe/Ni/Cr ternary alloy is given by Table 3.2. In the case of the ternary alloy, a solution of 10% perchloric acid in methanol was used. All the electropolishing was carried out at room temperature.

It was found that the polish produced on a given material depended on a number of variables. These included the applied potential difference between the specimen and the cathode, the distance of the specimen from the cathode, the flow rate of the electropolishing solution, the diameter of the jet that was used and the age of the electropolishing solution. When trying to find the best conditions for electropolishing a given material, this number of variables was reduced by keeping the specimen to cathode distance within the range 1.4 → 1.5 cms , and by using a constant electrolyte flow rate of 30 cc per minute from a 0.8 mm diameter jet. The choice of flow rate was such that the resulting pressure of the electrolyte on the specimen did not produce significant buckling of the thin areas of the specimen when perforation had occurred. The conditions that were found most suitable for electropolishing the different specimens are summarised in Table 3.3.

An electropolishing solution consists essentially of an oxidising agent and a solvent for the products of oxidation, and thus the concentration of dissolved specimen ions in an electropolishing solution increases with the use of the solution. It was found that the current between the

specimen and the cathode for a given applied potential difference increased with this 'age' of the solution, the current increasing by up to a factor of two for an almost fully used solution that needed replacing. Thus to obtain the same current density and therefore the same polishing conditions at the specimen, the applied potential difference had to be reduced for a used solution compared with a fresh solution. The relevant figures are given by Table 3.3.

A given specimen was thinned from one side for a short while just until the surface was polished. The specimen was then thinned from the other side and polishing was continued until perforation occurred. In the case of all the materials except the Ni/Cr 17% alloy and the stainless steel, the electropolishing was stopped as soon as perforation occurred. However, in the Ni/Cr 17% alloy and the stainless steel, preferential attack occurred at surface irregularities and it was therefore necessary to continue electropolishing for one or two seconds after perforation in order to obtain very thin areas around the edges of the holes.

When the electropolishing had been completed, the specimens were immediately washed to ensure that the polished surface was not chemically attacked by any remaining traces of electropolishing solution. To remove Lenoir's solution, the specimens were twice washed in a dish of distilled water, while to remove the perchloric/methanol polishing solution the specimens were twice washed in a dish of methanol. Great care was taken to ensure that the thin areas of a foil were not buckled by this washing procedure and the specimens were washed by a gentle up and down movement rather than a side to side one. The specimens were subsequently washed in methanol and allowed to dry before being examined under an optical microscope to ensure that no surface film remained. The specimens were then immersed in a dish of acetone which dissolved the non conducting lacquer. This process was repeated twice to ensure that all traces of the lacquer had been removed, and the specimens were then finally washed

in methanol and allowed to dry.

The electropolishing technique has been described in detail as it was found that consistently good foils containing large amounts of flat, thin, dislocation free areas could be prepared by electropolishing Ni, Ni/Cr 8%, Ni/Cr 17% or 321 stainless steel with Lenoir's solution in the manner described. In the case of the Fe/Ni/Cr ternary alloy, the preparation of good foils was, however, not so reproducible.

3.2 Impurity Analysis

3.2.1 Introduction

The damage structures generated by low dose heavy-ion irradiations of metals have been found to be very sensitive to the impurity content of the metals. In particular, English et al (1976) have found that as little as 17 atomic ppm of nitrogen, which is an interstitial impurity, reduces the number of vacancies retained in visible clusters in self-ion irradiated molybdenum by an order of magnitude. In the present series of experiments, all the alloys except the stainless steel were made up from the same batches of high purity nickel, chrome and iron (see section 3.1.2). In this way, any difference in minor impurity levels between the different materials was kept as low as possible. These impurity levels were analysed spectrographically (see section 3.2.2) and in addition, the amounts of carbon, oxygen and nitrogen present, which are interstitial impurities, were measured by activation analysis (see section 3.2.3). When a difference arose in the results obtained in different materials, it was therefore possible to determine whether this might have been caused by a difference in the minor impurity levels, or whether it was more likely to have been caused by a difference in the major composition of the materials.

3.2.2 Emission Spectrographic Analysis

The sample to be analysed was chemically pretreated to remove surface impurities. It was then weighed and placed in a previously analysed

electrode of highly purified graphite. The sample was then totally combusted by an arc discharge between water cooled electrodes. A quartz prism was used to record the emission spectra on a photographic plate, the emulsion of which had been calibrated by reference to the iron spectrum. The line intensity of the impurities in the sample were compared with those of controlled-level impurities in established standards and thus the impurity levels in the sample could be determined.

All the materials were analysed spectrographically apart from the Cr/Ni 83% alloy and the 321 stainless steel. The nickel single crystal samples that were analysed were in the form of electropolished discs, whereas the other materials that were analysed were in the form of strips that had previously been annealed alongside the specimen discs. The elements sought, along with the sensitivity of the method and the elements detected, are listed in Table 3.4.

3.2.3 High Energy γ Photon Activation Analysis

The carbon, oxygen and nitrogen impurity levels in a given sample were determined by production and measurement of their neutron deficient isotopes. These isotopes were formed by the reaction $A_x^N(\gamma,n)A_x^{N-1}$ when the elements were bombarded with high energy (35 to 45 MeV) γ photons. The presence of a particular isotope was then detected by separating it from the sample matrix and measuring its characteristic β^+ radiation. A detailed account of the determination of carbon levels in nickel using this method has been given by Hislop et al (1975).

The sensitivity of this technique depended upon (1) the specific activity induced in the element of interest, and (2) the background of the detector system used to measure the separated β^+ activity. The half-lives of the isotopes formed were 20.34 minutes for ^{11}C, 2.0 minutes for ^{15}O, and 10 minutes for ^{13}N and the time taken to separate either ^{11}C or $^{15}O + {}^{13}N$ and make an activity measurement was 20 minutes and 7 → 10 minutes respectively. This resulted in lower limits for detection under

optimum conditions of 0.002 μg C, 0.04 μg O and 0.03 μg N.

The low mass (∿ 2 mg) of the electropolished discs of the polycrystalline materials, which were only ∿ 75μ thick, meant that the lower limits for detection in samples of this type were of the order of 20 ppm O_2, 15 ppm N_2 and 1 ppm C. The results of English et al (1976) had indicated that even lower concentrations of nitrogen might influence the damage structures that were generated, and so to obtain greater sensitivity in the analysis, it was decided to analyse rolled down strips of the different materials which had been annealed alongside the specimen discs. In this way, any impurities introduced by the anneal would be detected, but not those introduced by the electropolishing procedure. However, it was possible to obtain a greater sensitivity in the analysis of the electropolished discs of nickel single crystal because of their greater thickness (∿ 200μ), and the low levels of carbon, oxygen and nitrogen present in these electropolished specimens (see Table 3.5) indicates that the electropolishing procedure did not introduce significant amounts of these interstitial impurities.

All the materials were analysed for carbon, oxygen and nitrogen by activation analysis apart from the stainless steel which was only analysed for oxygen as it was already known to contain significant amounts of other interstitial impurities (see Table 3.1). The results of these analyses are listed in Table 3.5. It can be seen from this table that the oxygen impurity content of the alloys was very high (between 190 → 1070 ppm $(\frac{w}{w})$), and that it increased with increasing chromium content. It was not thought that this oxygen was introduced during the annealing process since the stainless steel, which contained 18.09 wt.% chromium and was annealed for 1 hr. at 1050°C before analysis, only contained 32 ± 2 ppm $(\frac{w}{w})$ oxygen. As mentioned in section 3.1.2, an attempt was made to reduce the oxygen impurity level in the Ni/Cr 17% alloy by annealing it for 2 hrs. at 950°C in a flowing argon/hydrogen 5% reducing atmosphere. The oxygen

content after this anneal is listed in Table 3.5 along with the carbon and oxygen impurity levels of the second Cr/Ni 83% alloy that was made up using a different batch of chromium pellets.

The affect of the oxygen impurity on the generation of displacement cascade damage structures is discussed in section 5.5.

3.3 Irradiation Procedure

3.3.1 The Ion Accelerator

The accuracy of the experimental technique for determining defect yield values depended on the accuracy with which the number of ions incident on the thinned area of a specimen could be measured. The most important requirement of the ion accelerator was therefore that it should provide a highly uniform dose over the irradiated area, and that this dose should be measured to a high degree of accuracy, ideally within one or two percent. It was also necessary that the irradiating ion beam should only contain ions of the required type, and that these ions should have the specified energy.

The irradiations were carried out on the Harwell-Lintott Separator using 80 keV tungsten or nickel ions to doses of 2×10^{11} ions cm^{-2} and 6×10^{11} ions cm^{-2} respectively. The reasons for using these low doses so that, in general, cascade regions did not overlap with one another are discussed in section 1.4. In addition, the possibility of impurity effects arising from tungsten ions being implanted in a specimen was not thought to be important for a dose of 2×10^{11} ions cm^{-2} since, for an incident ion energy of 80 keV, the maximum concentration of tungsten impurity atoms was calculated as being only 2 ppm (Matthews 1976).

The heavy-ion accelerator is illustrated schematically in figure 3.2. The principles of operation of the ion source and the isotope separator have been described by Freeman (1969, 1970). The ion source consisted essentially of an arc chamber with a straight tungsten filament located behind a rectangular (4.2 x 0.15 cms) extraction slit. Nickel ions were

obtained by heating NiCl in an oven and feeding the vapour into the arc chamber. This vapour was then ionised by electrons from the heated filament that were attracted to the positively charged walls of the arc chamber. In the case of tungsten ions, these were obtained from the filament itself. In either case, the resulting plasma was constrained at the source by a magnetic field and a wedge shaped ion beam was extracted by maintaining the ion source at 40 kv (± 4v) and accelerating the ions through an earthed extraction electrode.

The dispersion of the extracted ion beam was controlled by the variable geometry analyser magnet, and it was possible to obtain a dispersed beam of the required ion that contained < 1% of impurity ions. The analyser magnet also enabled the focal length of the dispersed beam to be controlled over wide limits, and the beam could be focussed to a width of less than 0.10 cms on the target holder in the experimental target chamber. For irradiations carried out in the main target chamber, post acceleration of the ions to the potential of this chamber took place across a single gap electrode system.

The room temperature irradiations were carried out in the main target chamber and the methods of measuring the dose incident on a specimen and of scanning the beam across the target assemblies for these irradiations are described in the following section. The high temperature irradiations were carried out in the experimental target chamber and a description of the procedure for these irradiations is given in section 6.2.

3.3.2 Room Temperature Irradiations

The target assemblies for the room temperature irradiations were 13.5 cms x 0.6 cms aluminium bars which had had 0.3 cm diameter holes drilled in them. The pre-thinned specimen discs were held firmly in place in these holes by circlips to ensure that the specimens would be almost perpendicular to the ion beam during the irradiations. Some bars had been machined so that when the specimens were firmly seated in

position, they would be inclined seven degrees from perpendicular to the irradiating beam. These bars were used for the off-axis irradiation of the orientated single crystal specimens. The loaded bars were fixed to a 13.5 cms x 11 cms target plate which was placed on a rack in the main target chamber. There was no effective limit on the number of specimens that could be irradiated at the same time, since the target plate could hold up to fifteen bars and each bar could hold up to ten specimens.

When the target chamber had been evacuated to a pressure of $\sim 10^{-6}$ torr, the target plate was irradiated by mechanically scanning it through the stationary ion beam. In this way, there was no loss of angular definition of the ion beam during the scanning process, and this resulted in a highly uniform dose over the irradiated area. The dose was determined by using the insulated irradiating chamber as a Faraday cage, and simply measuring the total charge incident within the chamber during the irradiation.

One of the main problems that arises in accurately measuring the dose incident on a specimen is the possibility that the ion beam may contain a large number of neutral atoms, which are not detected by measuring the charge incident on a specimen. To check the accuracy of the dose measuring technique, Jenkins (1975) irradiated Cu_3Au, which is an ordered alloy, with 50 keV or 100 keV Cu^+ ions to a measured dose of 5×10^{10} ions cm^{-2}. Each ion or neutral atom incident on the ordered alloy produced a disordered region which could be imaged in an electron microscope by using a superlattice reflection. By comparing the number density of disordered regions with the number density of charged ions incident on the specimens, Jenkins concluded that there were very few neutral atoms in the beam when it was aligned accurately, and that the dose incident on a specimen was accurate to within better than 10% of the measured dose.

3.4 Electron Microscopy

The irradiated specimens were placed in a double-tilt goniometer holder and examined in a JEM 100B transmission electron microscope at an operating potential of 100 kv and a magnification of 60,000X. "Two-beam" diffraction conditions for a given (hkl) reflection were set up by tilting the specimen so that the hkl Kikuchi line passed through the hkl diffraction spot whilst the $\bar{h}\bar{k}\bar{l}$ Kikuchi line passed through the origin (Hirsch et al 1965 p.123).

To obtain accurate measurements of defect yields and image sizes, and also to facilitate the analysis of defect geometries, it was necessary to obtain high resolution electron micrographs. This required, amongst other precautions, that the spherical aberration, chromatic aberration and astigmatism of the objective lens should be kept as low as possible.

An initial alignment of the microscope was always carried out so that the rotation of the image caused by increasing or decreasing the objective lens current occurred about the centre of the viewing screen. This reduced the spherical aberration as the imaging electron beam was then aligned so that it passed down the optic axis of the objective lens. All the micrographs were taken under 'dark-field' conditions and the required diffracted beam was aligned to pass down the optic axis by tilting the electron beam before it entered the specimen. A 40μ objective aperture was used to reduce the number of inelastically scattered electrons that contributed to the image.

To reduce the chromatic aberration present in an image, the inelastic energy losses suffered by the electrons in passing through a specimen were kept to a minimum by taking micrographs of the thinnest ($< 10^3$ Å) area of a foil where it was possible to set up uniform "two-beam" conditions over the area of the micrograph. In addition, the specimen was always loaded in the microscope so that the irradiated surface corresponded to the electron exit surface as this further improved the visibility of the

smaller (< 25 Å diameter) defect clusters (see section 2.6). The thinness of the areas that were examined meant that the 'dark-field' exposure times were usually of the order of one second or less.

The visibility of the smaller defect clusters depended critically on the amount of objective astigmatism present. The objective lens was fitted with a compensating magnetic field to correct this astigmatism and this correction was carried out before each micrograph was taken, that is for each different area of foil after every tilting operation, by focussing on the defect clusters themselves. In the case of nickel, which is ferromagnetic, it was found that the objective astigmatism could not be corrected when the specimen was tilted through more than about 10^{o}, and so micrographs were always taken of areas that had been tilted by less than this amount.

As a result of the precautions that were taken, it was found that the minimum image size that could be resolved in the thin (< 10^3 Å) areas of a foil was of the order of 15 Å in diameter.

3.5 Determination of Defect Nature

The nature of the defect clusters was determined from the direction of the '$\underline{1}$' vector of an image in relation to the operating reflection $\underline{g}$ (see section 2.3).

The '$\underline{1}$' vectors of the images of the defect clusters generated by the tungsten ions and of the analysable defect clusters generated by the nickel ions were all found to be in the same direction relative to $\underline{g}$ when imaged using a $\underline{g}$ = <220> operating reflection. The high value of ξ_g for this reflection (ξ_{220} = 409 Å for 100 keV electrons in Ni (Hirsch et al 1965 p.496)) had resulted in all the defect clusters generated by the tungsten ions (mean depth of depcsited energy $\bar{x}$ = 55 Å (Matthews 1976)) and the analysable larger clusters generated by the nickel ions ($\bar{x}$ = 114 Å) lying within the first depth layer (0.3 ξ_{220} = 123 Å). It was therefore not necessary to measure the exact depths of the clusters

from the foil surface. The relationships between $\underline{l}$ and $\underline{g}$ for defect clusters lying within the first depth layer are given by figure 2.4.

3.6 Determination of Defect Geometry

It was not possible to obtain an unambiguous determination of the geometries of defect clusters smaller than about 35 Å in diameter, because the image contrast was not, in general, sufficiently well defined.

The geometries of the larger defect clusters were found by imaging the clusters using the low order reflections ($\underline{g}$ = ±002, $1\bar{1}1$, $1\bar{1}\bar{1}$, or $2\bar{2}0$) about a [110] pole. As discussed in section 2.4.2, the symmetry of an image depends on its $|\underline{g}.\underline{b}|$ value. The different $|\underline{g}.\underline{b}|$ values for Frank loops and perfect loops when imaged using the low order reflections about a [110] pole are listed in Table 2.1. Images obtained using $\underline{g}$ = ± [$2\bar{2}0$] were used to distinguish between inclined Frank loops ($|\underline{g}.\underline{b}|$ = 0, weak black-white contrast), inclined perfect loops ($|\underline{g}.\underline{b}|$ = 1, strong black-white contrast) and edge-on Frank or perfect loops ($|\underline{g}.\underline{b}|$ > 1, complex black-white contrast). Images obtained using g = ± [002] were then used to distinguish between edge-on perfect loops ($\underline{g}.\underline{b}$ = 0, 'butterfly' contrast) and edge-on Frank loops ($|\underline{g}.\underline{b}| = \frac{2}{3}$, strong black-white contrast). An analysis of the loop Burgers vector and additional confirmation of the loop geometry was obtained by comparing the experimental images with computer simulated images (see section 2.4.3).

3.7 Determination of Defect Yield Values

The true defect yield is defined as the fraction of cascades which collapse to form dislocation loops. What is actually measured, however, is the number of visible defect clusters that are produced per incident ion and this measured defect yield is, in general, less than the true defect yield. Factors that affect the measured defect yield are: the possibility that some of the loops may have slipped out of the foil under the influence of surface image forces; whether or not a particular loop geometry is in contrast for the chosen diffraction conditions; and

the minimum size at which a loop becomes observable. The factors that affect the visibility of small (< 25 Å diameter) defect clusters are considered in detail in section 2.6.

The defect yield was measured by counting the number of visible images of defect clusters in a given area of a foil imaged under dynamical "two-beam" conditions using a $\underline{g}$ = <200> diffraction vector. This diffraction vector was chosen as all the Frank loops, which in the present case made up more than 95% of the total loop population, showed strong black-white contrast. In addition, the inclined perfect loops at the <110> orientation showed strong black-white contrast while the edge-on perfect loops showed 'butterfly' contrast. An area of the foil was chosen where "two-beam" conditions could be set up so that there was no significant fluctuation in background image intensity over the area of the micrograph. This was necessary to ensure that there was no variation in the visibility of the smallest defect clusters over the chosen area. A high resolution micrograph of this area was then printed at a total magnification of 600,000X, and six equal areas each containing approximately eighty defect clusters were marked out on the print. The defect yield for this sample of the cluster population was equal to the ratio of the average value of the number of defect clusters in each of these areas to the number of ions incident on each area. The standard error of the mean was then calculated (see for example Topping,1962) to relate this defect yield value to the defect yield value for the defect cluster population as a whole.

A possible disadvantage of measuring defect yields from a single $\underline{g}$ = <200> micrograph is that defect clusters lying close to the boundary between two depth layers may not be visible. As discussed in section 2.6, the visibility of these clusters may be improved either by altering the position of the depth layer boundaries by imaging using a different diffraction vector, or by altering the effective depth of a cluster in a

foil by tilting the foil through a large angle (Stathopoulos 1977). This latter method was not possible in the present case because the objective astigmatism could not be corrected when nickel specimens were tilted through large (> 10^{o}) angles. However, the defect yield generated by 80 keV W^{+} ion irradiation of a <110> nickel single crystal specimen and measured from a single high resolution $\underline{g}$ = <200> micrograph was found to be the same, within experimental error, as the defect yield measured by comparing micrographs of the same area obtained using the four different low order reflections about the <110> pole. Thus in this case no significant error was introduced by measuring the defect yield from a single $\underline{g}$ = <200> micrograph. This is thought to be due to the fact that most of the defect clusters were located within the first depth layer with only a few of them lying close to the first depth layer boundary.

It is possible that the depth distributions of the defect clusters in the alloys might have been different from that in pure nickel. This might have introduced significant errors into the defect yields in the alloys as measured from single $\underline{g}$ = <200> micrographs as an increased proportion of the defect clusters might have been positioned close to the depth layer boundaries. This point is especially relevant to all the defect yields generated by the Ni^{+} ions as the defect clusters extended, in general, to greater depths than those generated by the W^{+} ions. However, the results of Stathopoulos (1977) indicate that defect clusters larger than 25 Å in diameter are visible even when lying in unfavourable depth positions as tilting the foil only increased the measured number of small (< 25 Å diameter) defect clusters. The identification of these small clusters is very subjective and even when great care is taken in distinguishing these clusters from background surface structures, there is still a large uncertainty in the true number of small defect clusters present. In the present experiments, this uncertainty has been compensated for by drawing size distribution curves normalised to 10^{2} incident ions (see

section 3.8.1) such that the area under a curve is proportional to the measured defect yield. A comparison of these curves obtained for different specimens shows whether any difference in the defect yields can be attributed solely to a difference in the visibility of the small (< 25 Å diameter) clusters, or whether it is due to a difference in the number of defect clusters in all the size groups.

The possibility existed that the defect yields in the high (> 80 ergs cm^{-2}) stacking fault energy nickel and nichrome alloys might have been a sensitive function of grain orientation, due to the surface interaction energy causing some of the Frank loops to unfault to perfect loops which might then have slipped out of the foil under the influence of surface image forces. (The effect of loop loss on the measured defect yields is considered in detail in section 4.5). As a precaution, it was therefore decided to only consider defect clusters in grains lying between 2^{o} and 10^{o} of a <110> orientation, that is apart from specific measurements of the defect yields and defect sizes carried out for the defects in {100} grains of some of the materials. Part of the accuracy of the experimental technique for determining defect yields therefore depended on the fact that there should be no significant change in the defect yield of a given material for any orientation lying within 10^{o} of a <110> pole, that is apart from the possibility of axial channelling occurring for ions incident within 1^{o} or 2^{o} of the <110> axis.

The accuracy of the experimental technique is considered in section 3.9.

3.7.1 Errors in the Defect Yield

The errors involved in the determinations of the defect yields, and estimates of their magnitudes, are listed below.

(1) There was an error in the measurement of the dose incident on a specimen. Evidence from high (> 10^{14} ions cm^{-2}) dose implantations of semiconductors indicated that the dose measuring technique was accurate

to within 2%. It was not thought to be so accurate for the lower ($\sim 10^{11}$ ions cm^{-2}) doses used in the present experiments, although Jenkins (1975) has shown that a measured dose of 5×10^{10} ions cm^{-2} was accurate, for a given specimen, to within better than 10% (see section 3.3.2). This error may have consisted of a systematic error, which would have affected all the specimens equally, as well as a random error between the different specimens. As it was not possible to distinguish between these two types of error, this error of 10% has been assumed to be completely random for the purpose of comparing the present defect yield values.

(2) There was a random counting error due to the finite number of defect clusters counted. This was given by the standard error of the mean, which is a measure of the accuracy with which the defect yield of a sample of the population is related to the defect yield of the population as a whole. In the present case, in which the counting was over six equal areas each containing approximately eighty defect clusters, the standard error of the mean was about ±5%. This could have been reduced, if necessary, by counting more of the defect clusters.

(3) There was a random error in the microscope magnification. When the height of a specimen in the objective lens was altered, the objective lens current necessary to form a focussed image changed. Thus the microscope magnification, which depended on the objective lens current, varied slightly from specimen to specimen, and also when a given specimen was tilted. The error this introduced in the magnification was calculated from the changes in the objective lens current. In addition, the magnification (10X) of the final print from which the defect yield values were determined was subject to a small error. The total random error in the magnification was less than ±2%. This resulted in a random error in the defect yield measurement, which depended on M^2, of less than ±4%.

As well as the random error, there may have been a systematic error in the magnification. This would have affected all specimens equally and

should not therefore affect conclusions regarding comparative yields, but only the absolute values of the yields.

(4) There were errors due to the orientation of a specimen during irradiation and observation.

(i) Because of the way the specimens were mounted using circlips, the orientation of a specimen during irradiation was not known to better than 5%. The error (< 0.4%) this caused in the dose measurement is included in the total error in the dose measurement given in paragraph (1).

(ii) Tilting a foil from horizontal in the microscope increased the measured value of the defect yield by a factor $(\mathrm{Cos}\theta_x\ \mathrm{Cos}\theta_y)^{-1}$, where θ_x and θ_y were the tilt angles in two perpendicular directions. The systematic error this introduced was less than 1.5% as the foils were only tilted through small (< 10^{o}) angles. This error could be corrected for as θ_x and θ_y were recorded when each micrograph was taken.

(5) A systematic error might have arisen from defect clusters being generated in a foil during examination in the microscope. This 'gun damage' would be confined to the top (electron entrance) surface of the foil and it could therefore be distinguished from the damage structures to be investigated which were always loaded to correspond to the bottom surface of the foil. During the present experiments, there was no evidence for any gun damage.

The error quoted on a defect yield value in this thesis is the sum of the random errors considered above. These random errors were added by taking the square root of the sum of their squares. The total random error was typically ±12%.

The errors discussed above make no allowance for a possible difference in the defect yields in different specimens due to a difference in the visibility of small (< 25 Å diameter) defect clusters. This could be

caused by a difference in the background structures of the foil surfaces, a difference in the resolution of the micrographs, or a difference in the number of defect clusters lying in unfavourable depth positions. When comparing defect yields, it is therefore necessary to refer to the relevant size distribution curves, normalised to 10^2 incident ions (see section 3.8.1), to see if any difference in the defect yields could be attributed solely to a difference in the visibility of the smallest defect clusters.

3.8 Measurement of Defect Sizes

Defect size measurements were taken from images obtained under "two-beam" diffraction conditions at the Bragg angle (S = 0) using a $\underline{g}$ = <002> operating reflection. The width of an image was measured as the length of the interface between the black and white lobes of the image, in the case of partially dissociated Frank loops the length of the longest interface was measured, and in relating this image width (W) to the defect size (d) an average value of $R = W/d = 1$ was applied to all the clusters, independent of their geometry or their position in the foil (Katerbau 1977). As discussed in section 2.5.4, this procedure was adopted to try and obtain a consistent determination of the defect sizes so that an accurate comparison could be made between the defect sizes in the different materials.

The measurement of an image width from a print is subjective and what is taken to be the edge of the image may vary with the print magnification and also the background intensity of the print. This latter point was especially relevant to the smaller defect clusters, some of which appeared to only show black dot contrast, as the image width in this case was taken as the largest diameter of the black dot, and what was measured depended on the contrast gradient, as well as the actual difference in contrast between the defect image and background. In addition, it was found that the measured width of an image that was out of focus or

astigmatic was, in general, greater than the measured width of that image when it was sharply resolved. To make the comparison between defect sizes in different specimens as accurate as possible, all the image width measurements were therefore taken from high resolution prints of approximately the same background intensity and of the same total magnification, 600,000X.

The value of R for a given defect cluster is a sensitive function of S, the deviation from the Bragg condition. Care was therefore taken to ensure that the micrographs from which image widths were going to be measured were obtained under the same dynamical (S = 0) diffraction conditions in each material, and that these conditions were constant over the micrograph. This had the added advantage that when the micrographs were printed, the background intensity was approximately the same for each print, and thus any variation in determining image widths due to a difference in background intensities was kept to a minimum.

The image widths were measured using an eyepiece that had a magnification of 8X.

3.8.1 Size Distribution Curves

The images that were measured in a given material were those that had been counted in determining the defect yield. The size distribution curves of the defect clusters in each material therefore corresponded to a sample of approximately 400 defect clusters. The curves were smoothly drawn through histograms of the number of clusters whose sizes lay within 5 Å size intervals, the error on the number N of defect clusters whose sizes were measured as lying within a given size interval being $\pm\sqrt{N}$. The eyepiece that measured the image widths was calibrated in divisions of 0.1 mm, and so the magnification (600,000X) of the prints from which the image widths were measured was chosen so that 5 Å corresponded to an integral number of these divisions. It was therefore a simple matter to determine the number of clusters whose sizes lay within 5 Å size intervals.

The size distribution curves were either normalised to 10^2 visible defect clusters or to a dose of 10^2 incident ions. In the former case, the curves could be used conveniently for a comparison between the size distributions of the defect clusters in the different materials. In the latter case, while the shape of a curve still represented the distribution of the visible defect cluster sizes, the area under a curve was proportional to the defect yield.

3.8.2 Calculation of Mean Defect Size and Cascade Efficiency

In the present case, the mean defect size has been taken to be the diameter of a cluster of mean area. This value is thought to be more representative of the defect sizes than that simply determined as the mean of the cluster diameters, as what is important is the mean number of vacancies retained in the clusters and this is proportional to the cluster areas.

The mean defect sizes were determined from the mean number of vacancies in the visible defect clusters in a given material. In relating the size of a cluster to the number of vacancies it contained, it was assumed that the clusters were hexagonal Frank loops and the cluster width was taken to be the maximum diameter of the hexagon. Figure 3.3 shows the calculated relationship between the number of vacancies in a loop and the loop size. While this graph was drawn from values calculated for loops in Ni, the difference in interatomic distance between Ni (2.49 Å) and γFe (2.52 Å) is so small that this graph was used for the defect clusters in all the materials.

The standard error of the mean (see for example Topping, 1962) was calculated to relate the mean defect size of the measured sample of the cluster population to that for the cluster population as a whole. In addition, the standard deviation was calculated to describe the distribution of defect sizes about the mean size.

The cascade efficiency is defined as the fraction of vacancies

generated that are retained in visible clusters in those cascades that form visible clusters. In the present case, it was calculated as the ratio of the number of vacancies in a defect cluster of mean size to the theoretical number of vacancies generated in the collision cascade. This theoretical number was calculated, using the standard formula of Norgett, Robinson and Torrens (1972), as being 513 for 80 keV Ni^+ ion irradiation of Ni, and 577 for 80 keV W^+ ion irradiation of Ni. Since iron and chromium both have similar atomic numbers and atomic weights to nickel, these values were used for the collision cascades generated in the alloys as well.

3.8.3 Errors in the Defect Sizes

The mean defect size and the standard deviation about the mean are parameters that can be used to describe the sizes of the visible defect clusters in a given specimen. Both these parameters are strongly dependent on the number of small (< 25 Å diameter) defect clusters visible in a foil. Thus in comparing the sizes of the defect clusters in different specimens, a better comparison is obtained from the size distribution curves (normalised to 10^2 visible clusters) themselves, rather than the parameters describing these curves.

The errors involved in determining the mean size of the visible clusters in a given specimen can be conveniently divided into random errors, which will affect the comparative values of the mean sizes in the different specimens, and systematic errors, which will only affect their absolute values. These errors are listed below.

(1) A systematic error was introduced by using an average value of $R = W/d = 1$ to relate the size of a defect (d) to the measured width of its image (W). As discussed in section 2.5.4, the value of R for a given defect geometry is not accurately known. However, since the defect geometries were similar in the different materials, the error introduced by using an average value of R = 1 is thought to have affected all the

materials equally for similar depth distributions of the damage structures. This systematic error may therefore have been different for the damage structures generated by the Ni^+ ions compared with that for the damage structures generated by the W^+ ions because of the difference in their depth distributions.

(2) A systematic error was introduced by the image measuring procedure. As discussed in section 3.8, what is measured as an image width is subjective and depends, among other variables, on the background intensity of the print and the print magnification. The precautions that were taken to be consistent in measuring image widths means that the mean defect sizes obtained in the present experiments can be used for comparative purposes, although the absolute values are not known.

(3) A random error was caused by the finite number ($\sim$ 400) of defect clusters that were measured in each specimen. This error, which is given by the standard error of the mean which relates the mean defect size of the measured sample of the cluster population to the mean defect size of the cluster population as a whole, was typically ±2%.

(4) The magnification of the prints from which the image widths were measured was subject to both a random error of ±2% and a systematic error (see section 3.7.1).

The errors quoted on the mean defect sizes in this thesis are the sum of the random errors, that is the standard error of the mean plus the random magnification error. This total random error was typically ±3%. It must be emphasised, however, that the errors quoted are only a measure of the accuracy with which the mean defect sizes may be compared and, in addition, they make no allowance for a possible difference in the visibility of the small defect clusters in different specimens.

3.9 Experiment to Test the Accuracy of the Experimental Technique

In order to make a valid comparison between the defect yields and defect sizes measured in the different materials, it was necessary that

the experimental procedure should produce consistent results for each material. In particular, neither the defect yield nor the distribution of defect sizes should show a significant change for any orientation lying within 2^{o} and 10^{o} of a <110> pole (see section 3.7).

To test the accuracy of the experimental technique, three nickel specimens were irradiated in the main target chamber with the same measured dose (2.10^{11} ions cm^{-2}) of 80 keV tungsten ions. Two of the specimens were polycrystalline nickel and these were irradiated with W^{+} and W^{++} ions. The third specimen was a <110> orientation of nickel single crystal which was irradiated 7^{o} off-axis with W^{+} ions. The two W^{+} ion irradiations were not carried out simultaneously. The exact orientation of the grains from which measurements were taken were randomly distributed within 10^{o} of a <110> pole. The defect yields, mean defect sizes and standard deviations of the defect sizes were determined following the procedures, and taking the precautions, outlined in this chapter. These values are listed in Table 3.6, and it can be seen that they correspond within the calculated experimental error. Thus no significant changes were caused by the different specimen orientations. In addition, the comparison between the W^{+} ion and W^{++} ion irradiations shows that no significant error was introduced into the dose measuring technique by using doubly charged ions. This point is relevant to the high temperature irradiation procedure described in section 6.2. While these results demonstrate the consistency of the experimental technique for measurements carried out in nickel specimens, a similar consistency was found whenever defect yield or defect size measurements were repeated in the alloys.

As discussed in sections 3.7.1 and 3.8.3, while the defect yields, mean defect sizes and standard deviations of the defect sizes are parameters that can be used to describe the numbers and sizes of the defect clusters, the errors quoted take no account of a possible difference in the visibility of the small (< 25 Å diameter) defect clusters, and a more

accurate comparison between the different specimens is obtained from their size distribution curves. These curves, either normalised to 10^2 incident ions (see figure 3.4) or 10^2 visible defect clusters (see figure 3.5), show good agreement from one specimen to another. This therefore gives confidence in using these curves when comparing defect yield values, and the distribution of defect sizes, in the different materials.

Table 3.1 Composition of the stainless steel used in the present experiments. The interstitial alloying elements are marked with an asterisk.

Table 3.2 Chemical composition of Lenoir's solution.

Table 3.3 The electropolishing solutions and the conditions that were used in electropolishing the different materials.

Element	C*	Si	Mn	Cr	Ni	Ti	P*	S*	Fe
Wt %	0.05	0.42	1.76	18.09	9.57	0.33	0.025	0.03	Bal

TABLE 3.1.

Chromium Trioxide	CrO_3	78 gms
Sulphuric Acid	H_2SO_4	67 cc
Orthophosphoric Acid	H_3PO_4	310 cc
Water	H_2O	120 cc

TABLE 3.2.

Material	Polishing Soln.	Current	Applied P.D.	
			Fresh Soln.	Aged Soln.
Ni	Lenoir's Soln.	110 ma	130 v	120 v
Ni/Cr 8%	Lenoir's Soln.	120 ma	150 v	130 v
Ni/Cr 17%	Lenoir's Soln.	165 ma	150 v	135 v
Fe/Ni/Cr	10% Perchloric Acid in Methanol	120 ma	300 v	——
321 St.St.	Lenoir's Soln.	130 ma	125 v	110 v

TABLE 3.3.

Table 3.4 The results, given in terms of ppm($^{W}/_{w}$), of the spectrographic analyses of the nickel single crystal (Ni*), and the polycrystalline Ni, Ni/Cr8%, Ni/Cr17% and Fe/Ni10%/Cr17%. M = major constituent. (Chemical pretreatment was carried out in silica ware and the Si result is therefore a maximum concentration).

Element Sought	Ni*	Ni	Ni/Cr6%	Ni/Cr17%	Fe/Ni/Cr
Ag	<5	<7	<7	<7	<7
Al	20	7	40	100	150
Ba	<5	<7	<7	7	7
Bi	<5	<15	<15	<15	<30
Ca	<50	<70	70	<70	70
Cd	<100	<150	<150	<150	<150
Cr	<5	30	~7%	~15%	~15%
Cu	5	15	30	15	15
Fe	<50	200	200	200	M
Ga	<5	<7	<7	<7	<70
In	<10	<15	<15	<15	<15
Mg	5	<7	7	7	7
Mn	<5	<7	<7	<7	<7
Mo	<5	<7	<7	<7	10
Na	<200	<300	<300	<300	<300
Ni	M	M	M	M	~10%
Pb	<20	<30	<30	<30	<30
Pt	<200	<300	<300	<300	<300
Sb	<300	<700	<700	<700	<700
Si	200*	700*	700*	150*	700*
Sn	<30	<50	<50	<50	<150
Sr	<5	<7	<7	<7	7
Ti	<10	<15	<15	<15	<15
Tl	<50	<70	<70	<70	<70
V	<5	<7	7	<7	<7
W	<50	<70	150	<150	<150
Zn	<200	<300	<700	<700	<700
Zr	<10	<30	<30	<30	<30

TABLE 3.4.

Table 3.5 Results of the activation analyses for carbon, oxygen and nitrogen (n.a. means that the material was not analysed for this impurity).

Table 3.6 The defect yields, mean defect sizes and standard deviations of the defect sizes for the defect clusters generated by 80 keV tungsten ion irradiations of nickel specimens orientated within 10^{o} of a <110> pole.

Material	Form of Sample	Impurity Content		
		ppm C (w/w)	ppm O (w/w)	ppm N (w/w)
Ni Single Crystal	Electropolished Discs	5	<6	<10
Ni Polycrystalline	Annealed Strip	57	<2	<3
Ni/Cr 8%	Annealed Strip	1	190	<1
Ni/Cr 17%	Annealed Strip	4.5	1070	<2.5
Fe/Ni10%/Cr17%	Annealed Strip	12.5	830	<2.5
321 St.St.	Annealed Strip	n.a.	32 ± 2	n.a.
Ni/Cr 17%	Strips annealed in Argon /5% Hydrogen	n.a.	1030	n.a.
Cr/Ni 83%	Annealed Strip	3 ± 2	510	n.a.

TABLE 3.5.

Incident Ion	Target	Defect Yield	Defect Sizes	
			Mean Size	Standard Deviation
80 KeV W^{+}	Ni⟨110⟩ Polycrystalline	0.81 ±0.09	37.3 ±0.9 Å	10.7 Å
80 KeV W^{++}	Ni⟨110⟩ Polycrystalline	0.70 ±0.08	36.3 ±1.0 Å	10.2 Å
80 KeV W^{+}	Ni⟨110⟩ Single Crystal	0.75 ±0.08	38.3 ±1.1 Å	11.7 Å

TABLE 3.6.

Figure 3.1 Schematic diagram of the jet polishing apparatus.

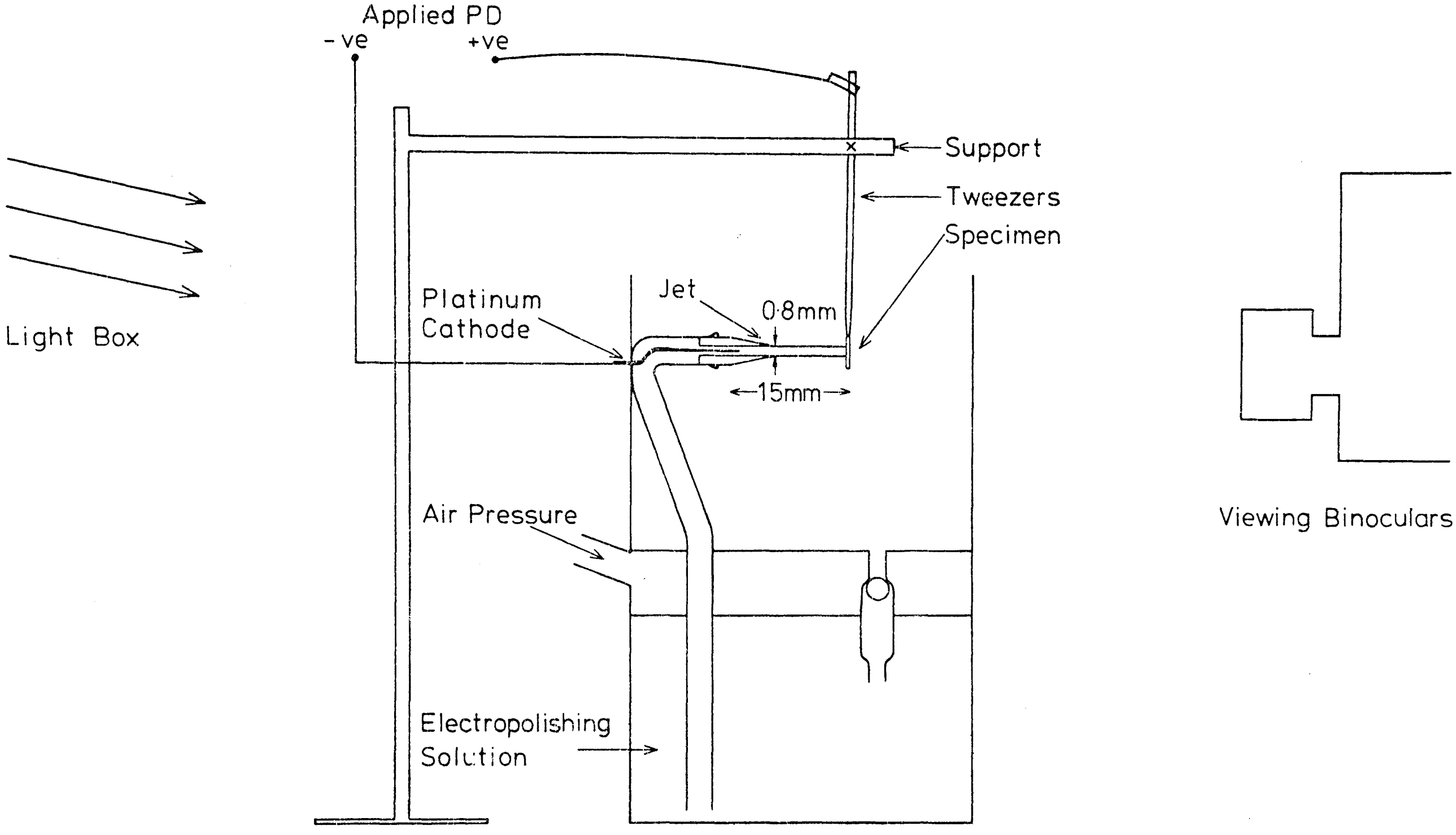
Applied PD
-ve
+ve
Support
Tweezers
Specimen
Platinum
Cathode
Jet
0·8mm
15mm
Light Box
Air Pressure
Electropolishing
Solution
Viewing Binoculars

Figure 3.2 Schematic diagram of the heavy-ion accelerator.

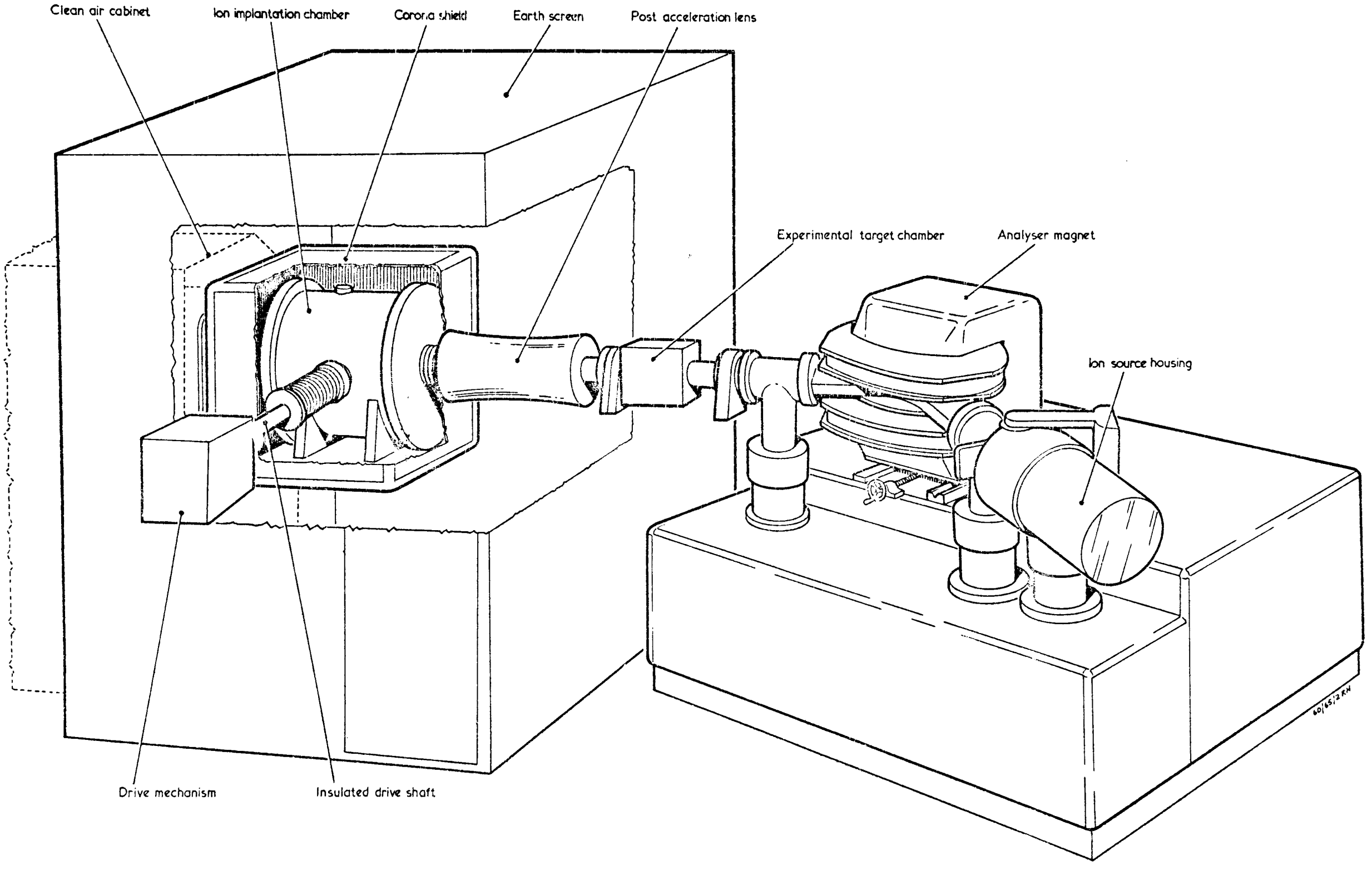
Clean air cabinet
Ion implantation chamber
Corona shield
Earth screen
Post acceleration lens
Experimental target chamber
Analyser magnet
Ion source housing
Drive mechanism
Insulated drive shaft
60/65/2 RH

Figure 3.3 Graph showing the calculated relationship between the number of vacancies in a loop and the loop diameter for hexagonal Frank loops in nickel.

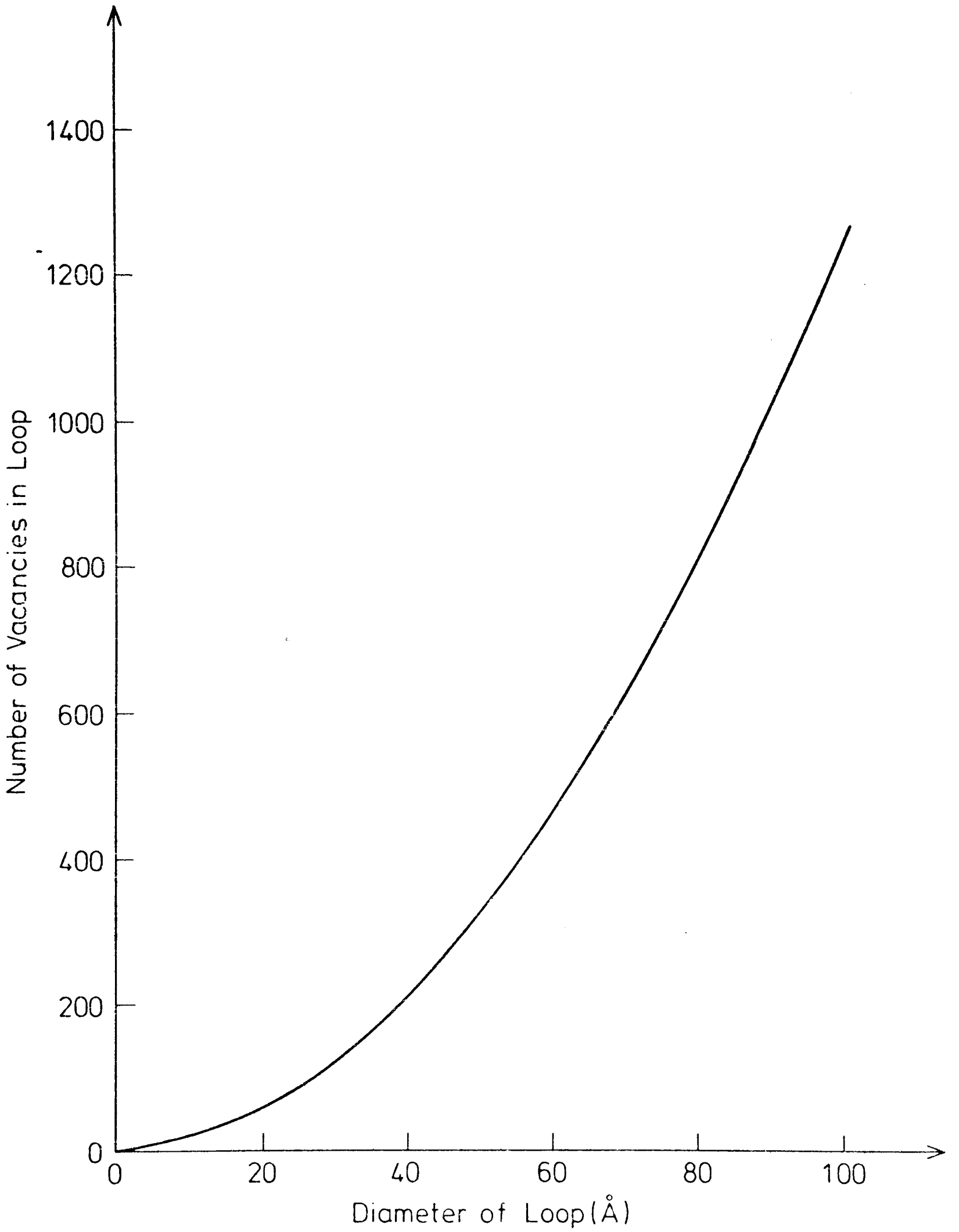
Number of Vacancies in Loop
1400
1200
1000
800
600
400
200
0
0
20
40
60
80
100
Diameter of Loop(Å)

Figure 3.4 Size distributions, normalised to doses of 10^2 incident ions, of the defect clusters generated by 80 keV tungsten ion irradiations of nickel specimens lying within 10° of a <110> orientation.

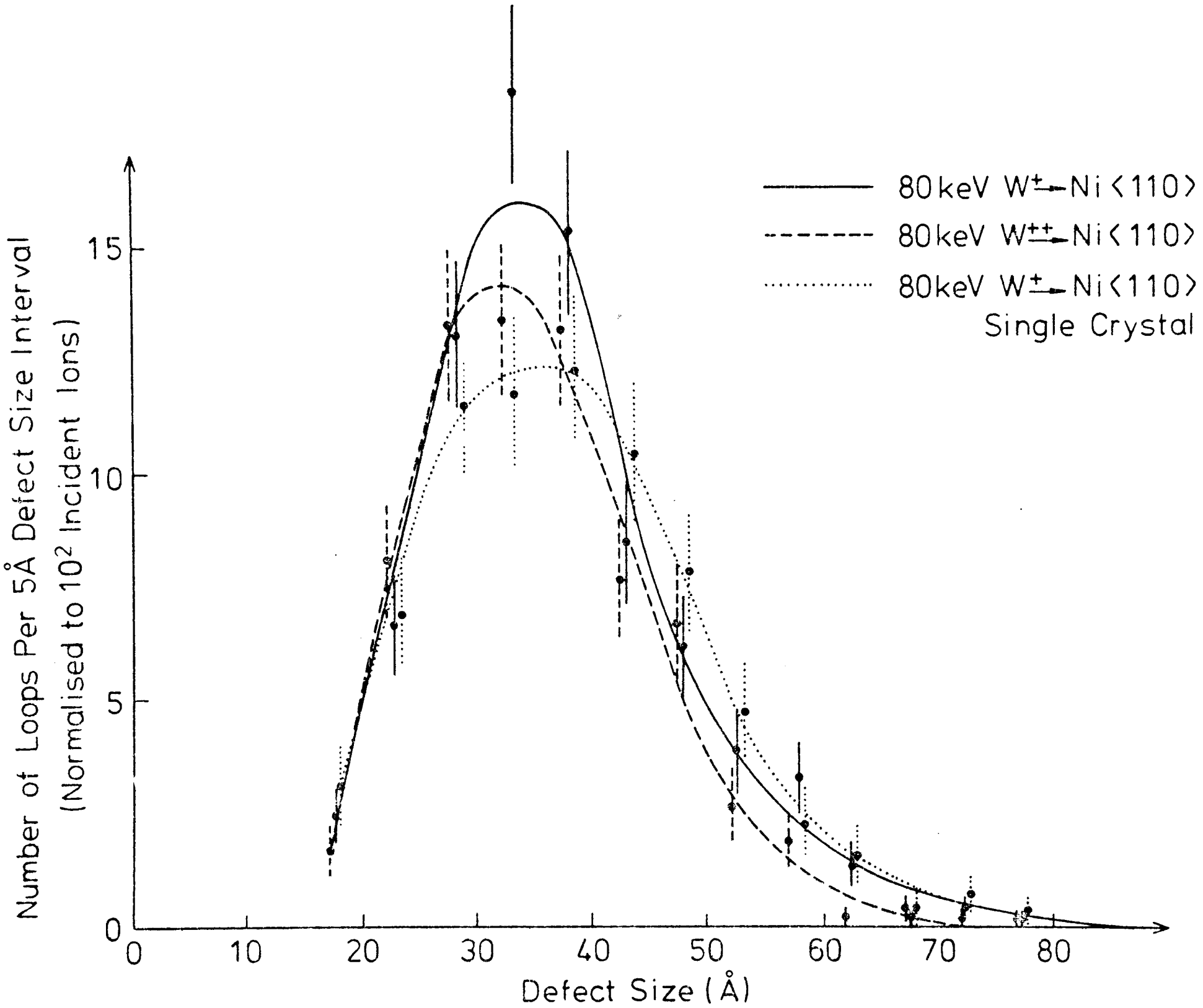
80keV W+→Ni⟨110⟩
80keV W++→Ni⟨110⟩
80keV W+→Ni⟨110⟩
Single Crystal
Number of Loops Per 5Å Defect Size Interval
(Normalised to 10² Incident Ions)
0
5
10
15
0
10
20
30
40
50
60
70
80
Defect Size (Å)

Figure 3.5 The size distribution curves of figure 3.4 normalised to 10^2 visible defect clusters.

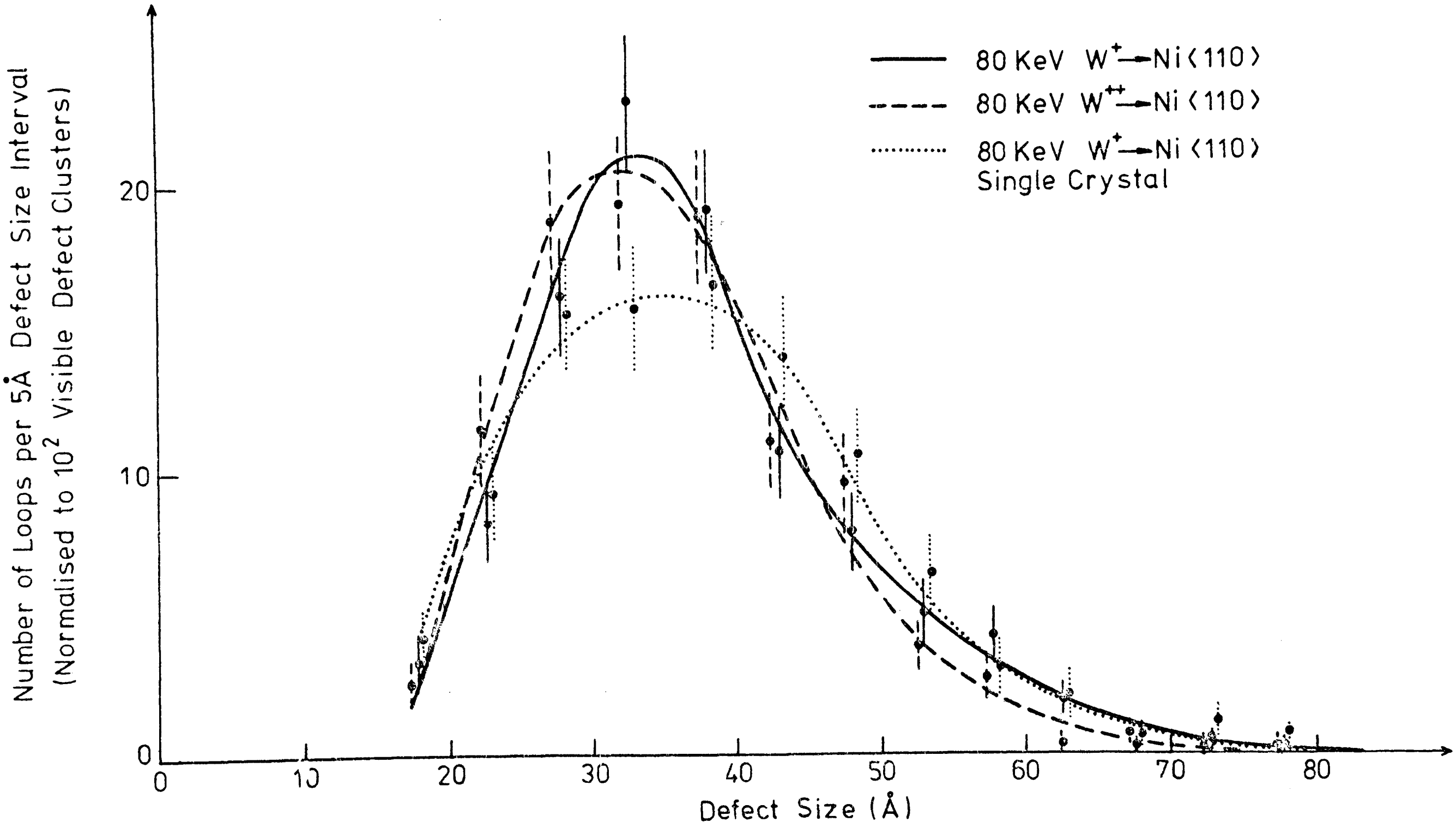
80 KeV W+→Ni⟨110⟩
80 KeV W++→Ni⟨110⟩
80 KeV W+→Ni⟨110⟩ Single Crystal
Number of Loops per 5Å Defect Size Interval (Normalised to 10² Visible Defect Clusters)
0
10
20
0
10
20
30
40
50
60
70
80
Defect Size (Å)

CHAPTER 4

The Damage Structures Generated in Nickel by Nickel and Tungsten Heavy-Ion Bombardment at Room Temperature

4.1 Introduction

No thorough analysis of the damage structures generated by low-dose, heavy-ion irradiations of nickel had been published in the open literature prior to the start of this research project. The initial part of the project was therefore concerned with an investigation of the displacement cascade damage structures generated in pure nickel by heavy-ion irradiations at room temperature. The results of this investigation, and a discussion of these results, are presented in this chapter.

The initial irradiations were carried out on <110> orientated specimens of nickel single crystal using 80 keV Ni^+ ions to doses of 6×10^{11} ions cm^{-2}. Damage was observed in the form of small dislocation loops, but the black-white contrast from these small loops was, in general, not sufficiently well defined to allow an unambiguous analysis of either the defect geometries or the defect natures. To increase the sizes of the defect clusters so that their geometries could be analysed, the irradiations were repeated using tungsten ions. So that the orientation dependence of the defect yield could be investigated, <100> single crystal specimens and polycrystalline nickel specimens were irradiated with 80 keV W^+ ions to doses of 2×10^{11} ions cm^{-2} as well as the <110> single crystal specimens.

The purity of the nickel specimens used in these irradiations, the irradiation procedure, and the methods used to determine the numbers, sizes, geometries and natures of the defect clusters are discussed in detail in Chapter 3.

4.2 Results

4.2.1 Defect Nature

An analysis of the defect natures indicated that all the analysable loops in both tungsten and nickel bombarded nickel were of vacancy type. This is in agreement with previous results obtained from heavy-ion irradiated nickel by Norris (1969) and Schindler et al (1976).

4.2.2 Defect Geometry

The image contrast from defect clusters smaller than about 35Å in diameter was not, in general, sufficiently well defined to allow the geometry of the clusters to be analysed. In the case of the self-ion irradiations, it was only possible to analyse a very small number (∿10%) of the visible defect clusters. The small size of the defect clusters generated by the Ni^+ ion irradiations, and the difficulties this caused in analysing the cluster geometries, can be seen from figure 4.3(a). The few clusters that could be analysed unambiguously were all found to be Frank dislocation loops.

The majority of the defect clusters generated by the tungsten ion irradiations were also too small to have their geometries analysed. It was therefore not possible to determine the relative frequencies of the different possible cluster geometries in relation to the defect population as a whole. The quantitative results given here only refer to that percentage (∿30%) of the visible defect clusters generated by the tungsten ions that were large enough to be analysed unambiguously.

The defect geometries were analysed from images of the defect clusters obtained using the low order reflections about a <110> pole (see section 3.6). This procedure is illustrated by figure 4.1. The majority of the defect clusters that were analysed were found to be Frank-type dislocation loops, although a small number (<5%) of inclined perfect loops were identified as well. An inclined perfect loop and an edge-on and an inclined Frank loop can be seen in figure 4.1. The theoretical energies of Frank loops and perfect loops in nickel, and the possible reasons why apparently energetically unfavourable perfect loops should form, are considered in section 4.3.

There was found to be an uneven distribution of image sizes among the four possible {111} Frank loop habit planes. Approximately 70% of the images which had widths greater than 50Å were formed by Frank loops

whose habit planes lay on the 'edge-on' planes. This is illustrated by figure 4.2 where it can be seen that most of the larger images were formed by Frank loops lying on the edge-on (α and γ) planes. A similar result has been found by Stathopoulos (1977) in heavy-ion bombarded copper. Possible reasons for this uneven distribution are discussed in section 4.4.

Despite the relatively high stacking fault energy in nickel, about 30% of the Frank loops that had image widths greater than 60Å had partially dissociated onto {111} planes other than the loop habit plane. An image (D) of such a dissociated loop with two lines of no contrast can be clearly seen in figure 4.2. Dissociated Frank loops have previously been observed in copper (Wilson and Hirsch 1972, Jenkins 1974) and silver (Jenkins 1974), materials with much lower stacking fault energies. The possibility that it may be energetically favourable for Frank loops to dissociate in nickel is considered in section 5.4.

4.2.3 Measured Defect Yields and Defect Size Distributions

4.2.3.1 Dependence on Mass of Incident Ion

The defect yield was found to be strongly sensitive to the mass of the incident ion.

Figure 4.3 shows the damage structures generated in <110> nickel single crystal specimens by (a) 80 keV Ni^+ ions to a dose of 6×10^{11} ions cm^{-2}, and (b) 80 keV W^+ ions to a dose of 2×10^{11} ions cm^{-2}. A comparison between these two micrographs shows that, on average, the defect clusters generated by irradiating with self-ions are smaller than those generated by irradiating with tungsten ions of the same energy. The measured size distributions of these defect clusters, taken over approximately four hundred defects in each specimen and normalised to doses of 10^2 incident ions so that the areas under the curves are proportional to the defect yields, are compared in figure 4.4. The error bars on the curves represent the statistical error on the number of

defects measured as lying within a given size interval (see section 3.8.1). The values of the defect yields, mean defect sizes and standard deviations of the defect sizes are listed in Table 4.1. The calculation of these parameters and the errors quoted is described in sections 3.7 and 3.8.

The defect yield and mean defect size were both much smaller for the Ni^+ ion irradiation than for the W^+ ion irradiation (see Table 4.1). This is clearly illustrated by figure 4.4 from which it can be seen that the peak of the size distribution curve occurs for a smaller defect size in the self-ion irradiated case, and that the area under the curve, which is proportional to the defect yield, is substantially reduced in the self-ion case.

Possible explanations why increasing the incident ion mass should increase the defect yield and mean defect size are considered in section 4.6.

4.2.3.2 Orientation Dependence

The measured defect yields and defect size distributions in a <110> single crystal specimen irradiated 7^o off axis and in polycrystalline specimens lying within less than 10^o of a <110> orientation were found to be the same within experimental error (see section 3.9). Thus apart from the possibility of axial channelling occurring for ions incident within 1^o or 2^o of the <110> axis, the defect yield is not strongly dependent on the precise orientation of a specimen lying close to a <110> orientation.

The damage structures generated by 80 keV W^+ ion irradiations of a <100> orientation of nickel single crystal and a <100> grain of polycrystalline nickel to doses of 2×10^{11} ions cm^{-2} are shown in figures 4.5(a) and 4.5(b) respectively. A comparison of these two micrographs indicates that the density of defect clusters is lower in the single crystal specimen than in the polycrystalline specimen. The measured size

distributions of the defect clusters in the two specimens, normalised to doses of 10^2 incident ions, are compared in figure 4.6. The values of the defect yields, mean defect sizes and standard deviations of the defect sizes are listed in Table 4.1.

The mean defect sizes in the two <100> orientated specimens were the same within experimental error and equal to that in the W^+ ion irradiated <110> single crystal specimen (see Table 4.1). However, while the defect yields in the <110> single crystal specimen and the <100> polycrystalline specimen were also the same within experimental error, the defect yield was lower in the <100> single crystal specimen. Possible reasons for this decrease in defect yield are considered in section 4.7.

4.3 Formation of Perfect Loops

An '$\underline{1}$' vector analysis of the geometries of the defect clusters generated by 150 keV xenon ion irradiation of nickel by Norris (1967) indicated that both Frank and perfect loops were present. More recently, Schindler et al (1976) have found that 30 keV copper ion irradiation of nickel produces only Frank-type dislocation loops. The fact that Norris identified perfect loops as well as Frank loops may have been due to the ambiguity of the '$\underline{1}$' vector analysis method. Alternatively, the results of Jenkins et al (1977) and English (1977a) indicate that apparently energetically unfavourable loops may be formed as a result of increasing the mass of the incident ion (see section 1.5.3.2).

In the present case, while perfect loops were only positively identified amongst the clusters generated by the tungsten ion irradiations, it is not possible to state that perfect loops were not present amongst the clusters generated by the nickel ion irradiations because the small size of these clusters prevented an unambiguous determination of most of the defect geometries. The possibility also exists that while perfect loops formed only a small number (<5%) of the total number of clusters,

generated by the tungsten ion irradiations, that were analysed, a greater number of Frank loops may have unfaulted to perfect loops, but some of these may have subsequently slipped out of the foil under the influence of surface image forces. This point is considered in section 4.5.

The theoretical energies of small Frank loops and small perfect loops in nickel are shown by figure 4.7. The loop energies in an infinite medium were calculated for hexagonal loops using the formulae given by Hirth and Lothe (1968) that are based on the exact analytic expressions for the self energy of a dislocation segment and for the interaction energies between straight segments of dislocations in isotropic materials given by Jøssang et al (1965). Thus these energies would be exact for hexagonal loops in an infinite isotropic material. However, the loops may not be hexagonal and nickel is anisotropic ($\frac{C_{11}-C_{12}}{2C_{44}} = 0.39$) so the actual energies may be somewhat different. The value of the stacking fault energy in nickel was taken as 125 ergs cm^{-2} (Carter and Holmes 1977). The reduction in energy of a loop due to its interaction with a neighbouring surface was calculated for loops lying at a distance $Z_o = 2\rho$ (ρ = loop radius) from the foil surface using the results of Jäger et al (1975) as described in section 4.4.1. Even though the reduction in energy due to the surface interaction can be greater for a perfect loop than for a Frank loop, for loops with diameters between 15 → 130Å, the centres of which lie at distances greater than the loop diameter from the foil surface ($Z_o \geq 2\rho$), the Frank loop is still the energetically more stable form.

However, the surface interaction energy is a very sensitive function of Z_o and ρ (using the infinitesimal loop approximation it varies as ρ^4/Z_o^3 (see section 4.4.1)) and thus the possibility exists that if a large loop lies close enough to the specimen surface, then the perfect loop may be the energetically more stable form. Thus if stresses are present which serve to nucleate the necessary partial dislocations, such Frank loops would then unfault to perfect loops. This possibility is more

fully discussed in section 4.4.1.

On one or two infrequent occasions, the image of a large defect cluster was observed to disappear while being viewed in the electron microscope. This may have been due to stresses induced by the electron beam causing a Frank loop to unfault to a perfect loop which then slipped out of the foil. If this is so, then it would indicate that a perfect loop can be the energetically more stable form. However, the Frank loop may have already unfaulted to an inclined perfect loop which remained in the foil, and the stresses may have just served to cause that perfect loop to slip out of the foil. It was not possible to differentiate between these two alternative explanations.

If the formation of perfect loops in nickel does depend on the surface interaction energy causing Frank loops to unfault, then the probability of this happening would be expected to increase with increasing incident ion mass, as, as discussed in section 4.6, the effect of increasing the incident ion mass is to generate larger clusters that lie closer to the specimen surface.

4.4 Uneven Distribution of Frank Loop Image Sizes on 'Edge-On' and 'Inclined' Planes

It was observed that for the <110> orientation the majority of the larger images was formed by Frank loops lying on the edge-on planes (see section 4.2.2). One possible explanation for this is that for a Frank loop of a given size, the image contrast is wider for loops lying on the edge-on planes compared with those lying on the inclined planes. However, the theoretical image widths for Frank loops of the same size lying on the edge-on and inclined planes are not appreciably different, and a comparison of these theoretical images (Saldin 1977) with the experimental images (see figure 4.2) indicates that while some of the inclined loops are as large as the larger edge-on loops, the Frank loops lying on the inclined planes are, on average, actually smaller than those

lying on the edge-on planes. More direct evidence for this difference in sizes has been obtained by Stathopoulos (1977) in heavy-ion bombarded copper. Stathopoulos compared the size distributions of the edge-on and inclined Frank loops generated and imaged close to a <110> orientation with the size distributions of the same defect clusters when imaged at a <100> orientation. For this orientation, all four {111} Frank loop habit planes are equally inclined to the specimen surface and Stathopoulos concluded that the Frank loops lying on the inclined planes at the <110> orientation were genuinely smaller than those lying on the edge-on planes.

Two possible explanations have been considered to account for the difference in the sizes of the Frank loops lying on the edge-on and inclined planes in nickel. One is that the large Frank loops lying on the inclined planes preferentially unfault to perfect loops which then slip out of the foil, while the large Frank loops lying on the edge-on planes do not unfault and therefore remain in the foil. Alternatively, the probability of a cascade region collapsing to form a large faulted loop may not occur with equal probability on all four {111} planes, being greater for the edge-on planes. These two possibilities are considered in the following two sections.

4.4.1 Loop Loss Due to Surface Image Forces

The total energy of a dislocation loop lying close to a surface is the sum of the elastic energy in an infinite medium plus the reduction in energy due to the interaction with the surface. For a given loop, this interaction energy depends on the loop Burgers vector $\underline{b}$, the loop normal $\underline{n}$ and the orientation of the surface $\underline{S}$. The possibility therefore exists that while the energy of a Frank loop of a given size is less than that of a perfect loop of the same size when both loops are in an infinite medium, a difference in the surface interaction energies may result in the total energy of the perfect loop being less than the total energy of

the Frank loop. The Frank loop may then unfault and if the image shear stress by which the resulting perfect loop is attracted to the surface exceeds the critical shear stress for microslip, then the perfect loop will glide out to the surface.

Jäger, Ruhle and Wilkens (1975) have calculated the interaction energy of a dislocation loop with a traction free surface and also the image force by which a loop is attracted to the surface for an elastically isotropic medium. These calculations employed the infinitesimal loop approximation and the results are only a good approximation for loops whose centres lie at distances greater than two loop radii from the surface of the foil ($Z_o > 2\rho$). Under this approximation, the elastic interaction energy is given by:-

$$E^{(i)} = - Q_e E_o$$

where $$E_o = f(\underline{n}', \underline{\beta}, \nu)$$

and $$Q_e = \frac{\pi b^2 \rho^4 \mu}{128(1-\nu)Z_o^3}$$

where $\underline{n}'$ and $\underline{\beta}$ are the direction cosines of $\underline{n}$ and $\underline{b}$ relative to $\underline{S}$, ν is Poisson's ratio and μ is the shear modulus. For perfect loops in nickel

$$Q_e = 1.10\ \rho^4/Z_o^3 \text{ eV}$$

where ρ and Z_o are measured in nanometres. In addition, the image shear stress which determines whether glide takes place is given by:-

$$T^{(i)} = Q_T T_o$$

where $$T_o = E_o |\beta_z|$$

and $$Q_T = \frac{3b\rho^3 \mu}{256(1-\nu)Z_o^4}$$

where the z direction is normal to the specimen surface.

A given Frank loop in an F.C.C. material can unfault to one of three possible perfect loop configurations and values for E_o and T_o have been

calculated for the four possible Frank loops and the perfect loops that they would unfault to for both [110] and [100] foil normals using the expression for E_o given by Jäger et al. The results of these calculations are given in Table 4.3.

The possibility that the surface interaction energy $E^{(i)}$ may cause a given Frank loop to unfault depends on whether the change in $E^{(i)}$ on unfaulting is greater than the energy difference between the Frank loop and the resulting perfect loop when both are in an infinite medium. Reference to Table 4.3 shows that for the [110] orientation, the greatest change in $E^{(i)}$ that occurs on unfaulting is when an inclined Frank loop (E_o = 18.10) unfaults to a 'flat-on' perfect loop (E_o = 29.79). The reduction in the energies of these loops in nickel due to the surface interaction energy is shown in figure 4.7 for the case of the loops lying at a distance $Z_o = 2\rho$ from the specimen surface. From this figure it can be seen that while the reduction due to $E^{(i)}$ is greater for the perfect loop than for the Frank loop, this energy is only a few percent of the energy in an infinite medium and does not appear sufficient to cause unfaulting. However, while the mean radius of the Frank loops generated by 80 keV W^+ ion irradiation of a <110> foil of nickel single crystal was found to be $\bar{\rho}$ = 19.1Å, and the mean depth of deposited energy has been calculated as $\bar{Z}_o$ = 55Å (see section 4.6) such that $\bar{Z}_o > 2\bar{\rho}$, much larger Frank loops of up to 80Å in diameter were also observed. The strong dependence of $E^{(i)}$ on ρ and Z_o indicated by the infinitesimal loop approximation ($E^{(i)} \propto \rho^4/Z_o^3$) may result in the perfect loop configuration being the energetically more stable form for these large loops if they lie close enough to the surface. As a guide to the possible magnitude of the difference in $E^{(i)}$ for such loops, if the infinitesimal loop approximation were applicable to the situation of a loop of diameter 75Å lying 40Å from the surface, then it would predict that the surface interaction energy of a perfect loop is 50 eV greater than for the

corresponding Frank loop. Since this difference in energy is almost equal to the energy difference between the loops in an infinite medium, the possibility exists that large Frank loops that lie within about 50Å of the surface may unfault due to their interaction with the surface.

The experimentally observed frequencies of $\underline{b} = \frac{a}{2}\langle 111\rangle$ perfect loops in B.C.C. materials have been satisfactorily explained using the calculations of Jäger et al applied to a model proposed by Häussermann (1972b). This model, which is described in more detail in section 1.5.3.2, proposes that if a Frank loop unfaults, then it will unfault to the one of the possible perfect loop configurations that has the lower total energy. The resulting perfect loops might or might not then glide out to the surface depending on the strength of the image shear stress acting on the loop. Since this model can satisfactorily explain the results for $\underline{b} = \frac{a}{2}\langle 111\rangle$ loops in B.C.C. materials, it appears reasonable to apply it to F.C.C. materials as well.

Thus reference to Table 4.3 shows that for the [110] orientation, if an inclined Frank loop unfaults then the perfect loop with the lowest total energy (highest E_o value) is 'flat-on' with $\underline{b} = \pm\frac{a}{2}[110]$. This loop has its Burgers vector normal to the surface ($|\beta_z| = 1$) and so there is a strong probability that it would slip out of the foil. Irrespective of whether loop loss does occur, such a loop would not be observed when imaged at the [110] pole because $\underline{b}$ lies in the reflecting planes for all $\underline{g}$s. In the case of an edge-on Frank loop unfaulting, the lowest energy perfect loop would be one of the four inclined perfect loops. The fact that some large, inclined perfect loops were identified is therefore consistent with the unfaulting of large, edge-on Frank loops. Under the infinitesimal loop approximation, the image shear stress acting on a loop varies as ρ^3/Z_o^4 and there would therefore appear to be a strong probability that if an edge-on Frank loop lies close enough to the surface for it to be energetically favourable for it to unfault, then the resulting

perfect loop would glide out of the foil. However, the image shear stress also depends on T_o and all the inclined perfect loops have $T_o = 3.13$. This low value, combined with the possibility of the loops being pinned by impurities, may explain why at least some of the inclined perfect loops did not glide out of the foil.

In conclusion, the calculations indicate that the surface interaction energy may cause unfaulting and that the probability of this unfaulting would be greater for the inclined Frank loops than for the edge-on Frank loops. Since inclined perfect loops have been observed, which would indicate that edge-on Frank loops have unfaulted, it is thought that the observed distribution of large Frank loops among the {111} planes could be accounted for by the surface interaction energy causing preferential unfaulting of large Frank loops lying on the inclined planes.

4.4.2 Cascade Collapse onto the 'Edge-On' and 'Inclined' Planes

It has been suggested by Jenkins (1974) and considered in more detail by Stathopoulos (1977) that cascade collapse onto a given {111} plane may be influenced by the orientation of that plane with respect to the shape of the cascade region. Because of the initial momentum of the incident ion, the cascade region is not spherical but is elongated in the direction of the incident ion. The values of $\langle \Delta X_D^2 \rangle^{\frac{1}{2}}$ and $\langle Y_D^2 \rangle^{\frac{1}{2}}$, which are measures of the cascade radii parallel and perpendicular to the incident ion direction, given in Table 4.2 quantitatively illustrate this. These values were calculated from LSS theory (see section 4.6) and they do not take into account the effect of the crystalline lattice. Lindhard (1965) has shown qualitatively that the lattice structure can result in the disordered region being extended even more in the incident ion-beam direction. The cascade region generated by an ion incident on a (110) foil is illustrated schematically in figure 4.8, along with the orientation of the four {111} planes relative to the cascade region.

In unstressed specimens, Frank loops are thought to nucleate with

equal probability on all four {111} planes and visible clusters are then formed by the short range diffusion of vacancies in the cascade region to these nuclei. Figure 4.8 shows that a vacancy will, on average, have a shorter distance to diffuse through to the habit plane of a Frank loop if it nucleates on an edge-on plane than if it nucleates on an inclined plane. The possibility therefore exists that, on average, more vacancies will diffuse to a Frank loop nucleated on an edge-on plane and thus the loops formed on the edge-on planes would, on average, be larger than those formed on the inclined planes. Thus this could also explain the observed distribution of loop sizes among the edge-on and inclined planes.

However, the results obtained in the W^+ ion irradiated alloys (see section 5.5.3) would indicate that once a Frank loop has nucleated within a cascade, then most of the vacancies within the core of the cascade region are drawn into the loop nucleus. Thus the distance a vacancy has to diffuse through to reach a Frank loop habit plane may not be such a critical factor in determining the eventual size of the loop, especially when one considers the small size of the cascade regions generated by the tungsten ions (see Table 4.2).

It is therefore considered that the preferential unfaulting of the large Frank loops lying on the inclined planes is the more probable explanation for the observed distribution of loop sizes on the edge-on and inclined planes.

4.5 Effect of Loop Loss on Defect Yield Values

If, as considered in section 4.4.1, the interaction with the surface caused some of the large Frank loops to unfault to perfect loops which then slipped out of the foil, the measured values of the defect yields would be lower than the true values. However, it is not thought that loop loss at the surface caused a significant reduction in the defect yields in the case of the W^+ ion irradiations for the reasons given

below. The effect would be expected to be even less for the Ni^+ ion irradiations.

A consideration of the magnitude of the reduction in loop energies that would be required to cause unfaulting showed that only large (>60Å diameter) loops lying within about 50Å of the surface are likely to have unfaulted. At the <110> orientation, numerous large edge-on Frank loops were observed. This, coupled with the small decrease in the surface interaction energy when an edge-on loop unfaults (see Table 4.3), suggests that only a small percentage of these loops unfaulted. In addition, some of the resulting inclined perfect loops remained in the foil. Any reduction in the defect yield would therefore be mainly due to the unfaulting of the inclined loops, and while it is thought that a high percentage of the large (>60Å diameter) inclined Frank loops did unfault, not all of them did so as some were still observed in the foils.

An estimate of the possible magnitude of the reduction in the defect yield due to inclined Frank loops unfaulting can be found from the facts that approximately 10% of the visible defect clusters in W^+ ion irradiated <110> orientated nickel had diameters greater than 60Å, and of these approximately 70% were edge-on Frank loops. If it is assumed that equal numbers of large (>60Å diameter) Frank loops were formed on the edge-on and inclined planes, then the reduction in the true defect yield caused by the inclined loops unfaulting would be about 4%. This is much less than the accuracy of the experimental technique for measuring defect yields which is about 12% (see section 3.7.1).

At the <100> orientation, all four {111} Frank loop habit planes are equally inclined to the specimen surface. Reference to Table 4.3 shows that the probability of the surface interaction energy causing the unfaulting of an inclined loop at the <100> orientation is less than for an inclined loop at the <110> orientation but greater than for an edge-on loop at the <110> orientation. However, the measured defect yield

values in <110> and polycrystalline <100> orientated specimens of nickel, and also in <110> and <100> grains of the two nichrome alloys (see section 5.2.3.1), are the same within experimental error. This therefore also indicates that, within the accuracy of the experimental technique, loop loss at the surface does not cause a significant reduction in the defect yield.

4.6 Increase in Defect Yield and Defect Sizes due to Increasing Incident Ion Mass

The main difference between irradiating nickel with 80 keV self-ions or tungsten ions is illustrated by figure 4.9 which shows the difference between the rates of energy deposition into elastic collisions as a function of the distance of the ion from the foil surface. These energy deposition curves were computed by Matthews (1974, 1976) using the computer programme of Manning and Mueller (1974). In this programme, the mean range and range straggling of a heavy ion in an amorphous material is obtained using LSS theory (Lindhard, Scharff and Schiott 1963) and the energy straggling is estimated by relating it to this range straggling. This programme takes into account the energy lost to inelastic processes both in the creation of the primary knock-on atoms and also within the cascades that they generate. The importance of including inelastic processes can be understood from the fact that the total energy deposited into elastic collisions (E_D) was computed by Matthews as being only 51 keV for an 80 keV Ni^+ ion and 58 keV for an 80 keV W^+ ion. The computed values of the mean depths of the deposited energy $\langle X_D \rangle$ and the second moments of the energy distribution functions $\langle \Delta X_D^2 \rangle^{\frac{1}{2}}$ and $\langle Y_D^2 \rangle^{\frac{1}{2}}$ are listed in Table 4.2. $\langle \Delta X_D^2 \rangle^{\frac{1}{2}}$ and $\langle Y_D^2 \rangle^{\frac{1}{2}}$ are measures of the cascade radii parallel and perpendicular to the incident ion direction. The average projected ranges of the incident ions $\langle X \rangle$ and an estimate of the maximum energy density within a cascade θ_o, calculated from the results of Sigmund (1974), are also given in Table 4.2. From this table it can be seen

that the cascade region generated by a W^+ ion is both more compact and closer to the surface than that generated by a Ni^+ ion.

The difference in the energies deposited into elastic collisions by an 80 keV Ni^+ ion or W^+ ion results in a difference in the number N_D of Frenkel pairs generated by one of these incident ions. These numbers have been calculated using the standard formula of Norgett, Robinson and Torrens (1972) and are also listed in Table 4.2.

The increase in the sizes of the defect clusters generated by the W^+ ions is thought to be partly due to the increase in the number of Frenkel pairs generated by a W^+ ion. In addition, as a cascade becomes more compact, the ratio of the cascade size to the mean length of a focussed replacement sequence decreases. This is thought to result in less recombination occurring as the interstitials are believed to be more efficiently separated from the vacancies (Wilkens 1975). Thus, on average, a greater proportion of the vacancies generated by a W^+ ion are thought to survive recombination and this is considered to be a contributory factor to the observed increase in defect sizes. The fact that the cascade generated by a W^+ ion is more compact may also result in more of the vacancies that survive recombination being drawn into a collapsed loop (see section 5.6). Finally, the closer proximity of the surface may result in it being a more efficient sink for migrating interstitials that have escaped from the cascades, and thus there would be less probability of a migrating interstitial being attracted to a collapsed loop.

The increase in the sizes of the defect clusters will result in an increase in the defect yield. Reference to figure 4.4 shows that the size distribution curve for the defect clusters generated by the W^+ ions is moved towards larger defect sizes compared with that for the clusters generated by the Ni^+ ions, and thus an increased proportion of the defect clusters are large enough to produce visible diffraction

contrast. However, it is not possible to determine whether the increase in defect yield can be completely accounted for by the increase in defect sizes as the position and height of the peak of the curve for the defect clusters generated by the Ni^+ ions may be strongly influenced by the decrease in the visibility of defect clusters with diameters less than about 25Å.

A cascade generated by a W^+ ion is, on average, more compact and contains more vacancies than one generated by a Ni^+ ion. Thus the average vacancy supersaturation $(C_v/C_o)_{av}$, where C_v is the local radiation induced vacancy concentration and C_o is the thermal equilibrium vacancy concentration, is higher within a cascade generated by a W^+ ion. As considered in more detail in section 5.6, the probability of a Frank loop being nucleated may be strongly dependent on the statistical fluctuations within $(C_v/C_o)_{av}$ producing a critical vacancy supersaturation at some region within a cascade which is high enough to overcome the energy barrier for faulted loop nucleation. Once the Frank loop is nucleated, however, the subsequent climb of the loop by further vacancy aggregation may be a much less sensitive function of C_v/C_o and most of the vacancies within the core of the cascade region may be drawn into the loop nucleus. Thus an increase in $(C_v/C_o)_{av}$ may result in more Frank loops being nucleated, as well as increasing the sizes of the loops. This may therefore be a contributory factor to the observed increase in defect yield.

An additional factor which may affect the defect yield is the proximity with which the cascades are generated to the specimen surface. Wilkens (1975) considered that stress relaxation at the surface may prevent cascades from collapsing. In addition, the probability of loop loss at the surface is thought to increase the closer a loop is formed to the surface, although this effect is not thought to be significant in the present experiments (see section 4.5). Any effect of the surface

would, however, be to reduce the measured number of defect clusters and this effect would be greater in the case of the W^+ ion irradiations than in the case of the Ni^+ ion irradiations. Thus any effect of the surface on the defect yields would be contrary to the trend observed.

It should be mentioned that while irradiating with tungsten ions results in larger defect sizes which considerably facilitate defect geometry analyses and defect yield evaluations, a comparison of the results obtained in different materials using tungsten ions may not be fully representative of the comparison that would be obtained using self-ions. This point is particularly relevant to the results obtained from the tungsten ion irradiations of the alloys presented in the next chapter, and a fuller discussion of this point is given in section 5.7.

4.7 Decrease in Defect Yield for <100> Single Crystal Specimen

Reference to figure 4.6 shows that the decrease in defect yield for the <100> single crystal specimen compared with the <100> polycrystalline specimen is due to a reduction in the number of loops, formed per 10^2 incident ions, that have diameters between 20 → 45Å. Thus the decrease is not simply due to a difference in the visibility of the small (<25Å diameter) defect clusters.

One possibility is that the single crystal specimen was, for some reason, subjected to greater stresses than the polycrystalline specimen and this may have resulted in an increased proportion of the Frank loops unfaulting to perfect loops which then slipped out of the foil. However, as discussed in section 4.4.1, the probability of a Frank loop unfaulting would be expected to increase with increasing loop size, and thus the difference in the defect yields that this would cause would be due to a difference in the measured numbers of the larger defect clusters. Figure 4.6 shows that this is not the case.

Close inspection of the dark-field micrograph of figure 4.5(a) shows that several of the defect clusters have black-white contrast such

that $\underline{g}.\underline{1} < 0$. It was found that when imaged using $\underline{g}$ = <220>, approximately 20% of the defect clusters in the <100> single crystal specimen could be identified as having $\underline{g}.\underline{1} < 0$, whereas in the <100> polycrystalline specimen and the <110> single crystal specimen this number was less than 2%. The mean depth of deposited energy for an 80 keV W^+ ion incident on nickel has been calculated as 55Å (see section 4.6), and the first depth layer ($0.3\ \xi_g$) for 100 keV electrons in nickel and a $\underline{g}$ = <220> operating reflection corresponds to a distance of about 123Å (Hirsch et al 1965, p.496). These values would indicate that, in general, the defect clusters formed by 80 keV W^+ ion irradiation of nickel are confined to the first depth layer. The results in the <100> polycrystalline specimen and the <110> single crystal specimen are therefore consistent with the defect clusters being vacancy in nature. This would indicate that the increased proportion of clusters in the <100> single crystal specimen having $\underline{g}.\underline{1} < 0$ is due to an increased proportion of the vacancy clusters lying at depths greater than the first layer rather than interstitial clusters being present. In addition, if interstitial clusters and vacancy clusters were both present instead of just vacancy clusters, one would expect an increase in the defect yield as the number of vacancy clusters would be expected to remain the same.

Both the increase in the number of clusters with $\underline{g}.\underline{1} < 0$ and the observed decrease in the defect yield in the <100> single crystal specimen can be accounted for if the irradiating W^+ ions were incident within 1^o or 2^o of the <100> axis so that axial channelling occurred. Despite the fact that the specimens were irradiated approximately 7^o off axis specifically to prevent axial channelling, this is considered possible because the inclination of a given thinned area of a specimen disc to the incident ion-beam direction was not, in general, the same as the inclination of the thick outer edge of the disc.

Häussermann (1972c) has measured the energy loss of a channelled

gold ion in tungsten as being about 14 eV/Å, and he found that the probability of an ion being dechannelled increased exponentially with foil thickness. The areas of foil examined in the present experiments were typically 1000Å thick and one would therefore expect some of the channelled ions to be dechannelled within the foil. This would result in vacancy clusters being generated throughout the foil, as well as those generated by the non-channelled ions which would be confined to the first depth layer, and the dark-field images of those in the second and fourth depth layers from either surface would have $\underline{g}.\underline{1} < 0$ (see section 2.3). The reduction in defect yield would be due to a proportion of the channelled ions passing completely through the foil without being dechannelled.

The results of Häussermann (1972c) would indicate that the energy loss of a channelled ion in passing through a 1000Å thick foil is of the order of 15 keV. This energy loss must be compared with the present incident ion energy of 80 keV. Thus if a channelled W^+ ion were dechannelled within a Ni foil about 1000Å thick, it is thought that the energy available for elastic collisions would not be significantly reduced compared with a non-channelled ion. This would therefore explain why the distribution of defect sizes in the <100> single crystal specimen is approximately the same as in the <100> polycrystalline specimen in which channelling is not thought to have occurred.

In conclusion, it is considered that axial channelling of a significant proportion of the incident ions can satisfactorily explain the observed reduction in defect yield in the <100> single crystal specimen.

4.8 Conclusions

(1) Irradiation of nickel with 80 keV Ni^+ or W^+ ions produces small (<80Å diameter) vacancy-type dislocation loops which nucleate heterogeneously at cascades.

(2) The loops nucleate and grow on {111} planes as Frank-type loops.

A small number unfault to perfect loops and this is thought to be due to their interaction with the surface.

(3) The defect yield and the distribution of defect sizes are strongly dependent on the mass of the incident ion.

(4) The measured defect yield is not influenced significantly by loop loss at the surface.

Table 4.1 The defect yields, mean defect sizes and standard deviations of the defect sizes for the defect clusters generated by 80 keV Ni^+ ion or W^+ ion irradiations of nickel.

Table 4.2 Calculated cascade parameters for 80 keV nickel or tungsten ions incident on nickel.

Incident Ion	Target	Defect Yield	Defect Sizes	
			Mean Size	Standard Deviation
80 KeV Ni^+	Ni⟨110⟩ Single Crystal	0.44 ± 0.05	30.8 ± 0.8 Å	10.1 Å
80 KeV W^+	Ni⟨110⟩ Single Crystal	0.75 ± 0.08	38.3 ± 1.1 Å	11.7 Å
80 KeV W^+	Ni⟨100⟩ Single Crystal	0.59 ± 0.07	36.2 ± 1.0 Å	11.9 Å
80 KeV W^+	Ni⟨100⟩ Polycrystalline	0.81 ± 0.09	35.2 ± 1.0 Å	11.5 Å

TABLE 4.1.

ION	Ni	W
Atomic Mass	59	184
E_D(KeV)	51	58
Number of Vacancies in Cascade	513	577
$\langle X \rangle$ (Å)	193	111
$\langle X_D \rangle$ (Å)	114	55
$\langle \Delta X_D^2 \rangle^{1/2}$ (Å)	81	39
$\langle Y_D^2 \rangle^{1/2}$ (Å)	57	26
θ_o (eV per atom)	0.25	2.53

TABLE 4.2.

Table 4.3 Calculated values of E_o and T_o for the four possible Frank loops and the perfect loops that they would unfault to for both [110] and [100] foil normals. The E_o values of the Frank loops (marked with an asterisk) have been multiplied by $b^2_{a/3\langle 111\rangle}/b^2_{a/2\langle 110\rangle} = 2/3$ so that a comparison of the E_o values of the Frank and perfect loops gives a direct comparison of their surface interaction energies.

n	b	SURFACE NORMAL S = [110]			SURFACE NORMAL S = [100]		
		Loop Type	E_o	T_o	Loop Type	E_o	T_o
$[\bar{1}11]$	$a/3[\bar{1}11]$	Edge-On Frank Loop	3.69*	----	Inclined Frank Loop	10.31*	----
		Shear ↓			Shear ↓		
$[\bar{1}11]$	$a/2[01\bar{1}]$	Inclined Perfect Loop	6.26	3.13	Edge-On Perfect Loop	6.81	0
$[\bar{1}11]$	$a/2[\bar{1}01]$	Inclined Perfect Loop	6.26	3.13	Inclined Perfect Loop	16.19	11.44
$[\bar{1}11]$	$a/2[1\bar{1}0]$	Edge-On Perfect Loop	4.61	0	Inclined Perfect Loop	16.19	11.44
$[\bar{1}1\bar{1}]$	$a/3[\bar{1}1\bar{1}]$	Edge-On Frank Loop	3.69*	----	Inclined Frank Loop	10.31*	----
		Shear ↓			Shear ↓		
$[\bar{1}1\bar{1}]$	$a/2[01\bar{1}]$	Inclined Perfect Loop	6.26	3.13	Edge-On Perfect Loop	6.81	0
$[\bar{1}1\bar{1}]$	$a/2[\bar{1}01]$	Inclined Perfect Loop	6.26	3.13	Inclined Perfect Loop	16.19	11.44
$[\bar{1}1\bar{1}]$	$a/2[\bar{1}10]$	Edge-On Perfect Loop	4.61	0	Inclined Perfect Loop	16.19	11.44
$[\bar{1}\bar{1}1]$	$a/3[\bar{1}\bar{1}1]$	Inclined Frank Loop	18.10*	----	Inclined Frank Loop	10.31*	----
		Shear ↓			Shear ↓		
$[\bar{1}\bar{1}1]$	$a/2[01\bar{1}]$	Inclined Perfect Loop	16.74	8.37	Edge-On Perfect Loop	6.81	0
$[\bar{1}\bar{1}1]$	$a/2[\bar{1}01]$	Inclined Perfect Loop	16.74	8.37	Inclined Perfect Loop	16.19	11.44
$[\bar{1}\bar{1}1]$	$a/2[\bar{1}10]$	Flat-On Perfect Loop	29.79	29.79	Inclined Perfect Loop	16.19	11.44
$[111]$	$a/3[111]$	Inclined Frank Loop	18.10*	----	Inclined Frank Loop	10.31*	----
		Shear ↓			Shear ↓		
$[111]$	$a/2[011]$	Inclined Perfect Loop	16.74	8.37	Edge-On Perfect Loop	6.81	0
$[111]$	$a/2[101]$	Inclined Perfect Loop	16.74	8.37	Inclined Perfect Loop	16.19	11.44
$[111]$	$a/2[110]$	Flat-On Perfect Loop	29.79	29.79	Inclined Perfect Loop	16.19	11.44

TABLE 4.3.

Figure 4.1 Dark-field images of the same area of a Ni specimen, irradiated with 80 keV W^+ ions, obtained using the low order reflections about an [011] pole. An edge-on Frank loop (α), an inclined Frank loop (δ,β) and an inclined perfect loop (P) are marked. (Thompson's tetrahedron is orientated so that it shows the different <111> and <100> directions on these micrographs).

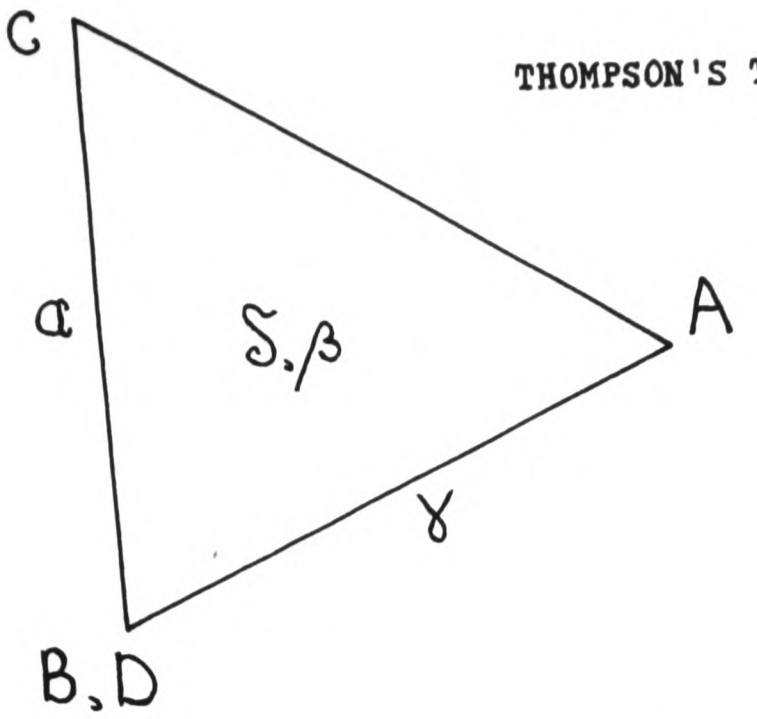

THOMPSON'S TETRAHEDRON

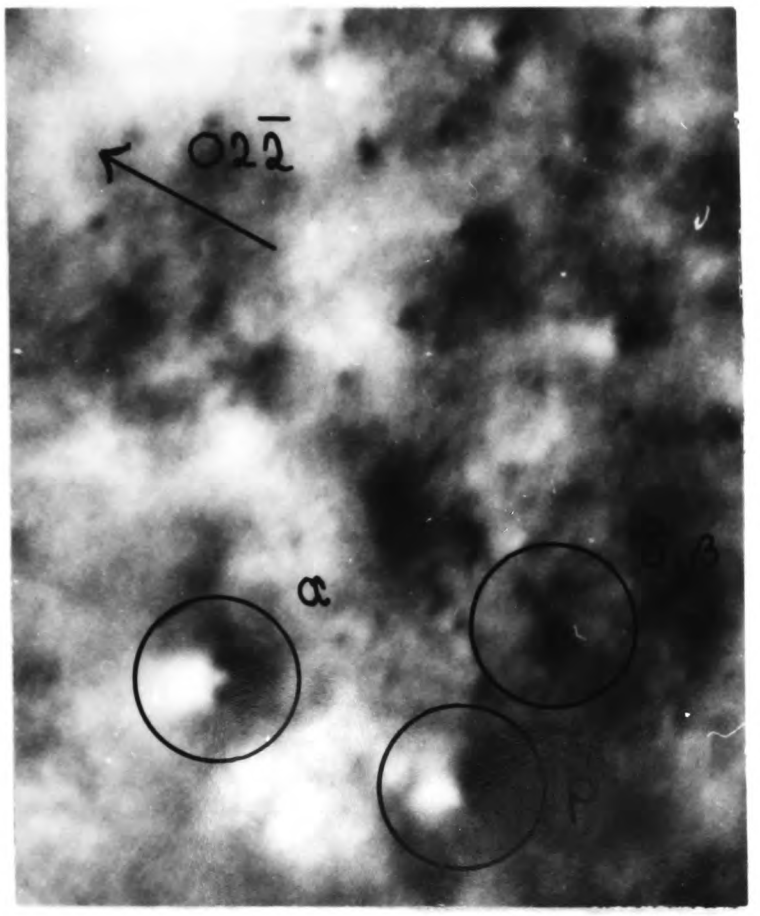

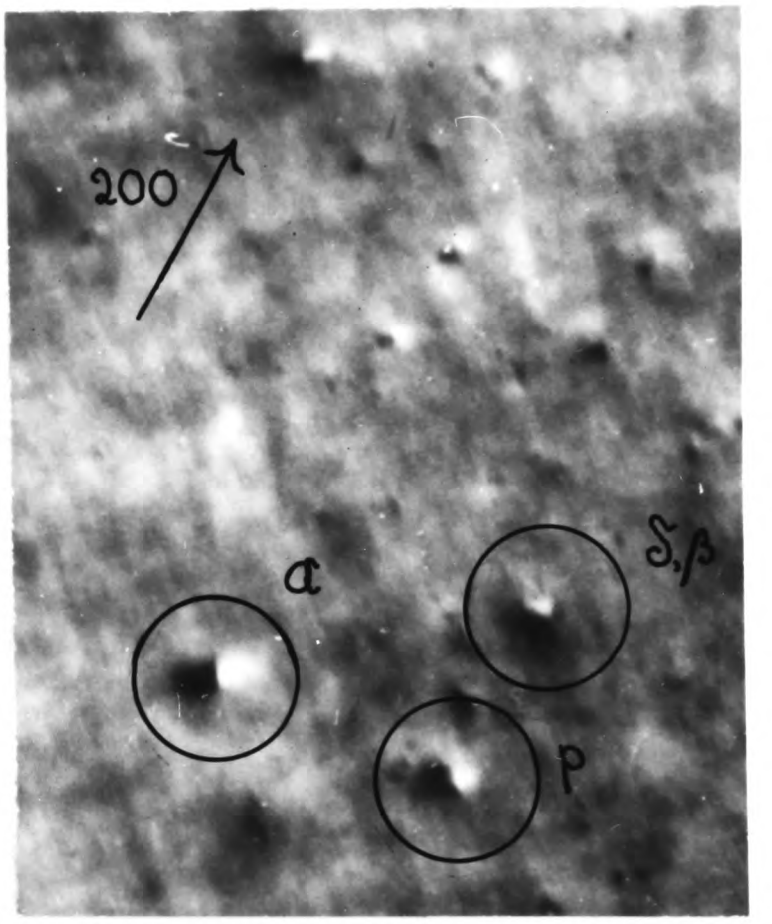

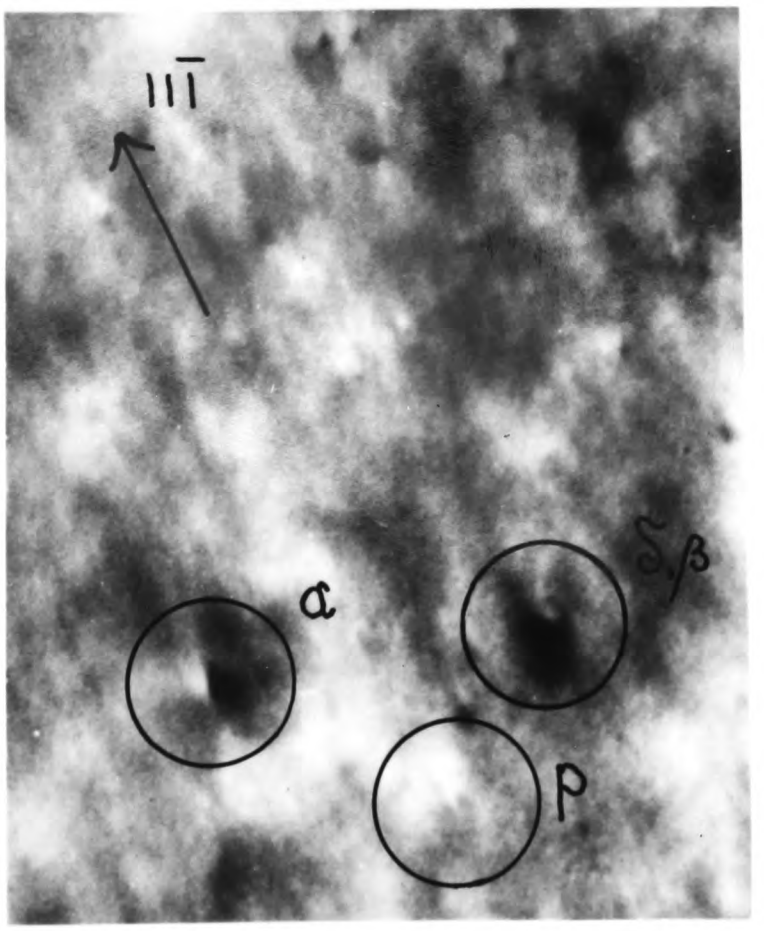

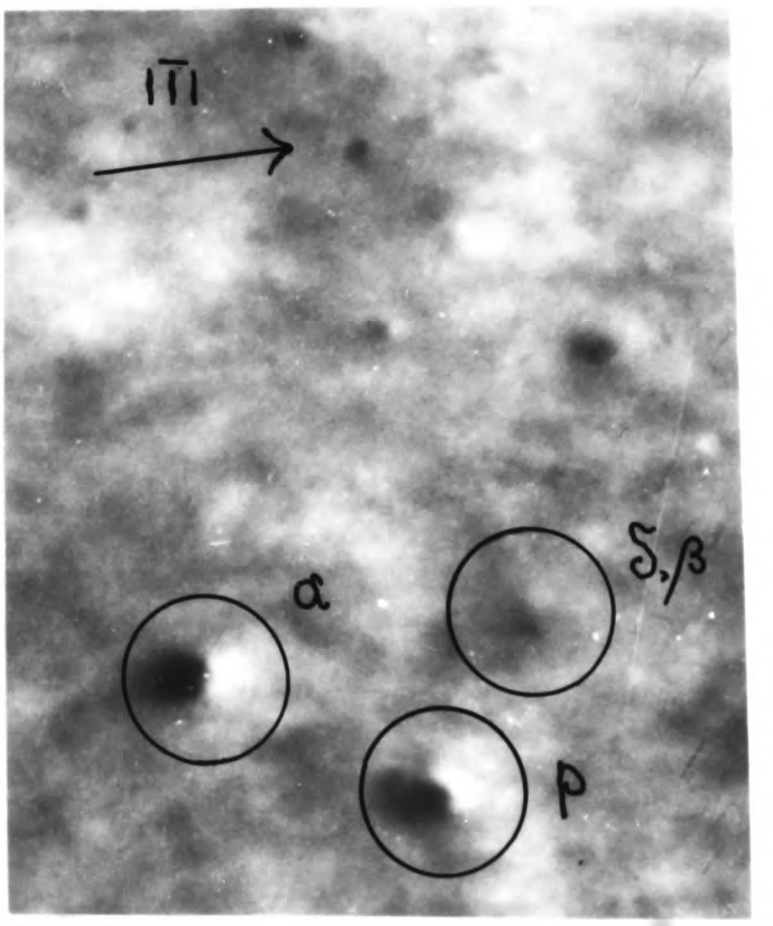

1,000 Å

Figure 4.2 A comparison of the $\underline{g}$ = <200> dark-field images of the defect clusters generated by 80 keV W^+ ion irradiation of a <110> nickel single crystal specimen with computer simulated images of Frank loops lying on the edge-on (α and γ) and inclined (δ and β) planes (Saldin and Whelan 1975). An inclined perfect loop (P) and a partially dissociated Frank loop (D) are circled as well.

COMPUTER SIMULATED FRANK LOOP IMAGES

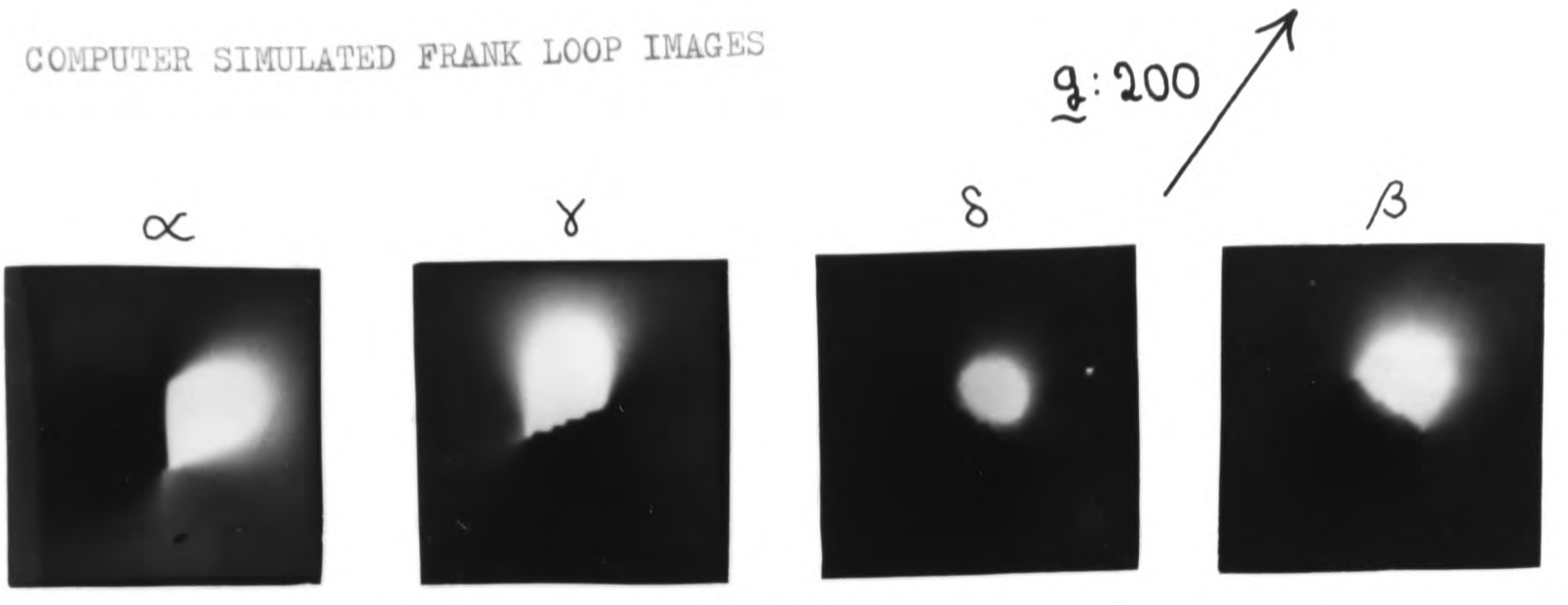

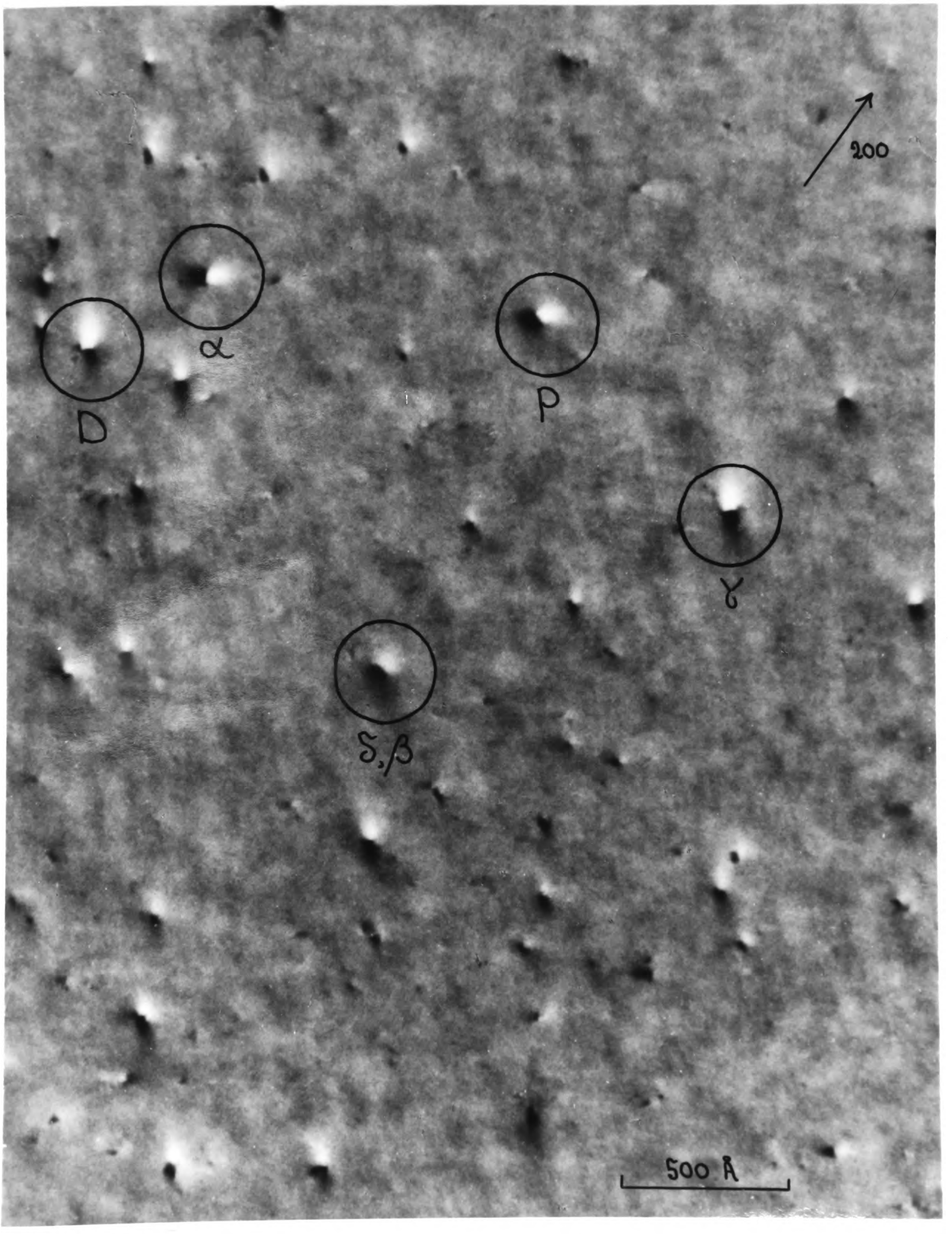

Figure 4.3 $\underline{g}$ = <002> dark-field images of the damage structures generated in <110> nickel single crystal specimens by irradiating with (A) 80 keV Ni^+ ions to a dose of 6×10^{11} ions cm^{-2} and (B) 80 keV W^+ ions to a dose of 2×10^{11} ions cm^{-2}. (The <111> and <100> directions on these micrographs are the same as those of the Thompson's tetrahedron that is drawn on this page).

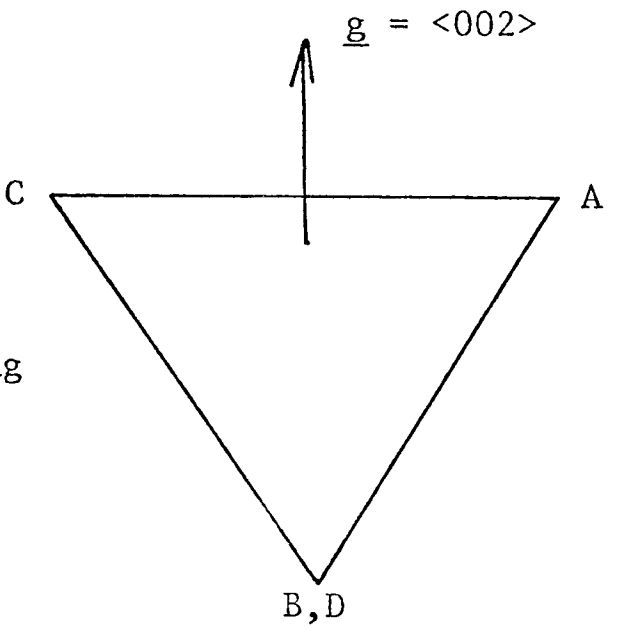

Thompson's tetrahedron viewed along a <110> direction.

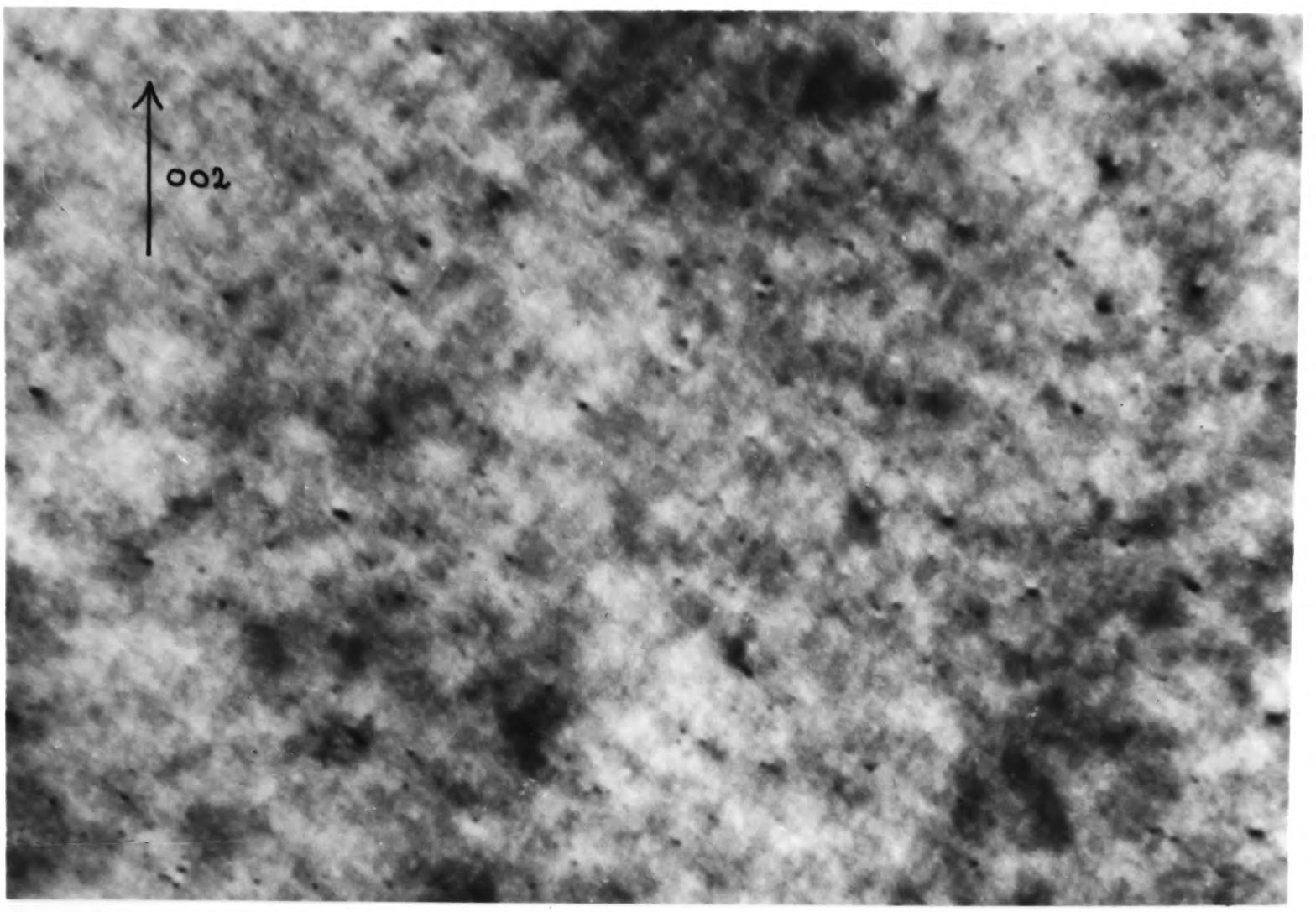

(A)

1000 Å

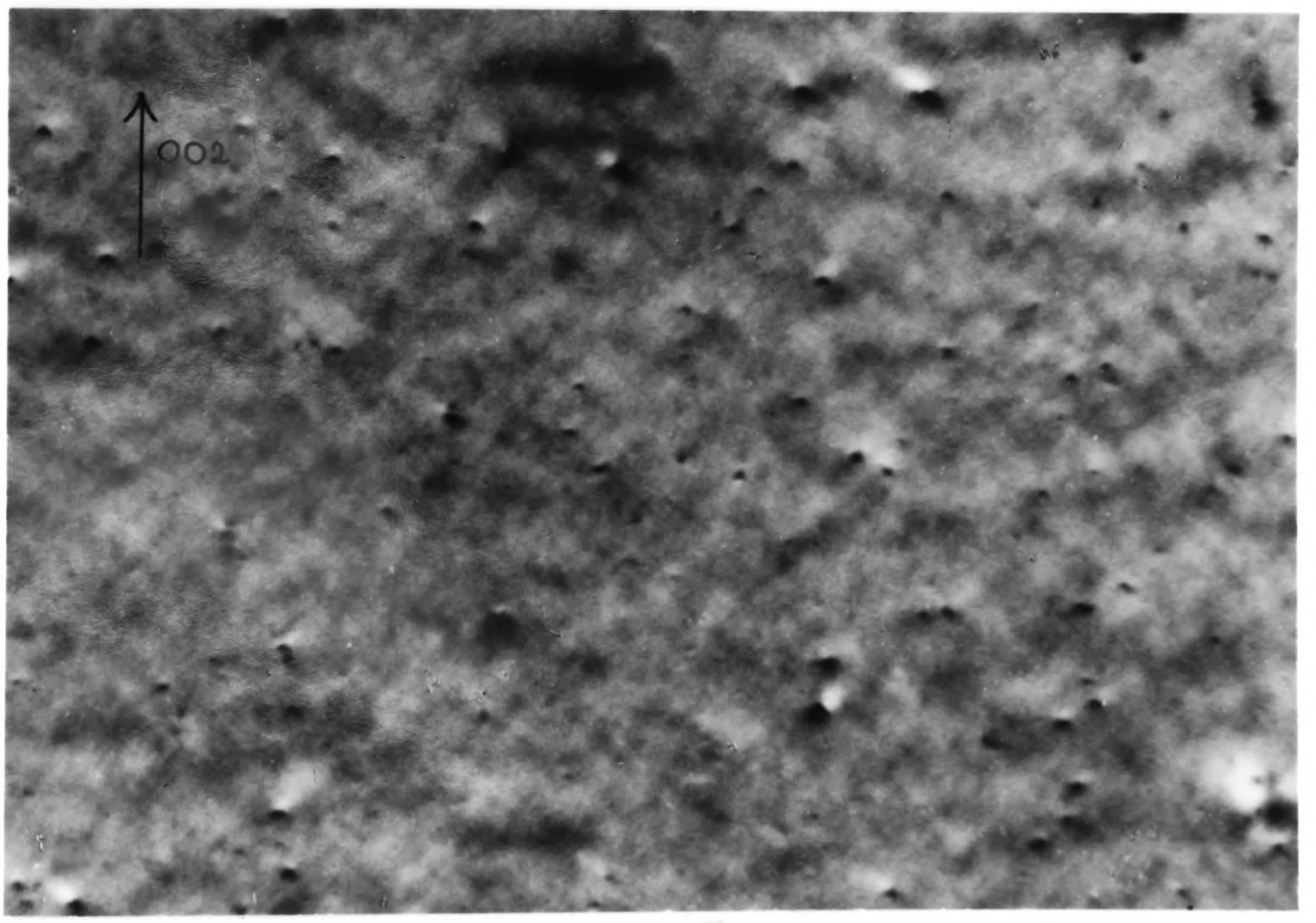

(B)

1000 Å

Figure 4.4 Size distributions, normalised to doses of 10^2 incident ions, of the damage structures illustrated by figure 4.3.

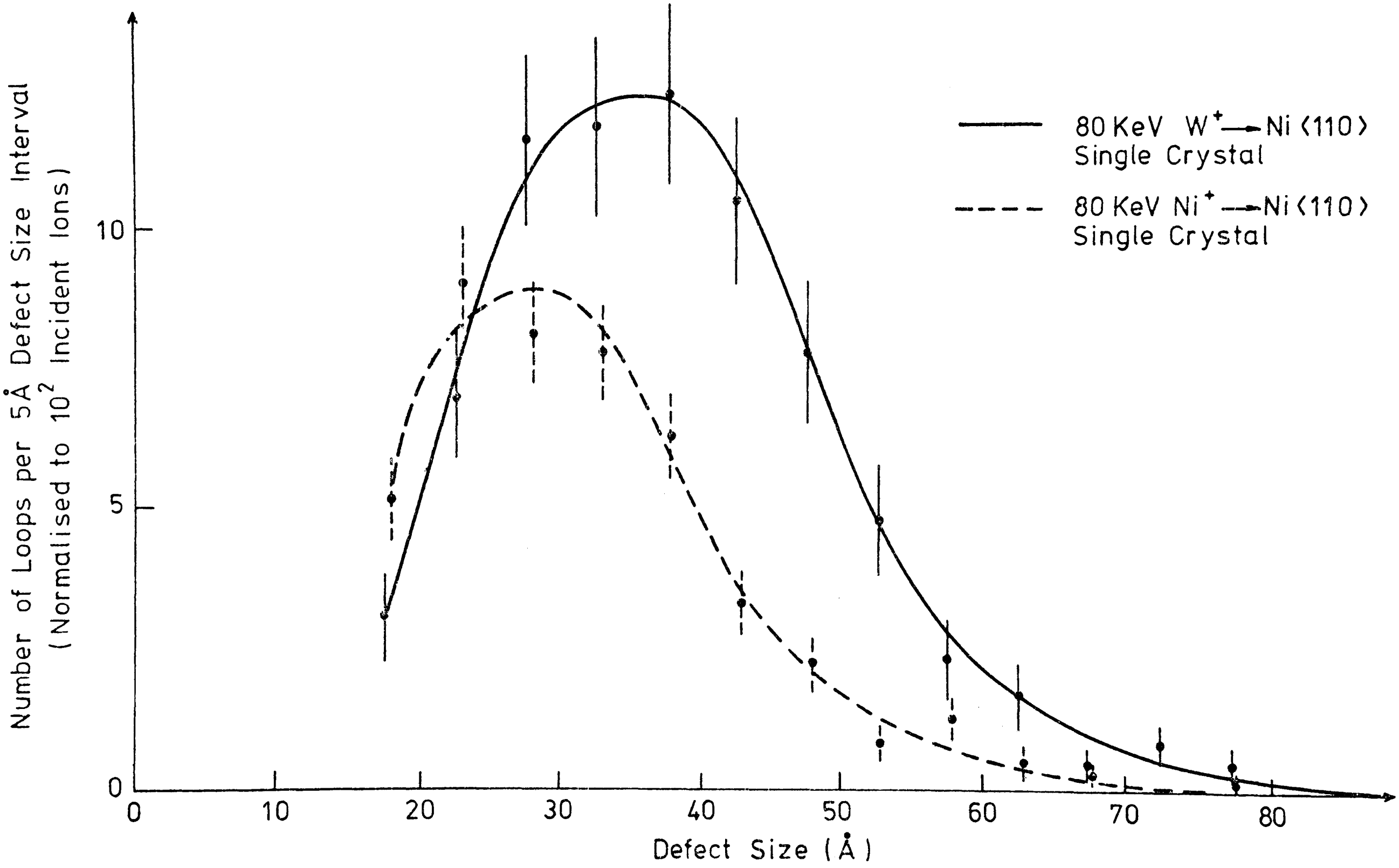
Number of Loops per 5Å Defect Size Interval
(Normalised to 10^2 Incident Ions)
0
5
10
0
10
20
30
40
50
60
70
80
Defect Size (Å)
80 KeV W+ → Ni ⟨110⟩
Single Crystal
80 KeV Ni+ → Ni ⟨110⟩
Single Crystal

Figure 4.5 $\underline{g}$ = <002> dark-field images of the damage structures generated by 80 keV W^+ ion irradiations of (A) a <100> nickel single crystal specimen and (B) a <100> grain of polycrystalline nickel to doses of 2×10^{11} ions cm^{-2}.

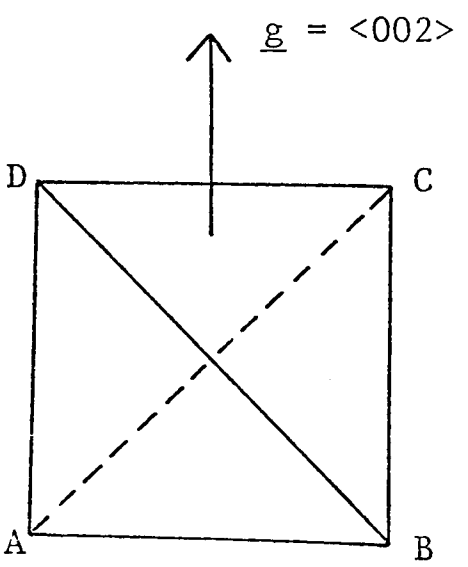

Thompson's tetrahedron viewed along a <100> direction.

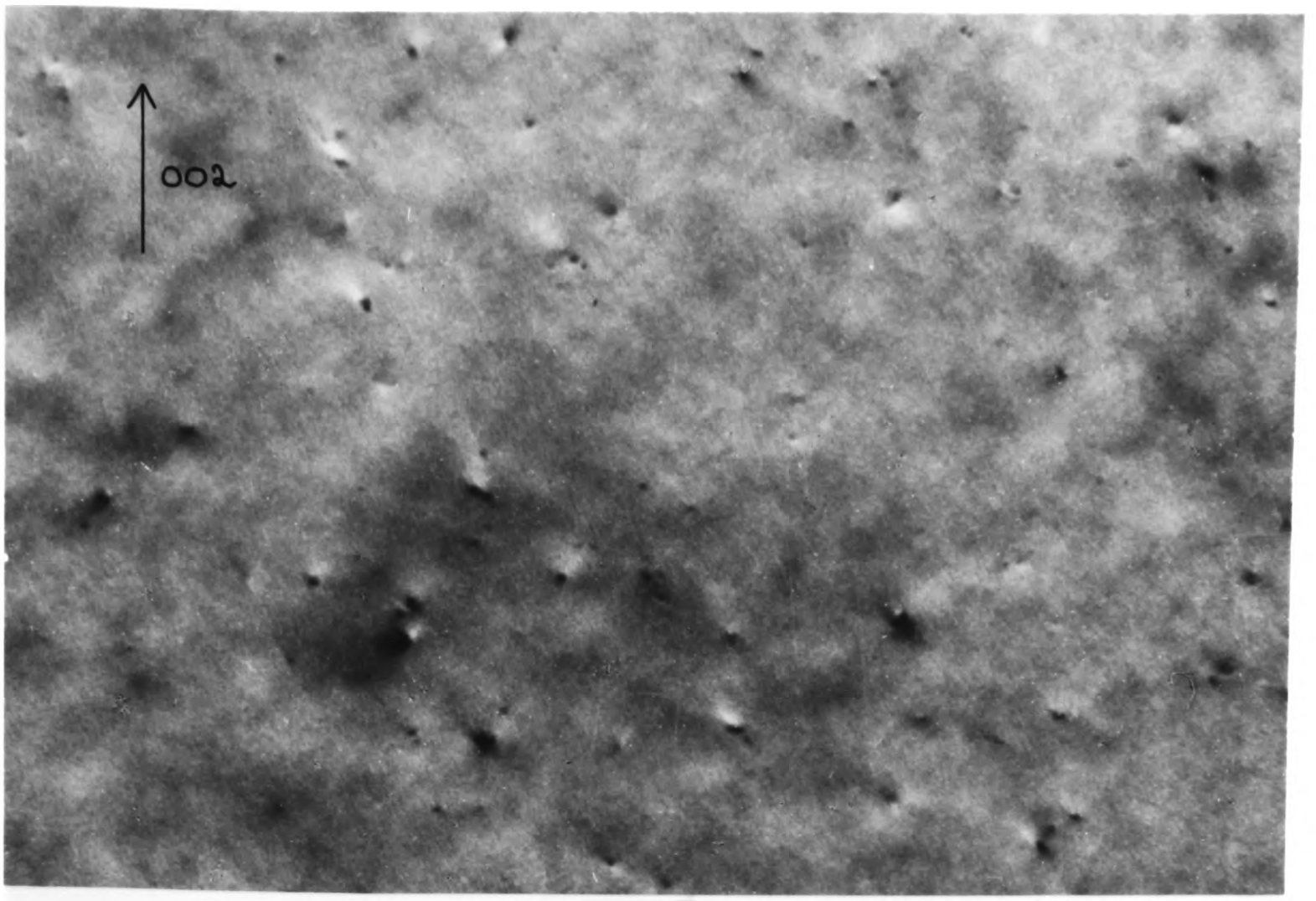

(A)

1000 Å

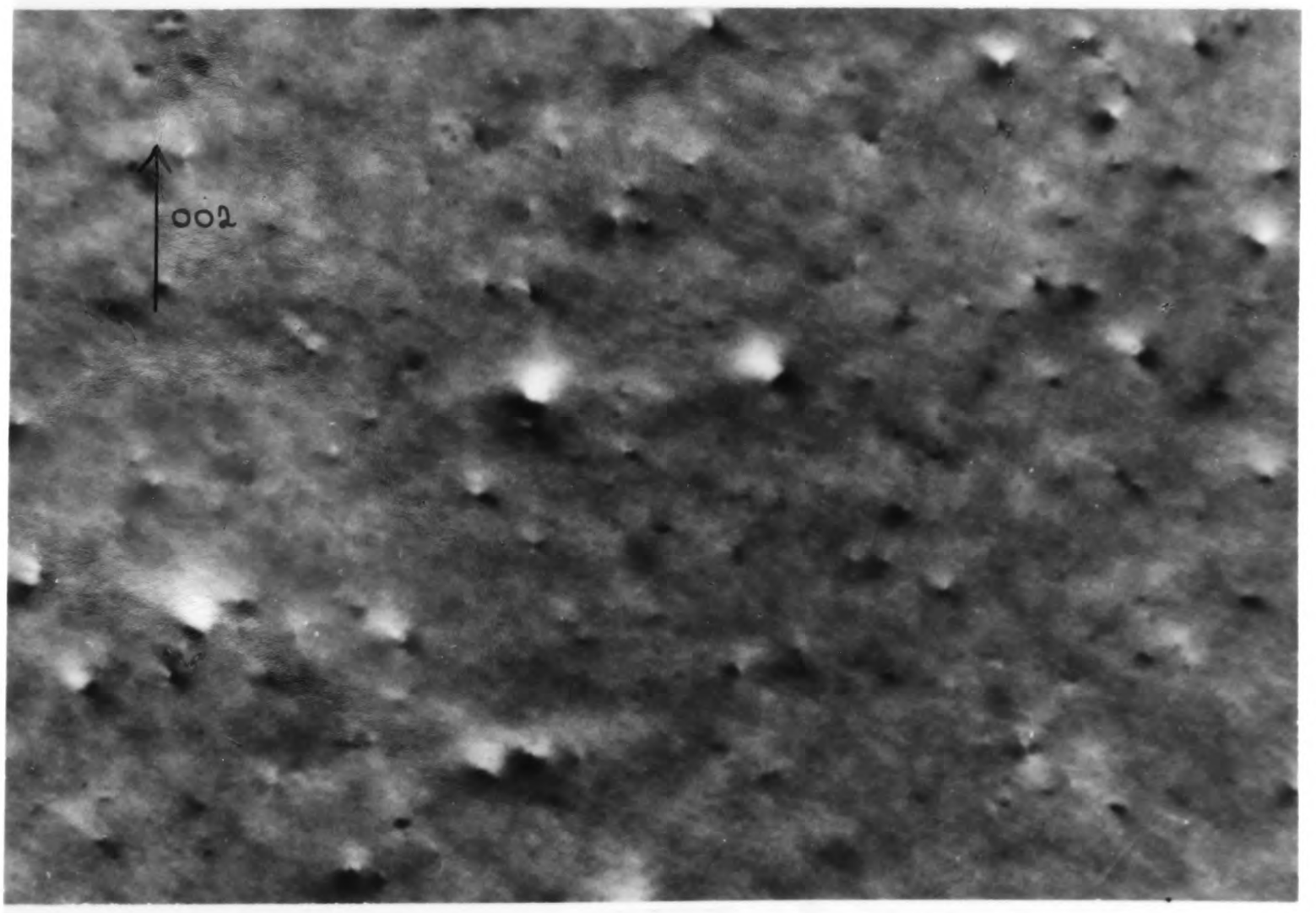

(B)

1000 Å

Figure 4.6 Size distributions, normalised to doses of 10^2 incident ions, of the damage structures illustrated by figure 4.5.

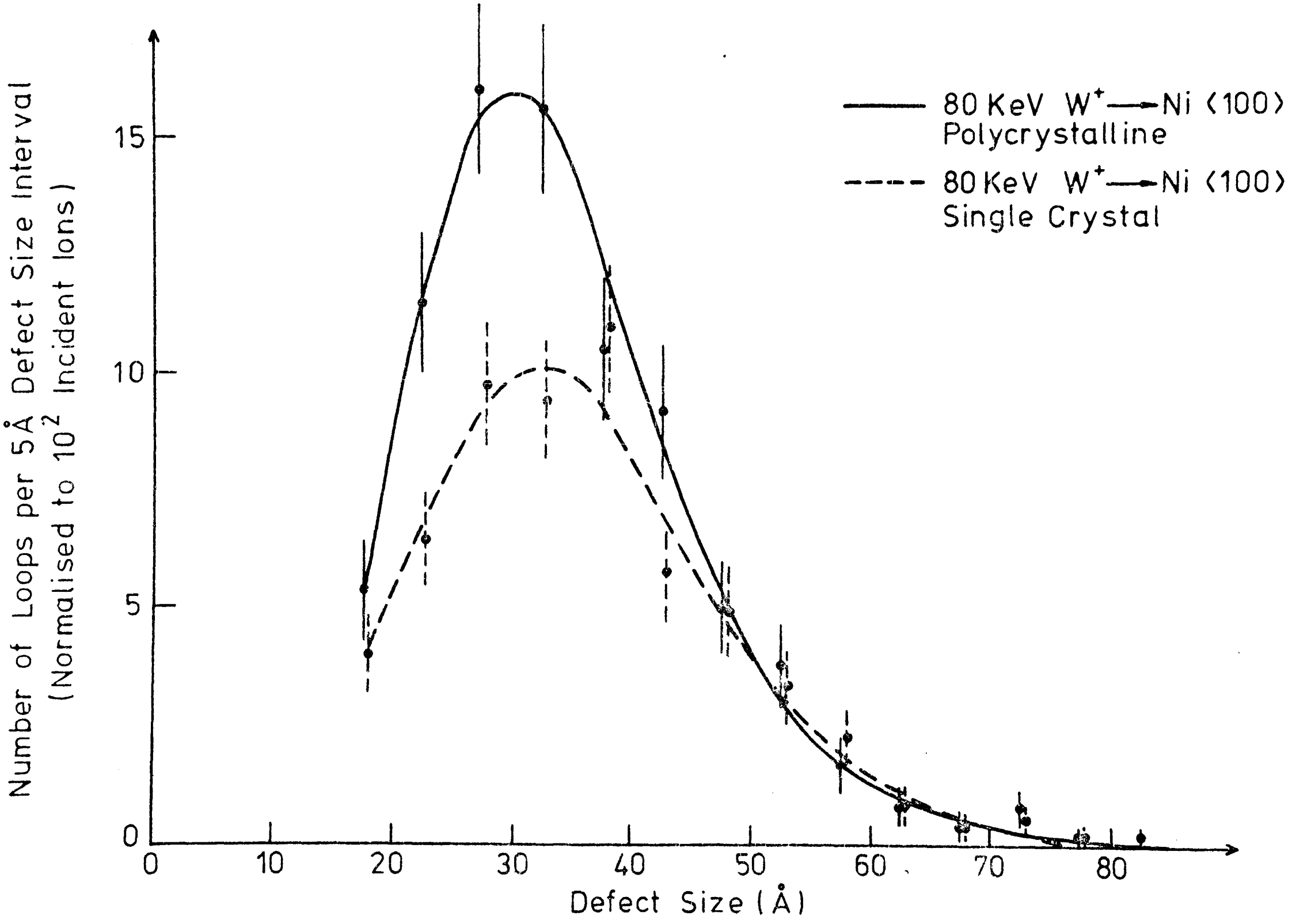
80 KeV W+ → Ni ⟨100⟩
Polycrystalline
80 KeV W+ → Ni ⟨100⟩
Single Crystal
Number of Loops per 5Å Defect Size Interval
(Normalised to 10^2 Incident Ions)
0
5
10
15
0
10
20
30
40
50
60
70
80
Defect Size (Å)

Figure 4.7 The theoretical energies of small Frank and perfect loops in nickel, including the reduction in energy due to loop interaction with the surface for 'inclined' Frank loops and 'flat-on' perfect loops at the <110> orientation for loops whose centres lie at a distance of two loop radii from the foil surface.

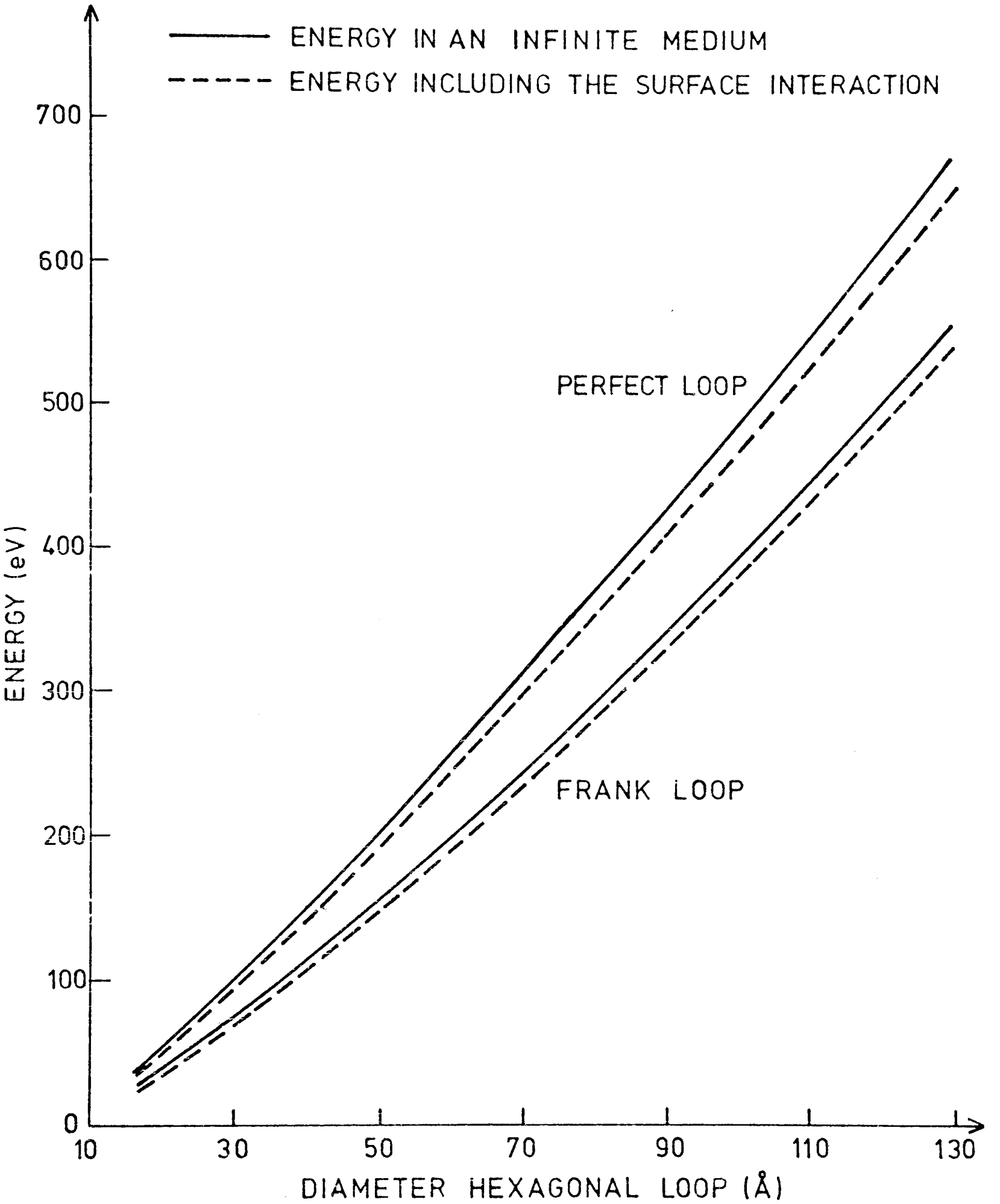
ENERGY IN AN INFINITE MEDIUM
ENERGY INCLUDING THE SURFACE INTERACTION
PERFECT LOOP
FRANK LOOP
ENERGY (eV)
700
600
500
400
300
200
100
0
10
30
50
70
90
110
130
DIAMETER HEXAGONAL LOOP (Å)

Figure 4.8 Schematic diagram showing the orientation of the four {111} planes in relation to the disordered cascade region generated by an ion incident normal to a (110) foil.

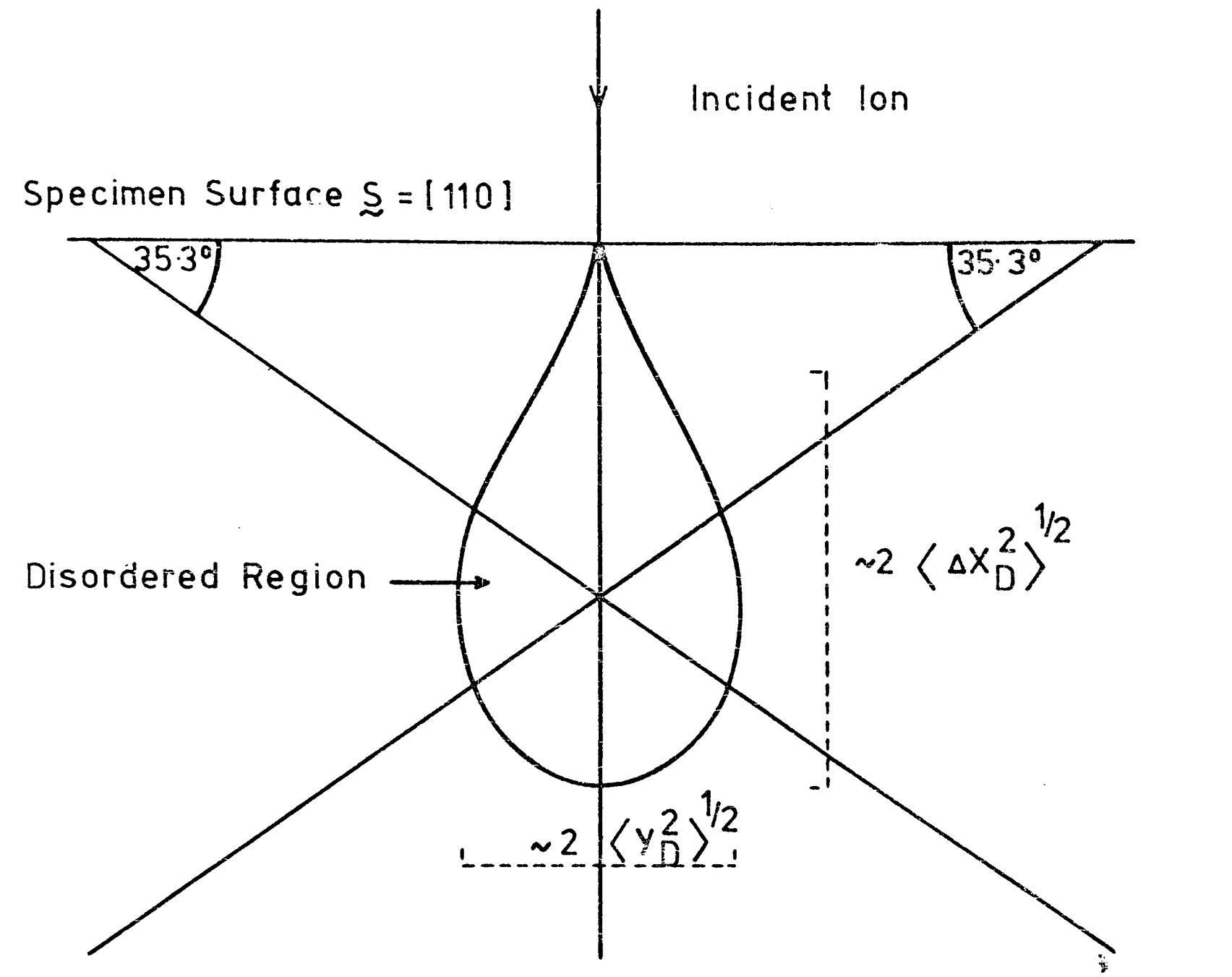
Incident Ion
Specimen Surface S = [110]
35·3°
35·3°
Disordered Region
~2 ⟨ΔX_D^2⟩^1/2
~2 ⟨y_D^2⟩^1/2
(111) Inclined Plane
(1$\bar{1}$1) or (1$\bar{1}\bar{1}$) Edge-On Planes
(11$\bar{1}$) Inclined Plane

Figure 4.9 The depth distributions of the energies deposited into elastic collisions for 80 keV tungsten and nickel ions incident on nickel (Matthews 1976). The values of the mean depths of deposited energy $\langle X_D \rangle$ and their RMS standard deviations $\langle \Delta X_D^2 \rangle^{\frac{1}{2}}$ that are obtained from these graphs are given in Table 4.2.

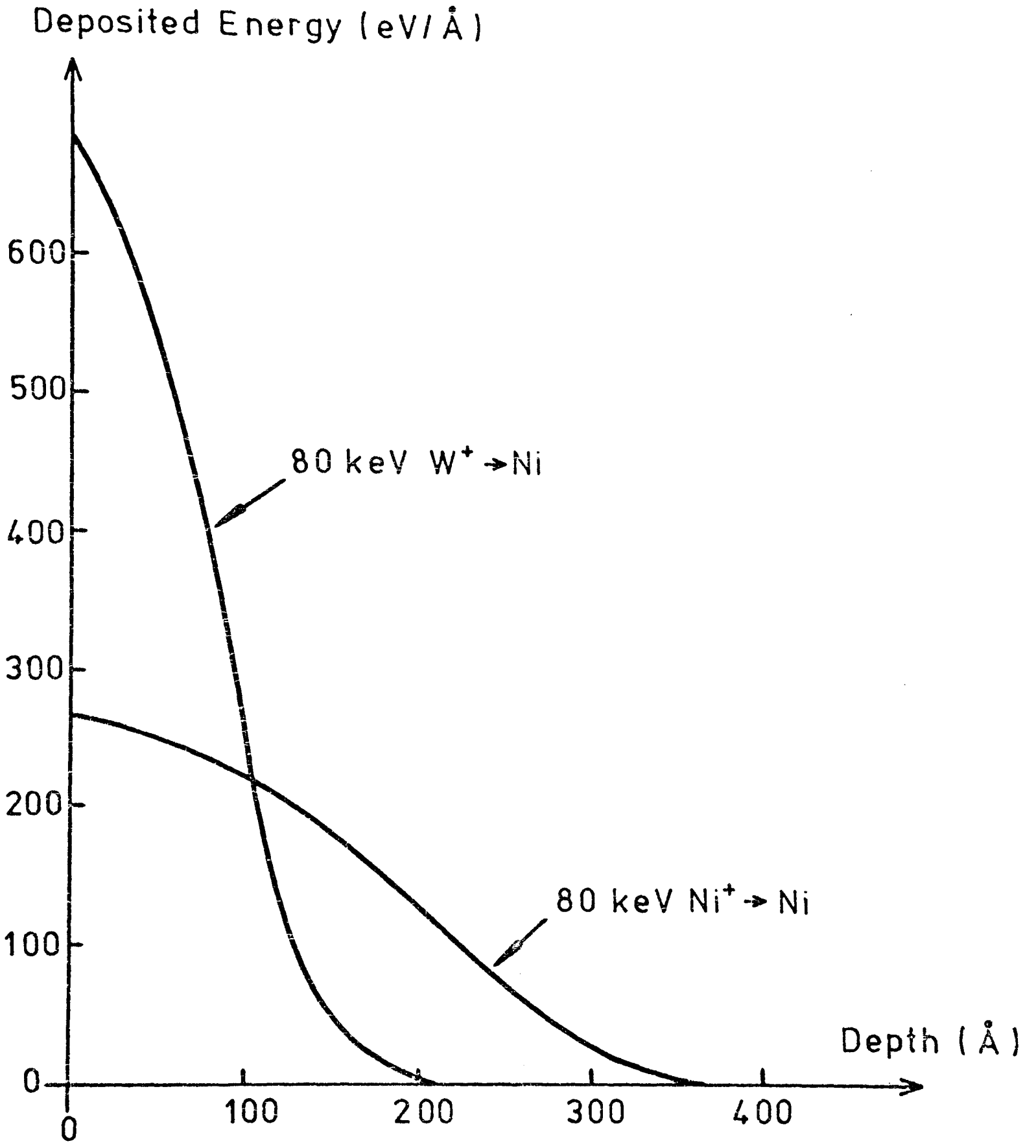
Deposited Energy (eV/Å)
600
500
400
300
200
100
0
80 keV W+ → Ni
80 keV Ni+ → Ni
Depth (Å)
0
100
200
300
400

CHAPTER 5

The Damage Structures Generated in the Alloys by Nickel and Tungsten Heavy-Ion Bombardment at Room Temperature

5.1 Introduction

Before the present work was carried out, no quantitative information existed as to possible changes in the damage structures produced by the collapse of displacement cascades with changes in composition of technologically important materials. As discussed in section 1.2, the void swelling rate at fast reactor operating temperatures is influenced by the steady-state vacancy cluster concentration, and this concentration is thought to depend, in part, on the numbers, the sizes and the geometries of the vacancy clusters that are formed by the collapse of displacement cascades. An investigation has therefore been carried out to compare the damage structures generated at room temperature by low-dose, heavy-ion irradiations of Ni, Ni/Cr8%, Ni/Cr17%, Fe/Ni10%/Cr17% and a 321 stainless steel. The reasons for choosing these particular materials are discussed in section 1.6.2.

To facilitate the analysis of the damage structures, the initial irradiations were carried out using 80 keV W^+ ions, to doses of 2×10^{11} ions cm^{-2}. Damage was observed in the form of small dislocation loops in all the materials. Because this damage might have been less representative of the damage generated by fast neutrons in reactor structural components than the damage that would be generated by self-ions, the irradiations were repeated using 80 keV Ni^+ ions to doses of 6×10^{11} ions cm^{-2}. Damage was again observed in the form of small dislocation loops, but the smaller size of the clusters made the analyses of the damage structures, and the interpretation of the changes in these structures, more difficult. The results of the determinations of the nature, geometries, numbers and sizes of the defect clusters generated by the above irradiations are presented in this chapter, along with a comparison between the damage structures generated by the W^+ ions in two Ni/Cr17% alloys with different oxygen impurity contents. A discussion of these results is given in terms of the influence of the alloying elements or impurities on the generation of the

damage structures. A discussion of the implication of these results to the void swelling in the different materials is deferred until Chapter 6, in which the variation of the steady-state vacancy cluster concentration with temperature is considered.

The purity of the materials used in these irradiations, the composition of the stainless steel, the irradiation procedure, and the methods used to determine the numbers, sizes, geometries and nature of the defect clusters are discussed in detail in Chapter 3.

5.2 Results

5.2.1 Defect Nature

An analysis of the nature of the defect clusters generated by the W^+ ions, and the larger analysable defect clusters generated by the Ni^+ ions, was consistent with the clusters in all the materials being vacancy in nature. This result in the stainless steel is in agreement with a previous result obtained in Cr^+ ion bombarded type 316 stainless steel (English et al 1975).

5.2.2 Defect Geometry

The image contrast from defect clusters smaller than about 35 Å in diameter was not, in general, sufficiently well defined to allow an unambiguous determination of the defect geometries. Thus it was only possible to analyse a very small number ($\sim$ 10%) of the visible defect clusters generated by the Ni^+ ion irradiations. However, all the clusters that could be unambiguously analysed, in all four alloys, were found to be Frank dislocation loops.

The W^+ ion irradiations increased the mean size of the defect clusters with the result that approximately 30% of the defect clusters in each material could be analysed. This analysis was carried out by comparing the images of the defect clusters obtained using the low order reflections about a <110> pole (see section 3.6). Unless otherwise stated, the following quantitative results on defect geometries only apply to those

defect clusters that could be analysed, and not to the defect cluster population as a whole.

The defect geometries in the Ni/Cr8% and Ni/Cr17% alloys were very similar to the defect geometries in pure nickel (see section 4.2.2). The majority of the defect clusters in the nichrome alloys were found to be Frank-type dislocation loops, although a small number ($\sim$ 5%) of perfect loops were also identified. In addition to inclined perfect loops, which were present as in nickel, a very small number (< 1%) of edge-on perfect loops was identified. Such an edge-on perfect loop, showing characteristic $\underline{g}.\underline{b} = 0$ 'butterfly contrast' when imaged using $\underline{g}$ = [200], is clearly visible in figure 5.1 which shows the same area of a Ni/Cr8% specimen imaged using the four low order reflections about a <110> pole. Possible reasons for the formation of edge-on and inclined perfect loops in the nichrome alloys are considered in section 5.3.

It can be seen qualitatively from the $\underline{g}$ = [200] micrograph of figure 5.1 that the majority of the larger images are those formed by Frank loops lying on the edge-on (α and γ) planes. It was found that in both nichrome alloys, approximately 70% of the images of Frank loops that were greater than 50 Å in diameter were formed by loops whose habit planes were on these edge-on planes. Possible reasons for this distribution, which was also observed in Ni, are discussed in section 4.4.

Some of the larger Frank loops in the nichrome alloys had partially dissociated onto {111} planes other than the loop habit plane. The proportion of Frank loops that were identified as being partially dissociated increased with increasing loop size, and while only 10% of the total number of clusters that were analysed appeared to have partially dissociated, this proportion increased to more than 30% for Frank loops with diameters greater than 60 Å. A similar result was found in Ni (see section 4.2.2). The possibility that it may be energetically favourable for small (< 80 Å diameter) Frank loops to partially dissociate in F.C.C.

materials with relatively high stacking fault energies, and a possible reason why only the larger loops were identified as being dissociated, are discussed in section 5.4.

The defect geometries in the Fe/Ni/Cr alloy and the stainless steel were similar. The analysis indicated that only Frank-type dislocation loops were present. No perfect loops were identified in either material. Possible reasons why perfect loops were identified in the nickel and the nichrome alloys and not in the ternary alloy and the stainless steel are considered in section 5.3. More than 60% of the defect clusters with diameters greater than 50 Å were analysed as being partially dissociated in both the ternary alloy and the stainless steel. This proportion is significantly larger, and extends to smaller defect sizes, than the proportions in nickel and the nichrome alloys. A possible reason for this difference is considered in section 5.4. Of the large (> 50 Å diameter) loops that had apparently not dissociated, approximately equal numbers lay on the edge-on and inclined planes.

5.2.3 Measured Defect Yields and Defect Size Distributions

5.2.3.1 W^+ Ion Irradiations

The damage structures generated in grains of polycrystalline Ni, Ni/Cr8% and Ni/Cr17% by irradiating with 80 keV W^+ ions to doses of 2×10^{11} ions cm^{-2} are shown in figure 5.2(a) for grains lying within 10^o of a <110> orientation, and in figure 5.2(b) for grains lying within 10^o of a <100> orientation. A comparison of these micrographs shows that the numbers and sizes of the defect clusters are approximately independent of orientation and are approximately the same in each material. The measured size distributions of the defect clusters in <110> grains of the three materials are compared in figure 5.3. These distributions, which were taken over a sample of approximately 400 defect clusters in each material , are normalised to a dose of 10^2 incident ions such that the area under a curve is proportional to the defect yield. The error bars

on the curves represent the statistical error on the number of defects measured as lying within a given size interval (see section 3.8.1). The measured values of the defect yields for both the <110> and <100> orientations, and the mean defect sizes and cascade efficiencies for the <110> orientations, are listed in Table 5.1. The calculation of these parameters and the errors quoted is described in sections 3.7 and 3.8. Reference to figure 5.3 and Table 5.1 shows that the distribution of the sizes of defects in {110} grains, and the measured defect yields, in both {110} and {100}grains, are the same within experimental error in all three materials.

Figure 5.4 shows the damage structures generated in {110} grains of Ni, Fe/Ni10%/Cr17% and 321 stainless steel by irradiating with 80 keV W^+ ions to doses of 2×10^{11} ions cm^{-2}. The measured size distributions of the defect clusters in these three materials, normalised to doses of 10^2 incident ions such that the areas under the curves are proportional to the defect yields, are compared in figure 5.5. The values of the measured defect yields, mean defect sizes and cascade efficiencies are listed in Table 5.1. It can be seen from figure 5.5 and Table 5.1 that while the mean defect sizes in all three materials are the same within experimental error, the measured defect yields show a decrease both between the Ni and the ternary alloy, and between the ternary alloy and the stainless steel. The similarity between the defect sizes is further illustrated by figure 5.6 which shows clearly that, within the experimental error, the distributions of the sizes of the visible defect clusters are the same in all three materials. The way in which alloying additions and minor impurities may influence the generation and collapse of displacement cascades, and possible reasons for the observed decrease in defect yields in the ternary alloy and the stainless steel are considered in detail in section 5.5.

The damage structures generated in <110> grains of the Ni/Cr17% alloy, which contained 1,070 ppm O($^{w}/_{w}$), and a second Ni/Cr17% alloy (Cr/Ni83%),

which contained 510 ppm O($^{w}/_{w}$), by irradiating with 80 keV W^{+} ions to doses of 2×10^{11} ions cm^{-2} are compared in figure 5.7. The measured size distributions of the defect clusters, normalised to doses of 10^{2} incident ions, are compared in figure 5.8. The values of the measured defect yields, mean defect sizes and cascade efficiencies are listed in Table 5.1. Reference to figure 5.8 and Table 5.1 shows that, within experimental error, the numbers and sizes of the defect clusters in these two Ni/Cr17% alloys are the same. All the alloys used in the present experiments contained significant amounts (190 → 1,070 ppm ($^{w}/_{w}$)) of oxygen, and the affect that this interstitial impurity might have had on the generation and collapse of the displacement cascades is considered in section 5.5.

5.2.3.2 Ni^{+} Ion Irradiations

Figure 5.9 shows the damage structures generated in <110> grains of Ni, Ni/Cr8%, Ni/Cr17% and 321 stainless steel by irradiating with 80 keV Ni^{+} ions to doses of 6×10^{11} ions cm^{-2}. The defect clusters in the stainless steel were only clearly visible in the very thin areas of a specimen by the edge of a hole. The measured size distributions of the defect clusters in the four materials, normalised to doses of 10^{2} incident ions, are compared in figure 5.10. The values of the measured defect yields, mean defect sizes and cascade efficiencies are listed in Table 5.2. Experimental difficulties in electropolishing specimens of the Fe/Ni/Cr alloy so that they were suitable for a T.E.M. study of small defect clusters prevented any results being obtained in this alloy in the case of the Ni^{+} ion irradiations.

Reference to Table 5.2 shows that while the mean defect sizes are approximately the same in all four specimens, the measured defect yields show an apparent systematic decrease in going from Ni through to the stainless steel. However, these defect yield values and the errors quoted take no account of a possible difference in the visibility of small

Material	Nature	Geometry	Defect Yield and Defect Sizes
		W^+ Ion Irradiations	
Ni	Vacancy (V)	Mostly Frank loops, some (<5%) inclined perfect loops.	Yield and defect sizes independent, within exp. error, of foil orientation for grains near {110} and {100}.
Ni/Cr8%	V	As for nickel plus some (<1%) edge-on perfect loops.	Yield and sizes similar to Ni.
Ni/Cr17%	V	As for Ni/Cr8%	Yield and sizes similar to Ni, unaffected by reducing oxygen content from 1070→510 ppm ($^W/_w$).
Fe/Ni10%/Cr17%	V	Only Frank loops. Number of partially dissociated loops and average degree of dissociation larger than in nickel.	Yield significantly reduced, cf. Ni and Ni/Cr alloys, but average size and distribution of sizes the same within exp. error.
321 St.St.	V	As for Fe/Ni10%/Cr17%	Yield further reduced cf. Fe/Ni10%/Cr17%, but average size and distribution of sizes still the same as in Ni within exp. error.
		Ni^+ Ion Irradiations	
Ni	V	Only Frank loops identified.	Yield considerably lower, and average size slightly lower, than in W^+ ion irradiated Ni.
Ni/Cr8%	V	As for nickel	Yield lower than in Ni^+ ion irradiated Ni.
Ni/Cr17%	V	As for nickel	Yield similar to Ni/Cr8%
321 St. St.	V	As for nickel	Yield considerably lower than in Ni or the Ni/Cr alloys.

(< 25 Å diameter) defect clusters in the different materials (see section 3.7.1), and figure 5.10 shows that a large part of the differences in the present defect yield values can be attributed to just such a difference. In addition, this figure shows that the positions of the peaks of the size distribution curves may be influenced by the decrease in the visibility of defect clusters with diameters less than about 25 Å. Care must therefore be taken in interpreting the data obtained from these Ni^+ ion irradiations.

Under the conditions chosen in the present experiments for measuring defect yields and defect sizes, all the defect clusters with diameters greater than about 25Å are thought to produce visible diffraction contrast (see section 2.6). Thus it is thought that a better comparison of the present Ni^+ ion irradiation results can be obtained by considering only those defect clusters with diameters greater than 25Å. Reference to figure 5.10 then shows that the defect yield in the Ni, which in this case is proportional to the area under the curve for defect sizes greater than 25Å, is greater than those in the two nichrome alloys, which are the same within experimental error, and these in turn are greater than that in the stainless steel. The values of the defect yields for defect clusters greater than 25Å in diameter are included in Table 5.2. The present reduction in defect yield between the Ni and the nichrome alloys was not observed in the case of the W^+ ion irradiations. A possible reason for this difference, and additional ways in which the damage structures generated by the heavier W^+ ions may not be fully representative of those generated by Ni^+ ions are considered in sections 5.5.4 and 5.7 respectively.

5.2.4 Summary of Results

The most important points of the experimental results presented in this chapter are summarised in the table on the opposite page.

5.3 Perfect Loop Formation

5.3.1 'Inclined' Perfect Loops

The formation of perfect loops in Ni is considered in sections 4.3 and 4.4.1. The calculations of section 4.4.1 indicate that, for a <110> orientation, inclined perfect loops may form in Ni as a result of the surface interaction energy causing the unfaulting of large ($\gtrsim$ 70 Å diameter) 'edge-on' Frank loops that lie within about 50 Å of the surface. As well as depending on the size of a Frank loop and its proximity to the surface, the probability that unfaulting will occur in a given material is thought to depend on the stacking fault energy of that material, as this determines mainly the energy difference between a Frank loop and the perfect loop it would unfault to when both are in an infinite medium. This energy difference increases, and the probability of unfaulting would therefore be expected to decrease, with decreasing stacking fault energy.

The stacking fault energy of Ni has been determined recently from weak-beam studies of dissociated edge-dislocations and faulted dipoles as being 125 ergs/cm^2 (Carter and Holmes 1977). The stacking fault energies of nichrome alloys have not so far been accurately determined, although comparative values of $\gamma/\mu b$, where μ is the shear modulus and b is the magnitude of the Burgers vector, have been determined from rolling texture data (Beeston and France 1968). These results indicate that $\gamma/\mu b$ (alloy)/ $\gamma/\mu b$ (nickel) is approximately equal to 0.85 for Ni/Cr8% and 0.67 for Ni/Cr17%. The stacking fault energy of an austenitic stainless steel containing Ni10%, Cr19% and of similar minor alloying content to the steel used in the present experiments was estimated by Whelan (1959) as being 13 ergs/cm^2, although Gallagher (1970) states that this value should be multiplied by a factor of 2 to take account of improvements in the theory relating node parameters to stacking fault energies. In addition, Gallagher has shown that the stacking fault energies of

commercial Fe/Ni/Cr18% alloys have an approximately linear dependence on their nickel contents. This would indicate that the stacking fault energy of the Fe/Ni10%/Cr17% alloy used in the present experiments is similar to that of the 321 stainless steel as it has the same nickel and chromium contents as the steel. While no data is available for the effect that oxygen has on the stacking fault energies of the present alloys, work on silver has shown no significant dependence of the stacking fault energy on oxygen content (Wilkens et al 1966). Approximate values of the stacking fault energies of the materials used in the present experiments obtained from a consideration of the above results are listed in Table 5.3.

Reference to Table 5.3 shows that while the stacking fault energies of the two nichrome alloys appear to be less than in pure Ni, these stacking fault energies are still relatively high (> 80 ergs/cm^2). Thus it is thought that the presence of inclined perfect loops in the nichrome alloys can be accounted for in a similar way to their presence in nickel, that is by the surface interaction energy causing the unfaulting of some of the larger 'edge-on' Frank loops.

The probability of an inclined perfect loop slipping out of a foil due to surface image forces would be expected to be greater in the Ni or the nichrome alloys than in the Fe/Ni/Cr alloy or the stainless steel, as the friction stress and the probability of loops being pinned by impurities would be expected to be higher in the less pure ternary alloy and steel. The fact that no inclined perfect loops were identified in the ternary alloy and the steel would therefore indicate that none of their 'edge-on' Frank loops had unfaulted. As approximately equal numbers of the large (> 50 Å diameter) undissociated Frank loops lay on the edge-on and inclined planes in the ternary alloy and the steel, this would also indicate a reduction in the probability of their inclined Frank loops unfaulting (see section 4.4.1). Reference to Table 5.3 shows that the

stacking fault energies of the ternary alloy and the steel are considerably lower than for nickel or the nichrome alloys. It is therefore thought that the reason that no inclined perfect loops were identified in the Fe/Ni/Cr alloy and the steel, whereas they were in the nickel and the nichrome alloys, is a reduced probability of Frank loops unfaulting in the ternary alloy and the steel due to the lower stacking fault energies of these materials.

5.3.2 'Edge-On' Perfect Loops

An 'edge-on' Frank loop at a <110> orientation can unfault to either one of two inclined perfect loops or to an edge-on perfect loop. The discussion of section 4.4.1 shows that when the reductions in loop energies due to their elastic interactions with the surface are taken into account, these reductions being proportional to the values of E_o given by Table 4.3, then it would appear to be energetically more favourable for an edge-on Frank loop to unfault to one of the inclined perfect loops. However, the difference in E_o values between an inclined perfect loop ($E_o = 6.26$) and an edge-on perfect loop ($E_o = 4.61$) is quite small and, in addition, these values were calculated for an unstressed, isotropic medium. Thus if stresses are present, it may be possible that the edge-on perfect loop is the lowest energy state. Edge-on perfect loops were only observed in the nichrome alloys, not in the pure nickel, and such stresses may therefore have been caused by the Cr alloying element or the oxygen impurity. An edge-on perfect loop would not slip out of a foil as a result of surface image forces as its Burgers vector is parallel to the surface. Thus the fact that only a very small number (< 1%) of such loops were identified means that only a very small number of such loops were formed. It is therefore thought that a possible explanation for the formation of the edge-on perfect loops is that they, like the inclined perfect loops, were formed by the surface interaction energy causing the unfaulting of some of the larger, edge-on Frank loops.

An alternative explanation for the formation of apparently energetically unfavourable perfect loops has been proposed by Jenkins et al (1977). They considered that the high energy density in the compact cascades generated by heavier ions such as Xe^+ ions, W^+ ions or molecular ions, may provide the source of energy required for shear to occur to a metastable perfect loop configuration. Thus it is possible that both the inclined and edge-on perfect loops identified in the present W^+ ion irradiations were formed as metastable states. However, an apparently consistent explanation of perfect loop formation in the present materials, which can also account for the observed distribution of large Frank loops lying on the edge-on and inclined planes, is obtained by considering the influence the surface interaction energy might have on the unfaulting of the Frank loops.

5.4 Partial Dissociation of Frank Loops

The sessile Frank partial dislocation ($\underline{b} = \frac{a}{3}\langle 111\rangle$) bounding a Frank loop may dissociate into sessile stair rod dislocations ($\underline{b} = \frac{a}{6}\langle 110\rangle$) lying along <110> directions and glissile Shockley partial dislocations ($\underline{b} = \frac{a}{6}\langle 211\rangle$) on intersecting {111} slip planes according to reactions of the type first proposed by Silcox and Hirsch (1959), that is:

$$\frac{a}{3}[111] \rightarrow \frac{a}{6}[101] + \frac{a}{6}[121],$$

$$(\frac{a^2}{3} \rightarrow \frac{a^2}{18} + \frac{a^2}{6}).$$

The Shockley partial dislocation is repelled by the stair rod dislocation and tends to bow out in its slip plane. In doing so it creates an area of stacking fault on its slip plane which opposes further dissociation. This dissociation is illustrated for the special case of a triangular Frank loop, with its edges along <110> directions, in figure 5.11. Part (a) of this figure shows the undissociated loop while part (b) shows the configuration when the Frank dislocations have slightly dissociated. The glissile Shockley partials mutually attract each other and may combine to form stair rod dislocations along <110> directions by reactions of

the type:

$$\frac{a}{6}[121] + \frac{a}{6}[\bar{1}\bar{1}\bar{2}] \rightarrow \frac{a}{6}[01\bar{1}],$$

$$(\frac{a^2}{6} + \frac{a^2}{6} \rightarrow \frac{a^2}{18}).$$

If the decrease in energy due to the shortening of the Shockley partials and their combination to form stair rod dislocations is larger than the resulting increase in stacking fault energy, then they will glide towards the vertex of a tetrahedron. This process is illustrated by figure 5.11(c).

The degree of dissociation of a triangular Frank loop can be conveniently defined by $x = L'/L$ where L' is the length of the dissociated edge and L is the length of the base (see figure 5.11(c)). The energies of the partially dissociated states of small triangular Frank loops in Ni (γ = 125 ergs/cm^2) and 321 stainless steel (γ = 25 ergs/cm^2) have been calculated using the formula of Jøssang and Hirth (1966). Their formula for a truncated tetrahedron ($0 < x < 1$) was derived by approximating the bowed out Shockley partials to straight line segments and the energy was then calculated using exact analytic expressions for the self energies and interaction energies between straight segments of dislocations in an infinite, continuous, isotropic medium (Jøssang et al 1965). The results of the calculations for Ni and 321 stainless steel are shown in the energy versus degree of dissociation (x) curves of figures 5.12 and 5.13. The continuum approximation breaks down as the configuration size approaches dislocation core dimensions, with the result that the above calculations may not be valid for $x \lesssim 0.1$. The values calculated for $x < 0.1$ are therefore indicated by broken lines.

Reference to figures 5.12 and 5.13 indicates that it is energetically favourable for a Frank loop to dissociate to a complete stacking fault tetrahedron ($x = 1$) in both Ni and 321 stainless steel for all the loop sizes (20 Å → 80 Å diameter) considered. However, these theoretical

curves are only valid for the special case of dissociated states of triangular Frank loops in an infinite, isotropic medium. In practice, a Frank loop climbing in a high vacancy supersaturation is thought to be approximately circular. As the local vacancy supersaturation decreases it is more favourable for segments of the loop to line up along <110> directions to allow the Frank partial dislocation to dissociate. Thus the loop is thought to become a more or less regular hexagon (Jenkins 1974). From a detailed consideration of the influence of surface image forces on the dissociation of such a loop, Jenkins proposed that particular edges of the hexagon may be preferentially degraded by vacancy migration with the eventual possibility of the loop becoming triangular in shape. However, the present energy versus degree of dissociation curves would have to be modified for non-triangular loops, as well as being modified by the interaction of a loop with a free surface and by the effects of elastic anisotropy. In addition, the maximum degree of dissociation of a non-triangular loop will be limited by the detailed geometry of the final loop configuration.

The above considerations show that the present calculations cannot be used to predict the theoretical degree of dissociation of a Frank loop in a given material. They can, however, be used to make a qualitative comparison between the relative driving forces for dissociation in the different materials. Reference to figures 5.12 and 5.13 shows that, for a loop of a given size, the rate of decrease of energy with dissociation is greater in the steel than in nickel. This is a result of the lower stacking fault energy in the steel. Thus if the degree of dissociation is limited by the loop configuration, there will be a stronger driving force in the steel for the detailed loop geometry to change so that more dissociation can occur. This may therefore result in the average degree of dissociation being higher for loops in the steel than for loops in nickel.

Whether a dissociated loop is identified as being dissociated is thought to depend on the degree of dissociation of the loop in relation to the loop size. A relatively high degree of dissociation is thought to be necessary for small loops, and such a degree of dissociation may not, in general, be possible because of the loop configuration. This may therefore explain why, in the present experiments, only large (> 50 Å diameter) loops were identified as being dissociated. In addition, it is possible that slightly dissociated states of these large loops may not have been identified as being dissociated. An increased average degree of dissociation in the Fe/Ni/Cr alloy and the stainless steel, due to their lower stacking fault energies, could therefore explain why more Frank loops were identified as being dissociated in these materials compared with the higher stacking fault energy nickel and nichrome alloys, and also why this dissociation appeared to extend to smaller loop sizes.

In conclusion, it is thought that the present experimental results are consistent with the dissociation of a Frank loop being limited by the detailed geometry of the loop configuration, with the increased proportion of dissociated loops that were identified in the Fe/Ni/Cr alloy and stainless steel being due to the lower stacking fault energy in these materials.

5.5 The Influence of Alloying Elements and Impurities on the Generation and Collapse of Displacement Cascades

5.5.1 Introduction

Some of the possible affects that alloying elements and impurities may have on the generation and collapse of displacement cascades are listed below, along with a discussion of these affects in relation to the present experimental results.

(1) The alloy or impurity atoms may defocus replacement collision sequences such that interstitials are less efficiently separated from the vacancies in the core of the cascades. This is thought to result in

increased recombination within the cascade and the resulting reduction in the vacancy supersaturation may reduce the probability of a cascade collapsing to nucleate a faulted loop. In addition, the average size of the defect clusters formed by cascade collapse would be reduced and this would cause a reduction in the defect yield due to an increased proportion of the defect clusters being too small to produce visible diffraction contrast. However, as discussed in section 5.5.2, it is not thought that the present reductions in the defect yields in the Fe/Ni/Cr alloy and the stainless steel, compared with that in pure nickel, can be accounted for by the defocussing of replacement collision sequences.

(2) If the ions incident on a thin crystal are channelled, then the presence of alloy or impurity atoms might be expected to increase the probability of dechannelling occurring within the crystal. This would then result in an increase in the defect yield due to an increase in the number of cascades generated within the crystal. As discussed in more detail in section 5.5.2, the results of the present experiments indicate that no significant axial or planar channelling occurred in any of the alloys investigated. Thus the dechannelling of channelled incident ions is not thought to be important in the present case.

(3) The alloy or impurity atoms may increase the probability per unit path length of channelled or quasi-channelled knock-on atoms being dechannelled. The effect that this might have depends on the energy of the channelled knock-on atom. If it has sufficient energy to generate another disordered region, then this increased probability of being dechannelled would reduce the separation of the disordered regions and this might increase the effective number of vacancies which are involved in the possible nucleation and growth of a single Frank loop. If, on the other hand, a knock-on atom has a low energy such that it is essentially an interstitial escaping from the cascade, then this increased probability of being dechannelled would tend to increase vacancy-

interstitial recombination thereby reducing the number of vacancies in the disordered regions.

As considered in section 5.5.3, it is thought that the present experimental results can be accounted for if the probability of a Frank loop being nucleated within a cascade may vary from one material to another, but that once this nucleation occurs, most of the vacancies within the core of that cascade region are then drawn into the loop. If this is so, the similarity of the distribution of defect sizes generated by a given ion in nickel and all the alloys (see for example figures 5.3 and 5.6) would indicate that, in the present case, the overall effect of the dechannelling of knock-on atoms is not significant.

(4) The alloy or impurity atoms may reduce the average threshold displacement energy E_d in a given material resulting in so called 'subthreshold' displacement events (Bauer and Sosin 1964). The distortion of the lattice caused by an impurity atom may result in the atoms of the major constituent being less tightly bound so that their displacement energies are reduced. In addition, if the impurity atom is undersized then its displacement energy may be less than that of the major constituent. The theoretical defect production model of Norgett et al (1972) indicates that the number of Frenkel pairs generated within a cascade is directly proportional to E_d^{-1}. Thus any reduction in E_d would result in more vacancies being generated within a cascade and this could have an important effect both in increasing the probability of a Frank loop being nucleated and in increasing the final size that that loop would grow to.

The above effect would be expected to increase with increasing size difference between substitutional impurity or alloying atoms and the atoms of the major constituent. In the present case, the atomic radii (r_a) of Cr (r_a = 1.28 Å) and Fe (r_a = 1.26 Å) are similar to that of Ni (r_a = 1.25 Å (Smithells 1976)) and thus one would not expect any significant reduction in the displacement energies due to these substitutional

alloying elements.

The possible effect of interstitial impurity atoms is not clear. Displacements of such atoms within cascades is not itself important, since the displacement of an interstitial atom does not create a vacancy. However, it is likely that interstitial impurity atoms are more effective than substitutional impurity atoms in reducing local displacement energies, since their strain fields are stronger. However, this may be partly compensated for by the interstitial impurities acting as vacancy traps (see (5) below). In the present case, the effect of the interstitial impurity atoms on the average displacement energies may not have been important since the total concentrations of such atoms in the crystals were relatively low.

The experimental evidence which shows that the average sizes of the defects generated by a given ion are similar in all the materials studied, suggests that subthreshold displacement events were not important in the present alloys.

(5) The alloy or impurity atoms may act as 'trapping sites' for either interstitial or vacancy point defects. This trapping occurs if there is a reduction in the energies of an impurity atom and a point defect when they are located close to each other. Thus interstitial impurities will be very effective as vacancy traps. However, as discussed in (4) above, the effect of this trapping is thought to be partly compensated for by subthreshold displacement events near such interstitial atoms.

Undersized substitutional impurity atoms are thought to be particularly effective in trapping interstitials, although the binding energies depend on the electron interactions as well as on the size effect (Trinkaus 1975). Such undersized atoms may therefore act as nucleation sites for interstitial clusters and by trapping interstitials that have escaped from a cascade, they may reduce the probability of them

returning to the cascade, thereby reducing the amount of recombination that occurs. While the formation of submicroscopic interstitial clusters may be important in determining the amount of recombination that occurs within a cascade, the present Cr and Fe alloying atoms are of similar size to the Ni atoms and thus they are not thought to have altered the probability of such clusters nucleating.

Oversized substitutional impurity atoms are thought to be effective in trapping vacancy point defects. As discussed in section 5.6, the size a loop nucleus grows to is thought to depend on the number of vacancies that diffuse to that loop nucleus. Thus by increasing the effective vacancy migration energy, such impurity atoms may reduce the final size of a loop. As discussed in section 5.7, this effect may be more important in a cascade generated by a Ni^+ ion than in a more compact cascade generated by a W^+ ion. However, because the present Cr and Fe alloying atoms are similar in size to Ni atoms, it is not thought that they acted as vacancy traps.

(6) The alloy or impurity atoms may influence directly the process by which a loop is nucleated within a cascade by altering the effective energy barrier opposing faulted loop nucleation. This could be a result of the alloy or impurity atoms altering the stacking fault energy of a material or, as suggested by English et al (1977), impurity atoms may stabilise the uncollapsed vacancy aggregates so that they form submicroscopic voids rather than loops. As considered in section 5.5.3, a difference in the energy barriers opposing faulted loop nucleation is thought to be the most probable explanation for the present reductions in the defect yields in the alloys as compared with those in pure nickel.

5.5.2 Comparison of Present Results with Previous Results of Other Authors

A discussion of the results obtained by other workers from low dose, heavy-ion irradiations of alloys is given in section 1.6.1. In this section, the explanations proposed to account for these results are

considered in relation to the present results.

The defect yield and cascade efficiency values measured by English et al (1975) in an austenitic stainless steel (type 316) irradiated with 40 → 200 keV Cr^+ ions to doses of 5×10^{12} ions cm^{-2} are similar to the values obtained from the present Ni^+ ion irradiations of type 321 stainless steel. English et al attributed the reduction in defect yield and cascade efficiency in the steel compared with a pure F.C.C. material such as Cu as being due to the alloys and impurities in the steel defocussing replacement collision sequences. However, as explained in section 5.5.1, any reduction in defect yield caused by the defocussing of replacement collision sequences would be accompanied by a decrease in the defect sizes. The similarity of the defect sizes in W^+ ion irradiated Ni, Fe/Ni10%/Cr17% and 321 stainless steel is clearly illustrated by figure 5.6. Thus it is not thought that the differences in the defect yields in these W^+ ion irradiated materials can be accounted for by the defocussing of replacement collision sequences. In addition, the similarity of the mean defect sizes in the Ni^+ ion irradiated materials (see Table 5.2) would indicate that the defocussing of replacement collision sequences is not of major importance in accounting for the differences in their defect yields. The fact that the present alloys all contained significant amounts of interstitial impurities (see Tables 3.1 and 3.5), which are thought to be most effective in defocussing replacement collision sequences, would therefore indicate that if this defocussing does occur, then it is of minor significance compared with other alloying or impurity effects.

A systematic investigation of the affect of alloying on cascade generation and cascade collapse has been carried out by Stathopoulos (1977) in 30 keV Cu^+ ion or W^+ ion irradiated Cu and substitutional Cu alloys. The alloys studied were Cu-Al (0.44 → 15.8 at.%), Cu-Ge (3.9 → 7.6 at.%), Cu-Ni (10.1 at.%), Cu-Si (8.3 at.%), Cu-Zn (26.1 at.%) and Cu-Be (2.25 at.%). These alloys were chosen so that the effects of

changes in stacking fault energies and differences in either the masses or sizes of the alloying atoms could be investigated. Stathopoulos found that the defect yields in the alloys were, without exception, all higher than in pure Cu, with the sizes of the increases correlating qualitatively with the size difference between the alloying atoms and the Cu atoms. The defect yields in the Cu-Al and Cu-Ge alloying systems increased approximately linearly with increasing solute concentration. The cascade efficiencies were generally of the same order or slightly higher than in Cu. By considering the climb of a dislocation loop in a supersaturation of vacancies, Stathopoulos concluded that the supersaturation within a cascade ($C_v/C_o \approx 10^{14}$) was so high that a loop would always climb, and that the increases in the defect yields in the alloys were therefore due to increases in the number of cascades generated within a crystal. He considered that the most likely explanation for his results was the alloying additions causing the dechannelling of incident ions that had been channelled between planes, the probability of dechannelling depending on the size of the solute atoms. It was not thought that axial channelling had occurred as the specimens were all single crystals orientated along a 'non-channelling' direction. Other impurity effects were considered to influence mainly the sizes of the loops, as they were not thought to alter C_v/C_o sufficiently to influence the probability of cascade collapse. However, in arriving at these conclusions, Stathopoulos did not differentiate between the nucleation of a faulted loop and the subsequent climb of that loop. As discussed in section 5.6, it is thought that the probability of a faulted loop being nucleated has a much more critical dependence on the vacancy supersaturation within a cascade than does the subsequent climb of that loop. Thus it is thought that the conclusions of Stathopoulos may not be valid.

The defect clusters that were considered in the present alloys were all located in grains lying within 10^o of a <110> orientation. Thus it

is possible that some of the incident ions may have been axially channelled along the <110> inter row channels or, alternatively, planar channelled between the {100} or {111} planes. The defect yields and defect sizes generated by 80 keV W^+ ion irradiations of three different Ni specimens randomly orientated about a <110> pole, for which the probabilities of planar channelling might be expected to be different, were found to be the same within experimental error (see section 3.9). Thus this would tend to indicate that planar channelling does not occur to any significant extent for W^+ ions in Ni. If this is so, it is unlikely to occur to any significant extent in the alloys either because of their greater interstitial impurity contents. It is possible for ions incident within 1^o or 2^o of the <110> axis to be axially channelled, but the arguments of section 4.7 would indicate that if such channelling does occur, then visible defect clusters are likely to be generated throughout a thin foil rather than being confined to the first depth layers. This is also thought to apply if the incident ions are planar channelled. In all the present alloys, less than 3% of the defect clusters generated by the W^+ ion irradiations showed black-white contrast with $\underline{g}.\underline{1} < 0$ when imaged using $\underline{g}$ = <220>. This would therefore indicate that these vacancy clusters were nearly all confined to the first depth layer for this reflection (see section 2.3). Thus it is not thought that channelling occurred to any significant extent in any of the W^+ ion irradiated materials, and the reductions in defect yields in the Fe/Ni/Cr alloy and the stainless steel cannot therefore be accounted for by an increased proportion of the incident ions being channelled as compared with pure nickel. The reductions in defect yields in the two Ni^+ ion irradiated nichrome alloys compared with nickel may perhaps have been caused by the incident ions being channelled, but it is thought to be unlikely that significant channelling would have occurred in both of these alloys, especially since no significant difference was found between the defect

yields measured in different {110} grains of these specimens.

In conclusion, neither the defocussing of replacement collision sequences nor the channelling of incident ions are thought to be able to account for the present experimental results.

5.5.3 Explanation Proposed for Present Reductions in the Defect Yields

The present reductions in defect yields in the W^+ ion irradiated Fe/Ni/Cr alloy and 321 stainless steel and in the Ni^+ ion irradiated nichrome alloys and stainless steel compared with those in pure Ni are not accompanied by reductions in the average defect sizes (see Tables 5.1 and 5.2). The similarity of the distributions of the defect sizes in the W^+ ion irradiated Ni,Fe/Ni/Cr alloy and stainless steel is clearly illustrated by figure 5.6. Thus despite the large differences in the defect yields, it would appear that the average number of vacancies in a loop in a collapsed cascade is approximately the same for these three materials. This would therefore indicate that the reductions in the defect yields are caused by a reduction in the probability of a cascade collapsing. This is consistent with the theoretical considerations of the following section (5.6) which indicate that once a faulted loop is nucleated within a cascade, then most of the vacancies within the core of the cascade will be drawn into the loop which will therefore, in general, climb to form a visible defect cluster. It is therefore considered that the most probable explanation for the present reductions in defect yields is that they were caused by a reduction in the probability of a faulted loop being nucleated.

In pure metals, the energy barrier opposing faulted loop nucleation appears to depend mainly on the stacking fault energy of the material (see for example Table 5.4). In the present case, the stacking fault energies of the Fe/Ni/Cr alloy and the stainless steel are thought to be much lower, and those in the nichrome alloys slightly lower, than in pure nickel (see Table 5.3). Thus the reduction in the probability of a

faulted loop being nucleated cannot be accounted for by the changes in the stacking fault energies. The Fe/Ni/Cr alloy and the stainless steel both had the same major alloying composition, but the stainless steel contained a higher level of minor impurities (see Table 3.1). Thus the reduction in defect yield in the stainless steel compared with the Fe/Ni/Cr alloy would indicate that the minor impurities may have been important in determining whether a loop was nucleated or not. This would tend to be supported by the theoretical considerations of Russell and Powell (1973) which indicate that the free energy barrier opposing loop nucleation may be increased by the presence of interstitial impurity atoms (see section 5.6). The nichrome alloys and the Fe/Ni/Cr alloy all contained significant amounts of oxygen (190 → 1070 ppm ($^{w}/_{w}$) (see Table 3.5)) and the affect that this interstitial impurity may have had on loop nucleation in these materials is considered in section 5.5.4. The discussion of this section indicates that the reduction in the defect yield in the W^{+} ion irradiated Fe/Ni/Cr alloy compared with the nickel and the nichrome alloys, and in the Ni^{+} ion irradiated nichrome alloys compared with the nickel, could have been caused by this impurity increasing the energy barrier opposing loop nucleation. However, since it was not a feasible proposition to analyse the materials for all impurities, it is possible that significant amounts of other interstitial impurities may have been present which could also have opposed loop nucleation. This might then explain why the defect yields in the stainless steel were lowest of all, since while the steel only contained 32 ppm ($^{w}/_{w}$) oxygen, it contained a high level of known interstitial impurities (see Table 3.1) and since it was a commercial alloy it probably contained significant amounts of other impurities as well.

In conclusion, it is thought that the present reductions in the defect yields in the alloys as compared with pure nickel can be accounted for by a reduction in the probability of a faulted loop being nucleated, and this is more likely to have been caused by the presence of minor

impurities rather than by a change in the major composition of an alloy.

5.5.4 Affect of the Oxygen Impurity on Cascade Collapse

No data has been published for the solubility of oxygen in the present alloys, although its solubility in pure nickel is known to increase with decreasing temperature from 120 ppm ($^{w}/w$) at 1200°C to 200 ppm ($^{w}/w$) at 600°C (Seybolt 1936). Thus while the total oxygen contents of the Ni/Cr8%, Ni/Cr17%, Cr/Ni83% and Fe/Ni/Cr alloys are known (see Table 3.5), the amount of oxygen in solution, which is thought to have most affect in influencing cascade collapse, may be different since some of the oxygen, especially in the higher oxygen content alloys, may have precipitated out of solution. Thus while the Ni/Cr17% and Cr/Ni83% alloys that were compared in the present experiments contained 1070 and 510 ppm ($^{w}/w$) oxygen respectively, the amounts of oxygen in solution may have been the same and this would then account for the defect yields generated by the W^{+} ion irradiations of these two alloys being the same within experimental error (see section 5.2.3.1).

If it is assumed that the nichrome alloys are saturated with oxygen, then a possible self-consistent explanation for some of the trends in the results is obtained if it is further assumed that the oxygen in solution plays a role in inhibiting cascade collapse.

It is probable that there is a significant difference between the amounts of oxygen in solution in the polycrystalline Ni (containing < 2 ppm ($^{w}/w$)0) and that in solution in the Ni/Cr8% and Ni/Cr17% alloys (containing ≥190 ppm ($^{w}/w$)0). Thus the reduction in the defect yields in the Ni^{+} ion irradiated nichrome alloys as compared with pure nickel could have been caused by the interstitial oxygen that was in solution either increasing the energy barrier opposing loop nucleation or perhaps turning an uncollapsed vacancy disc into a gas containing void (see section 5.6). There was no difference in the defect yields generated by the W^{+} ion irradiations of these three materials and this could have been due to the perturbing influence of

the oxygen having less effect in opposing the nucleation of a faulted loop in a cascade generated by a W^+ ion. As discussed in section 5.6, the average vacancy arrival rate at a cluster within a cascade generated by a W^+ ion is expected to be higher than in a cascade generated by a Ni^+ ion, and thus an increase in the critical size a cluster has to grow to before it becomes a stable nucleus may have less effect in a cascade generated by a W^+ ion. Thus it is thought that the oxygen may account for the present variations in defect yields between the nickel and the nichrome alloys.

The oxygen could also account for the reduction in the defect yield in the W^+ ion irradiated Fe/Ni/Cr alloy as compared with nickel and the nichrome alloys if the solubility of the oxygen is much higher in the Fe/Ni/Cr alloy. However, the relevant solubilities are not known and, as considered in section 5.5.3, the reduction in the probability of a loop being nucleated could equally well be due to the presence of other interstitial impurities which were not analysed for. Thus, in the case of the Fe/Ni/Cr alloy, it is uncertain whether the observed reduction in the defect yield can be accounted for by the oxygen impurity.

5.6 Nucleation and Climb of a Faulted Loop in a Displacement Cascade

Consider a circular, faulted loop of radius R in a material with a vacancy supersaturation C_v/C_o. The energy of the loop is given by the sum of the elastic energy of the dislocation line (τ per unit length) and the stacking-fault energy ($\pi R^2 \gamma$). The line tension τ for an edge dislocation loop in an isotropic elastic medium, excluding the dislocation core energy, is given by (Friedel 1964):

$$\tau = \frac{\mu b^2}{4\pi(1-\nu)} \ln \frac{2R}{b_o}$$

where μ is the shear modulus, ν is Poisson's ratio, $\underline{b}$ is the loop Burgers vector, and b_o (which is of the order of b) the core radius. Suppose that a vacancy impinges on the loop and is absorbed. The increment δR in the loop radius is given by

$$2\pi R\delta R = B^2$$

where B^2 is the cross-sectional area of the vacancy in the loop habit plane. The total free energy change δE is given by the increase in loop energy minus the free energy of the vacancy ($G = kT \ln C_v/C_o$), that is:

$$\delta E = \gamma 2\pi R\delta R + 2\pi R\delta\tau + 2\pi\tau\delta R - kT \ln C_v/C_o$$

$$= B^2 \left[\gamma + \frac{\mu b^2}{4\pi R(1-\nu)} \left(1 + \ln \frac{2R}{b_o}\right)\right] - kT \ln C_v/C_o.$$

For a given vacancy supersaturation there is a critical loop size R', given by

$$\frac{\mu b^2}{4\pi R'(1-\nu)} \left(1 + \ln \frac{2R'}{b_o}\right) = \frac{kT}{B^2} \ln C_v/C_o - \gamma,$$

for which δE is zero. Loops with radius $R < R'$ will tend to emit more vacancies than they absorb and so shrink, while loops with radius $R > R'$ will tend to grow, as long as sufficient supersaturation is maintained.

It is not possible to apply rigourously the above considerations to the situation of a dislocation loop in a supersaturation of vacancies within a displacement cascade since this supersaturation is not, in general, uniform within the cascade and the effective 'temperature' of a cascade region is uncertain. However, if vacancies can diffuse within the cascade region, and the experimental evidence suggests that they can even when diffusion in the bulk material is not possible, then in the approximation that the model is applicable, taking a typical initial value of the average supersaturation within a cascade of $C_v/C_o = 10^{14}$, the temperature T = 300 K to be of the crystal as a whole, taking $B^2 = a^2\sqrt{3}/4$ for a vacancy in a {111} loop habit plane, $b_o = b = \frac{a}{3}\langle 111\rangle$, and using the values of a, μ, ν and γ for Ni listed in appendix 1 gives the radius of a faulted loop in equilibrium in a cascade in Ni as being $R'_{Ni} \approx 2b$. For such a small radius, a loop cannot be considered as

circular and, in addition, the energy of the dislocation core may form a large part of the total loop energy. However, the calculations indicate that the critical loop size in Ni for $C_v/C_o = 10^{14}$ is quite small and may correspond to a cluster containing about ten vacancies. Once a loop of critical size starts to climb, the vacancy supersaturation necessary for further climb rapidly decreases ($C_v/C_o < 10^{10}$ for $R_{Ni} > 4b$) and becomes much less than the average vacancy supersaturation within a cascade, which only changes slowly as vacancies are removed by the climb of a loop.

If a loop larger than the critical size is nucleated within a cascade, then it will tend to grow as further vacancies impinge on it. The interaction energy between the elastic stress fields of an edge dislocation and a vacancy point defect is given by (Cottrell 1953):

$$E_i = \frac{4\mu\varepsilon b r_o^3 \sin\theta}{x}$$

where r_o is the radius of an atom, $(1+\varepsilon)r_o$ is the radius of the vacancy, $\underline{x}$ is the position of the vacancy in relation to the dislocation, and θ is the angle between $\underline{x}$ and the dislocation Burgers vector $\underline{b}$ and is positive for the regions around the dislocation under compressive hydrostatic stress. This interaction energy results in a net attractive force on the vacancies in the cascade region drawing them towards the dislocation bounding a loop nucleus. The actual force acting on a vacancy in a cascade is modified somewhat by the interactions between the vacancies themselves. However, the vacancies will tend to diffuse towards a loop nucleus which will therefore grow until no more vacancies are drawn onto the bounding dislocation.

The factors that are thought to determine the final size a loop grows to are: the number of Frenkel pairs that are generated within a cascade and the amount of recombination that occurs, that is the total number of vacancies that survive in the cascade region; the spatial distribution

of these vacancies in relation to the loop nucleus; and the mobility of the vacancies, which may be influenced by impurities acting as vacancy traps, at the time the loop is nucleated. The distribution of the defect sizes in a given material is thought to be the result of statistical variations in these factors.

The above considerations would indicate that if a faulted loop larger than some critical size is nucleated within a cascade, then most of the vacancies in the core of the cascade will be drawn towards that nucleus which will, in general, subsequently climb to form a visible defect cluster. Thus it is thought that the number of visible defect clusters generated in a given material is determined mainly by the probability of a critical sized faulted loop being nucleated. This probability does not appear to depend simply on the average vacancy supersaturation $(^{C}v/C_{o})_{av.}$ within a cascade being higher than a critical value for a given material, as this would result in true defect yields being either close to zero or close to unity depending on the value of $(^{C}v/C_{o})_{av.}$ It is thought that experimentally observed defect yields, which generally have values between 0 and 1, are consistent with there being a critical vacancy supersaturation within a cascade in a given material above which a faulted loop will be nucleated, but that this critical supersaturation is higher than $(^{C}v/C_{o})_{av.}$ which is typically in the range $10^{14} \rightarrow 5.10^{14}$. Thus the probability of a faulted loop being nucleated is thought to depend on the statistical fluctuations of $^{C}v/C_{o}$ within the cascade producing a vacancy supersaturation at some region within the cascade which is high enough to result in the nucleation of a faulted loop.

The nucleation of a vacancy loop in a steady-state supersaturation of vacancies in an infinite medium has been studied theoretically by Russell and Powell (1973) who considered the change ΔG^{o}_{n} in the free energy of a system when n vacancies aggregate to form a loop. This change is given by

$$\Delta G^{o}_{n} = - nkT \ln {}^{C}v/C_{o} + W(n) \qquad (5.1)$$

where W(n) is the energy of a loop containing n vacancies. The variation of ΔG^o_n with n is plotted in figure 5.14. In agreement with the earlier considerations of this section, it can be seen that the free energy of a system initially increases as the vacancies aggregate, but that there is a critical sized nucleus corresponding to n_k vacancies above which further vacancy aggregation reduces the free energy. Thus once a cluster contains more than n_k vacancies it is stable and will tend to grow as further vacancies impinge on it.

The free energy barrier ΔG^o_k opposing loop nucleation depends on the vacancy supersaturation C_v/C_o and the value of W(n) (see equation 5.1). By taking W(n) to be the energy of a collapsed vacancy loop, Russell and Powell found that supersaturations corresponding to more than one vacancy per atom were required theoretically to give loop nucleation. Thus, in agreement with the conclusions that Davis (1967) had made from a study of loop nucleation in quenched aluminium, they considered that the critical nucleus more closely corresponded to a disc of vacancies that had not yet collapsed into a loop. Once past the critical size, such a disc of vacancies would grow rapidly by vacancy absorption until its free energy was greater than that of a collapsed loop containing the same number of vacancies, at which size it would collapse to form a faulted loop.

The above considerations are again not rigorously applicable to the nucleation of a dislocation loop in a supersaturation of vacancies within a cascade, as such a supersaturation only contains a limited number of vacancies and it is not a steady state. However, whether a loop nucleates as a faulted loop or as an uncollapsed vacancy disc, there is an energy barrier opposing this nucleation. To overcome this energy barrier requires that a critical sized nucleus is formed, and this requires that the rate of arrival of vacancies at a cluster, which is initially smaller than the critical size, exceeds the rate at which such a cluster emits vacancies. Thus the theoretical considerations are consistent with

the probability of a loop being nucleated within a cascade depending on the statistical variations in the distribution of the vacancies within a cascade. The probability of a loop being nucleated is expected to increase with increasing incident ion mass, for similar incident ion energies, as irradiating with a heavier ion generates approximately the same number of Frenkel pairs but in a smaller cascade volume, and thus the average vacancy arrival rate at a given point in a cascade will be higher.

The calculations of Russell and Powell (1973) indicate that the energy barrier opposing loop nucleation and the size of a critical nucleus are increased by the presence of interstitial atoms (see figure 5.15). Thus such atoms might be expected to reduce the probability of a critical sized nucleus being formed. In addition, Russell and Powell considered that the presence of dissolved gas atoms could interfere with vacancy loop nucleation, depending on the concentration and mobility of the gas atoms, by turning a vacancy disc smaller than the critical size into a gas-containing void.

In conclusion, it is thought that the critical vacancy supersaturation required to nucleate a faulted loop within a cascade is higher than $(C_v/C_o)_{av.}$ and thus the probability of a faulted loop being nucleated depends on the statistical fluctuations of the vacancy supersaturation within the cascade region. However, once a faulted loop nucleus starts to climb, the vacancy supersaturation necessary for further climb is normally much less than $(C_v/C_o)_{av.}$ and a loop nucleus will, in general, climb to form a visible defect cluster.

5.7 Limitations of W^+ Ion Damage in Representing Ni^+ Ion Damage

The damage structures generated by self-ion irradiations are more representative of fast neutron damage than the damage structures generated by irradiating with other ions. Thus, in the present case, it is important to realise the limitations of W^+ ion damage in representing Ni^+ ion damage.

Irradiating the present materials with W^+ ions generated approximately the same number of Frenkel pairs as irradiating with Ni^+ ions but in a much

smaller volume (see section 4.6). Thus it is thought that the probability of producing a vacancy supersaturation at some region within a cascade which is significantly higher than that required for loop nucleation will be increased in a cascade generated by a W^+ ion compared with one generated by a Ni^+ ion. Thus the influence of perturbations in opposing loop nucleation may have less affect in a cascade generated by a W^+ ion. As discussed in section 1.5.4.2, the defect yield in molybdenum irradiated with 60 keV self-ions starts to fall off at temperatures above 200°C while the defect yields generated by 60 keV Xe^+ or W^+ ions remain constant at least up to 425°C (English et al 1977, English 1977b). Since vacancies are mobile in molybdenum for temperatures greater than about 200°C, it is possible that at such temperatures some of the vacancies may migrate from a cascade into the surrounding lattice. If this is so, then the differences in the defect yields may be due to a reduction in the average vacancy supersaturation $(C_v/C_o)_{av.}$ in a cascade generated by a Mo^+ ion reducing the probability of attaining the critical supersaturation required for loop nucleation, whereas a reduction in the $(C_v/C_o)_{av.}$ in the cascades generated by the heavier ions may have less affect in reducing this probability. The energy barrier opposing faulted loop nucleation is thought to be higher in molybdenum than in the present materials because of its much higher stacking fault energy. Thus the perturbing influence of vacancies migrating away from a cascade may have less affect on loop nucleation in the present materials. However, the possibility exists that the present temperature dependencies of the defect yields in Ni and Ni/Cr17% irradiated with W^+ ions (see section 6.3) may not be fully representative of the dependencies that would have been obtained using Ni^+ ions. Even if the probability of loop nucleation is athermal for both Ni^+ ion and W^+ ion irradiations, the larger average size of the clusters generated by the W^+ ions will result in the temperature range over which the defect yield falls to zero, as a result of the loops thermally emitting vacancies, being

moved towards higher temperatures.

As considered in section 5.6, it is thought that interstitial impurities may increase the energy barrier opposing loop nucleation. The higher vacancy supersaturations within a cascade generated by a W^+ ion may result in this additional barrier having less effect than in a cascade generated by a Ni^+ ion. This is thought to be a possible reason why the defect yields generated by the present Ni^+ ion irradiations of the two nichrome alloys were lower than in pure Ni, while the defect yields generated by the W^+ ion irradiations were the same, within experimental error, in all three materials (see section 5.5.4). In addition, because the cascade generated by a W^+ ion is more compact, the average distance of a vacancy from a dislocation bounding a loop will be reduced and thus the average force drawing a vacancy towards a loop will be increased (see section 5.6). The effect of impurities acting as vacancy traps may therefore be reduced in a cascade generated by a W^+ ion as compared with in a cascade generated by a Ni^+ ion. Thus one disadvantage in comparing the damage structures generated by W^+ ion irradiations of different materials is that the perturbing influence of impurities in these materials, both in reducing the probability of a loop being nucleated and in reducing the number of vacancies drawn into a loop, may not produce any effect whereas they might in the case of self-ion or neutron irradiations.

Irradiating the present materials with W^+ ions resulted in the formation of defect clusters which were, on average, larger than those generated by irradiating with Ni^+ ions. Possible reasons for this are considered in section 4.6. As discussed in section 4.4.1, it is thought that the probability of a Frank loop unfaulting to a perfect loop increases with increasing loop size. Thus while irradiating with W^+ ions increased the proportion of defect clusters whose geometries could be unambiguously analysed, the geometries that were analysed may not be fully representative of the geometries of the defect clusters generated by the Ni^+ ions.

In conclusion, while irradiating the present materials with W^+ ions increased the average sizesof the defect clusters which considerably facilitated the analysis of the defect geometries and the interpretation of the defect yield data, neither the defect geometries nor the variations of the defect yields with impurity content or temperature that were produced by irradiating with the W^+ ions may be completely representative of the defect geometries and the variations in the defect yields that would be produced by irradiating with Ni^+ ions.

5.8 Conclusions

(1) Irradiation of Ni/Cr8%, Ni/Cr17%, Fe/Ni10%/Cr17% and 321 stainless steel with 80 keV Ni^+ or W^+ ions produces small (<80 Å diameter) vacancy-type dislocation loops which nucleate heterogeneously at cascades.

(2) The loops nucleate and grow on {111} planes as Frank loops. In the low stacking fault energy Fe/Ni/Cr alloy and stainless steel the loop geometries all remain based on the Frank loop. In the high stacking fault energy Ni/Cr alloys some of the larger (>50 Å diameter) loops unfault to perfect loops.

(3) In each alloy the defect yields generated by the W^+ ion irradiations are considerably higher, and the average defect sizes slightly higher, than those generated by the corresponding Ni^+ ion irradiations.

(4) The distributions of the visible defect sizes generated by either the Ni^+ ion or W^+ ion irradiations of all the alloys are similar to the corresponding distribution in pure nickel.

(5) The defect yields in the Ni^+ ion irradiated nichrome alloys are lower than in pure nickel while those generated by the W^+ ion irradiations are the same as in pure nickel, within experimental error. This is thought to be due to the perturbing influence of impurities have less affect in the denser cascades generated by the W^+ ions.

(6) The reductions in defect yields in the Ni^+ ion irradiated nichrome alloys and stainless steel and the W^+ ion irradiated Fe/Ni/Cr alloy and

stainless steel compared with those in pure nickel are thought to be due to a reduction in the probability of a loop being nucleated.

(7) The oxygen impurity may have reduced the probability of a loop being nucleated by increasing the energy barrier opposing the nucleation.

Table 5.1 The defect yields, mean defect sizes and cascade efficiencies of the damage structures generated by 80 keV W^+ ion irradiations of the alloys.

Table 5.2 The defect yields, mean defect sizes and cascade efficiencies of the damage structures generated by 80 keV Ni^+ ion irradiations of the alloys.

MATERIAL	FOIL ORIENTATION	DEFECT YIELD	MEAN DEFECT SIZE	CASCADE EFFICIENCY
Ni	⟨110⟩	0.81 ± 0.09	37.3 ± 0.9 Å	0.32
	⟨100⟩	0.81 ± 0.09	35.2 ± 1.0 Å	0.28
Ni/Cr 8%	⟨110⟩	0.92 ± 0.10	34.8 ± 0.9 Å	0.28
	⟨100⟩	0.83 ± 0.09	———	———
Ni/Cr 17%	⟨110⟩	0.86 ± 0.10	34.3 ± 0.9 Å	0.28
	⟨100⟩	0.75 ± 0.09	———	———
Cr/Ni 83%	⟨110⟩	0.88 ± 0.10	35.5 ± 1.0 Å	0.29
Fe/Ni10%/Cr17%	⟨110⟩	0.47 ± 0.06	35.3 ± 1.0 Å	0.29
321 St.St.	⟨110⟩	0.25 ± 0.03	37.8 ± 0.9 Å	0.33

TABLE 5.1.

MATERIAL	FOIL ORIENTATION	DEFECT YIELD (>25 Å)	MEAN DEFECT SIZE	CASCADE EFFICIENCY
Ni	⟨110⟩	0.44 ± 0.05 (0.30 ± 0.04)	30.8 ± 0.8 Å	0.25
Ni/Cr 8%	⟨110⟩	0.25 ± 0.04 (0.19 ± 0.03)	31.5 ± 0.8 Å	0.26
Ni/Cr 17%	⟨110⟩	0.17 ± 0.03 (0.14 ± 0.02)	33.0 ± 0.9 Å	0.28
321 St.St.	⟨110⟩	0.05 ± 0.01 (0.04 ± 0.01)	32.0 ± 1.0 Å	0.26

TABLE 5.2.

Table 5.3 Values of the stacking fault energies in nickel and the alloys obtained from a consideration of the experimental results discussed in section 5.3.1.

Table 5.4 Comparison of the defect yields generated by 80 keV or 90 keV self-ion irradiations of αFe (Jenkins et al 1977), Cu (Wilson 1970) and Ni (present work), materials of similar atomic weights, indicating a strong dependence of the defect yield on the stacking fault energy γ of a material. N_D is the theoretical number of Frenkel pairs generated within a cascade and θ_o is a measure of the maximum energy density within a cascade.

MATERIAL	STACKING FAULT ENERGY
Ni	125 ergs/cm^2
Ni/Cr 8%	~105 ergs/cm^2
Ni/Cr 17%	~85 ergs/cm^2
Fe/Ni10%/Cr17%	~25 ergs/cm^2
321 St.St.	~25 ergs/cm^2

TABLE 5.3.

INCIDENT ION TARGET	AT.WEIGHT	N_D	θ_o (eV/atom)	γ (ergs/cm^2)	DEFECT YIELD
80 KeV $Fe^+ \longrightarrow$ αFe	55.8	507	0.21	$\gg$125	0.0
80 KeV $Ni^+ \longrightarrow$ Ni	58.7	513	0.25	125	0.44
90 KeV $Cu^+ \longrightarrow$ Cu	63.5	578	0.21	40	>1.25

TABLE 5.4.

Figure 5.1 Dark-field images of the same area of a Ni/Cr8% specimen, irradiated with 80 keV W^+ ions, obtained using the low order reflections about an [011] pole. Most of the larger images of the defect clusters are formed by Frank loops lying on the edge-on (α and γ) planes. An edge-on perfect loop (P) and an inclined Frank loop (δ,β) are circled.

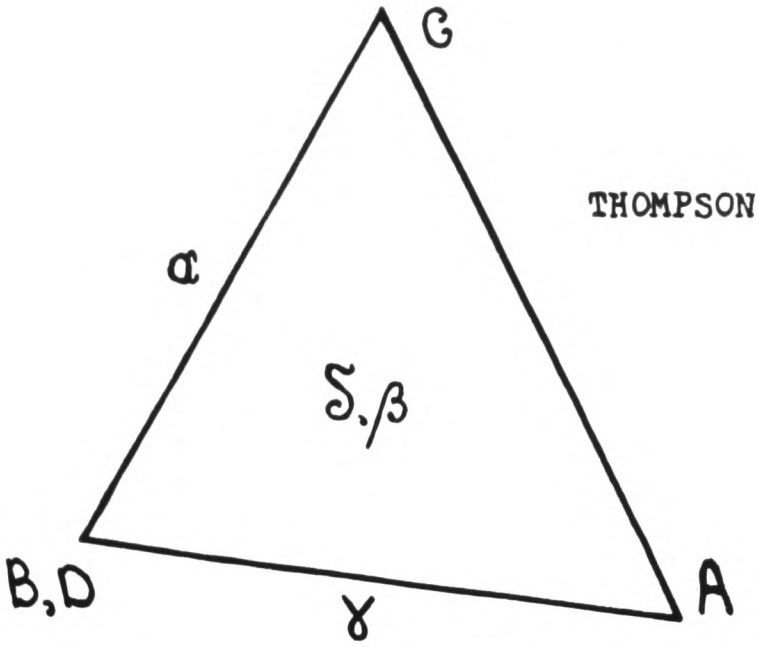

THOMPSON'S TETRAHEDRON

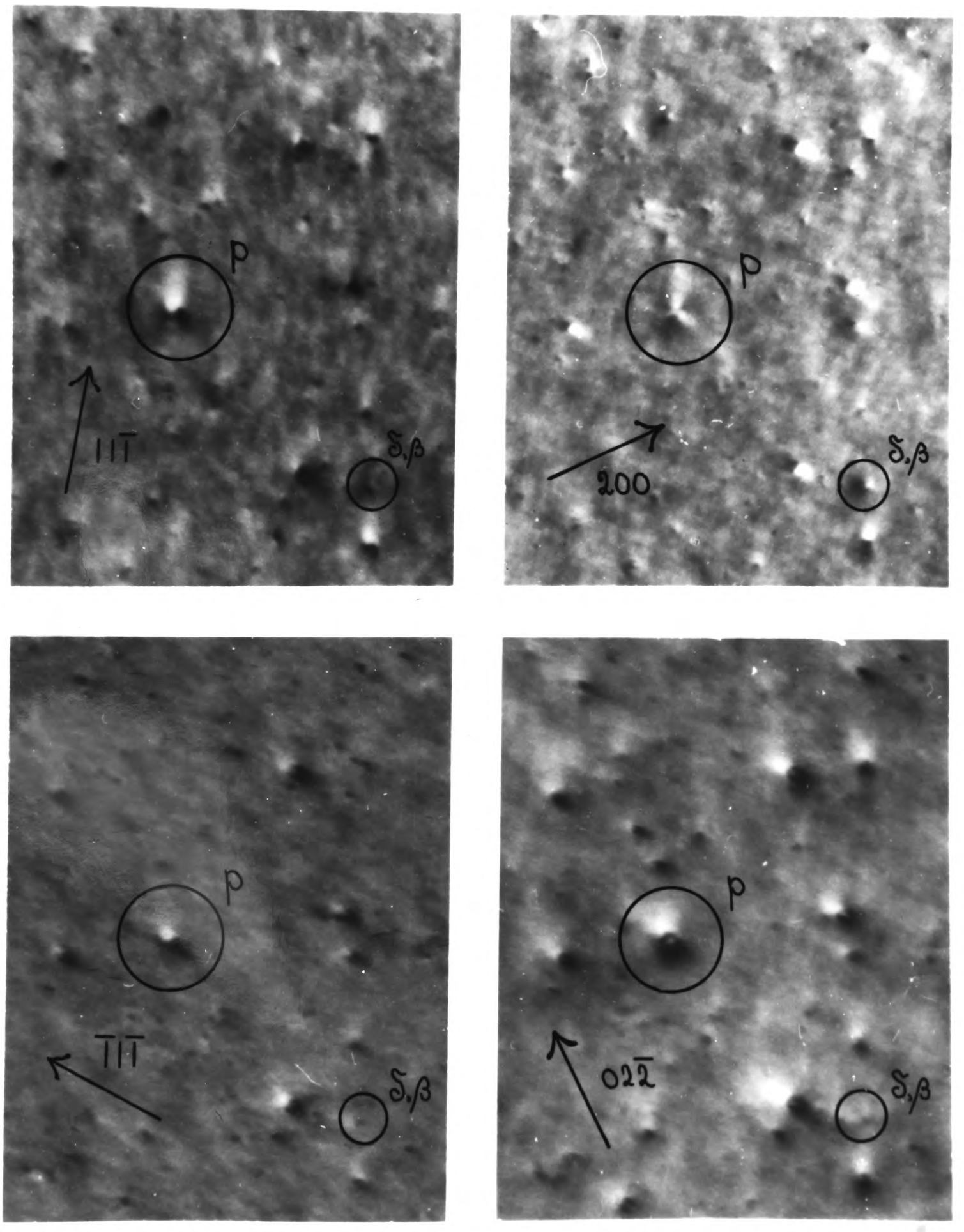

1,000 Å

Figure 5.2(a) $\underline{g}$ = <002> dark-field images of the damage structures generated by 80 keV W^+ ion irradiations of <110> grains of polycrystalline Ni, Ni/Cr8% and Ni/Cr17% to doses of 2×10^{11} ions cm^{-2}.

Thompson's tetrahedron viewed along a <110> direction.

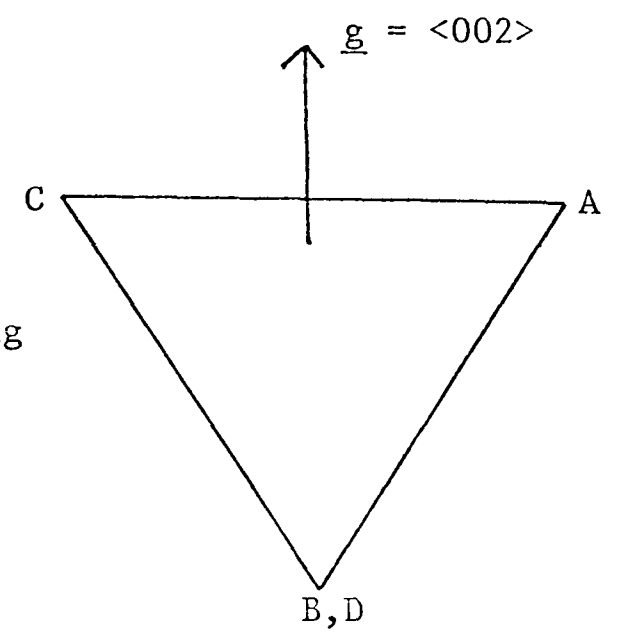

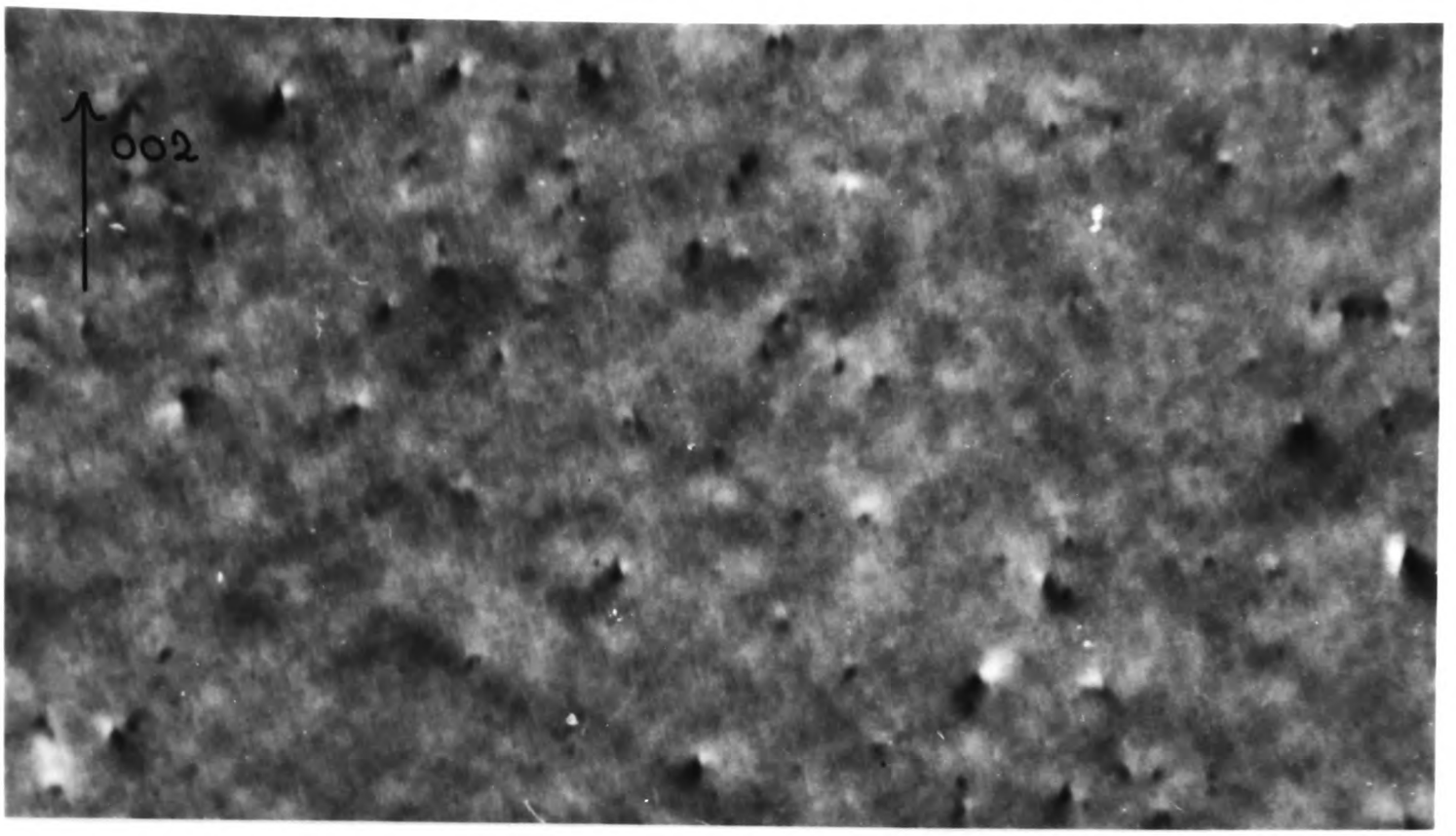

Ni⟨110⟩

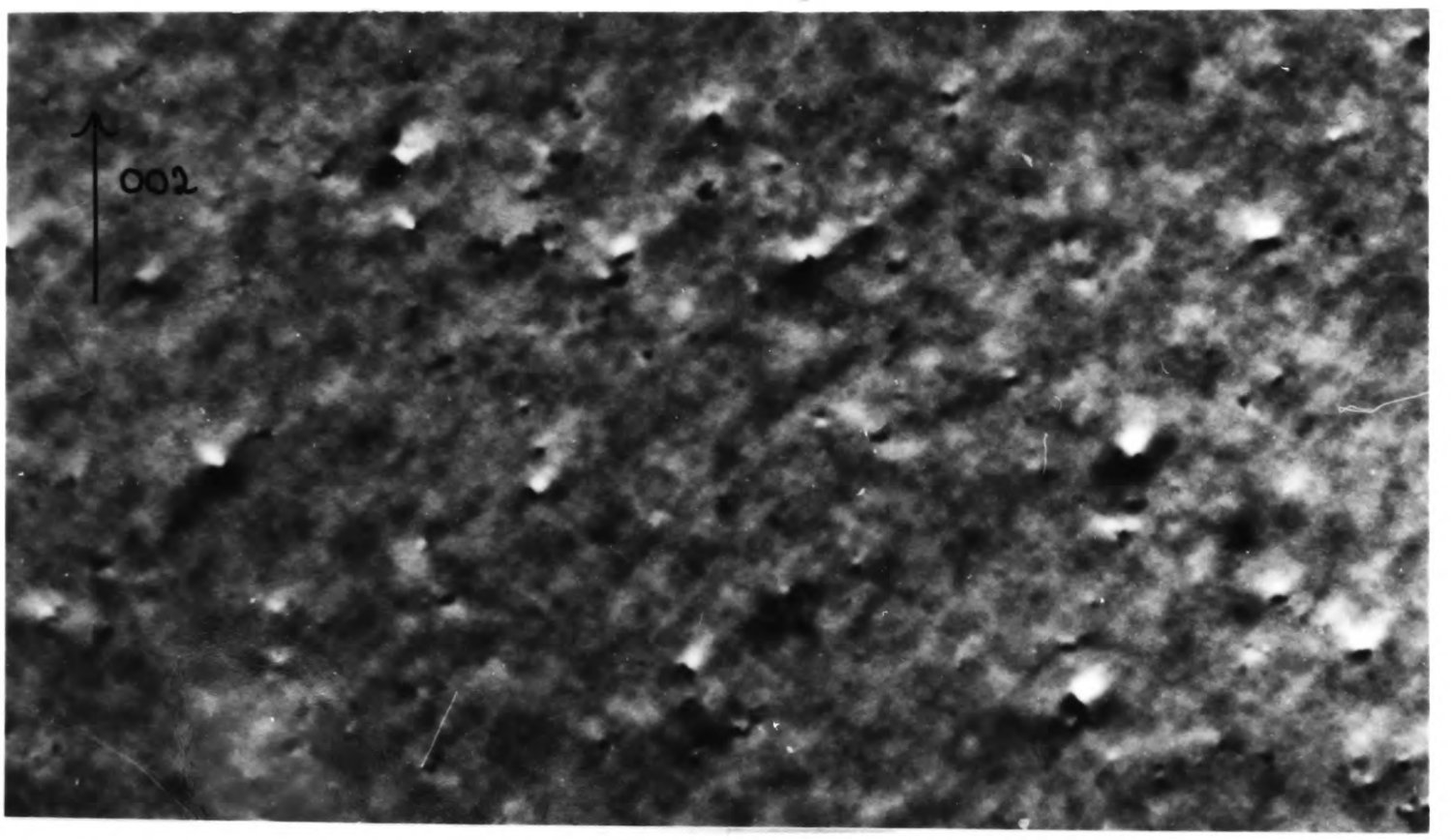

Ni/Cr8%⟨110⟩

Ni/Cr17%⟨110⟩

1,000 Å

Figure 5.2(b) $\underline{g}$ = <002> dark-field images of the damage structures generated by 80 keV W^+ ion irradiations of <100> grains of polycrystalline Ni, Ni/Cr8% and Ni/Cr17% to doses of 2×10^{11} ions cm^{-2}.

Thompson's tetrahedron viewed along a <100> direction.

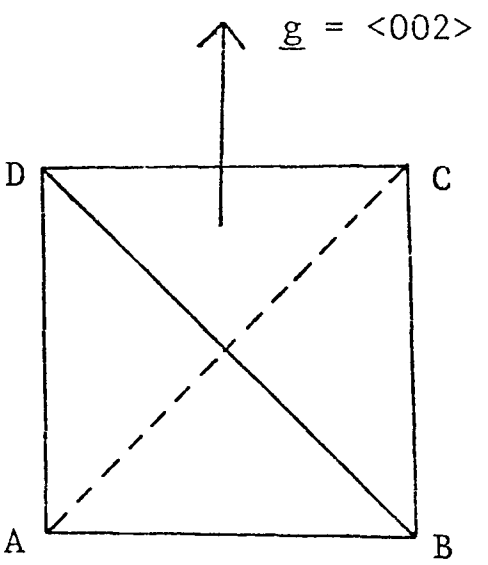

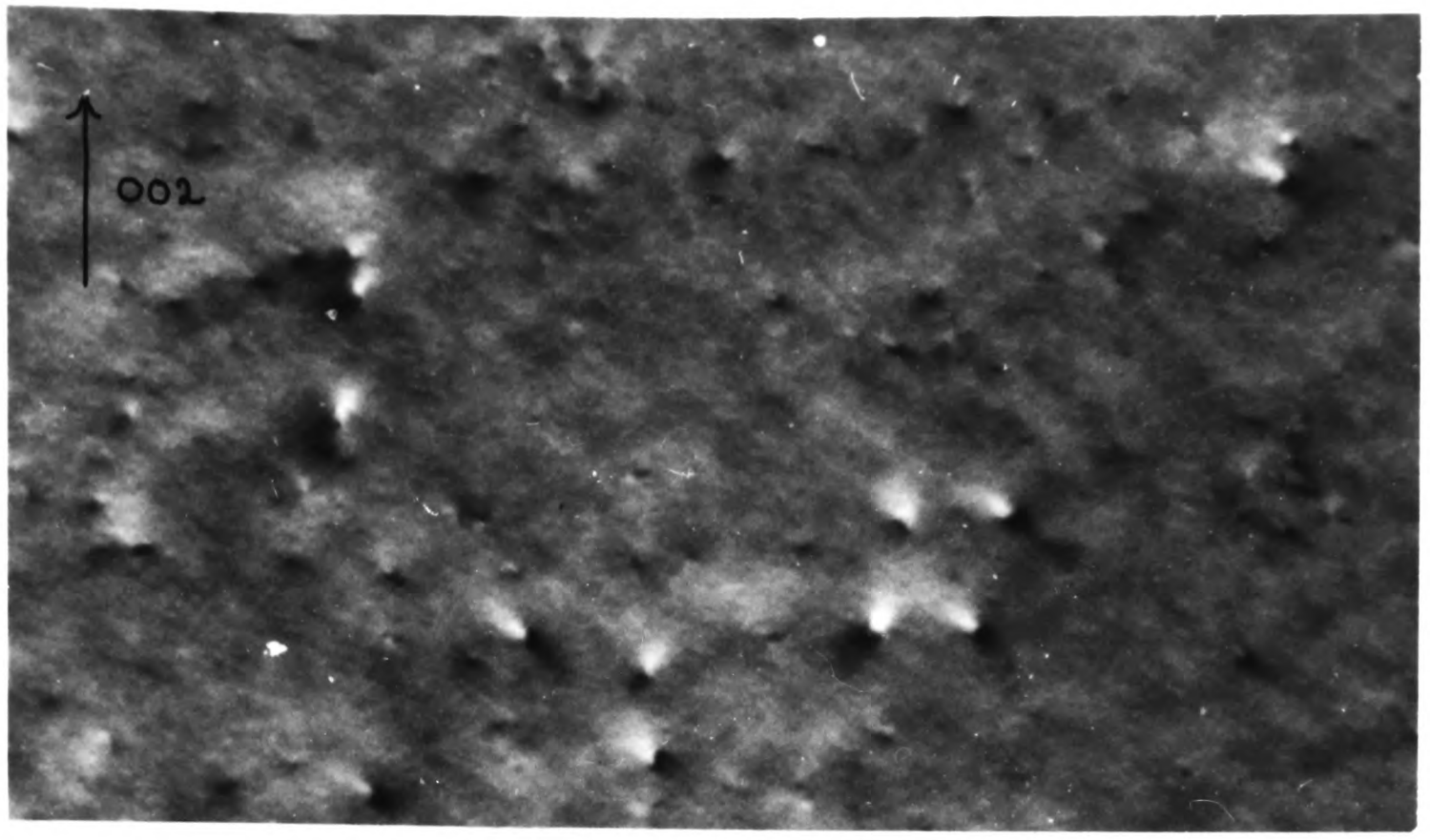

Ni⟨100⟩

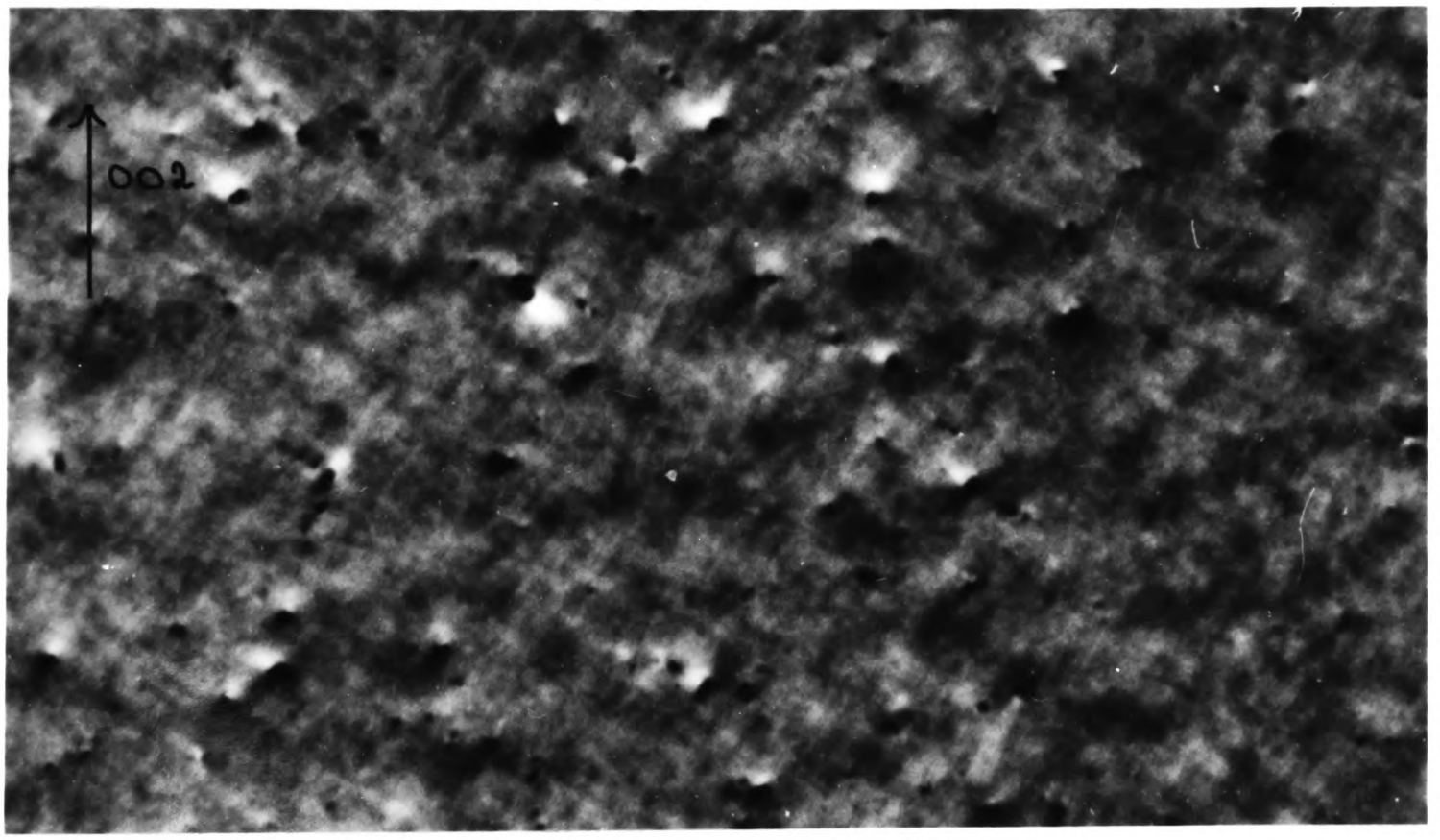

Ni/Cr8%⟨100⟩

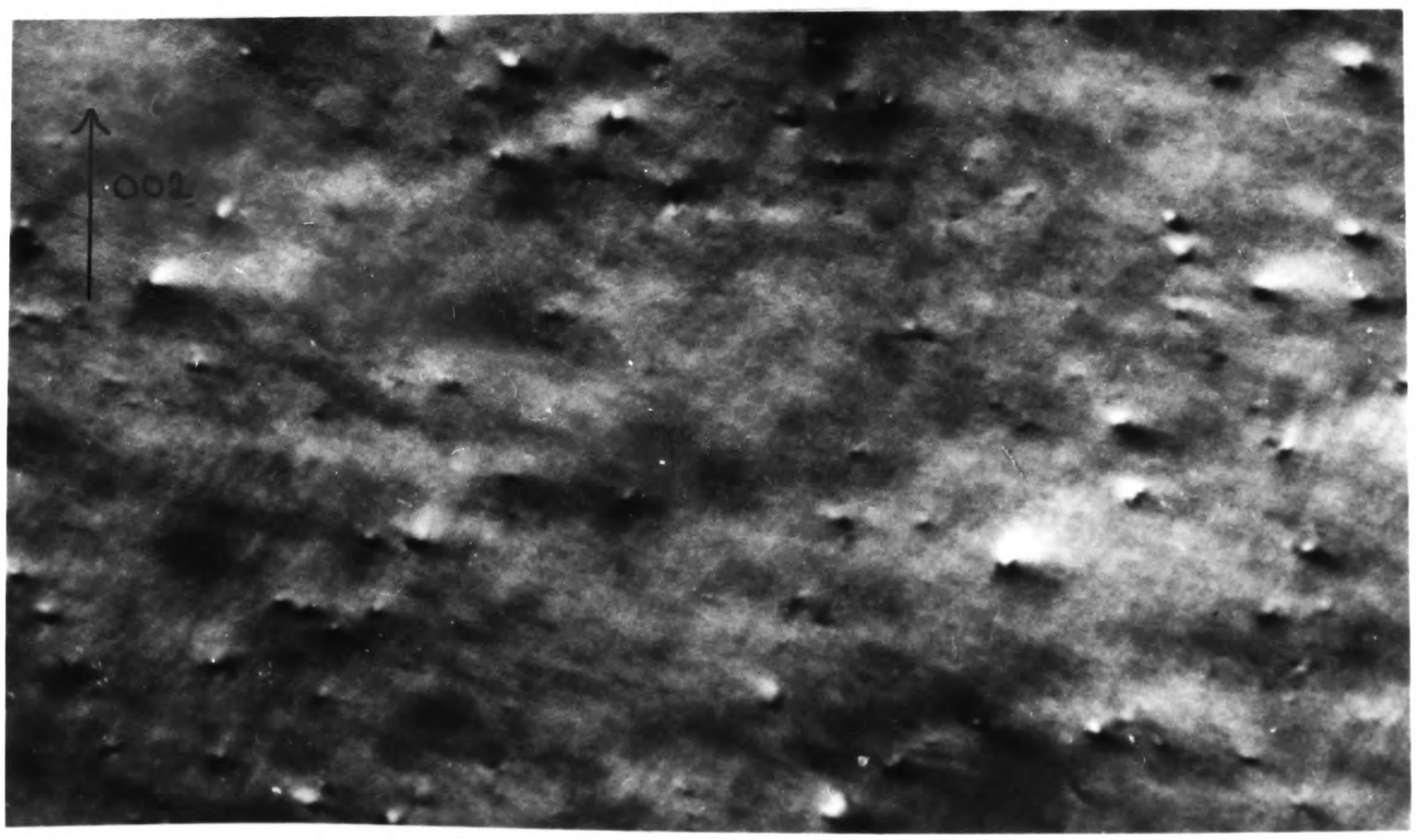

Ni/Cr17%⟨100⟩

1,000 Å

Figure 5.3 Size distributions, normalised to doses of 10^2 incident ions, of the damage structures illustrated by figure 5.2(a).

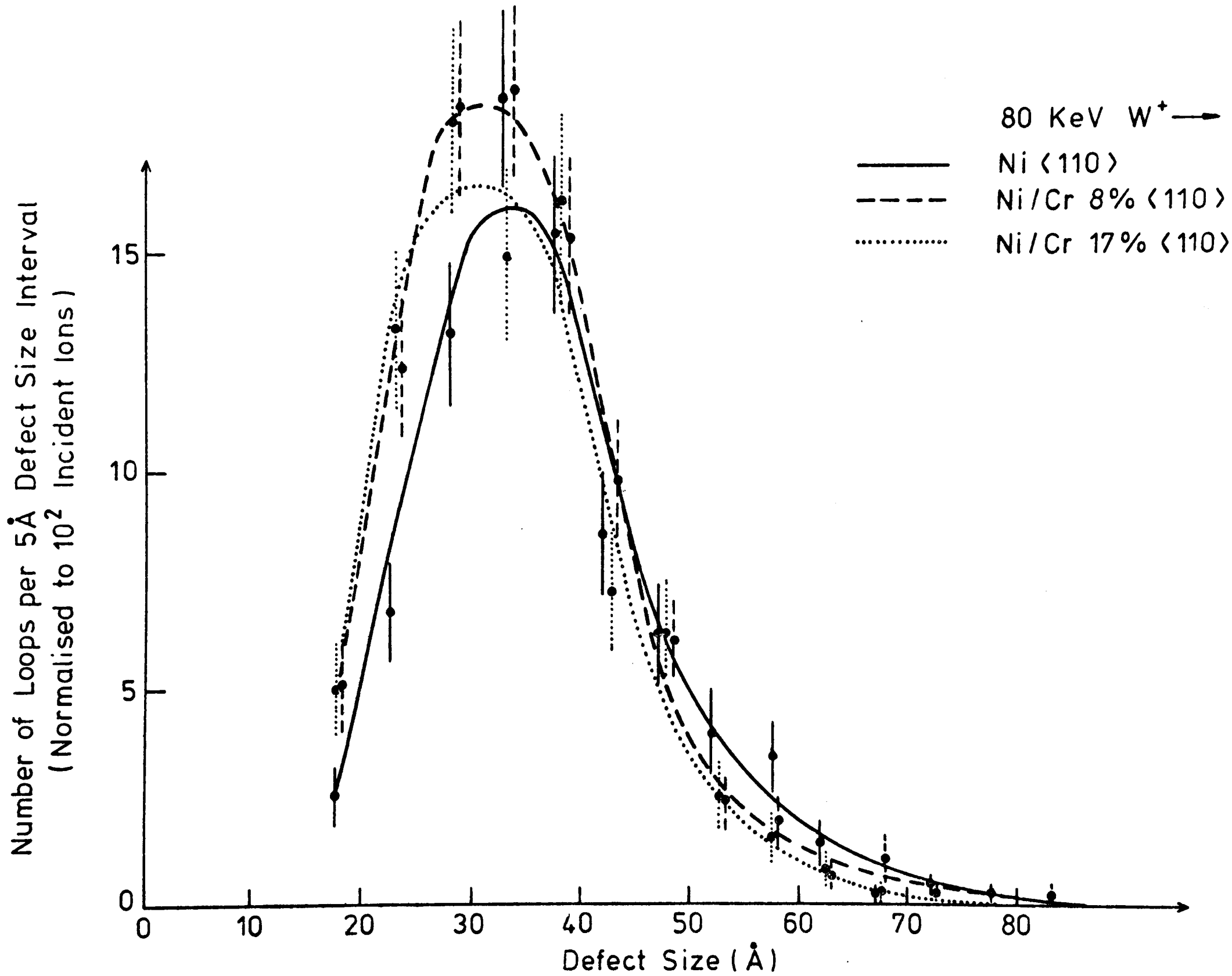
80 KeV W+
Ni ⟨110⟩
Ni/Cr 8% ⟨110⟩
Ni/Cr 17% ⟨110⟩
Number of Loops per 5Å Defect Size Interval
(Normalised to 10² Incident Ions)
0
5
10
15
0
10
20
30
40
50
60
70
80
Defect Size (Å)

Figure 5.4 $\underline{g}$ = <002> dark-field images of the damage structures generated by 80 keV W^+ ion irradiations of <110> grains of Ni, Fe/Ni10%/Cr17% and 321 stainless steel to doses of 2×10^{11} ions cm^{-2}.

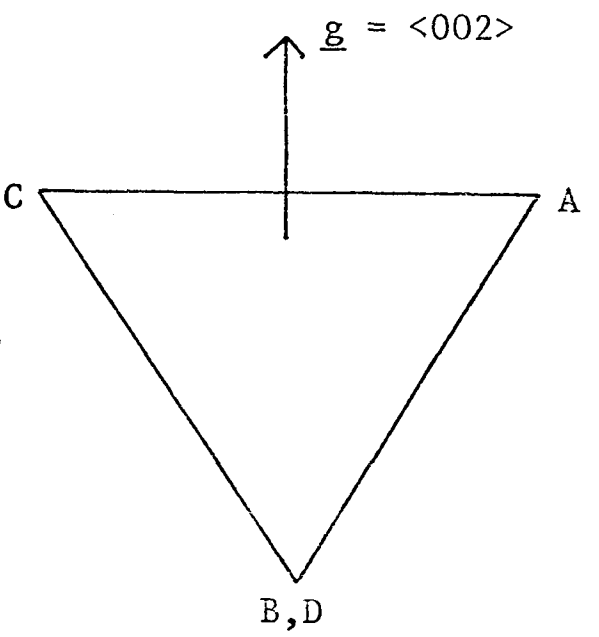

Thompson's tetrahedron viewed along a <110> direction.

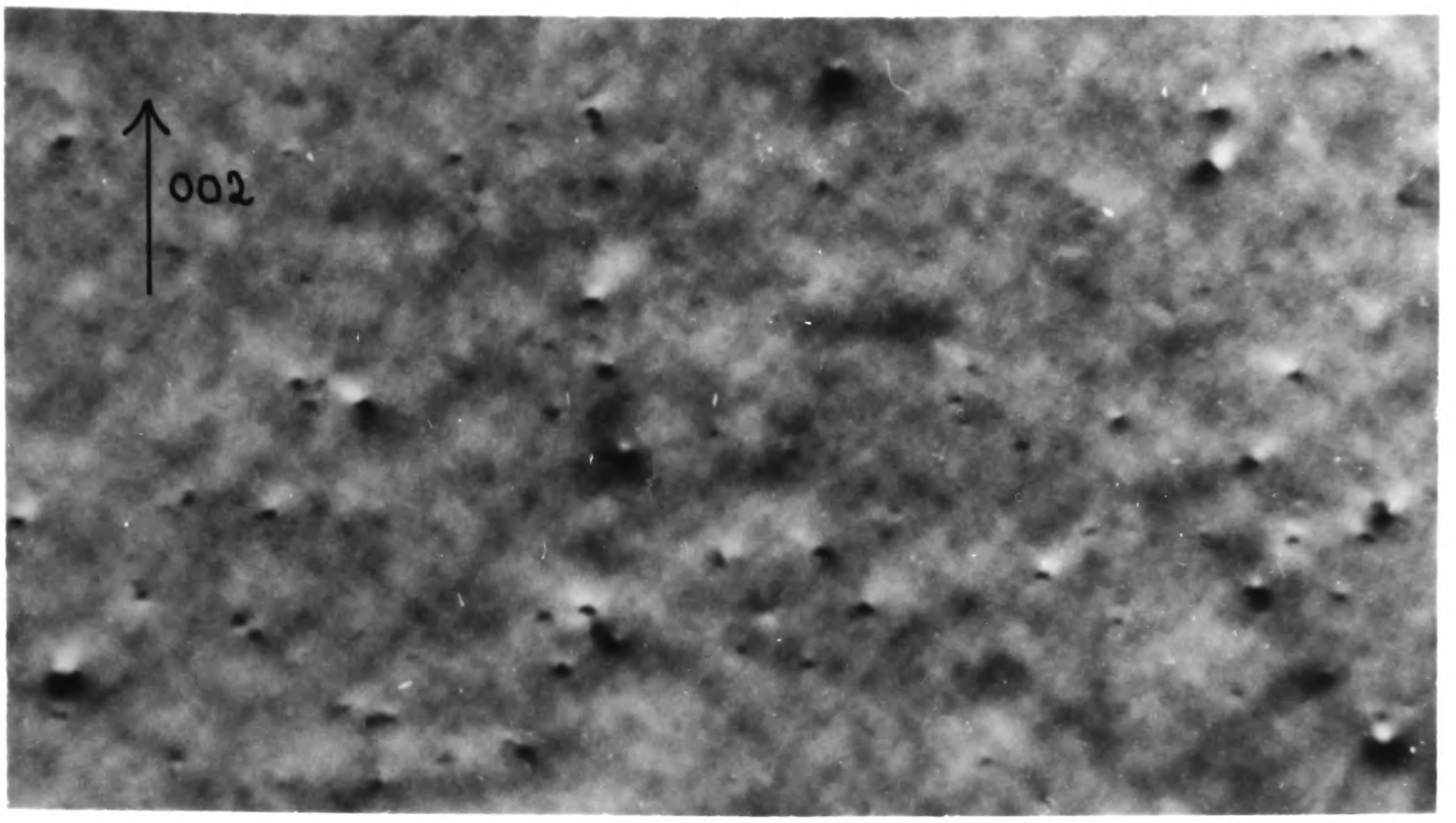

Ni

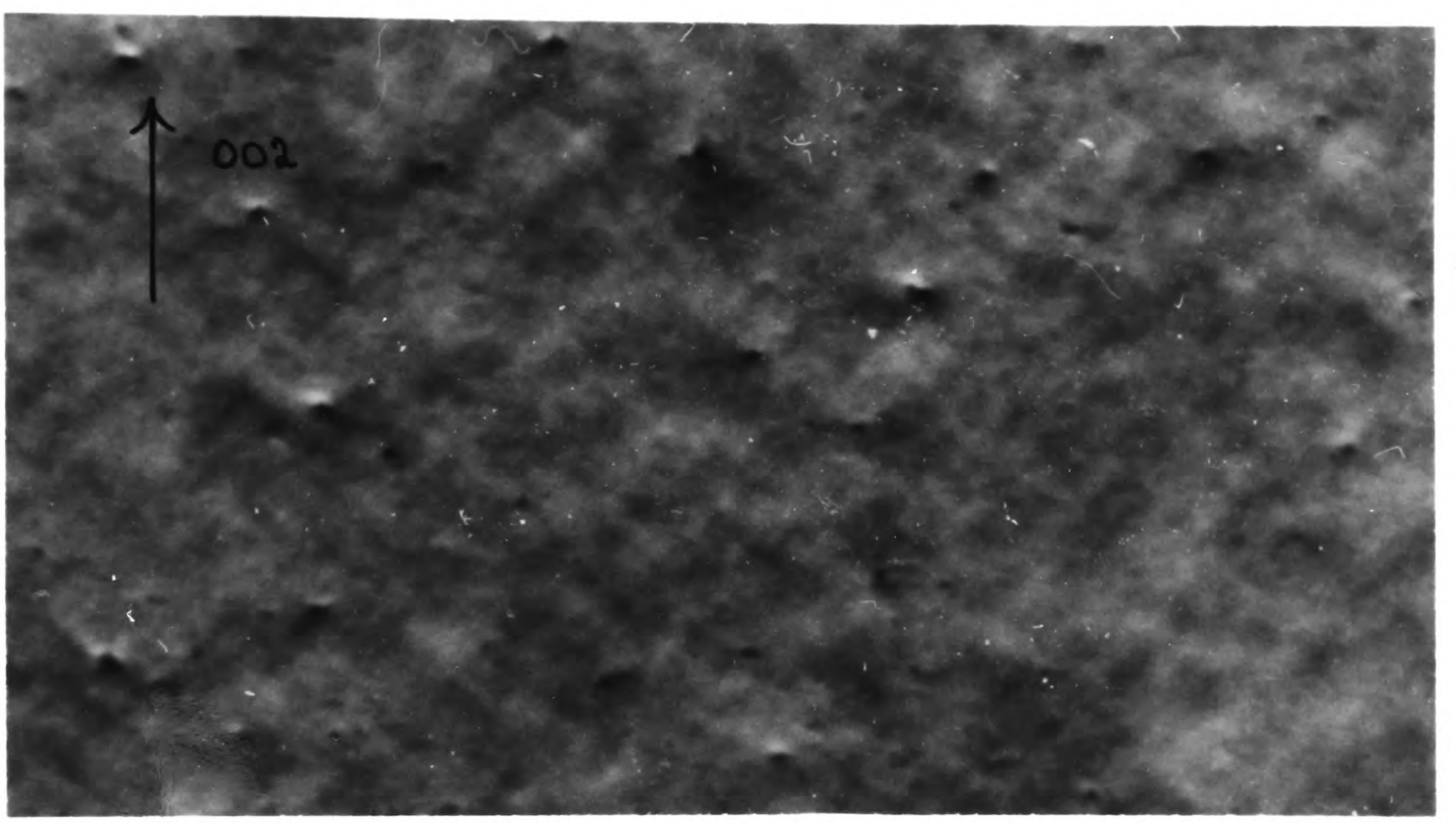

Fe/Ni10%/Cr17%

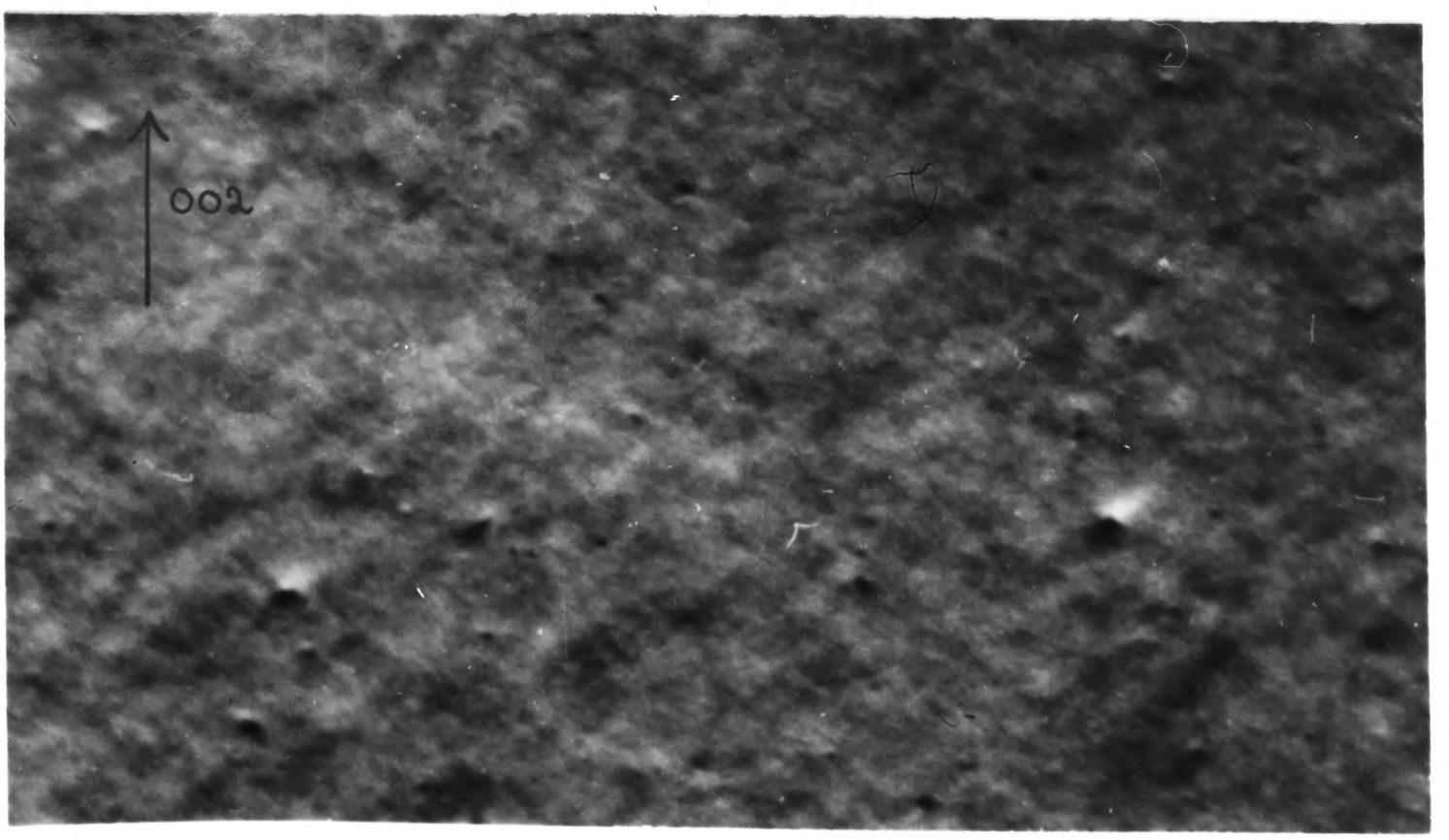

321 St.St.

1,000 Å

Figure 5.5 Size distributions, normalised to doses of 10^2 incident ions, of the damage structures illustrated by figure 5.4.

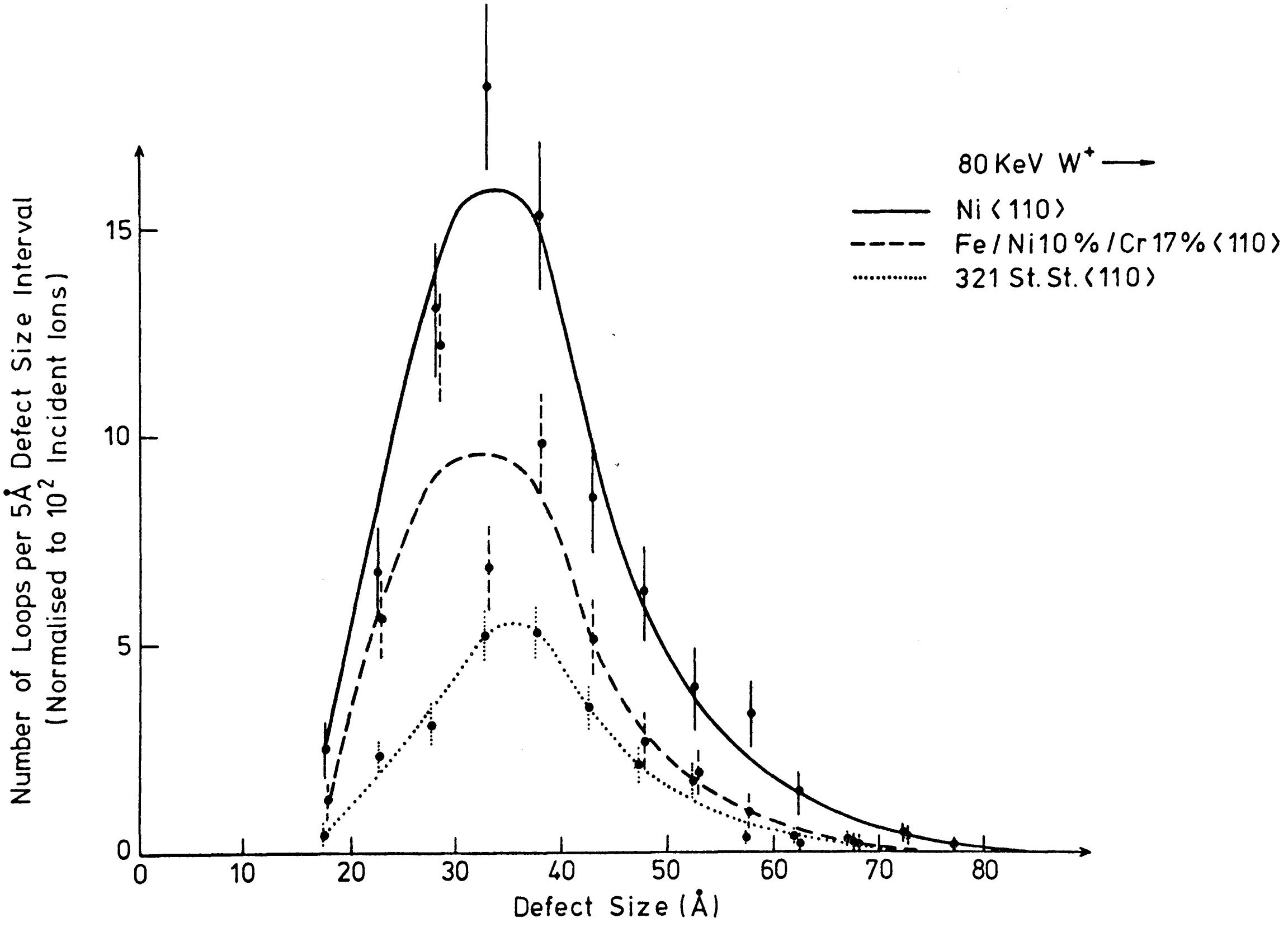
80 KeV W+
Ni ⟨110⟩
Fe / Ni 10 % / Cr 17 % ⟨110⟩
321 St. St. ⟨110⟩
Number of Loops per 5Å Defect Size Interval
(Normalised to 10² Incident Ions)
0
5
10
15
0
10
20
30
40
50
60
70
80
Defect Size (Å)

Figure 5.6 Size distributions, normalised to 10^2 visible defect clusters, of the damage structures illustrated by figure 5.4.

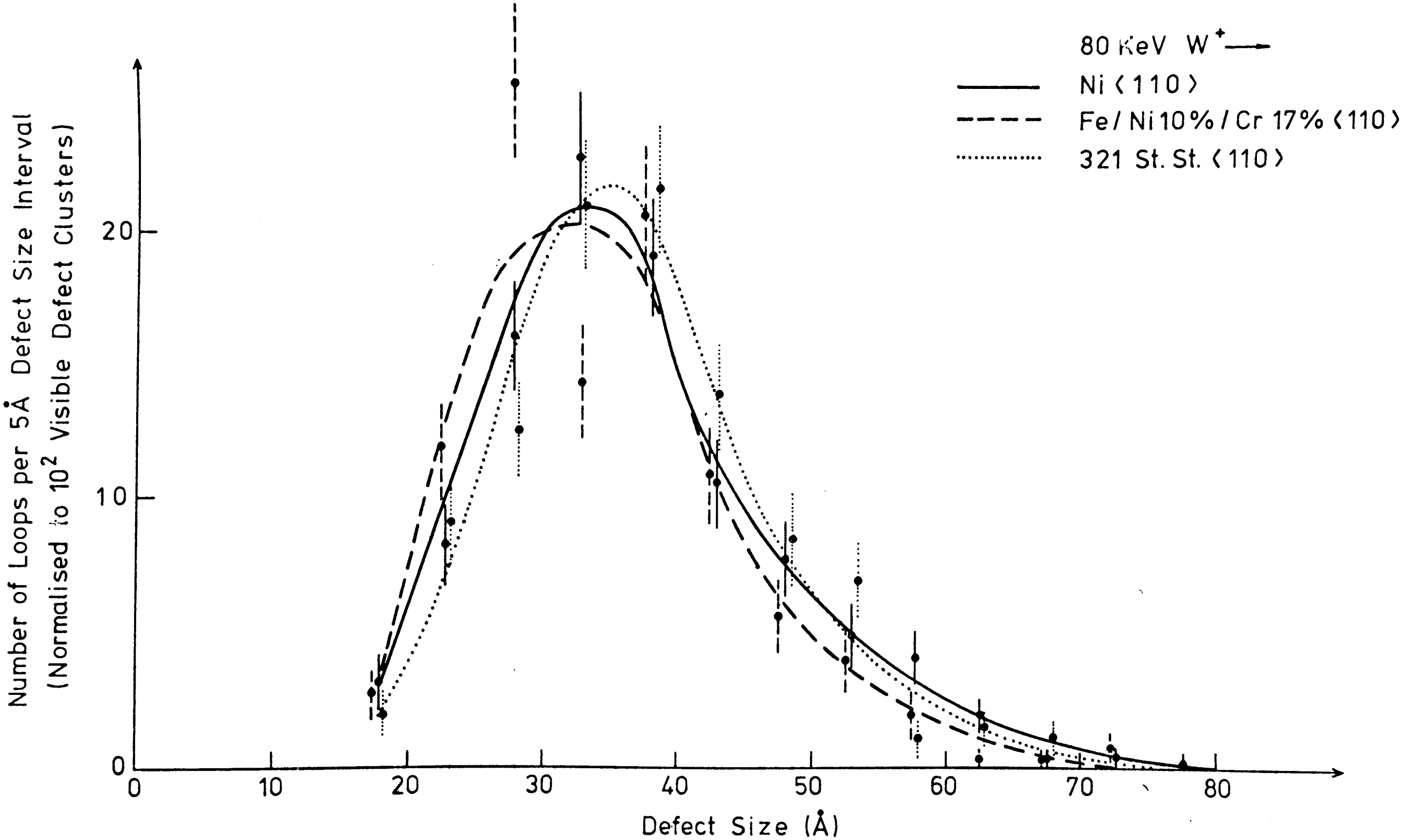
80 KeV W+
Ni ⟨110⟩
Fe/Ni 10%/Cr 17% ⟨110⟩
321 St. St. ⟨110⟩
Number of Loops per 5Å Defect Size Interval
(Normalised to 10² Visible Defect Clusters)
0
10
20
0
10
20
30
40
50
60
70
80
Defect Size (Å)

Figure 5.7 $\underline{g}$ = <002> dark-field images of the damage structures generated by 80 keV W^+ ion irradiations of <110> grains of Ni/Cr17% (containing 1070 ppm ($^W/_w$) oxygen) and Cr/Ni83% (containing 510 ppm ($^W/_w$) oxygen) to doses of 2×10^{11} ions cm^{-2}.

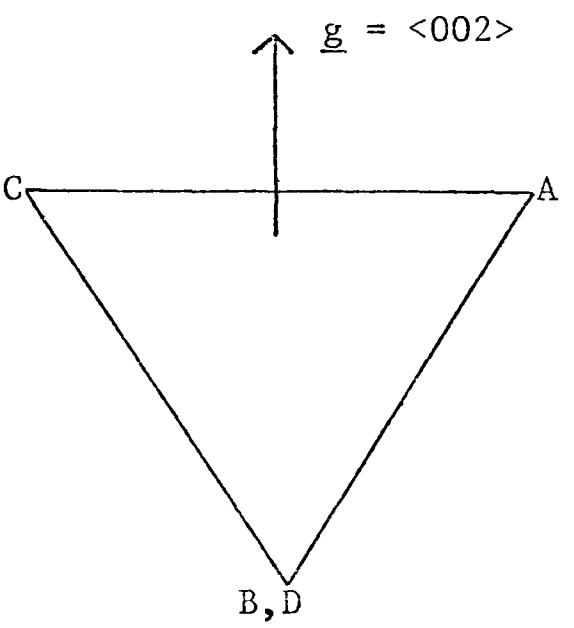

Thompson's tetrahedron viewed along a <110> direction.

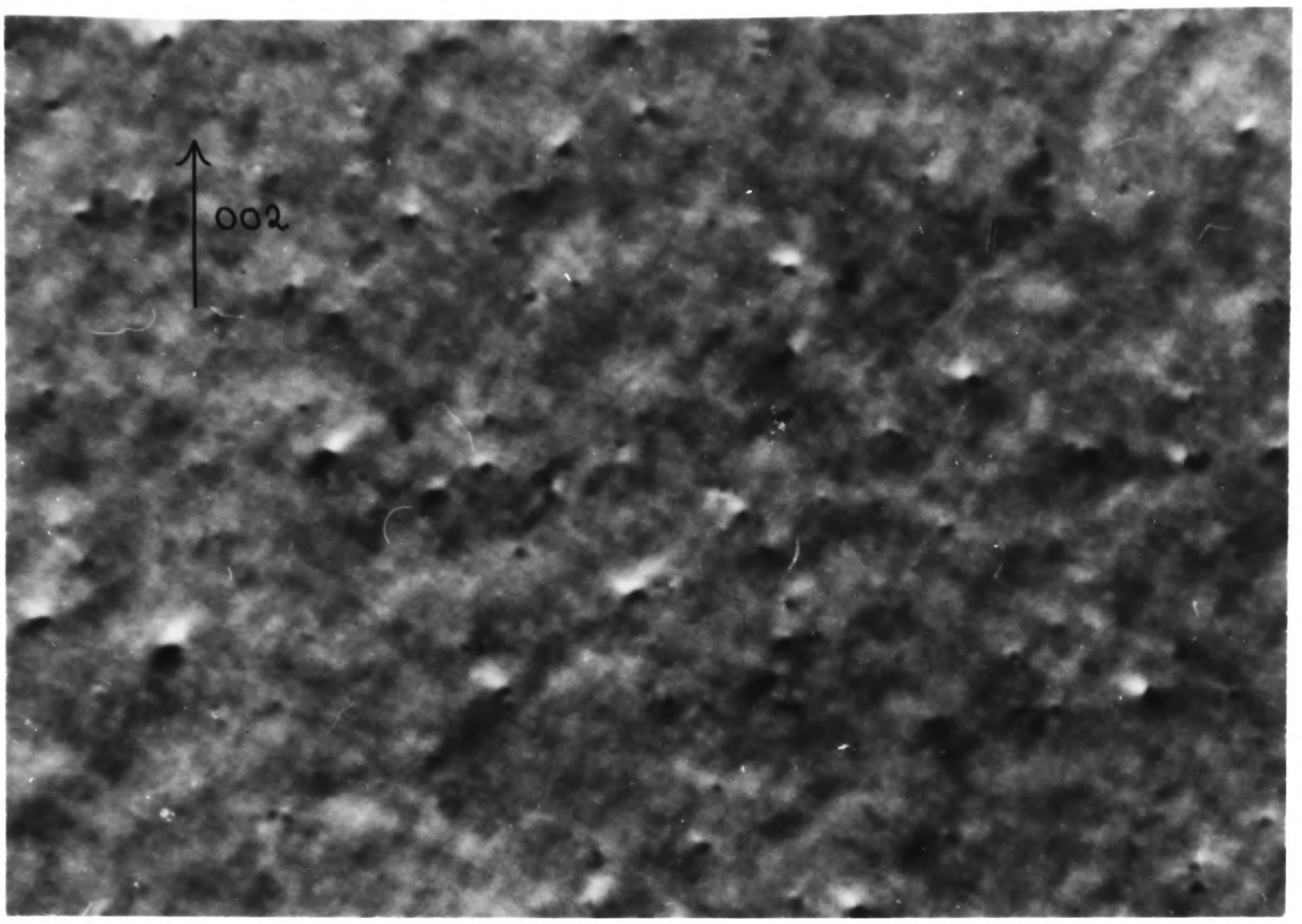

Ni/Cr 17%

1,000 Å

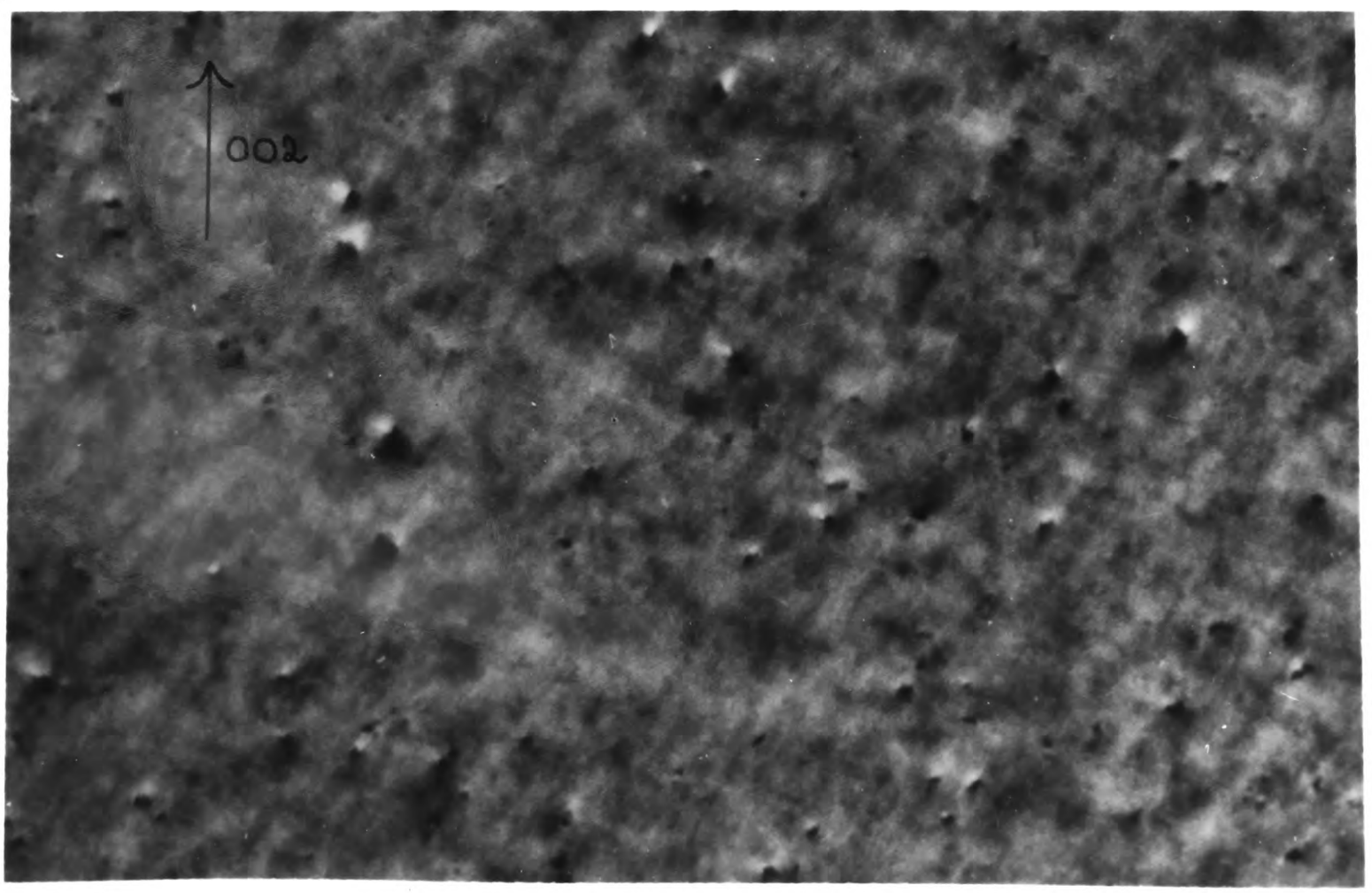

Cr/Ni 83%

1,000 Å

Figure 5.8 Size distributions, normalised to doses of 10^2 incident ions, of the damage structures illustrated by figure 5.7.

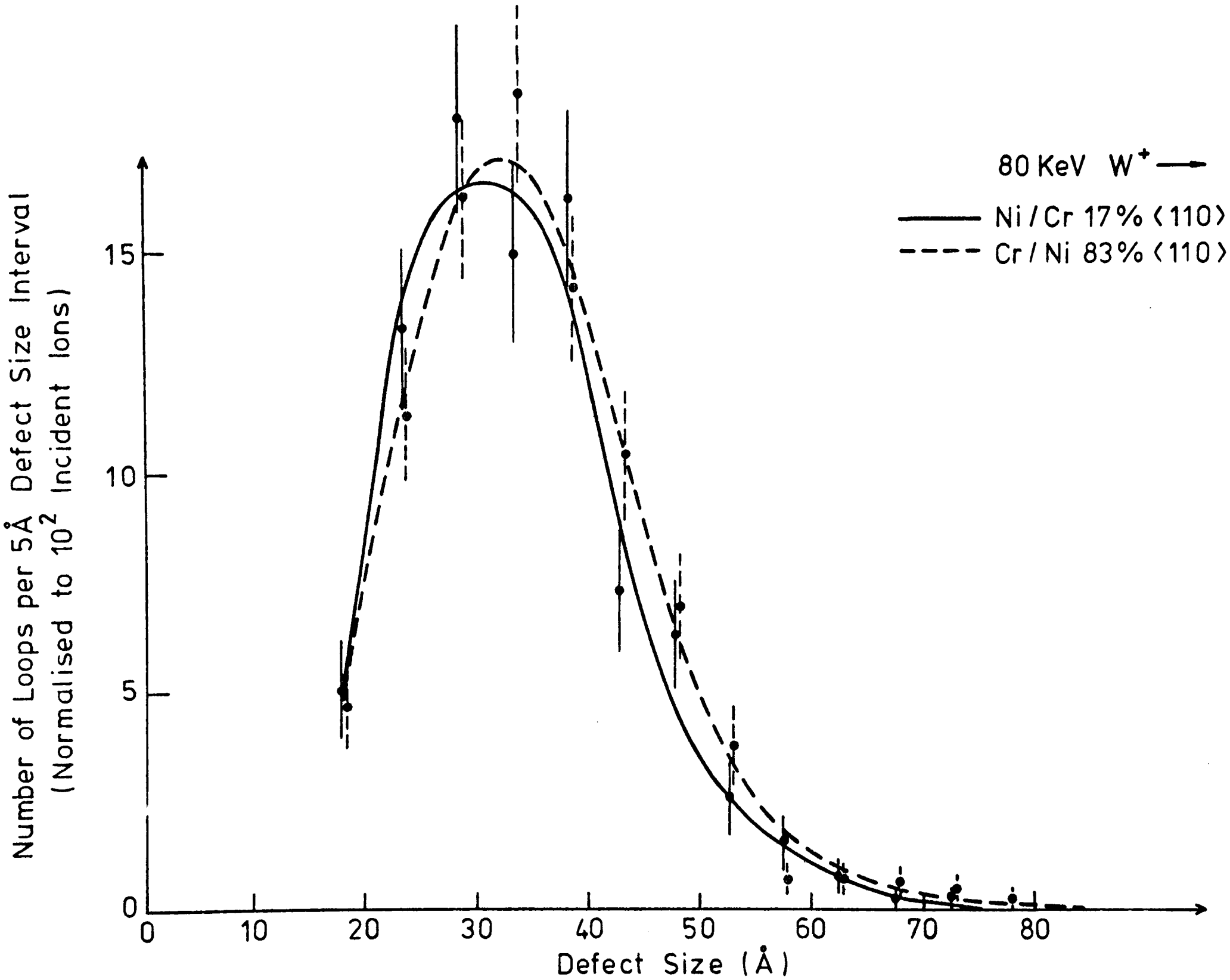
80 KeV W+
Ni / Cr 17% ⟨110⟩
Cr / Ni 83% ⟨110⟩
Number of Loops per 5Å Defect Size Interval
(Normalised to 10^2 Incident Ions)
0
5
10
15
0
10
20
30
40
50
60
70
80
Defect Size (Å)

Figure 5.9 $\underline{g}$ = <002> dark-field images of the damage structures generated by 80 keV Ni^+ ion irradiations of <110> grains of Ni, Ni/Cr8%, Ni/Cr17% and 321 stainless steel to doses of 6×10^{11} ions cm^{-2}.

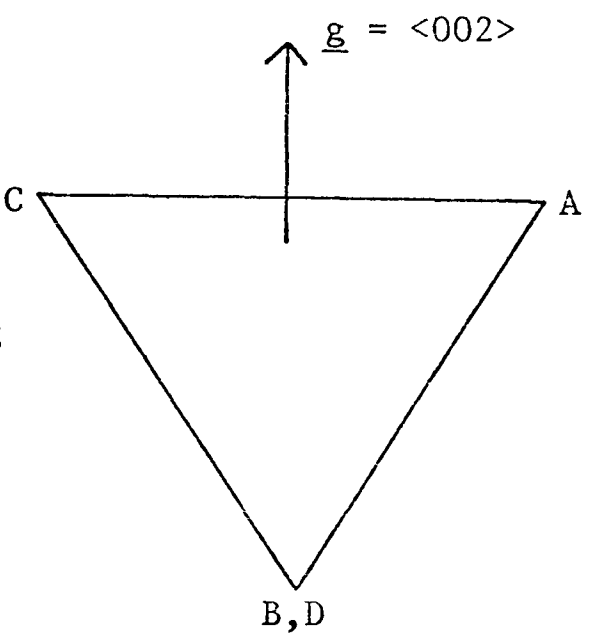

Thompson's tetrahedron viewed along a <110> direction.

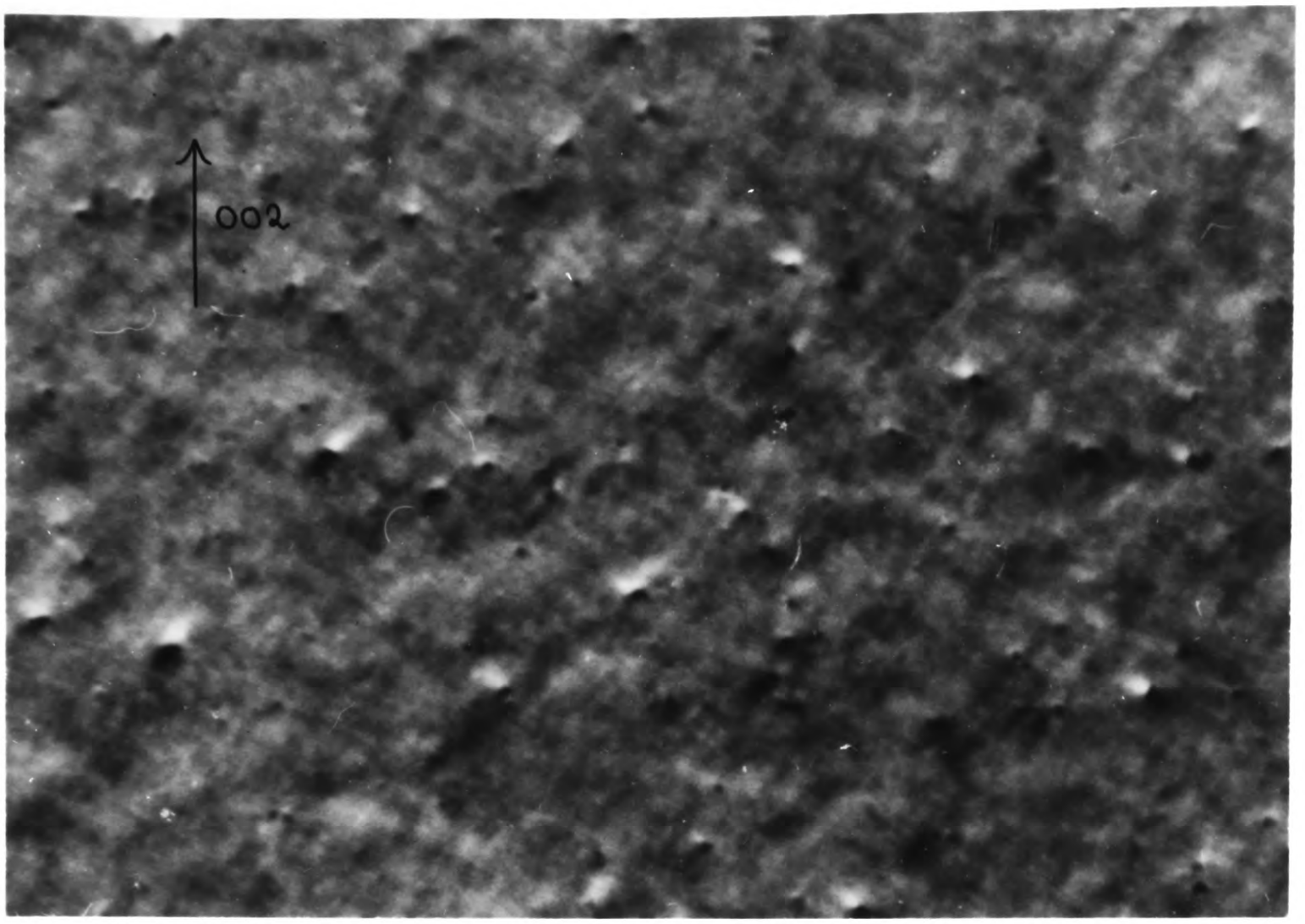

Ni/Cr 17%

1,000 Å

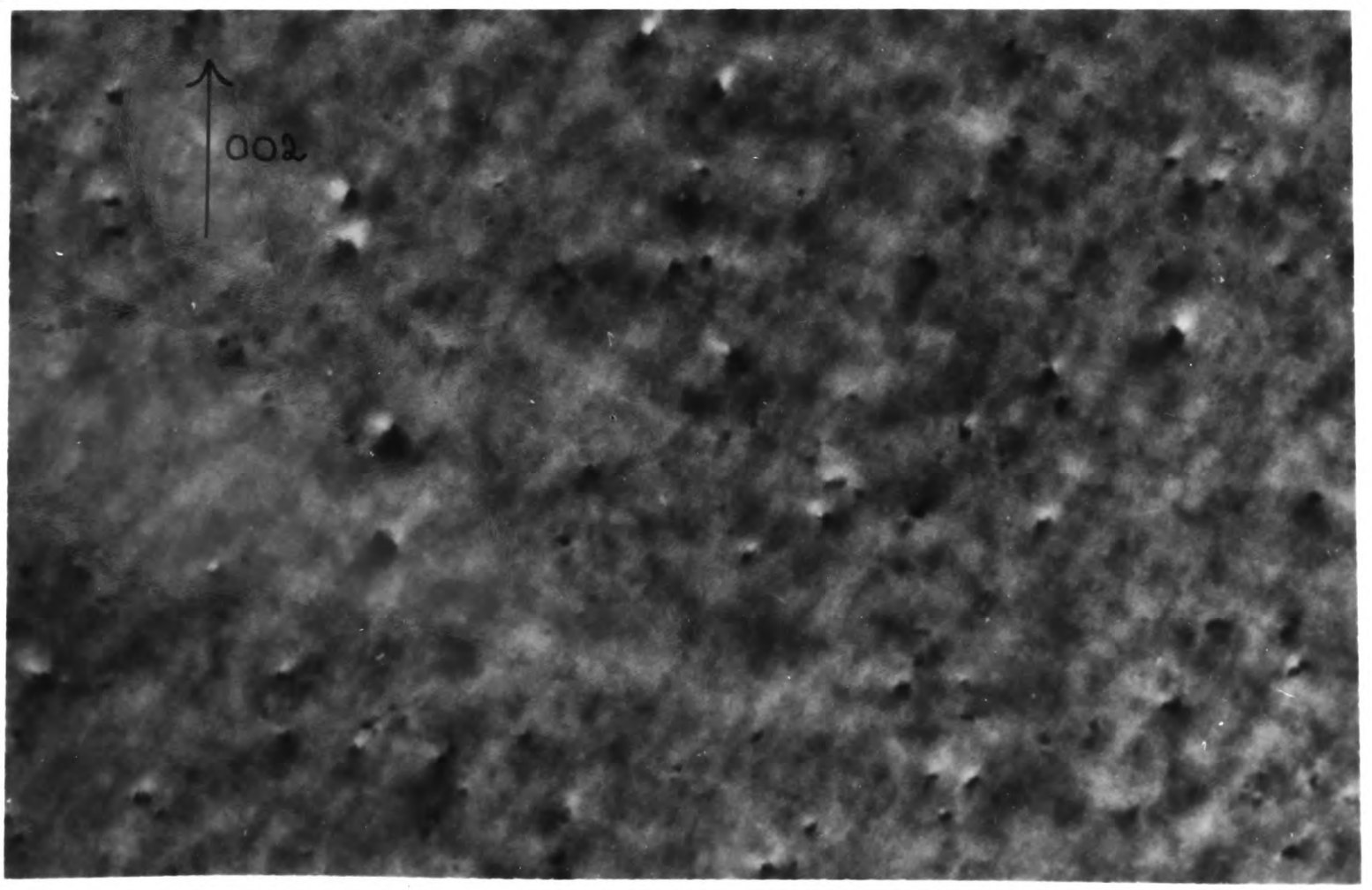

Cr/Ni 83%

1,000 Å

Figure 5.10 Size distributions, normalised to doses of 10^2 incident ions, of the damage structures illustrated by figure 5.9.

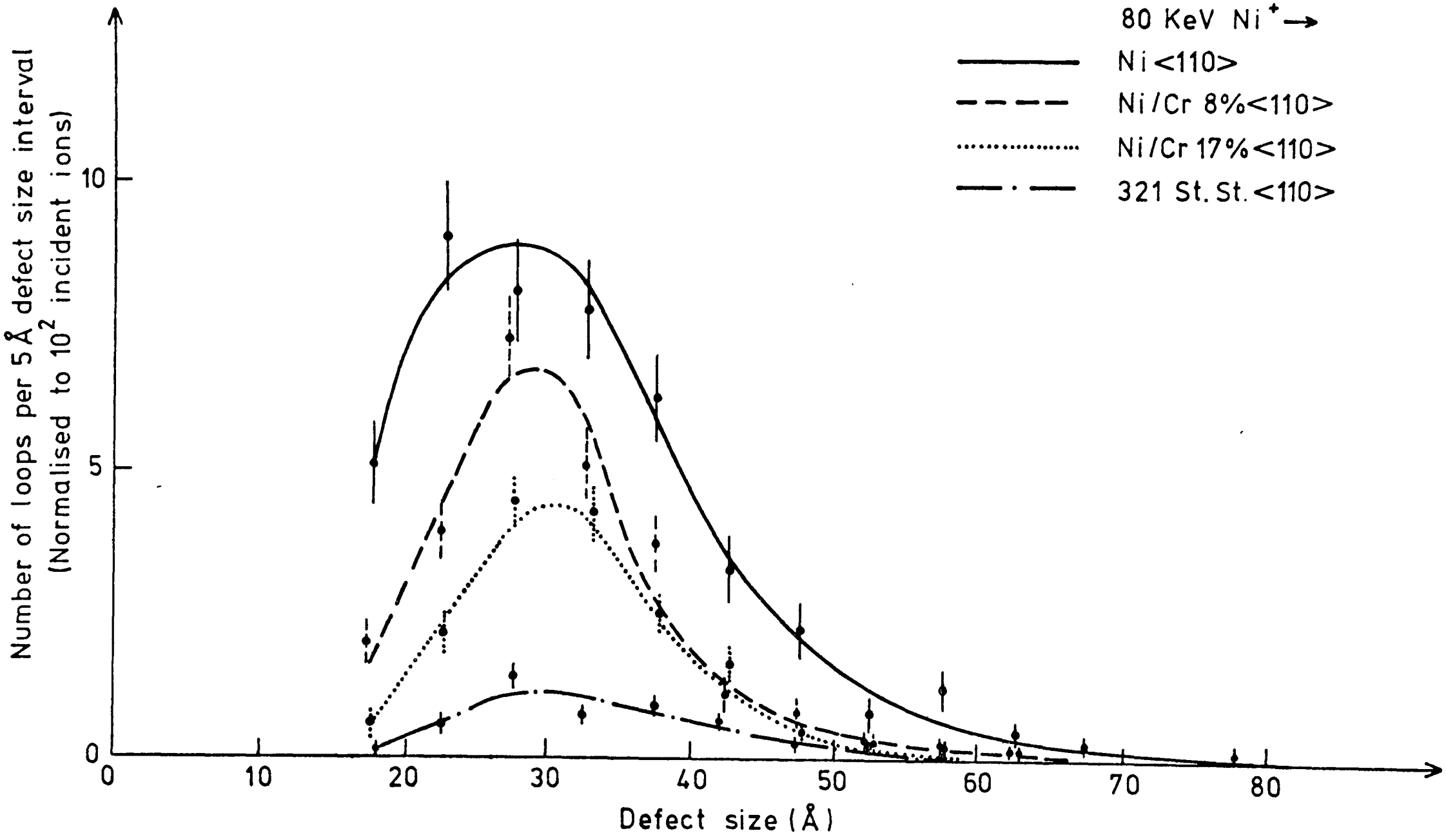
80 KeV Ni+ →
Ni <110>
Ni/Cr 8% <110>
Ni/Cr 17% <110>
321 St. St. <110>
Number of loops per 5 Å defect size interval
(Normalised to 10^2 incident ions)
0
5
10
0
10
20
30
40
50
60
70
80
Defect size (Å)

Figure 5.11 Schematic diagrams illustrating the stages in the dissociation of a triangular Frank loop (a), with its edges along <110> directions, to a stacking fault tetrahedron (d) by the Silcox-Hirsch mechanism.

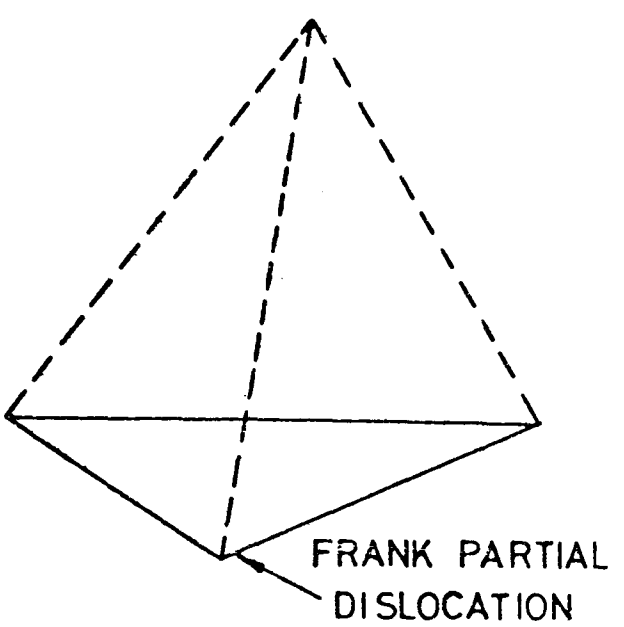
FRANK PARTIAL
DISLOCATION

(a)

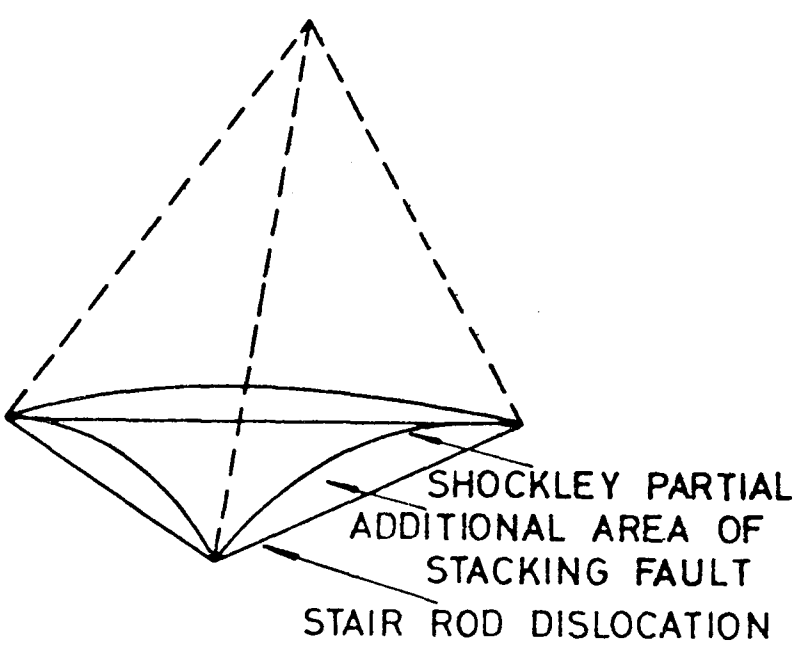
SHOCKLEY PARTIAL
ADDITIONAL AREA OF
STACKING FAULT
STAIR ROD DISLOCATION

(b)

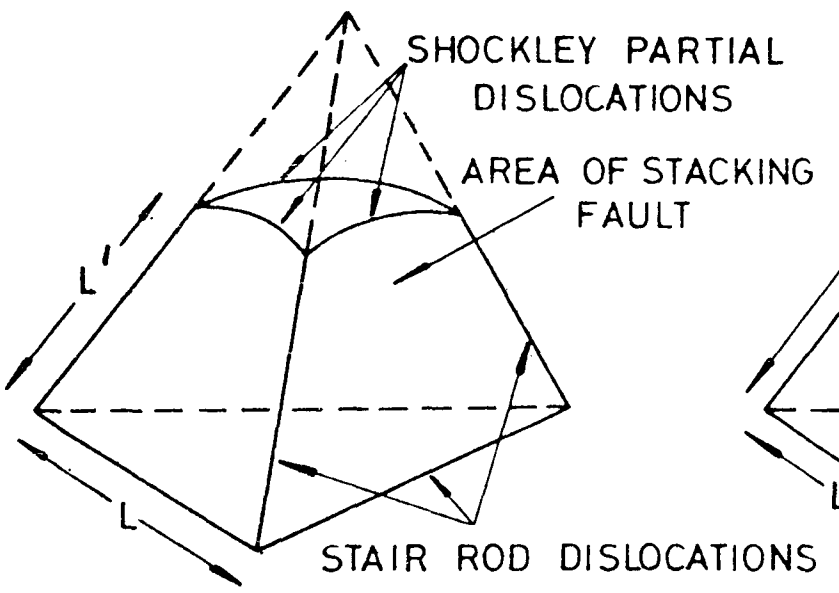
SHOCKLEY PARTIAL
DISLOCATIONS
AREA OF STACKING
FAULT
L
L
STAIR ROD DISLOCATIONS

(c)

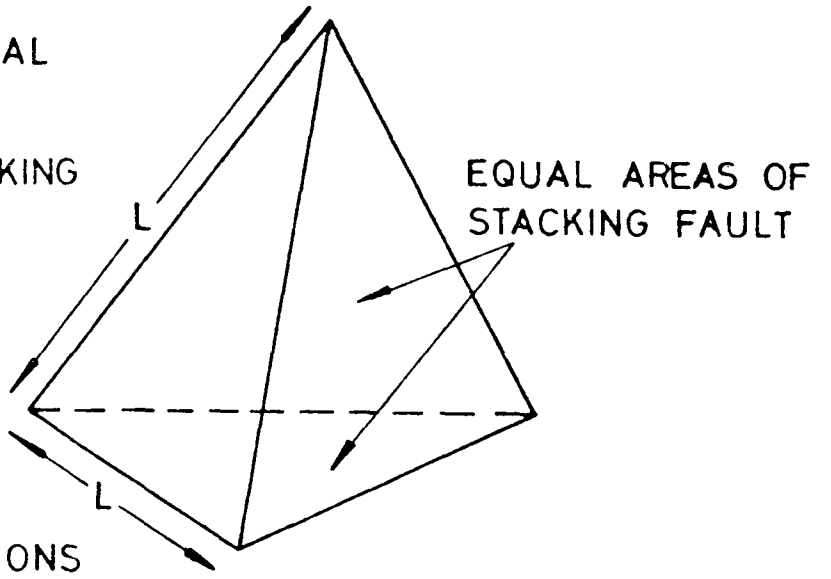
EQUAL AREAS OF
STACKING FAULT
L
L

(d)

Figure 5.12 Graphs showing the energies of the partially dissociated states (L = length of edge of base, L' = length of the dissociated edge) of small triangular Frank loops in Ni (γ = 125 ergs/cm^2) calculated using the formula of Jøssang and Hirth (1966).

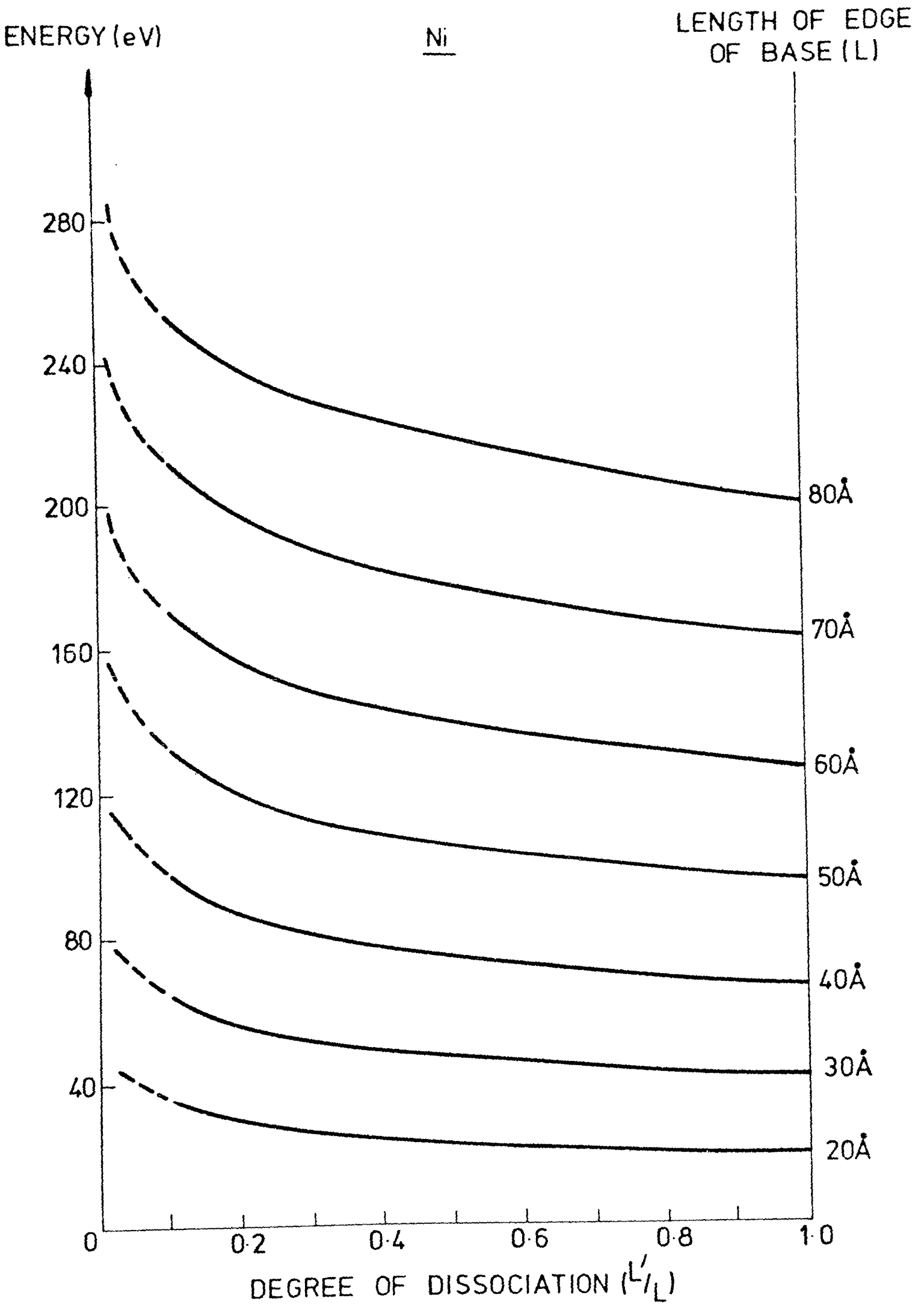
ENERGY (eV)
Ni
LENGTH OF EDGE OF BASE (L)
280
240
200
160
120
80
40
0
0·2
0·4
0·6
0·8
1·0
80Å
70Å
60Å
50Å
40Å
30Å
20Å
DEGREE OF DISSOCIATION (L'/L)

Figure 5.13 Graphs showing the energies of the partially dissociated states (L = length of edge of base, L' = length of the dissociated edge) of small triangular Frank loops in 321 stainless steel (γ = 25 ergs/cm^2) calculated using the formula of Jøssang and Hirth (1966).

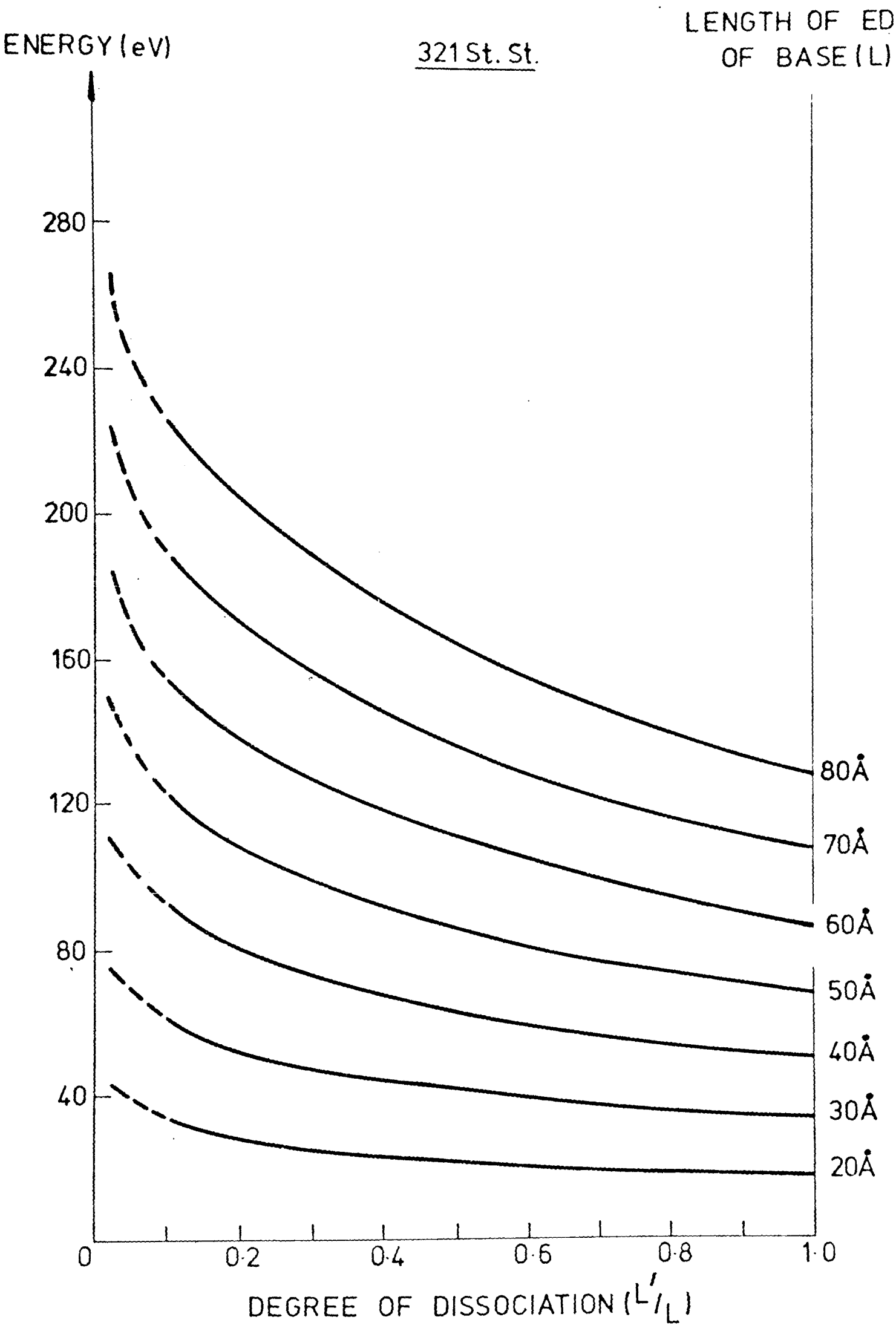
321 St. St.
LENGTH OF EDGE OF BASE (L)
ENERGY (eV)
280
240
200
160
120
80
40
80Å
70Å
60Å
50Å
40Å
30Å
20Å
0
0·2
0·4
0·6
0·8
1·0
DEGREE OF DISSOCIATION (L'/L)

Figure 5.14 Schematic diagram showing the change ΔG^{o}_{n} in the free energy of a system when n vacancies aggregate to form a loop. ΔG^{o}_{k} is the free energy barrier opposing loop nucleation which is overcome when a critical sized nucleus containing n_k vacancies is formed (Russell and Powell 1973).

Figure 5.15 Schematic diagram showing the effect of interstitial involvement on vacancy loop nucleation. ΔG^{o}_{k} is the free energy barrier to nucleation if only vacancies are present and n_k is the number of defects in the critical nucleus. $\Delta G'_{k}$ is the activation barrier if interstitials are present to interfere with the nucleation process and n'_{k} is the corresponding critical nucleus size (Russell and Powell 1973).

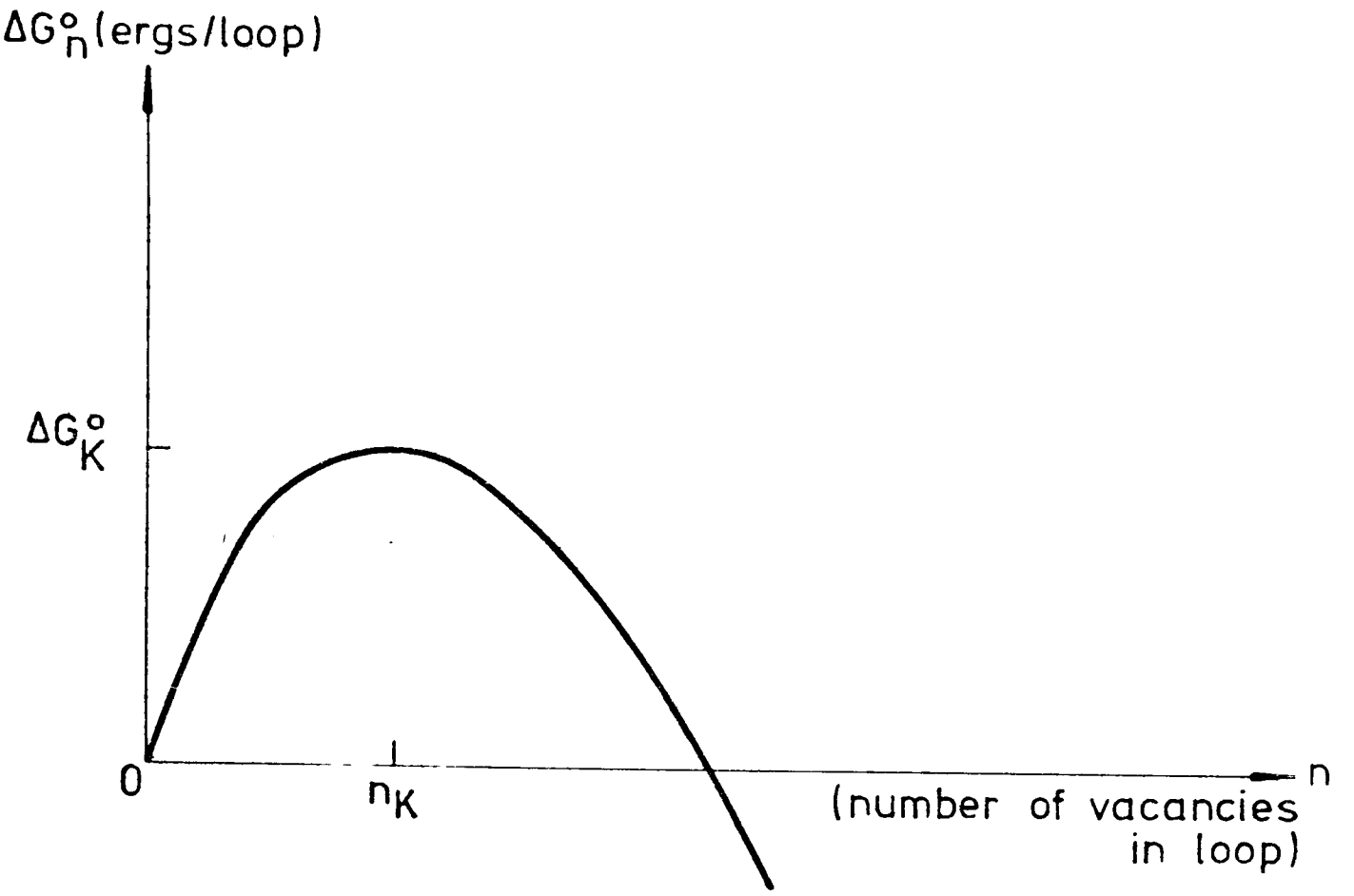
ΔG°_{n} (ergs/loop)
ΔG°_{K}
0
n_K
n
(number of vacancies in loop)

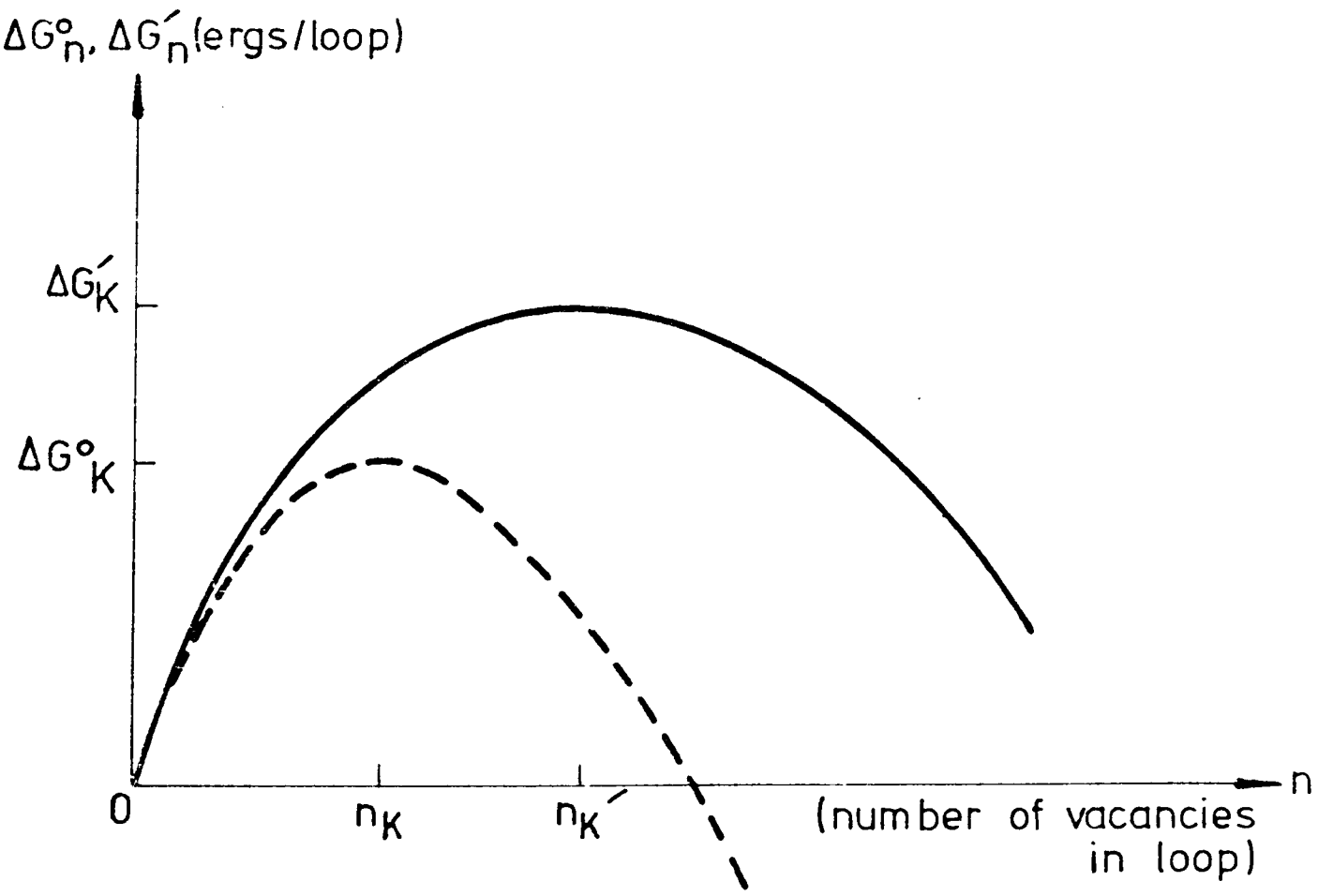
ΔG°_{n}, $\Delta G'_{n}$ (ergs/loop)
$\Delta G'_{K}$
ΔG°_{K}
0
n_K
n_K'
n
(number of vacancies in loop)

CHAPTER 6

The Temperature Dependence of the Defect Yield in Tungsten Ion Bombarded Ni and Ni/Cr17%

6.1 Introduction

The void swelling rate at fast reactor operating temperatures is reduced by the presence of a steady-state concentration of vacancy clusters which, in a given material and at a given temperature, depends on both the vacancy cluster production rate and the vacancy cluster lifetimes (see section 1.2, also Foreman and Makin 1978). The way this steady-state concentration varies with temperature can be conveniently studied by investigating the temperature dependence of the defect yield. As no results had been published previously for the temperature dependence of the defect yield in Ni, and as no investigation had been carried out as to the effect of alloying on steady-state vacancy cluster concentrations, it was decided to complete the present experimental work by investigating the temperature dependence of the defect yield in Ni and the Ni/Cr17% alloy. The results of this investigation, and a discussion of these results, are presented in this chapter.

Since a previous attempt to investigate the temperature dependence of the defect yield in self-ion irradiated Ni (English, C.A., unpublished) had proved somewhat inconclusive because of the small size of the defect clusters coupled with specimen contamination during irradiation at elevated temperatures, it was decided in the present case to increase the average size of the defect clusters by irradiating with tungsten ions. Thus the irradiations were carried out using 80 keV W^{++} ions to doses of 2×10^{11} ions cm^{-2} over a range of temperatures up to 500°C, which was the highest irradiation temperature possible.

The purity of the Ni and Ni/Cr17% specimens used in these irradiations and the methods used to determine the numbers and sizes of the defect clusters are discussed in detail in Chapter 3. The irradiation procedure is described in detail in the following section.

6.2 High Temperature Irradiation Procedure

A description of the heavy-ion accelerator used for these irradiations

is given in section 3.3.1.

The high temperature irradiations were carried out in the experimental target chamber of this accelerator. As it was only possible to accelerate ions through 40 kv before reaching this target chamber, it was necessary to use doubly charged ions to obtain the required ion energy (80 keV). Because of the possibility of charge exchange occurring for doubly charged ions, with the result that the number of ions incident on a specimen would be higher than the measured number, a comparison was carried out, in the main target chamber, between the damage structures generated by a measured dose of 2.10^{11} ions cm^{-2} of 80 keV W^{++} ions and 80 keV W^{+} ions. The results of this comparison are given in section 3.9. Within the accuracy of the experimental technique, the numbers and sizes of the defect clusters were the same in both cases, and it was concluded that using doubly charged ions did not introduce any significant error into the dose measurement.

The target assembly used in the high temperature irradiations was a cylindrical molybdenum block with a single row of four, 3 mm diameter holes drilled in the top of it. The specimens were loaded in these holes underneath copper retaining grids and held firmly in position by circlips. As well as ensuring that the specimens would be normal to the ion beam, the circlips held the specimens in good thermal contact with the target block. The target assembly was then mounted in the experimental target chamber and heated by an insulated electrical winding, placed in the base of the cylinder, to the required irradiation temperature. It was held at this temperature for ten minutes before being irradiated, to ensure that the specimens would be in thermal equilibrium with the block. The temperature of the block was measured using a chromel-alumel thermocouple attached to the face of the target assembly and was known to an accuracy of $\pm 2^{o}C$.

The target assembly was mounted 3 cms behind a graphite beam defining aperture and the ion beam was scanned over this aperture by applying small fluctuations to the ion source potential. The dose incident on the specimens was found from the charge falling on the target assembly and

a surrounding Faraday cup. Additional suppression of secondary electrons was obtained using a 100 gauss magnetic field. Since the ion beam had a divergence of $\pm 2^{o}$, the exact area that had been irradiated was found by placing a lightly greased aluminium foil in front of the target assembly. The ion beam 'burnt' this foil and so the irradiated area could be measured directly. It was also possible to put a beam stop directly in front of the target assembly. By comparing the charge falling on the beam stop with that falling on the target assembly, a check could be made to ensure that there was no leakage current from the heater windings in the base of the target assembly.

When the irradiation had been completed, the heating coil was switched off, the vacuum of the target chamber was isolated, and the target assembly was rapidly cooled by introducing vapourised liquid nitrogen into the target chamber. Figure 6.1 shows typical post irradiation cooling curves for the target assembly. The time elapse between completing an irradiation and introducing the nitrogen varied slightly from one irradiation to another as the cooling procedure was carried out manually, but was typically about twenty seconds.

The number of defect clusters remaining in a foil of a given material after irradiation at temperatures (in the present case $>400^{o}C$) at which the clusters shrink by thermal emission of vacancies depends on the irradiation temperature, the irradiation time and the post irradiation cooling rate. Thus absolute values for the defect yields at these high temperatures do not exist. What was obtained in the present case were comparative values of the defect yields at a given temperature in Ni and Ni/Cr17%. To make this comparison as accurate as possible, two specimens of each material were irradiated simultaneously for five seconds at each irradiation temperature. Thus the irradiation temperature, the irradiation time and the post irradiation cooling rates were identical for both materials.

It was found that the dose measurement in the experimental target

chamber was not as accurate as in the main chamber. To try and obtain consistency in the experimental results the following procedure was therefore adopted. After the ion beam had been aligned, a room temperature irradiation was carried out in the experimental target chamber. Then without altering the beam in any way, the high temperature (500°C, 450°C, 400°C and 350°C) irradiations were carried out and these were followed by a final room temperature irradiation. Two Ni and two Ni/Cr17% specimens were irradiated in each irradiation, and it was assumed that if the defect yield values in these materials were the same in the final room temperature irradiation as they were in the initial room temperature irradiation, then the high temperature irradiations had also received this constant dose.

A contributory problem to the measurement of the 'dose' incident on a particular specimen at high temperatures was the possibility of surface deposits on either the specimens, specimen grids, specimen circlips or target block outgassing into the ion beam. This could then result in impurity atoms or molecules being carried along in the ion beam and implanted into a specimen. To minimise this problem, only clean grids and circlips were used, and the highest temperature irradiation was carried out first so that the effect of any outgassing from the target block would be reduced for the subsequent irradiations carried out at lower temperatures.

Another problem that arose at high temperatures was the formation of a contamination layer on the surface of the specimens. This is thought to have been caused by the ion beam breaking down hydrocarbon vapours that were present in the vacuum. At attempt was made to improve the vacuum ($\sim 10^{-6}$ torr) in the experimental target chamber by adding an extra diffusion pump, but severe contamination still occurred for all irradiations carried out at temperatures greater than 400°C. This contamination caused some difficulty in determining defect yield values as it tended to reduce the visibility of the small (<25 Å diameter) defect clusters.

This was especially relevant to the Ni specimens irradiated at 500°C in which these small clusters formed a high proportion (∿30%) of the total number of visible defect clusters.

6.3 Results

6.3.1 Measured Defect Yields and Defect Size Distributions

The damage structures generated in <110> grains of Ni and Ni/Cr17% specimens by irradiating with 80 keV W^{++} ions to doses of 2×10^{11} ions cm^{-2} at room temperature, 400°C, 450°C and 500°C are shown in figures 6.2 and 6.3 respectively. The measured defect yields for these specimens, along with those for specimens irradiated at 350°C, are plotted in figure 6.4. The measured size distributions of the defect clusters, taken over samples of approximately four hundred defect clusters in each specimen and normalised to doses of 10^2 incident ions such that the areas under the curves are proportional to the defect yields, are compared in figure 6.5 for the Ni specimens irradiated at room temperature, 450°C and 500°C, and in figure 6.6 for the Ni/Cr17% specimens irradiated at room temperature and 500°C. The error bars on the curves represent the statistical error on the number of defects measured as lying within a given size interval (see section 3.8.1).

Reference to figure 6.4 shows that while the defect yields in the Ni specimens irradiated at room temperature, 350°C, 400°C and 450°C are the same within experimental error, the defect yield in the Ni specimen irradiated at 500°C is significantly lower. Reference to figure 6.5 shows that the reduction in the defect yield at 500°C, compared with those at 450°C and room temperature, is due to a reduction in the number of defect clusters, generated per 10^2 incident ions, that have diameters $\gtrsim$ 30 Å. Possible reasons for the decrease in the defect yield in Ni at temperatures greater than 450°C are considered in section 6.4.

Reference to figure 6.4 shows that the defect yields in the Ni/Cr17% specimens irradiated at room temperature, 350°C, 400°C, 450°C and 500°C are

the same within experimental error. In addition, reference to figure 6.6 shows that apart from a slight reduction in the number of small (<25 Å diameter) defect clusters in the Ni/Cr17% specimen irradiated at 500°C compared with that irradiated at room temperature, the distribution of the defect sizes in these two specimens are the same within experimental error. The possible reasons why the defect yield in the Ni/Cr17% alloy should remain constant up to at least 500°C, while it falls off in Ni for temperatures above 450°C, are considered in section 6.5.

6.3.2 Defect Nature and Defect Geometry

The experimental work described in this chapter was primarily concerned with the determinations of the defect yields at the different irradiation temperatures. Thus no thorough analysis of either the defect natures or the defect geometries was carried out. However, a comparison of the directions of black-white streaking, relative to $\underline{g}$, of the images of the defect clusters on the $\underline{g}$ = <200> micrographs from which the defect yields were measured, indicated that the majority of the defect clusters were vacancy in nature for all the irradiation temperatures. In addition, a comparison of the $\underline{g}$ = <200> images with computer simulated images (see section 2.4.3) indicated that there was no significant change in the geometries of the defect clusters with increasing irradiation temperature. In both the Ni and Ni/Cr17% alloy, most of the larger defect clusters for all the irradiation temperatures appeared to be Frank-type dislocation loops. Some perfect loops were identified as well. In agreement with the results from the room temperature irradiations of the alloys (see section 5.2.2), both edge-c.. and inclined perfect loops appeared to be present in the nichrome alloy while only inclined perfect loops appeared to be present in the nickel. Some of the Frank loops had partially dissociated onto {111} planes other than the loop habit plane. The proportion that had partially dissociated did not appear to vary significantly with increasing irradiation temperature although, because of specimen

contamination, the image contrast at 500°C was not, in general, sufficiently well defined to determine whether a loop was dissociated or not.

6.4 Reduction in Defect Yield in Ni at 500°C Compared with Lower Irradiation Temperatures

Reference to figure 6.5 shows that the reduction in defect yield in Ni at 500°C compared with the yields for lower irradiation temperatures (≤450°C) is due to a reduction in the number of clusters, generated per 10^2 incident ions, that have diameters $\gtrsim$ 30 Å. Three possible explanations have been considered to account for this reduction. These are: (1) increased vacancy-interstitial recombination within a cascade; (2) increased loop loss at the surface; and (3) thermal emission of vacancies from the loops.

The mean depth of deposited energy for 80 keV W^+ ion irradiation of nickel has been calculated as 55 Å (see section 4.6). It is therefore probable that the surface acts as an efficient sink for interstitials that escape from a cascade. Some of the interstitials may form submicroscopic clusters, but these would be stable against thermal emission of interstitials up to temperatures much higher than 500°C. Thus it is not thought that an increase in the irradiation temperature from 450°C to 500°C should alter significantly the probability of an interstitial that has escaped from a cascade returning to a cascade. Nor is the original probability of an interstitial escaping from a cascade thought to be altered significantly by this small change in temperature. Thus it is considered unlikely that the observed reduction in the defect yield is due to increased vacancy-interstitial recombination within a cascade.

As considered in section 4.4.1, the probability of a Frank loop unfaulting to a perfect loop which may subsequently slip out of a foil is thought to be strongly dependent on the depth of the loop in a foil and is only likely to occur for loops lying within less than about 50 Å of the surface. There is no reason to suppose that the depth distribution

of the damage structures in the present experiments is altered significantly by an increase in the irradiation temperature. Thus while an increase in this temperature from 450°C to 500°C may increase the probability of a Shockley partial dislocation being nucleated so that a Frank loop may unfault to a lower energy perfect loop, it is not thought to alter the proportion of loops for which the perfect loop may be the energetically stable form. Reference to figure 6.5 shows that the maximum loop diameter in Ni irradiated at 500°C was approximately 60 Å compared with 80 Å at room temperature and 450°C. To account for this reduction in the maximum defect size, all the Frank loops larger than 65 Å in diameter, irrespective of their depth in the foil, would have had to unfault to perfect loops, all of which subsequently slipped out of the foil. It is therefore considered unlikely that increased loop loss at the surface can completely account for the observed reduction in the defect yield.

The third possible explanation is considered in detail in the following section.

6.4.1 Thermal Emission of Vacancies from Dislocation Loops

The first study of the thermal emission of vacancies from dislocation loops was carried out by Silcox and Whelan (1960) who annealed loops in quenched aluminium. They considered that the shrinkage rate of a vacancy loop under conditions in which vacancies can diffuse rapidly to a sink is determined mainly by the rate at which the bounding dislocation emits vacancies. This rate was calculated using the model of Friedel (1956, 1964) in which vacancies are emitted from jogs with the rate of shrinkage given by the product of the jog concentration (assumed to have an average value of $\nu_{\frac{1}{2}}$ for an undissociated circular loop (Silcox and Whelan 1960)) and the jog velocity. For an edge loop, in which partial dissociation does not occur, this shrinkage rate is given by:

$$\frac{dr}{dt} = -\frac{3D_v^s}{b}\left[\exp\left(F_c B^2/kT\right) - 1\right] \qquad (6.1)$$

where D_v^s is the self-diffusion coefficient, F_c is the driving force per unit length of dislocation for loop shrinkage by vacancy emission and B^2 is the cross-sectional area of a vacancy in the loop habit plane.

However, Silcox and Whelan also considered that if the diffusion of vacancies away from a loop is not sufficiently rapid, then a local vacancy supersaturation will be set up at the dislocation which will tend to suppress the net emission of vacancies, as the chemical stress of the supersaturation will effectively reduce F_c. The shrinkage rate in this case would be determined by the rate of transport of vacancies away from the dislocation by diffusion. The results of Dobson et al (1967) indicate that the shrinkage rate of dislocation loops in quenched aluminium is, in fact, diffusion controlled and for a loop situated in the middle of a foil (thickness 2t) and parallel to the foil surface is given by:

$$\frac{dr}{dt} = -\frac{2\pi D_v^s}{b\ln(t/b)}\left[\exp\left(F_c B^2/kT\right) - 1\right] \qquad (6.2)$$

when r > t (where the diffusion equation is solved for cylindrical symmetry), and by:

$$\frac{dr}{dt} = -\frac{2D_v^s}{b}\left[\exp\left(F_c B^2/kT\right) - 1\right] \qquad (6.3)$$

when r < t (where the diffusion equation is solved for spherical symmetry). In deriving these equations, Dobson et al made no detailed assumptions about the state of the dislocation core other than that it can maintain the vacancy concentration in the lattice surrounding the loop at its equilibrium concentration $C_o \exp\left(F_c B^2/kT\right)$ where C_o is the vacancy concentration at the surface.

In quenched materials, vacancy loops are nucleated throughout a specimen. In the present experiments, the vacancy loops were all located within less than about 100 Å of the surface and it is therefore possible that the diffusion of vacancies to the surface may have been sufficiently rapid that the shrinkage rate was controlled by the rate of emission of

vacancies. However, as was pointed out by Silcox and Whelan (1960) and Whelan (1966), both emission and diffusion limited conditions lead to essentially the same functional form for the rate of shrinkage of a loop, the only differences being in the numerical factors. This can be seen from equations 6.1, 6.2 and 6.3. Thus, on the basis of the models described above, the temperature at which significant thermal emission of vacancies starts to occur and therefore at which loops start to shrink will be approximately the same whether the shrinkage rate is emission controlled or diffusion controlled.

In successfully accounting for the temperature dependence of the defect yield in 30 keV self-ion irradiated copper, English et al (1976) proposed a model in which an athermal cascade collapse process is counterbalanced at elevated temperatures by loop shrinkage due to thermal emission of vacancies. The loop shrinkage rate, in the absence of any incident flux of vacancies or interstitials, was taken to be that given by equation 6.3 and the lifetime (t_L) of a loop was calculated as the time it took a loop to shrink from its initial radius r_o to a radius r_{min} = 7.5 Å at which the loop would no longer show visible diffraction contrast, that is:

$$t_L = \frac{-b}{2D_v^s} \int_{r_o}^{r_{min}} [\exp (F_c B^2/kT) - 1]^{-1} \, dr \qquad (6.4)$$

where $D_v^s = D_o \exp(-Q/kT)$ in which D_o is the diffusion constant and Q is the activation energy for self-diffusion. F_c was calculated from the expression for the self-energy of a circular loop given by Bacon and Crocker (1965) as:

$$F_c = \{ \frac{3\mu b^2}{8\pi r} (\ln \frac{8r}{\delta} - 0.125) + \gamma \}$$

where γ is the stacking fault energy for a faulted loop, μ is the shear modulus and δ is the dislocation core radius.

As considered previously, while the shrinkage rate of loops located close to a surface may not be limited by the diffusion of vacancies away

from a loop, equation 6.3 should still be a reasonable approximation to the actual shrinkage rate. Thus the theoretical lifetimes of small (< 100 Å diameter) Frank loops in nickel have been calculated (English, C.A., private communication) for the irradiation temperatures of current interest using the expression of English et al (equation 6.4) and the values of b, D_o, Q, μ and γ listed in appendix 1. The results of these calculations are shown by figure 6.7.

These lifetimes have been used to calculate the expected measured defect yield in nickel as a function of the irradiation temperature on the assumption that the distribution of the sizes of the defect clusters generated at a given temperature is the same as the distribution generated at room temperature. This assumption may not be strictly valid since, even if the nucleation and the average number of vacancies involved in the growth of a Frank loop is independent of temperature, at temperatures where significant vacancy emission occurs a loop may start to emit vacancies before it has grown to the size it would reach at room temperature.

In the present experiments, the high temperature irradiation time of five seconds was followed by an anneal at the irradiation temperature for approximately twenty seconds before the specimens were cooled rapidly to temperatures less than about 450°C (see figure 6.1) at which significant loop shrinkage in nickel did not occur (see figure 6.5). Since the anneal was much longer than the irradiation time, a reasonable approximation to the actual situation can be made by taking the generation of all the defect clusters to be instantaneous followed by an anneal equal to the actual irradiation time plus the annealing time. Thus, assuming that loop shrinkage during the cooling was negligible, an estimate of the defect yield at a given irradiation temperature can be found from the proportion of the loops generated at room temperature which have lifetimes greater than twenty five seconds at that irradiation temperature. This theoretical variation in the defect yield, obtained using the loop lifetimes of

figure 6.7 and the distribution of the defect sizes in nickel irradiated at room temperature as given by figure 6.5, is shown by figure 6.8. This theoretical variation in the yield is not affected significantly by small differences in the loop shrinkage rates, as for example between the emission controlled or diffusion controlled rates of equations 6.1, 6.2 and 6.3, nor by small changes in the post irradiation annealing time.

Reference to figure 6.8 shows that vacancy loop shrinkage due to thermal emission of vacancies would result in a sharp decrease in the defect yield for irradiation temperatures greater than about 400°C. Because of the approximations that have been made and some uncertainty in the values of the parameters used in calculating the loop lifetimes, this is thought to be in relatively good agreement with the experimentally observed variation in the defect yield which shows a sharp decrease for irradiation temperatures greater than 450°C (see figure 6.4).

In conclusion, it is thought that the reduction in defect yield in Ni irradiated at 500°C can be satisfactorily accounted for by a model, originally proposed by English et al (1976), in which an athermal cascade collapse process is counterbalanced at elevated temperatures by loop shrinkage due to thermal emission of vacancies.

6.5 Possible Reasons for the Difference in Defect Yields in Ni and Ni/Cr17% at 500°C

The difference in the defect yields in Ni and Ni/Cr17% irradiated at 500°C (see section 6.3.1) cannot be due to a difference in the irradiation procedure as, as described in section 6.2, both specimens were irradiated simultaneously and the irradiation temperature, the irradiation time and the post irradiation cooling rates were therefore identical for both materials. The present results, coupled with the explanation proposed to account for the temperature dependence of the defect yield in Ni (see section 6.4), would indicate that significant thermal emission of vacancies from loops in the Ni/Cr17% alloy does not occur until temperatures greater

than 500°C.

The results of the calculations on the loop lifetimes indicate that the lifetime of a loop of a given size in Ni at 450°C is approximately fifteen times longer than the lifetime of that loop at 500°C (see figure 6.7). Thus to account for the defect yield in the Ni/Cr17% alloy dropping off at temperatures at least greater than 500°C while it starts to drop off in Ni at temperatures greater than 450°C requires that the loop lifetimes in the Ni/Cr17% alloy at 500°C are at least fifteen times longer than the corresponding loop lifetimes in Ni. Three factors are thought to contribute to this increase in the loop lifetimes. These are: (1) the effect of loop dissociation; (2) the dependence of F_c on the stacking fault energy; and (3) the variation in the diffusion coefficients.

As considered previously, the diffusion of vacancies away from a vacancy loop lying close to a surface may be sufficiently rapid that the shrinkage rate is emission controlled. This particularly applies to dissociated loops as the vacancy emission rate from a dislocation is reduced when a dislocation dissociates, as the jog formation energy increases. The emission controlled shrinkage rate of a partially dissociated loop will therefore be lower than the shrinkage rate of an undissociated loop as given by equation 6.1. The energy of formation of a jog on a dissociated dislocation increases with decreasing stacking fault energy and will therefore be higher in the Ni/Cr17% alloy ($\gamma \approx 85$ ergs/cm^2) than in Ni ($\gamma \approx 125$ ergs/cm^2). Since the theoretical calculations of section 5.4 indicate that it is energetically favourable for small (< 80 Å diameter) Frank loops to partially dissociate in Ni, and therefore in the Ni/Cr 17% alloy as well, the increase in the jog formation energy on a dissociated dislocation in the Ni/Cr17% alloy compared with the Ni could therefore account for an increase in the loop lifetimes in the Ni/Cr17% alloy. However, it is uncertain whether it could account completely for the magnitude of the increase in the loop lifetimes.

The stacking fault energy of the Ni/Cr 17% alloy is lower than that of Ni and thus the driving force (F_c) for loop shrinkage will be lower in the Ni/Cr17% alloy. However, for the small (< 80 Å diameter) loop sizes generated in the present experiments the stacking fault energy term is only a small part of F_c. This is illustrated by the fact that F_c for a 60 Å diameter loop in nickel is reduced by less than 5% in reducing γ from 125 ergs/cm^2 to 85 ergs/cm^2. Thus it is not thought that the reduction in the stacking fault energy can account completely for the increase in loop lifetimes in the Ni/Cr17% alloy.

The values of the self-diffusion coefficients ($D_v^s = D_o \exp(^{-Q}/kT)$) for the Ni/Cr17% alloy are not known. However, the self-diffusion coefficient for Cr (D_o = 0.20 cm^2/sec, Q = 3.20 eV) is lower than for Ni (D_o = 1.77 cm^2/sec, Q = 2.96 eV) and Lazarus (1960) states that, for homogeneous binary alloys, the rates of self-diffusion of both constituents are, in general, reduced by the addition of a slower diffusing species as a finite impurity. In the present case, the Ni/Cr17% alloy is not homogeneous in the immediate vicinity of a dislocation because of the interaction energy of the Cr atoms with the elastic stress field of the dislocation. However, the self-diffusion coefficients for the Ni/Cr 17% alloy may be lower than that in Ni, and equation 6.4 shows that the increase ΔQ in the activation energy for self diffusion that is necessary to increase the loop lifetimes by a factor of fifteen, given by exp $^{\Delta Q}/kT = 15$, is only 0.19 eV. This is less than the difference between the activation energies for self diffusion in nickel and chromium. Thus it is possible that a reduction in the self-diffusion coefficients in the Ni/Cr17% alloy as compared with that in Ni could account completely for the increase in loop lifetimes in the alloy.

In conclusion, the difference in the defect yields in Ni and Ni/Cr17% irradiated at 500°C is thought to be due to the loops in the alloy having significantly longer lifetimes, and the major contribution to the increase

in lifetimes may be due to the Cr alloying atoms reducing the self-diffusion coefficient in nickel.

6.6 Implication of Present Results to the Void Swelling in Ni/Cr Alloys

The results presented in this chapter show that displacement cascades collapse to form dislocation loops in Ni and Ni/Cr17% at temperatures at least up to 500°C, that is within the void formation temperature range for these materials. As considered in section 1.2, the presence of a steady-state concentration of transient vacancy loops at void formation temperatures will reduce the effective damage rates and consequently the void swelling rates by providing additional sites for vacancy-interstitial recombination. While the present results on the temperature dependences of the defect yields in Ni and Ni/Cr17% obtained using W^+ ions may not be fully representative of the temperature dependences that would have been obtained using self-ion or neutron irradiations (see section 5.7), they indicate that the steady-state concentration of vacancy clusters in Ni/Cr17% at 500°C will be greater than that in Ni because of the significantly longer lifetimes of the loops in the Ni/Cr 17% alloy. Thus by considering the affect that the displacement cascade damage structures have on reducing the void swelling rates, one would expect a lower swelling rate in Ni/Cr17% at 500°C than in Ni. This is in agreement with the experimental observations of Hudson and Ashby (1974) which showed that the void swelling in nickel-chromium (9% and 27.5%) alloys at 525°C is lower than in pure nickel (see section 1.3).

The steady-state vacancy cluster concentration in a given material at a given temperature depends on both the vacancy cluster production rate and the vacancy cluster lifetimes. The defect yields generated in Ni and Ni/Cr17% by 80 keV W^+ ion irradiations at room temperature are the same within experimental error (see section 5.2.3.1). The present results therefore serve to underline the importance, when considering the influence that displacement cascade damage structures have on void swelling

rates, of comparing the damage structures generated in different materials at the temperatures where void swelling occurs and not just at room temperature.

6.7 Conclusions

(1) Irradiation of Ni and Ni/Cr17% with 80 keV W^{++} ions in the temperature range 20°C → 500°C produces small (< 80 Å diameter) vacancy-type dislocation loops which nucleate heterogeneously at cascades.

(2) The defect yield in Ni remains constant with increasing irradiation temperature up to ∿450°C and then decreases sharply at higher temperatures.

(3) The defect yield in the Ni/Cr17% alloy remains constant with increasing irradiation temperature up to at least 500°C.

(4) The temperature dependence of the defect yield in the Ni and Ni/Cr17% alloy can be accounted for by an athermal cascade collapse process which is counterbalanced at elevated temperatures by loop shrinkage due to thermal emission of vacancies.

(5) The influence of the displacement cascade damage structures in reducing the void swelling rates is expected to be greater in the Ni/Cr17% alloy at 500°C than in the Ni.

Figure 6.1 Typical post irradiation cooling curves for specimens irradiated at elevated temperatures.

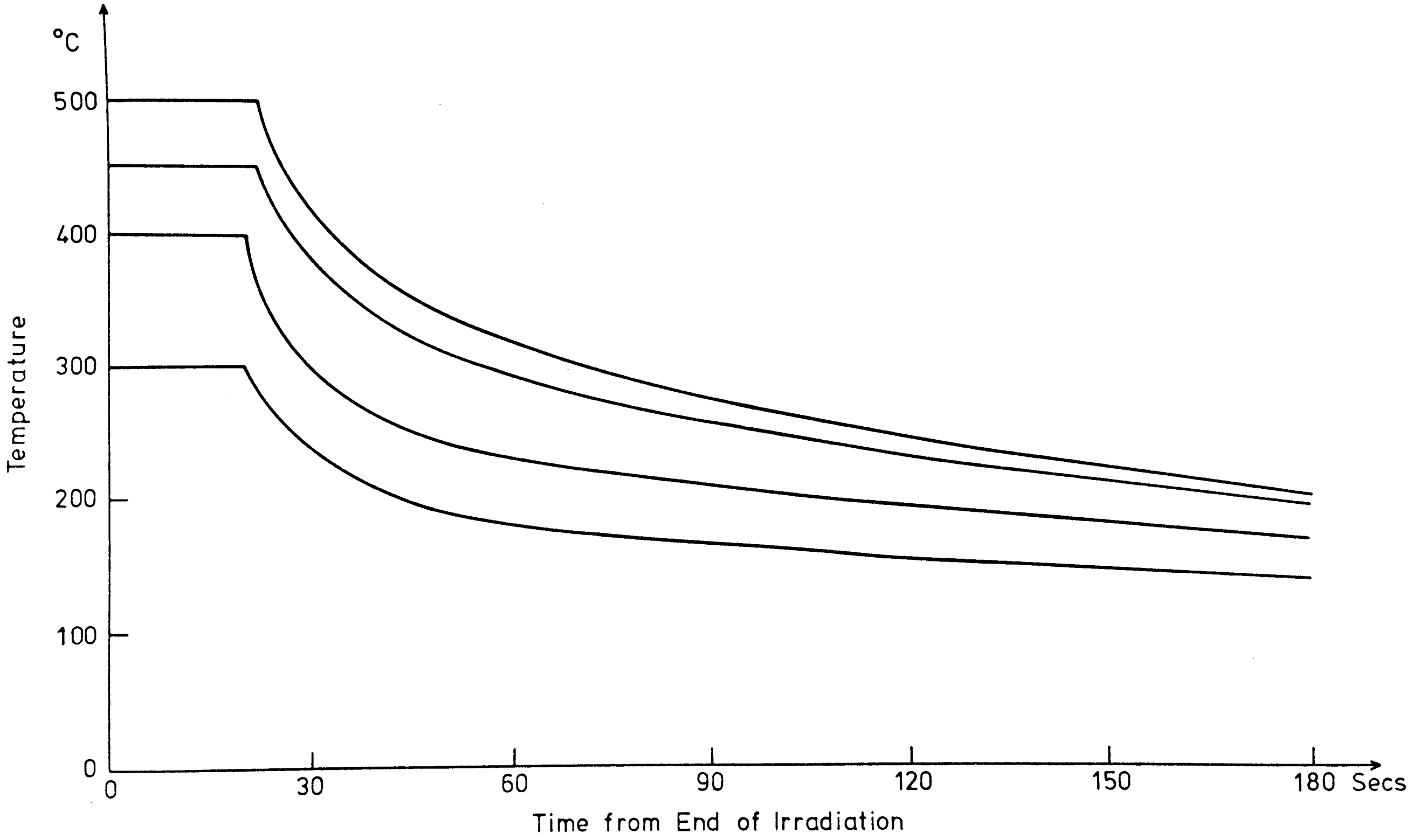
°C
500
400
300
200
100
0
Temperature
0
30
60
90
120
150
180 Secs
Time from End of Irradiation

Figure 6.2 $\underline{g}$ = <002> dark-field images of the damage structures generated by 80 keV W^{++} ion irradiations of <110> grains of Ni at room temperature, 400°C, 450°C and 500°C to doses of 2×10^{11} ions cm^{-2}.

Thompson's tetrahedron viewed along a <110> direction.

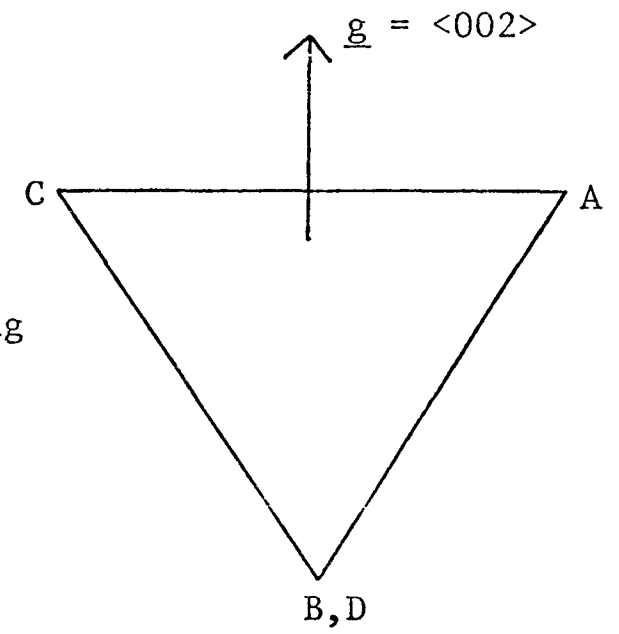

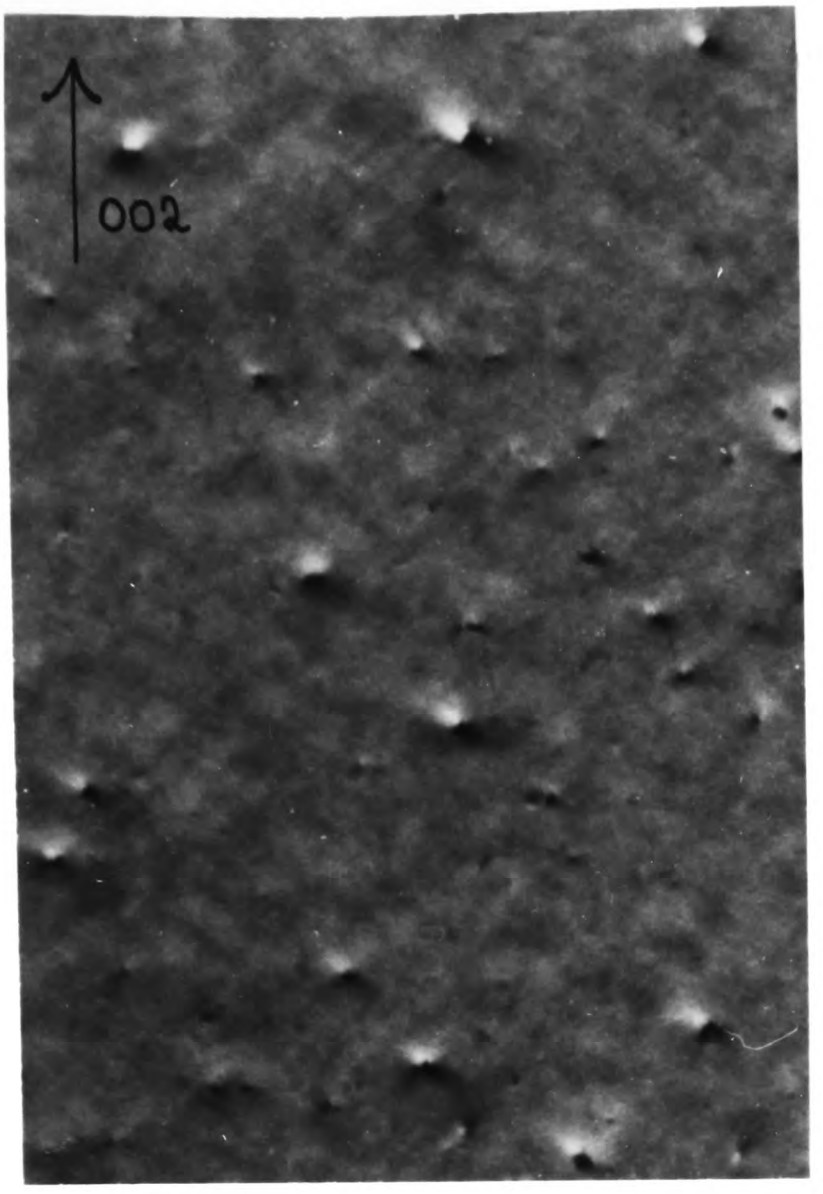

Ni R.Temp.

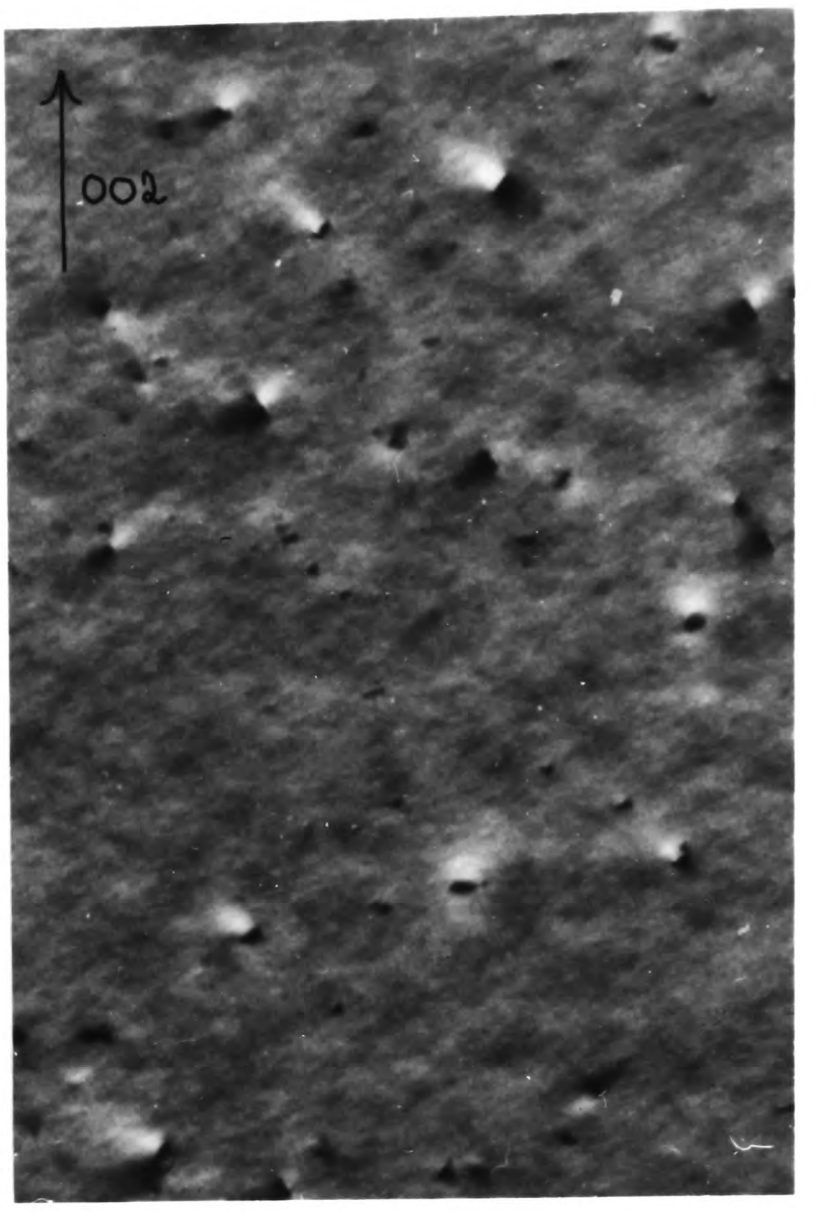

Ni 400°C

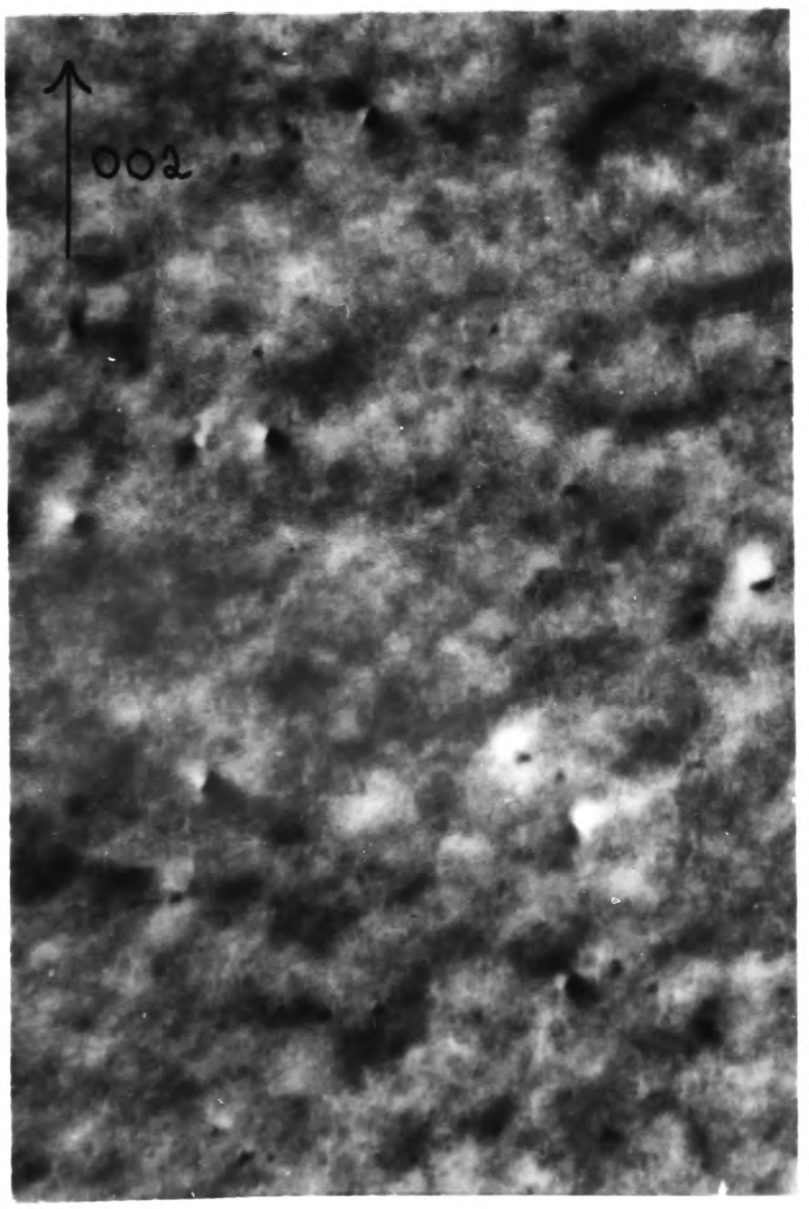

Ni 450°C

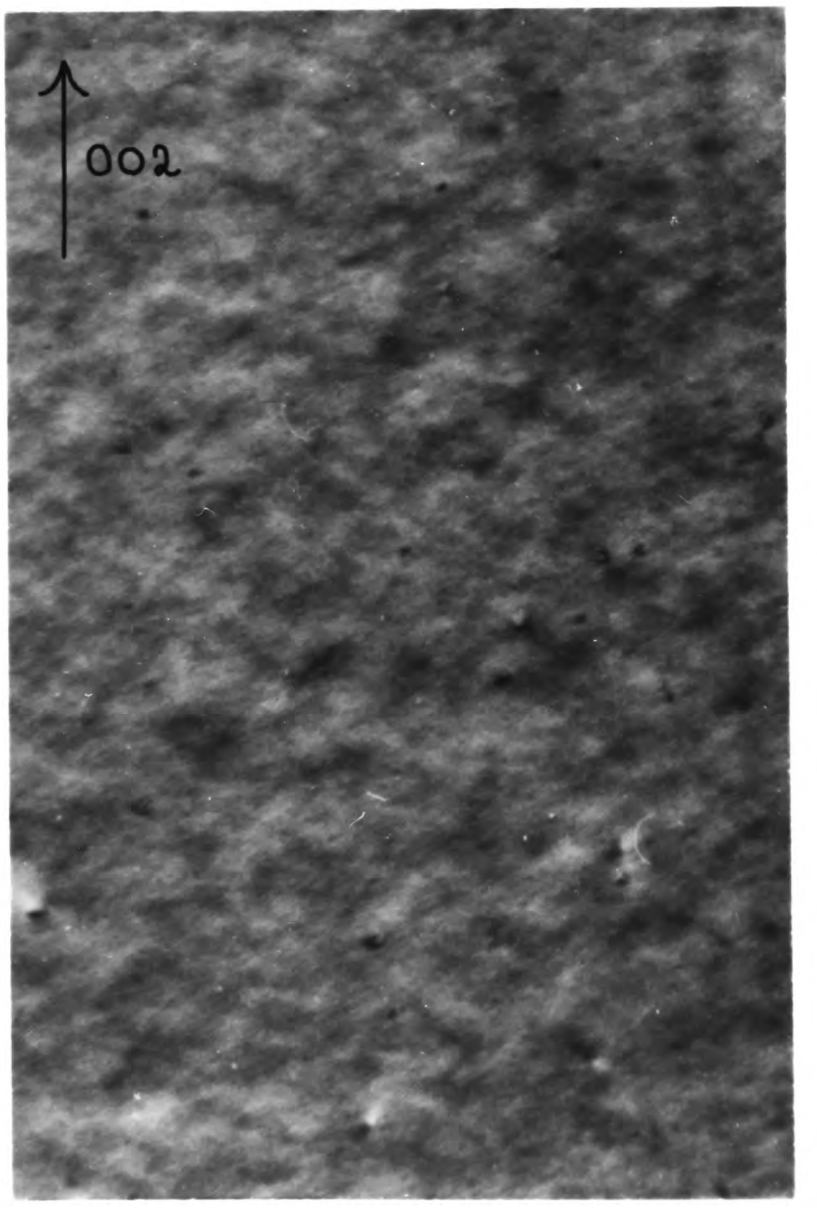

Ni 500°C

1,000 Å

Figure 6.3 $\underline{g}$ = <002> dark-field images of the damage structures generated by 80 keV W^{++} ion irradiations of <110> grains of Ni/Cr17% at room temperature, 400°C, 450°C and 500°C to doses of 2×10^{11} ions cm^{-2}.

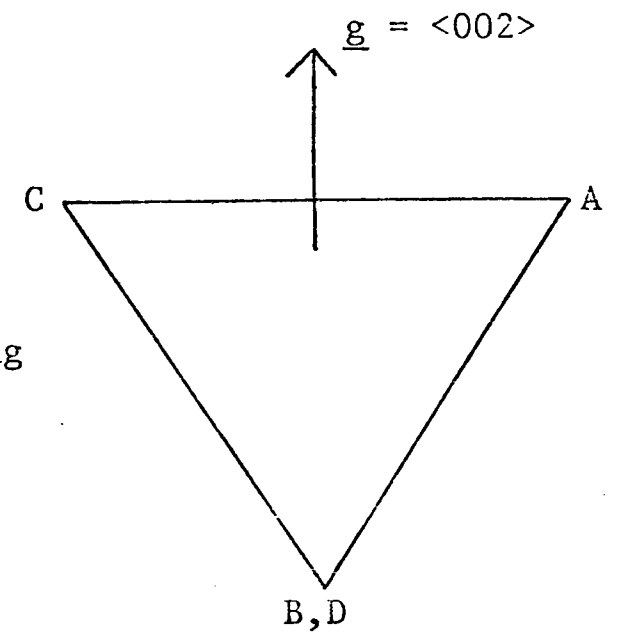

Thompson's tetrahedron viewed along a <110> direction.

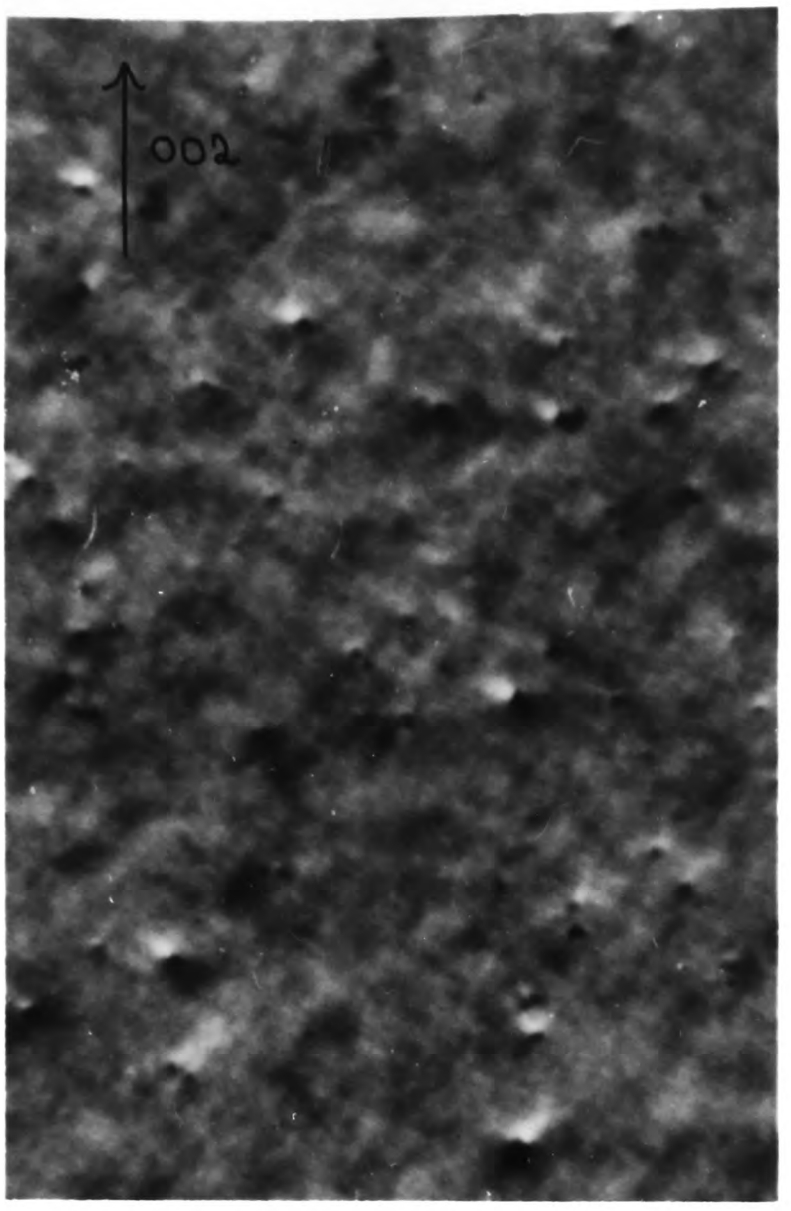

Ni/Cr 17% R.Temp.

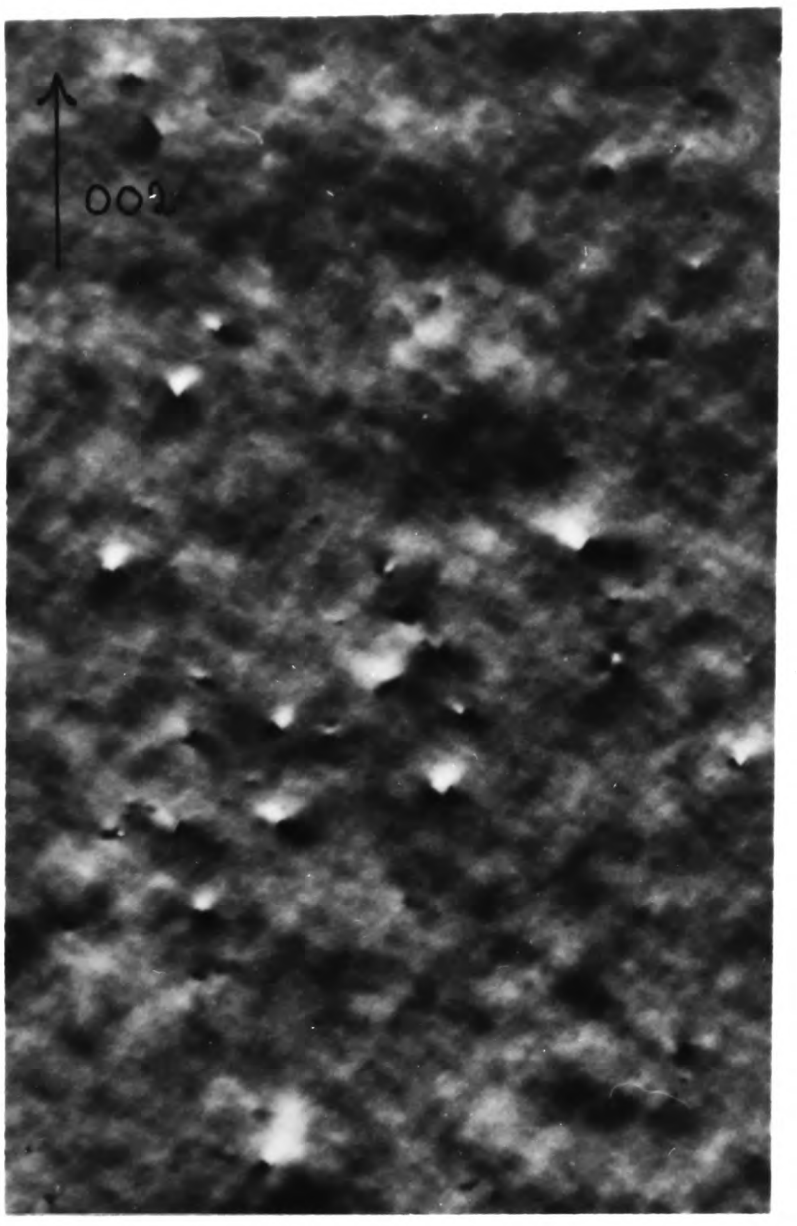

Ni/Cr 17% 400°C

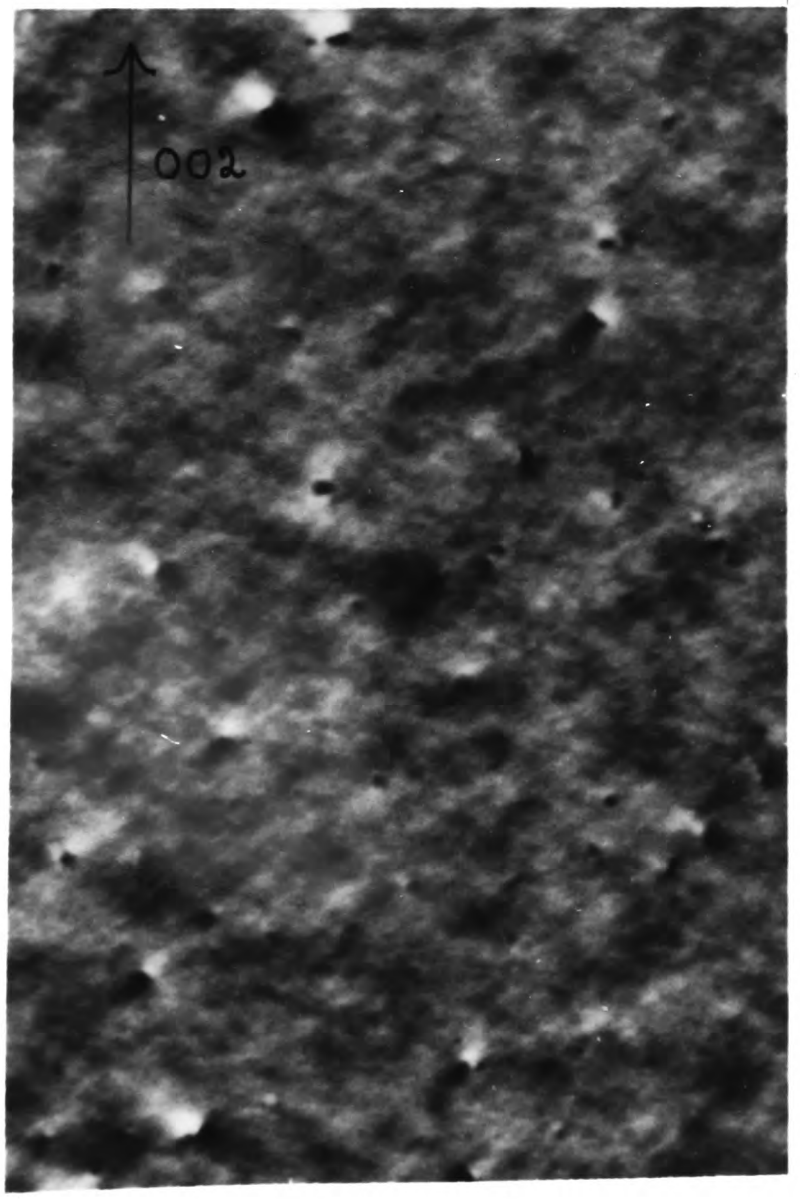

Ni/Cr 17% 450°C

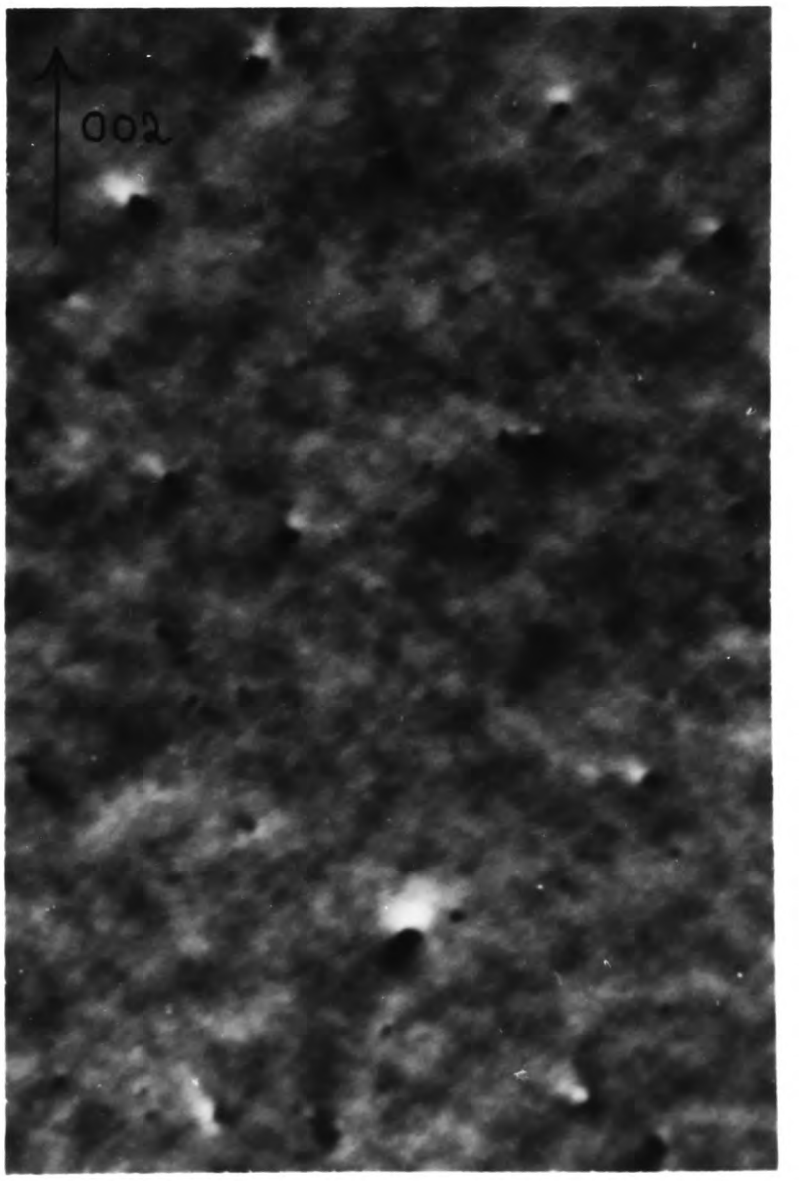

Ni/Cr 17% 500°C

1,000 Å

Figure 6.4 Graphs showing the measured defect yields generated by 80 keV tungsten ion irradiations of <110> grains of Ni and Ni/Cr17% as functions of the irradiation temperature.

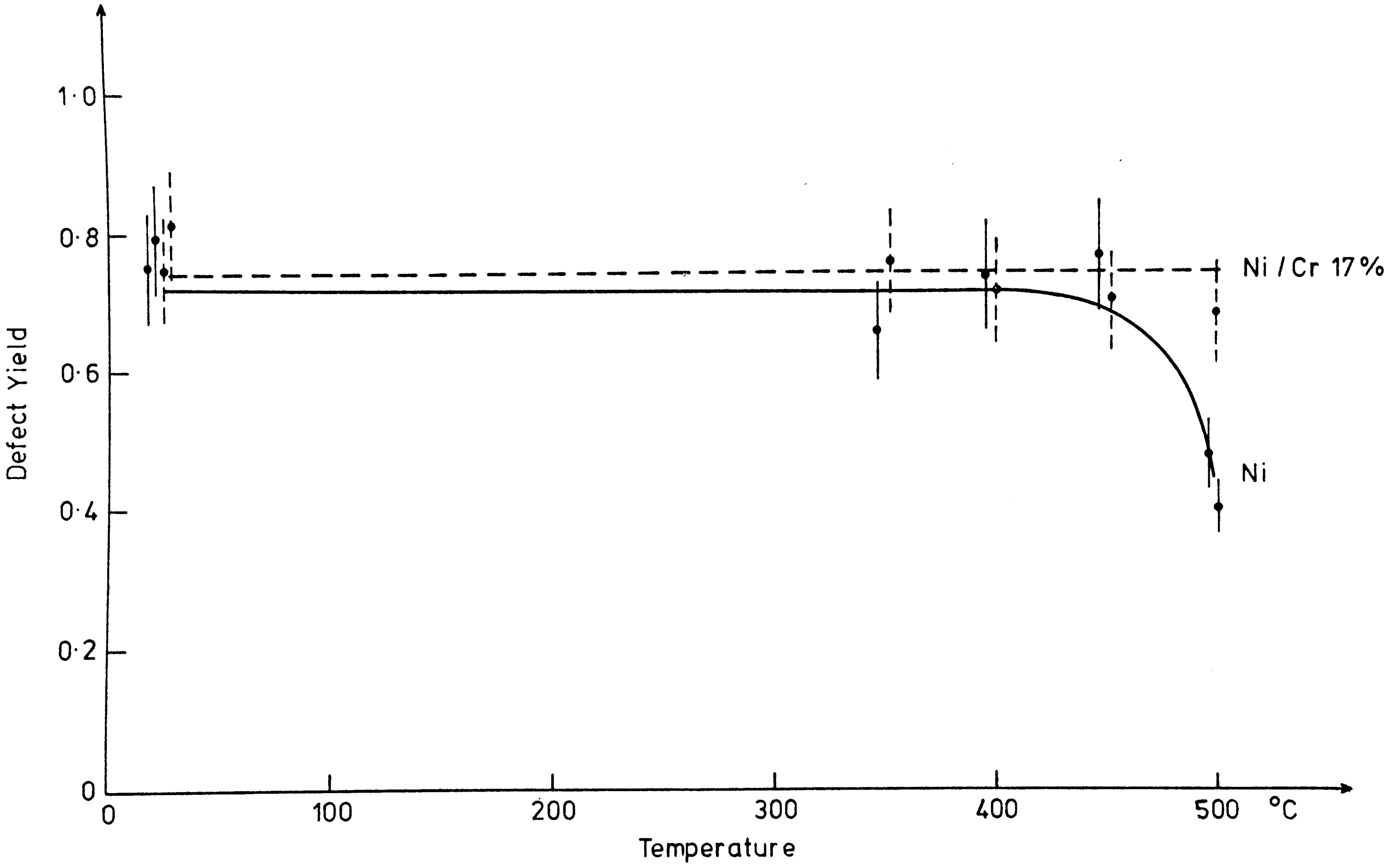
1·0
0·8
0·6
0·4
0·2
0
Defect Yield
Ni / Cr 17 %
Ni
0
100
200
300
400
500
°C
Temperature

Figure 6.5 Size distributions, normalised to doses of 10^2 incident ions, of the damage structures, illustrated by figure 6.2, generated by 80 keV tungsten ion irradiations of <110> grains of Ni at room temperature, 450°C and 500°C.

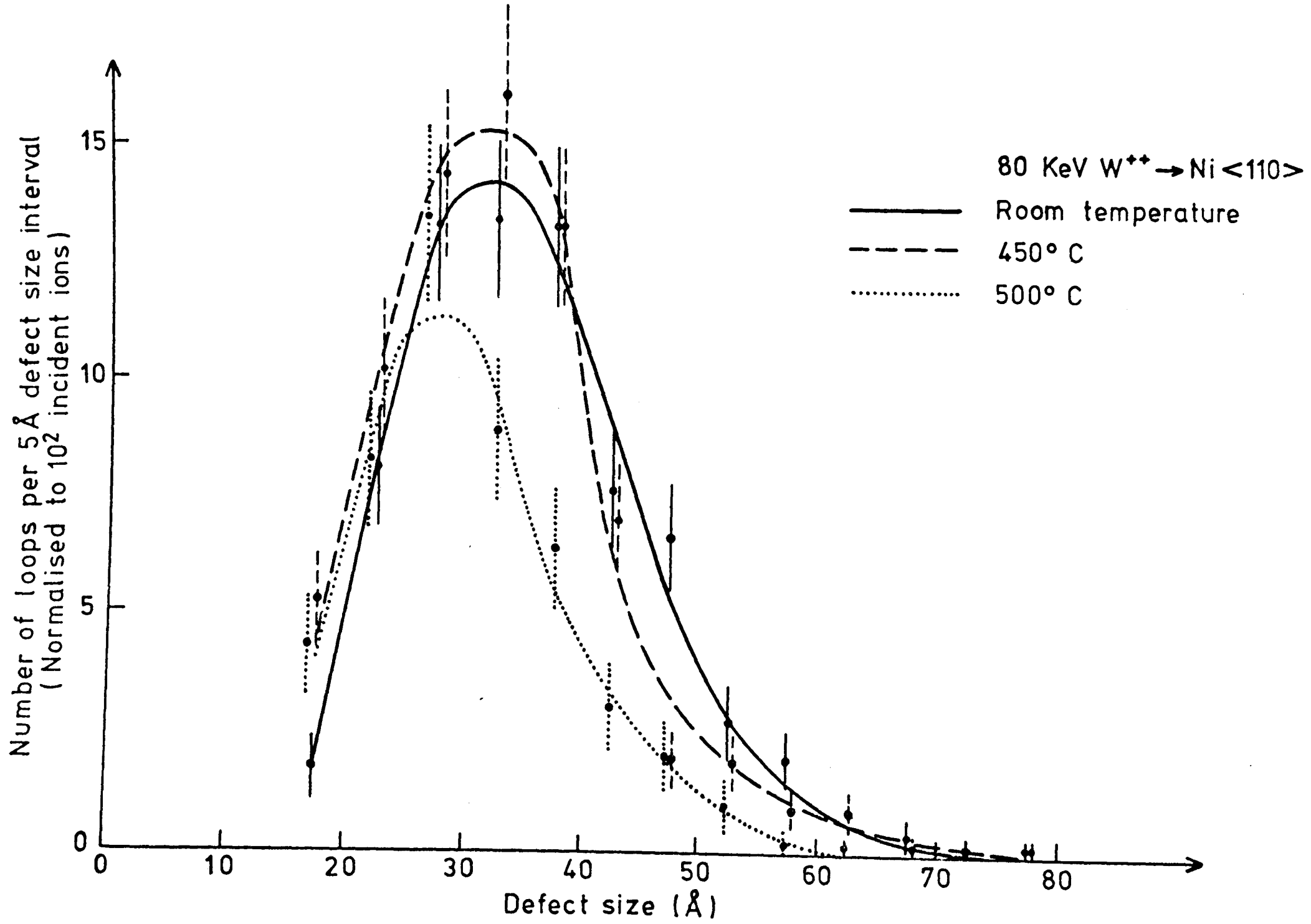
80 KeV W++ → Ni <110>
Room temperature
450° C
500° C
Number of loops per 5 Å defect size interval
(Normalised to 10² incident ions)
0
5
10
15
0
10
20
30
40
50
60
70
80
Defect size (Å)

Figure 6.6 Size distributions, normalised to doses of 10^2 incident ions, of the damage structures, illustrated by figure 6.3, generated by 80 keV tungsten ion irradiations of <110> grains of Ni/Cr17% at room temperature and 500°C.

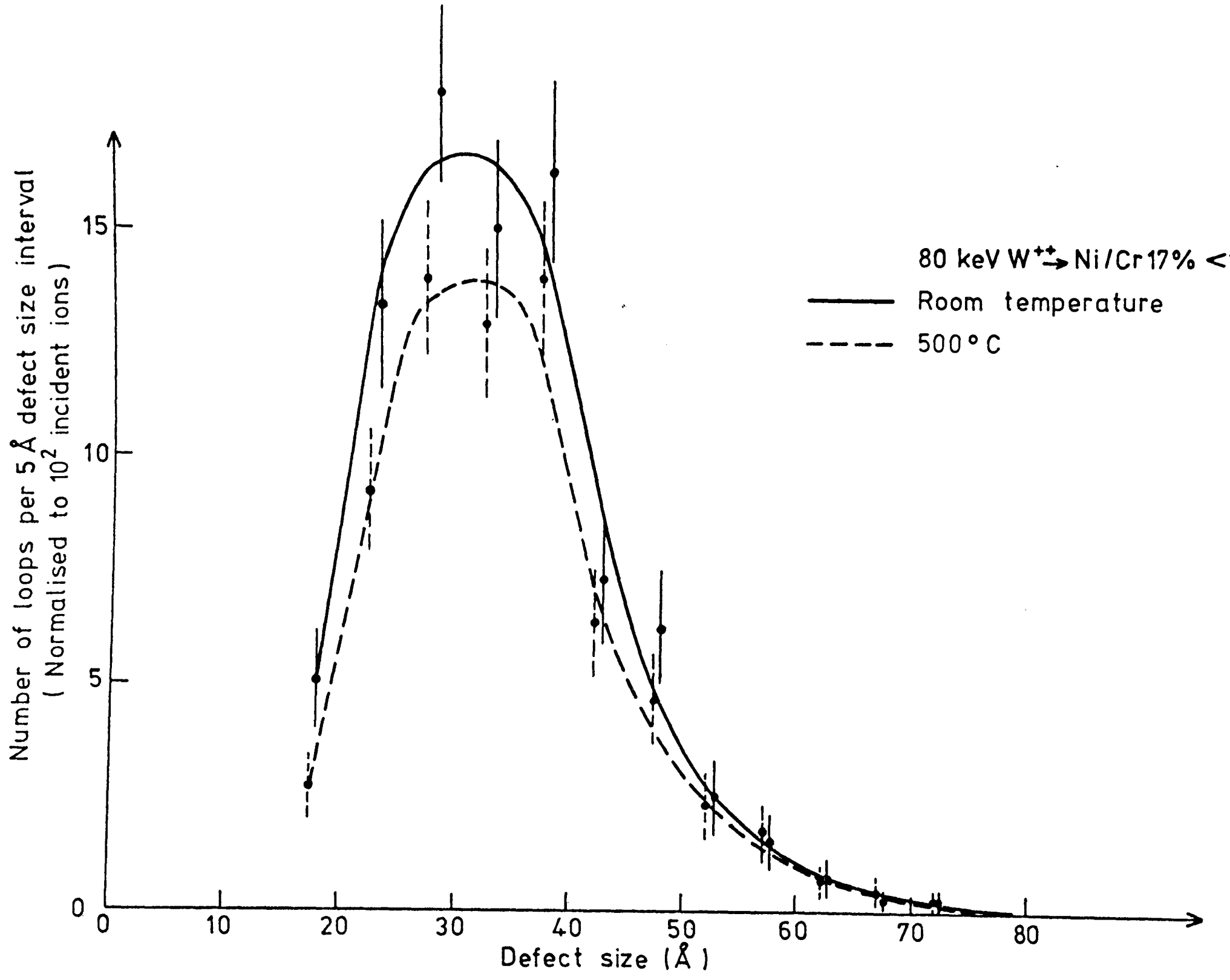
80 keV W++ → Ni/Cr 17% <110>
Room temperature
500 °C
Number of loops per 5 Å defect size interval
(Normalised to 10^2 incident ions)
0
5
10
15
0
10
20
30
40
50
60
70
80
Defect size (Å)

Figure 6.7 The theoretical lifetimes, calculated from equation 6.4, of small Frank loops in Ni as a function of the initial loop diameter and the irradiation temperature T (English, C.A., private communication).

Figure 6.8 The calculated variation in the defect yield in Ni with increasing irradiation temperature as a result of loop shrinkage due to thermal emission of vacancies.

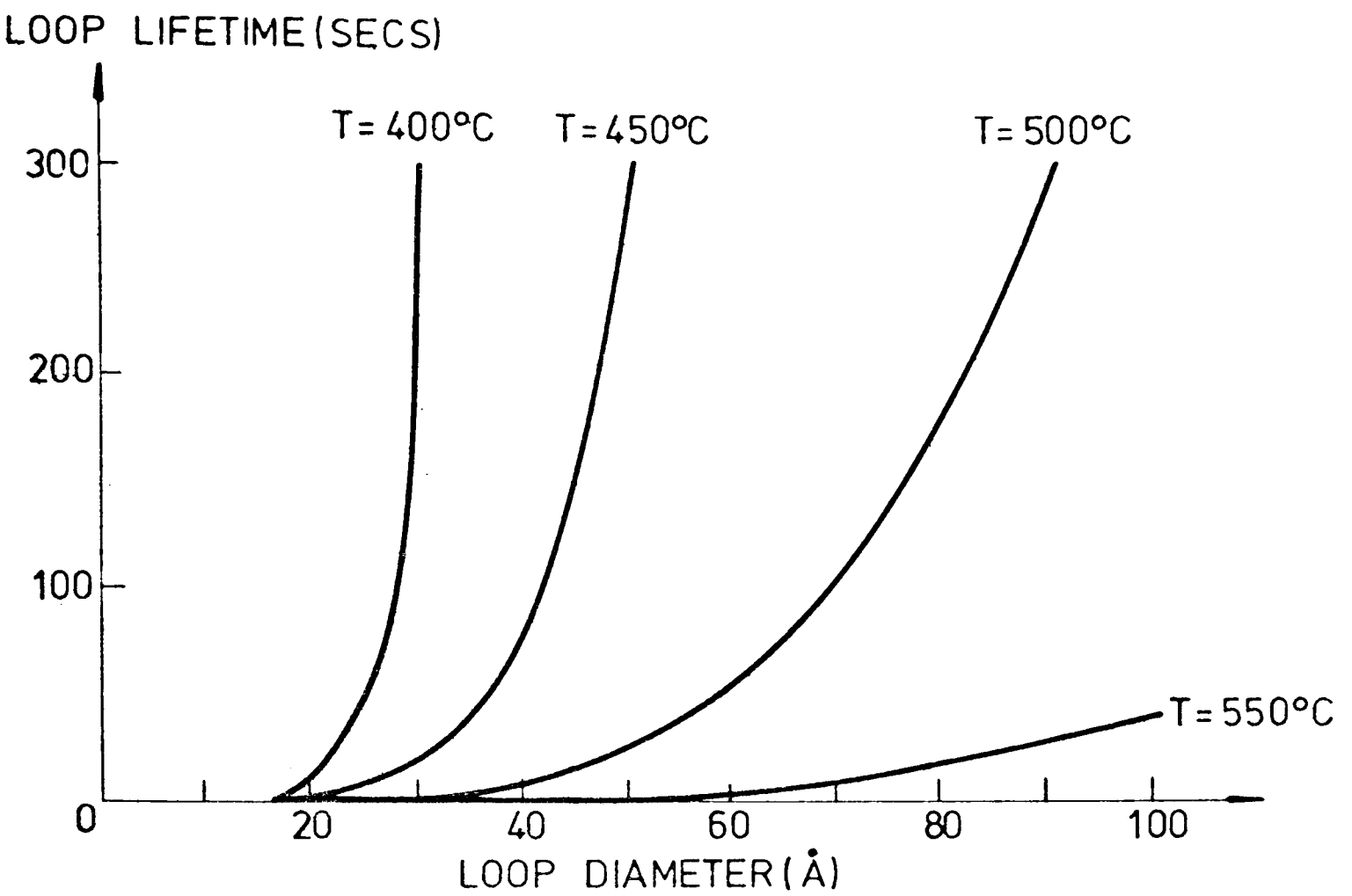
LOOP LIFETIME (SECS)
T = 400°C
T = 450°C
T = 500°C
T = 550°C
300
200
100
0
20
40
60
80
100
LOOP DIAMETER (Å)

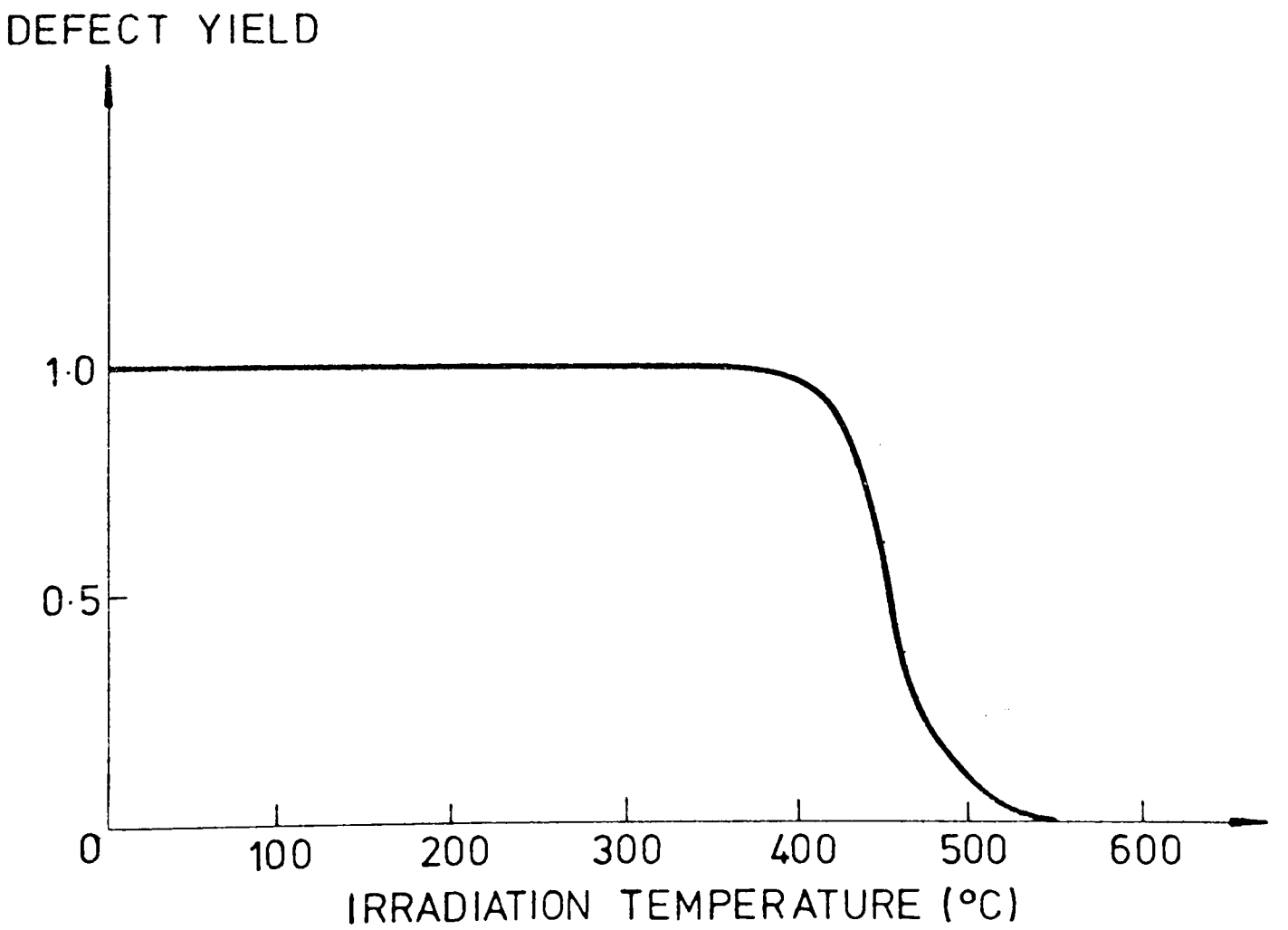
DEFECT YIELD
1·0
0·5
0
100
200
300
400
500
600
IRRADIATION TEMPERATURE (°C)

CHAPTER 7

Concluding Remarks and Suggestions for Further Work

7.1 Concluding Remarks

The present work was carried out because little information existed as to the effect that alloying had on cascade collapse in materials of technological importance. The original objectives of the research project are discussed in section 1.6.2. This section summarises the results that have been obtained with regard to these objectives, while the following section (7.2) considers suggestions for further work in the light of the present results.

The results of the present work indicate that alloying Ni with 8% or 17% Cr, an element of similar atomic radius and atomic weight, has little significant effect either on the probability of a cascade collapsing to form a faulted loop nucleus or on the average number of vacancies involved in the subsequent growth of that loop nucleus. The reductions in defect yields in the W^+ ion irradiated Fe/Ni/Cr alloy and stainless steel and in the Ni^+ ion irradiated nichrome alloys and stainless steel compared with the yields generated by irradiations of pure nickel, these reductions in yields not being accompanied by a change in the average defect size nor in the distribution of the defect sizes generated by a given ion species, are thought to be the result of minor impurities reducing the probability of a faulted loop being nucleated by increasing the energy barrier opposing this nucleation.

Although the elastic interaction of a loop with the specimen surface is thought to have resulted in some of the large (>60Å diameter) Frank loops in the high stacking fault energy nickel and nichrome alloys unfaulting to perfect loops, some of which subsequently slipped out of the foil, this loop loss did not cause any significant reduction in the defect yields which, within experimental error and, apart from the possibility of axial channelling occurring, were found to be independent of the foil orientation. The defect yields were, however, strongly sensitive to the mass of the irradiating ions being between a factor of

2 and 5 higher in the case of the W^+ ion irradiations.

The effect of alloying on the defect geometries was determined by the stacking fault energy of the alloy. In the high stacking fault energy nickel and nichrome alloys a small number (<5%) of perfect loops were identified in addition to the Frank loops. In the low stacking fault energy Fe/Ni/Cr alloy and stainless steel, however, only Frank-type dislocation loops were present and both the proportion of loops identified as partially dissociated and the average degree of dissociation were greater than in the nickel and the nichrome alloys.

While the addition of Cr to Ni had no significant effect on the damage structures generated at room temperature, the lifetimes of the loops in the Ni/Cr17% alloy at 500°C were longer, by a factor of more than ten, than the corresponding loop lifetimes in Ni. This may be an important factor in accounting for the difference in the void swelling characteristics of nickel and nichrome alloys that was observed by Hudson and Ashby (1974).

Finally, while the temperature dependence of the cascade collapse process was only investigated for cascades generated by W^+ ions, the results indicate that for these ions the probability of a cascade collapsing to nucleate a faulted loop in both Ni and Ni/Cr17% is independent of temperature at least up to 500°C.

7.2 Suggestions for Further Work

The present results indicate that interstitial impurity atoms may reduce significantly the probability of a faulted loop being nucleated within a cascade. In addition, the results of English et al (1977) have shown a strong dependence of the defect yield in self-ion irradiated molybdenum on interstitial impurity content. So far, no systematic investigation has been carried out as to the effect of interstitial impurity atoms on cascade generation and cascade collapse, and this therefore seems an interesting area for further research.

The affect of alloying on the steady-state vacancy cluster concentrations at temperatures within the void formation temperature range would also seem to be an area that requires further investigation. Alloying nickel with elements with higher self-diffusion coefficients than itself might yield information as to whether the increase in loop lifetimes in the Ni/Cr17% alloy at 500°C compared with in Ni is due mainly to a difference in the self-diffusion coefficients, or whether it is due mainly to other factors such as the change in the stacking fault energy and the effects of loop dissociation. In addition, if experimentally possible, it would be interesting to see at what temperature the defect yield in the Ni/Cr17% alloy starts to drop off, and whether it correlates qualitatively with the sharp increase in void swelling in a Ni/Cr27.5% alloy observed for irradiation temperatures greater than 540°C (Hudson and Ashby 1974).

APPENDIX 1

Values of Some Parameters for Nickel

Stacking fault energy[1]	$\gamma = 125$ ergs/cm^2
Shear modulus[2]	$\mu = 9.47 \times 10^{11}$ dynes/cm^2
Poisson's ratio[2]	$\nu = 0.276$
Diffusion constant[3]	$D_o = 1.77$ cm^2/sec.
Activation energy for self-diffusion[3]	$Q = 2.96$ eV
Lattice constant[4]	$a = 3.524$ Å
Interatomic distance	$b_{\frac{a}{2}\langle 110\rangle} = 2.49$ Å
Burgers vector for Frank loop	$b_{\frac{a}{3}\langle 111\rangle} = 2.03$ Å

[1]Carter and Holmes 1977
[2]Hirth and Lothe 1968 p.762
[3]Bakker 1968
[4]Pearson 1967

REFERENCES

Bacon, D.J. and Crocker, A.G., 1965, Phil. Mag., 12, 195.

Bakker, H., 1968, Phys. Stat. Sol., 28, 569.

Bauer, W. and Sosin, A., 1964, J. Appl. Phys., 35, 703.

Beeston, B.E.P. and France, L.K., 1968, J. Inst. Metals, 96, 105.

Bethe, H.A., 1928, Ann. Phys. Lpz., 87, 55.

Bishop, J.F.W., 1974, Proc. Conf. on 'Fast Reactor Power Stations', B.N.E.S., London, 295.

Blewitt, T.H., Kirk, M.A. and Scott, T.L., 1975, Proc. Conf. Fund. Aspects of Rad. Damage in Metals, USERDA, Gatlinburg, Tennesse, 152.

Bourret, A. and Dautreppe, D., 1968, Phys. Stat. Sol., 29, 283.

Bragg, W.L., 1913, Proc. Camb. Phil. Soc., 17, 43.

Brailsford, A.D. and Bullough, R., 1972, J. Nucl. Matls., 44, 121.

Brinkman, J.A., 1954, J. Appl. Phys., 25, 961.

Bullough, R., Eyre, B.L. and Krishan, K., 1975, Proc. Roy. Soc., A346, 81.

Bullough, R., Maher, D.M. and Perrin, R.C., 1971, Phys. Stat. Sol. (b), 43, 689.

Bullough, R. and Nelson, R.S., 1973, UKAEA (Harwell) Report, AERE-R7353.

Bullough, R. and Perrin, R.C., 1969, Proc. Conf. on Rad. Damage in Reactor Materials, IAEA, Vienna, 2, 233.

Carter, C.B. and Holmes, S.M., 1977, Phil. Mag., 35, 1161.

Cawthorne, C. and Fulton, E.J., 1966, Nature, 216, 575.

Chadderton, L.T., 1965, Radiation Damage in Crystals (Methuen), 151.

Cockayne, D.J.H., 1972, Z. Naturf., 27a, 452.

Cockayne, D.J.H., Ray, I.L.F. and Whelan, M.J., 1969, Phil. Mag., 20, 1265.

Cole, M., Bucklow, I.A. and Grigson, C.W.B., 1961, Brit. J. Appl. Phys., 12 , 296.

Cottrell, A.H., 1953, Dislocations and Plastic Flow in Crystals (Oxford University Press), 57.

Davis, T.L., 1967, J. Appl. Phys., 38, 3756.

Dean, C.F., 1974, UKAEA (Winfrith) Report, AEEW-M1242.

Diehl, J., Diepers, H. and Hertl, B., 1968, Can. J. Phys., 46, 647.

Diepers, H. and Diehl, J., 1966, Phys. Stat. Sol., 16, K109.

Dobson, P.S., Goodhew, P.J. and Smallman, R.E., 1967, Phil. Mag., 16, 9.

English, C.A., 1977a, To be published.

English, C.A., 1977b, To be published.

English, C.A., Eyre, B.L., Bartlett, A.F. and Wadley, H.N.G., 1977, Phil. Mag., 35, 533.

English, C.A., Eyre, B.L., Shoaib, K. and Williams, T.M., 1975, J. Nucl. Matls., 58, 220.

English, C.A., Eyre, B.L. and Summers, J., 1976, Phil. Mag., 34, 603.

Eyre, B.L., 1973, J. Phys. F., 3, 422.

Eyre, B.L. and Bullough, R., 1965, Phil. Mag., 12, 31.

Eyre, B.L., Maher, D.M. and Bartlett, A.F., 1971, Phil. Mag., 23, 439.

Eyre, B.L., Maher, D.M. and Perrin, R.C., 1974, Proc. 8th Intl. Congress on Electron Microscopy, Canberra, 1, 436.

Eyre, B.L., Maher, D.M. and Perrin, R.C., 1976, UKAEA (Harwell) Report, AERE-R8223.

Eyre, B.L., Maher, D.M. and Perrin, R.C., 1976b, UKAEA (Harwell) Report, AERE-R8224.

Föll, H. and Wilkens, M., 1977, Phys. Stat. Sol. (a), 39, 561.

Foreman, A.J.E. and Makin, M.J., 1978, UKAEA (Harwell) Report, AERE-R9030.

Freeman, J.H., 1969, UKAEA (Harwell) Report, AERE-R6138.

Freeman, J.H., 1970, UKAEA (Harwell) Report, AERE-R6254.

Friedel, J., 1956, Les Dislocations (Paris: Gauthier-Villars), 72.

Friedel, J., 1964, Dislocations (Pergamon Press).

Friedrich, W., Knipping, P. and Laue, M., 1913, Ann. Physik., 41, 971.

Gallagher, P.C.J., 1970, Met. Trans., 1, 2443.

Greenwood, G.W., Foreman, A.J.E. and Rimmer, D.E., 1959, J. Nucl. Matls., 1, 305.

Harries, D.R., 1974, UKAEA (Harwell) Report, AERE-R7934, 287.

Hashimoto, H., Howie, A. and Whelan, M.J., 1960, Phil. Mag., 5, 967.

Hashimoto, H., Howie, A. and Whelan, M.J., 1962, Proc. R. Soc., A269, 80.

Häussermann, F., 1972a, Phil. Mag., 25, 537.

Häussermann, F., 1972b, Phil. Mag., 25, 561.

Häussermann, F., 1972c, Phil. Mag., 25, 583.

Häussermann, F., Katerbau, K.H., Rühle, M. and Wilkens, M., 1973, J. Microscopy, 98(2), 135.

Häussermann, F., Rühle, M. and Wilkens, M., 1972, Phys. Stat. Sol.(b), 50, 445.

Heald, P.T. and Speight, M.V., 1977, J. Nucl. Matls., 64, 139.

Hirsch, P.B., 1966, Unpublished lecture to Symposium on the Nature of Small Defect Clusters, UKAEA (Harwell) Report, AERE-R5269.

Hirsch, P.B., Howie, A., Nicholson, R.B., Pashley, D.W. and Whelan, M.J., 1965, Electron Microscopy of Thin Crystals (Butterworths).

Hirsch, P.B., Howie, A. and Whelan, M.J., 1960, Phil. Trans. R. Soc., A252, 499.

Hirth, J.P. and Lothe, J., 1968, Theory of Dislocations (McGraw-Hill), 319.

Hislop, J.S., Sanders, T.W., Webber, T.J. and Williams, D.R., 1975, UKAEA (Harwell) Report, AERE-R8182.

Holmes, S.M., Eyre, B.L. and Perrin, R.C., 1976, Proc. 6th European Congress on Electron Microscopy, Jerusalem, 279.

Howe, L.M., McGurn, J.F. and Gilbert, R.W., 1966, Acta. Met., 14, 801.

Howie, A., 1963, Proc. Roy. Soc., A271, 268.

Howie, A. and Whelan, M.J., 1961, Proc. Roy. Soc., A263, 217.

Hudson, J.A., 1975, UKAEA (Harwell) Report, AERE-R7922.

Hudson, J.A. and Ashby, S.J., 1974, UKAEA (Harwell) Report, AERE-R7934, 140.

Hudson, J.A., Francis, S., Mazey, D.J. and Nelson, R.S., 1973, ASTM STP, 529, 326.

Jäger, W., Rühle, M. and Wilkens, M., 1975, Phys. Stat. Sol. (a), 31, 525.

Jäger, W. and Wilkens, M., 1975, Phys. Stat. Sol. (a), 32, 89.

Jakeman, D., 1966, Physics of Nuclear Reactors (The English Universities Press).

Jenkins, M.L., 1974, Phil. Mag., 29, 813.

Jenkins, M.L., 1975, Private communication.

Jenkins, M.L., Cockayne, D.J.H. and Whelan, M.J., 1973, J. Microscopy, 98(2), 155.

Jenkins, M.L., English, C.A. and Eyre, B.L., 1977, Submitted to Phil. Mag.

Jenkins, M.L. and Wilkens, M., 1976, Phil. Mag., 34, 1155.

Johnston, W.G. Rosolowski, J.H., Turkalo, A.M. and Lauritzen, T., 1974, J. Nucl. Matls., 54, 24.

Jøssang, T. and Hirth, J.P., 1966, Phil. Mag., 13, 657.

Jøssang, T., Lothe, J. and Skylstad, K., 1965, Acta. Met., 13, 271.

Katerbau, K.H., 1976, Phys. Stat. Sol. (a), 38, 463.

Katerbau, K.H., 1977, Private communication.

Katerbau, K.H., Rühle, M. and Wilkens, M., 1974, Proc. 8th Intl. Congress on Electron Microscopy, Canberra, 1, 438.

Lazarus, D., 1960, Solid State Physics (Academic Press), 10, 101.

Lindhard, J., 1965, Mat. Fys. Medd. Dan. Vid. Selsk., 34, No. 14.

Lindhard, J., Scharff, M. and Schiøtt, H.E., 1963, Mat. Fys. Medd. Dan. Vid. Selsk., 33, No. 14.

McIntyre, K.G., 1967, D. Phil. Thesis, Cambridge University.

McIntyre, K.G. and Brown, L.M., 1966, J. Phys. Radium, 27, C3-178.

Maher, D.M., 1970, Proc. 7th Intl. Congress on Electron Microscopy, Grenoble, 2, 349.

Maher, D.M., Bullough, R. and Perrin, R.C., 1971, Phys. Stat. Sol. (b), 43, 707.

Maher, D.M., Loretto, M.H. and Bartlett, A.F., 1971, Phil. Mag., 24, 181.

Makin, M.J. and Walters, G.P., 1974, UKAEA (Harwell) Report, AERE-R7934, 299.

Manning, I. and Mueller, G.P., 1974, Computer Physics Comm., 7, 85.

Marwick, A.D., 1975, J. Nucl. Matls., 55, 259.

Matthews, M.D., 1974, UKAEA (Harwell) Report, AERE-R7805.

Matthews, M.D., 1976, Private communication.

Merkle, K.L., 1966, Phys. Stat. Sol., 18, 173.

Merkle, K.L., 1969, Proc. Conf. on Rad. Damage in Reactor Materials, IAEA, Vienna, 159.

Nelson, R.S., Hudson, J.A. and Mazey, D.J., 1974, UKAEA (Harwell) Report, AERE-R7934, 119.

Noggle, T.S., Oen, O.S. and Crump, J.C., 1970, Proc. 28th Nat. Conf. EMSA, Houston, 406.

Norgett, M.J., Robinson, M.T. and Torrens, I.M., 1972, AERE Harwell Report, TP494.

Norris, D.I.R., 1967, UKAEA (Harwell) Report, AERE-R5269, 433.

Norris, D.I.R., 1969, Phil. Mag., 19, 527.

Ohr, S.M., 1976, Phys. Stat. Sol. (a), 38, 553.

Okamoto, P.R. and Wiedersich, H., 1974, J. Nucl. Matls., 53, 336.

Pearson, W.B., 1967, Lattice Spacings and Structures of Metals and Alloys (Pergamon Press), 2, 85.

Ruault, M.O., Jouffrey, B., Chaumont, J. and Bernas, H., 1975, Proc. Conf. Fund. Aspects of Rad. Damage in Metals, USERDA, Gatlinburg, Tennesse, 134.

Rühle, M., 1967a, Phys. Stat. Sol., 19, 263.

Rühle, M., 1967b, Phys. Stat. Sol., 19, 279.

Rühle, M., 1969, Proc. Conf. on Rad. Damage in Reactor Materials, IAEA, Vienna, 1, 126.

Rühle, M. and Wilkens, M., 1970, Proc. 7th Intl. Congress on Electron Microscopy, Grenoble, 2, 311.

Rühle, M., Wilkens, M. and Essmann, U., 1965, Phys. Stat. Sol., 11, 819.

Russell, K.C. and Powell, R.W., 1973, Acta. Met., 21, 187.

Saldin, D.K., 1977, To be published.

Saldin, D.K. and Whelan, M.J., 1975, Proc. of EMAG 75, Bristol, 393.

Schindler, R., 1978, Rad. Effects, 35, 17.

Schindler, R., Rühle, M., Frank, W. and Wilkens, M., 1976, Comm. in Physics, 1, 119.

Seybolt, A.U., 1936, Dissertation, Yale University.

Sigmund, P., 1974, Appl. Phys. Lett., 25, 169.

Silcox, J. and Hirsch, P.B., 1959, Phil. Mag., 4, 72.

Silcox, J. and Whelan, M.J., 1960, Phil. Mag., 5, 1.

Silsbee, R.H., 1957, J. Appl. Phys., 28, 1246.

Smithells, C.J., 1976, Metals Reference Book (5th Edition), (Butterworths).

Stathopoulos, A.Y., 1977, D. Phil. Thesis, Oxford University.

Topping, J., 1962, Errors of Observation and Their Treatment (3rd Edition), (Institute of Physics and The Physical Society).

Trinkaus, H., 1975, Proc. Conf. Fund. Aspects of Rad. Damage in Metals, USERDA, Gatlinburg, Tennesse, 254.

Whelan, M.J., 1959, Proc. Roy. Soc., A249, 114.

Whelan, M.J., 1966, Phil. Mag., 14, 195.

Wilkens, M., 1975, Proc. Conf. Fund. Aspects of Rad. Damage in Metals, USERDA, Gatlinburg, Tennesse, 98.

Wilkens, M., Rapp, M. and Differt, K., 1966, Z. Metallk., 57, 746.

Wilkens, M. and Rühle, M., 1966, Phys. Stat. Sol., 16, K105.

Wilkens, M. and Rühle, M., 1972, Phys. Stat. Sol. (b), 49, 749.

Williams, T.M., 1971, Proc. Conf. on 'Voids Formed by Irradiation of Reactor Materials', B.N.E.S., Reading, 205.

Wilson, M.M., 1970, D. Phil. Thesis, Oxford University.

Wilson, M.M. and Hirsch, P.B., 1972, Phil. Mag., 25, 983.

Yoffe, E.H., 1970, Phil. Mag., 21, 833.